Thèse n° 9491

# On Energy Control of Modular Multilevel Converters

Présentée le 6 avril 2023

Faculté des sciences et techniques de l'ingénieur
Laboratoire d'électronique de puissance
Programme doctoral en énergie

pour l'obtention du grade de Docteur ès Sciences

par

**Milan UTVIĆ**

Acceptée sur proposition du jury

Dr S.-R. Cherkaoui, président du jury
Prof. D. Dujic, directeur de thèse
Prof. S. Kenzelmann, rapporteur
Dr I. Colak, rapporteuse
Prof. C. Jones, rapporteur

École
polytechnique
fédérale
de Lausanne

2023

École Polytechnique Fédérale de Lausanne
Power Electronics Laboratory
Station 11
1015 Lausanne, Switzerland

http://pel.epfl.ch

*”Progress is made by trial and failure;*
*the failures are generally a hundred times*
*more numerous than the successes;*
*yet they are usually left unchronicled.”*

William Ramsay

# Abstract

Owing to the advancements in the area of power electronics, efficient and flexible ac to dc conversion is made possible, bringing back into focus the idea of the dc power transmission at various voltage levels. Several technical and economical factors advocate for building future distribution grids as dc instead of ac, as well as reusing the existing ac distribution infrastructure and converting it to dc.

Among various ac-dc converter topologies, the modular multilevel converter (MMC) stands out with its high reliability, availability achieved through redundancy, high efficiency due to low switching frequencies, elimination of bulky filters and transformers, and fast transient response. It is modular and scalable, offering the possibility to meet any voltage level using commercially-available semiconductors. For all these advantages the MMC family of converters has already found its application in various dc-ac, ac-dc, ac-ac, and dc-dc conversion tasks.

The MMC typically consists of a high number of submodules (SMs), built of a switching module and a floating capacitor, acting together as a variable voltage source. To ensure a proper operation of the converter, the voltage (energy) within the capacitors should be maintained around predefined values.

This thesis explores different mechanisms of the energy control within the standard dc-ac modular multilevel converter. The energy control mechanisms are identified and different methods for their realization are proposed. With respect to the existing solutions, presented solutions are intuitive, simple to implement, and extendable to different topologies from the MMC family of converters.

Due to its high availability achieved through redundancy, the MMC is nowadays applied in various applications, where a high degree of availability is expected, such as in high voltage dc (HVdc) transmission lines. For these reasons, it is also meant to operate properly under faulty conditions, such as grid unbalances, or a failure of a submodule. The proposed energy control methods are analysed for their application under such conditions, and a control method valid under normal and faulty conditions is proposed.

The modular multilevel matrix converter (M3C) is an ac-ac converter belonging to the family of MMCs. It shares the same need for the energy control as the standard ac-dc MMC. The proposed energy control concepts were analysed for the application in the M3C converter, for its various modes of operations and under faulty conditions. A novel energy control scheme was proposed, ensuring full control over the M3C arm energy content under all conditions.

Apart from the energy control, being the core of the thesis, this thesis also presents the development of an experimental test platform used for testing physical MMC submodules. Prior to being used in the real medium voltage (MV) converter, in-house developed submodules are exposed to the electrical and thermal stresses identical to the ones found in a real converter. In addition, the test platform was used to verify the submodule control, monitoring and protection features.

**Keywords:** modular multilevel converter, modular multilevel matrix converter, medium voltage, energy control

# Résumé

Grâce aux progrès dans le domaine de l'électronique de puissance, une conversion du courant alternatif (alternative current- ac) en courant continu (direct current- dc) flexible et efficace est rendue possible, relançant l'idée d'une transmission de puissance en courant continu à différents niveaux de tension. Différents facteurs techniques et économiques favorisent la construction des futurs réseaux de distribution en courant continu au lieu du courant alternatif ainsi que la réutilisation de l'infrastructure des réseaux de distribution ac existant pour la convertir en dc.

Parmi les différentes topologies de convertisseurs ac-dc, le convertisseur modulaire multiniveaux (Modular Multilevel Converter- MMC) se démarque de par sa haute fiabilité, sa disponibilité– de par la redondance des équipements, sa haute efficacité– de part les basses fréquences de commutation, l'élimination des filtres volumineux et des transformateurs, et sa réponse transitoire rapide. Il est modulaire et extensible, offrant la possibilité d'atteindre n'importe quel niveau de tension en utilisant des semiconducteurs disponibles commercialement. Pour tous ces avantages, la famille de convertisseurs MMC a d'ores et déjà trouvé son application dans de nombreuses tâches de conversion dc-ac, ac-dc, ac-ac et dc-dc.

Le MMC est typiquement constitué d'un grand nombre de sous-modules, eux-mêmes faits de l'assemblage d'un module de commutation et d'un condensateur flottant, agissant ainsi comme des sources de tension variables. Afin d'assurer la bonne opération du convertisseur, la tension aux bornes des capacités (et donc leur énergie) doit être maintenue autour de valeurs prédéfinies.

Cette thèse explore les différents méchanismes du contrôle de l'énergie au sein du convertisseur modulaire multiniveaux dc-ac standard. Les méchanismes de contrôle de l'énergie sont identifiés et différentes méthodes pour leur réalisation sont proposées. Par rapport aux solutions existantes, les solutions présentées sont intuitives, simples à implémenter et applicables à différentes topologies de la familles des convertisseurs modulaires multiniveaux.

Grâce à sa grande disponibilité réalisée par redondance, le MMC est aujourd'hui utilisé dans de nombreuses applications, où un haut degré de disponibilité est attendu, comme dans les lignes de transmission haute tension dc. Pour ces raisons, il doit aussi opérer en cas de faute, comme des déséquilibres dans le réseau, ou la panne d'un sous-module. Les méthodes de contrôle de l'énergie proposées sont analysées pour leur utilisation dans ces situations, et une méthode de contrôle valide en situation normale ou de faute est proposée.

Le convertisseur modulaire multiniveaux matriciel (modular multilevel matrix converter– M3C) est un convertisseur ac-ac appartenant à la famille des MMCs. Il partage le même besoin pour le contrôle de l'énergie que le convertisseur MMC ac-dc standard. Les concepts de contrôle de l'énergie proposés ont été analysés pour leur application au convertisseur M3C, pour ses différents modes d'opération, et lors de fautes. Une nouvelle méthode de contrôle de l'énergie a été proposé, assurant un contrôle total du contenu énergétique du bras M3C, dans toutes les conditions.

Mis à part le contrôle de l'énergie, qui est le coeur de la thèse, cette thèse présente aussi le développement d'une plateforme de test expérimental utilisée pour le test des unités physiques des sous-modules du MMC. Avant d'être utilisés pour un vrai convertisseur de tension moyenne, les sous-modules développés au sein du laboratoire ont été exposés aux stress électriques et themiques identiques à ceux trouvés dans un vrai convertisseur. En plus, la plateforme de test a été utilisée pour vérifier le contrôle des sous-modules, la supervision et les capacités de protection.

**Mots-clés**: convertisseur modulaire multiniveaux, convertisseur modulaire multiniveaux matriciel, moyenne tension, contrôle de l'énergie

# Acknowledgments

At the end of this part of my life, I want to express a sincere gratitude to my thesis supervisor, Dražen Dujić, who granted me the opportunity to explore the unknown, gain confidence and immeasurable professional experience. His challenging spirit made me test my limits, and grow professionally and personally. I specially want to thank him for his support and understanding during some difficult moments on the way. Thank you, Dražen!

I wish to thank the thesis jury members: Dr. Ilknur Colak (Schneider Electric), Prof. Stephan Kenzelmann (HES-SO Valais), and Prof. Colin Jones (EPFL) for accepting to evaluate this work. I also wish to thank Dr. Rachid Cherkaoui (EPFL) who accepted the role of jury president.

The work on this thesis was conducted within the frame of the Swiss Centre for Competence in Energy Research on the Future Electrical Infrastructure (SCCER-FURIES), with the financial support of the Swiss Innovation Agency (Innosuisse- SCCER program).

I also wish to thank all my professors from the University of Belgrade, who sparked my interest for the field of power electronics, especially to Prof. Slobodan Vukosavić, but also to my colleagues and friends Stefan Milovanović, Vladan Lazarević and Ivan Petrić, who excelled and continue to excel in the field, providing an inexhaustible source of inspiration.

I was privileged to spend three months in Traction Converter Development department of ABB Switzerland, as an intern during my PhD studies. I wish to thank Dr. Thomas Von Hoff and Dr. Stephan Kenzelmann, for providing me such an opportunity, but also to all the colleagues from the department for their kind attitude and support during the time.

I wish to thank my colleagues Philippe Bontemps, Max Dupont and Yanick Frei, for having read the thesis and provided some valuable suggestions.

Many thanks to all my friends for their unconditional support during the last years. Special gratitude to a group of Serbian friends from Lausanne, with whom I shared plenty of joyful and memorable moments.

I would use the opportunity to mention the names of some people who have had an important influence on me during my education: Miroslav Baščarević, Milan Đusić, Branko Kasalović, Ljubiša Krstović, Tatjana A. Mihajlović, Branka Kasalović, Gordana Božović, and Nebojša Đorđević.

Many things would have been different if it was not for my fiancée Marija. I thank her for her love and support through all these years.

The biggest gratitude I owe to my family, my parents and two sisters, for their unconditional love and understanding. This thesis I dedicate to them.

Lausanne, December 2022

# List of Symbols

| | |
|---|---|
| $C_{\mathrm{sm}}$ | Capacitance of a submodule |
| $N$ | Number of submodules within an arm |
| $V_{\mathrm{c}}^{\Sigma}$ | Total average voltage in the arm submodules |
| $i_{\mathrm{dc}}$ | dc terminal current |
| $i_{\mathrm{x,circ}}$ | Circulating current component in the arms of the phase leg $x$ |
| $i_{\mathrm{x,comm}}$ | Arm-common current component in the arms of the phase leg $x$ |
| $i_{\mathrm{x,diff}}$ | Arm-differential current component in the arms of the phase leg $x$ |
| $i_{\mathrm{xy}}$ | Current of the arm connecting the terminal nodes $x$ and $y$ |
| $i_{\mathrm{x}}$ | Current of the terminal $x$ |
| $i_{\Delta,\mathrm{x}}$ | Arm-common current component used for the arm-differential energy control in the phase leg $x$ |
| $i_{\Sigma,\mathrm{x}}$ | Arm-common current component used for the arm-sum energy control in the phase leg $x$ |
| $p_{\mathrm{xy}}$ | Power of the arm connecting the terminal nodes $x$ and $y$ |
| $u_{\mathrm{CM}}$ | Common-mode voltage |
| $u_{\mathrm{dc}}$ | dc terminal voltage |
| $u_{\mathrm{x,comm}}$ | Arm-common voltage component in the arms of the phase leg $x$ |
| $u_{\mathrm{x,diff}}$ | Arm-differential voltage component in the arms of the phase leg $x$ |
| $u_{\mathrm{xy}}$ | Voltage of the arm connecting the terminal nodes $x$ and $y$ |
| $u_{\mathrm{x}}$ | Phase voltage of the phase $x$ |
| $v_{\mathrm{c}}$ | Submodule capacitor voltage |
| $w_{\mathrm{xy}}$ | Energy of the arm connecting the terminal nodes $x$ and $y$ |
| $w_{\Delta,\mathrm{x}}$ | Difference between the arm energies in the phase leg $x$ |
| $w_{\Sigma,\mathrm{x}}$ | Sum of the arm energies in the phase leg $x$ |

# Contents

# 1
# Introduction

## 1.1 Winds of change

Although spanning over three centuries, electrical power systems are recently experiencing dramatic changes, governed by a multitude of factors. Technological disruptions, climate-change-related policies and energy economy are introducing a new era of electricity production, transmission and consumption.

Improvements in technology have driven wind and solar power plants to become the least expensive way of electricity generation in 2021, for most of the major markets globally [1]. Repercussions of such circumstances are that 82 % of newly installed electricity generation capacity in 2020 is from renewables, out of which 91 % (238 GW) are newly installed solar and wind power plants [2]. To meet the objectives set by the Paris Climate Agreement, newly installed capacity in solar and wind will have to surpass the current trends almost five-fold in the years preceding 2030. Depending on decarbonization pathways adopted by different countries, utility-scale solar power plants are expected to reach between 7.3 TW and 16.5 TW of installed capacity in 2050, compared to 714 GW in 2020. Wind power plants are expected to have the largest share in the electricity generation mix, with between 7 TW and 25 TW of installed capacity.

Global electricity demand is expected to increase almost four-fold by 2050, due to the greater energy demand in general, but also due to the greater use of electricity as the final energy source. Direct use of electricity as the final source is expected to dramatically increase in transportation, i.e. electric vehicles and short and mid-haul aircraft, in low-temperature industrial processes, and buildings [1]. Hydrogen is also expected to constitute a significant portion in the total energy mix, being used in power generation, industrial processes and transportation. Hydrogen production through the process of electrolysis is expected to account for almost 40% of electricity demand growth in the upcoming decades [3].

With the novel ways of electricity production and consumption, electrical power grids are also undergoing severe changes. Transmission power grids have already adopted the high voltage dc (HVdc) technology for a long-distance and offshore power transmission, whereas the same is expected to happen in medium voltage (MV) distribution grids. Such changes are driven by efficiency improvements, increased reliability and reduced overall costs. The key enablers of the transition are ever evolving power electronics converters and switching devices, which have paved the way for a new breed of electrical power systems.

## 1.2 Turn towards the dc grids

### 1.2.1 Benefits of the dc transmission

Owing to the advancements in the area of power electronics, efficient and flexible ac to dc conversion is made possible, bringing back into focus the idea of dc power transmission. Several technical and economical factors advocate for building future distribution grids as dc instead of ac, as well as reusing the existing ac distribution infrastructure and converting it to dc.

Using the same infrastructure, i.e. overhead transmission lines or underground cables, current capacity can be improved due to the several effects not present in dc networks. Skin effect increases the resistance of the ac transmission line/cable, thus creating additional power losses, and reducing the rated current of a given ac cable. Capacitive leakage current is another phenomenon that reduces the current capacity of the ac transmission line, particularly when it is realized using cables. Finally, dielectric losses are more pronounced in cables transmitting ac currents, resulting in reduced current capacity and accelerated ageing of a cable.

Voltage capacity of the existing transmission lines is also improved if they are operated under dc. Inductive voltage drop effectively reduces the voltage at the end terminal of the ac transmission line, the effect not present in dc. Insulation of the existing cables is designed for the peak voltage in ac systems, which permits the rated voltage increase of a replacement dc system.

Aforementioned technical benefits of the dc power transfer over the ac, lead to its application and consideration in several areas, previously dominated by ac.

### 1.2.2 Current and future applications of the dc power transfer

Increase of the capacity due to the absence of reactive current, as well as stability issues, have rendered HVdc power transmission systems a favourable solution for a long-distance power transfer. Bulk power transfer by undersea cables is another application area of the HVdc power transmission, mainly due to a high parasitic capacitive current in the ac systems. HVdc power transfer by undersea cables is principally used for interconnecting two power systems, or for the power transfer from offshore wind power plants. Although modern HVdc power systems date back to 1950s [4], last two decades have seen a massive increase in the HVdc projects worldwide, mainly driven by the Asian mainland power system projects, and large installations of offshore wind power plants globally.

Not only does the employment of dc technology shows advantage over ac in HVdc applications, but also in the collection grids for renewable energy sources, such as solar and wind. Various research studies were conducted showing the advantage of the medium voltage dc (MVdc) over the medium voltage ac (MVac) collection grids, both in terms of economical parameters and energy efficiency [5], [6]. In addition, studies from ABB [7], [8] show the economical and practical benefits of having offshore wind farms directly connected to the onshore substations by means of ±60 kV MVdc grids, for the offshore wind farms less than 70 km distant from the shore.

Due to the proliferation of distributed renewable energy sources, energy storage systems, ultra-fast charging stations for electric vehicles, future distribution grids might also shift from ac to dc. Moreover, the existing ac distribution cables can be re-purposed to dc, resulting in improved capacity, efficiency and flexibility, as suggested by [9]. Another study [10] shows that distribution system operators (DSOs) can benefit from future MVdc distribution grids, as the total costs of installation

and operation are heavily in favour of the MVdc over the standard low voltage ac (LVac) distribution grids.

Modern ships have electrical power distribution systems realized mainly as dc, either low voltage (LV) or MV. The key benefit of the on-board dc distribution is the absence of synchronization between multiple generators, permitting the use of high-speed generators without a gearbox, which results in improved efficiency and lower footprint [11]. Besides, it also results in reduced power losses and easier integration of energy storage systems, necessary for pulsed loads on military ships. In vessels with the total installed power of up to 20 MW, low voltage dc (LVdc) distribution systems are typically employed, whereas for higher rated power systems MVdc from 1 kV to 35 kV is considered [12].

Although the shift towards dc offers evident benefits, it will certainly not exist as a standalone in the future. Given the maturity of ac electrical power systems, the likely future scenario will be a hybrid grid, adopting the benefits of both systems. Power electronics converters will thus have an indispensable role in interfacing ac and dc grids, while at the same time providing the active and reactive power-flow control, fully electronic failure management and fast protection of associated equipment, as well as electronic current limitation in both ac and dc systems [13].

## 1.3 Medium voltage ac-dc converters

Potential contenders for the ac-dc converters in MV applications can be found in diode rectifiers, thyristor rectifiers, monolithic active rectifiers and modular multilevel converters. Each type of converter has its merits and weaknesses, and the following paragraphs aim to highlight the most important ones.

Diode rectifiers (DRs) are simple, robust and inexpensive converters, with a long legacy in ac-dc conversion. Nevertheless, the fact that it is an uncontrollable converter, where dc voltage is determined by the ac, means that the converter cannot remain in operation under a fault at either ac or dc side, neither can it actively control the fault current. In addition, they require bulky filters at the ac side to suppress the induced current harmonics. All these drawbacks do not satisfy the criteria for an ac-dc stage employed in modern MVdc grids.

Thyristor rectifiers (TRs) have a long tradition in HVdc applications, and even nowadays they are employed in extremely-high-power HVdc projects, such as recently commissioned 12 GW Xinjiang-Anhui ultra-HVdc project [14]. Contrary to uncontrollable DRs, TRs are controllable two quadrant converters, yet with the dynamics determined by the ac grid frequency. Although being able to provide dc voltage of both polarities, which is a desirable property in case of dc side faults, their slow dynamics, induced current harmonics, and inability to perform active current control on the ac side, puts them in unfavourable position for such an application.

A monolithic active rectifier is a type of converter able to actively control the dc side voltage and ac side currents, while allowing bidirectional power flow. Closed-loop control of the voltage across the output dc capacitor provides a dc voltage of good quality. A disadvantage of this converter is that its dc voltage is unipolar, and the range within it can be controlled is determined by the ac line-line voltage. Consequently, it cannot actively suppress dc fault currents, despite its high control bandwidth, determined by the switching frequency.

Typical representative of such a converter type is a two-level (2L) voltage-source converter (VSC),

commonly used in the range up to 1800 V. A limiting factor for its application in the higher voltage range is the maximum blocking voltage of commercially available power semiconductors applicable in VSCs, which is a couple of kilovolts. Although series connection of semiconductors could potentially solve the issue, it is coupled with a number of practical difficulties. Since the voltage is pulse-width-modulated, filters are required at the converter terminals, which could significantly contribute to the price of the installation. Additionally, fast changes of the pulse-width-modulated voltage at the ac terminals cause significant stress on the insulation of any equipment connected to the converter terminals, especially in the MV range.

The issues associated with the 2L VSCs can be alleviated by using multilevel monolithic VSC topologies, such as the neutral point clamped (NPC) converter, active NPC, and flying capacitor converters. NPC converters are type of diode-clamped converters which offer multilevel output voltage generation. Their voltage level can be increased compared to the 2L VSC, without employing semiconductors with higher ratings, owing to the clamping diodes. However, the problem is that the number of diodes is quadratically dependent on the number of levels. In practice, three-level NPC is the most frequently encountered converter of this type, typically found in MV drives.

Previously mentioned VSCs lack the ability to actively suppress the dc fault currents, lack true redundancy, and are not easily scalable to a higher voltage, which makes them unsuitable for the conversion tasks assumed for an ac-dc converter in future MV applications.

Modular multilevel converter (MMC) has been introduced by *Marquardt et al.* in 2002 [15], and has since then attracted a lot of interest by both academia and industry. It was originally proposed as a VSC for HVdc applications, and since its first commercial use in 2011, it has become a standard VSC solution for HVdc projects. Being the VSC it can offer many advantages over the traditionally-used line-commutated converters (LCCs), such as fast transient response, decoupled control of the active and reactive currents, easier control of multiterminal HVdc networks, and black-start capability [16]. Compared to the previously used two-level IGBT-stacked VSC, it offers improved reliability achieved through redundancy, improved efficiency, as well as elimination of bulky filters, due to the nearly-sinusoidal voltage.

A building block of the MMC is a submodule (SM) (c.f. **Fig. 1.1**), consisting of a storage dc capacitor and mostly HB or FB switching module. In order to meet certain voltage requirements, SMs are stacked in

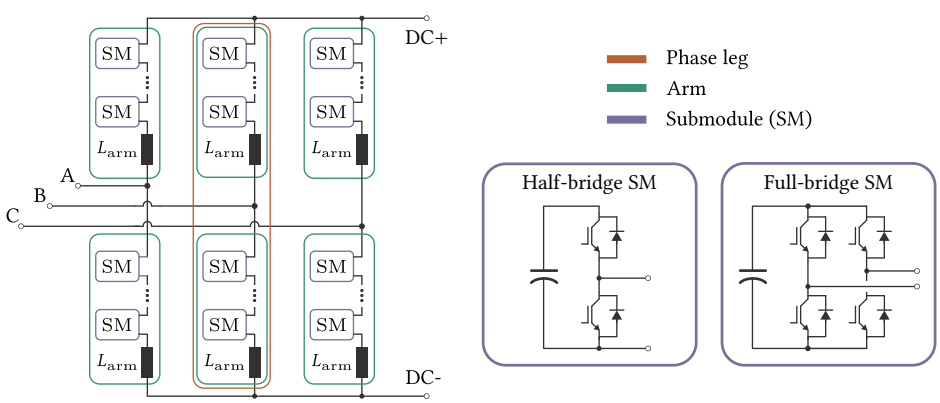


**Fig. 1.1** Schematic of a three-phase (3PH) ac/dc modular multilevel converter. Building block of the converter is a submodule (SM), which is typically realized as a half-bridge (HB) or full-bridge (FB).

series, thus being able to interface any voltage level using commercially-available semiconductors. For that reason the MMC is said to be *scalable*. The fact that they are built of identical SMs is a desirable property for any converter, both from the technical and economical point of view. Technically, *modularity* of the converter allows employment of redundancy principle, thus increasing converter's availability, as well as ease of maintenance, since a failed SM can be easily replaced. Economically, production of identical SMs is cost effective, due to the economy of scale [17].

Another advantage of the MMC is its very high efficiency, owing to the low switching frequencies of individual SM. Namely, in order to gain certain bandwidth in control of the ac and dc variables, converter terminal voltages are changed with a frequency being the product of the individual SMs switching frequency and the number of SMs being employed. Therefore, in case of high number of SMs, as in HVdc applications, switching frequency of an individual SM can be as low as fundamental AC terminal voltage frequency, thus ensuring high converter efficiency.

Due to the multilevel voltage waveforms, filtering requirements are reduced or even completely eliminated, thus further reducing the cost and the footprint of the overall installation.

Last, but not least, in order to control the dc voltage across its terminals, a dc link capacitor is not necessary at all [13], as the MMC benefits from its distributed capacitors over the SMs. Absence of a centralized dc link capacitor allows fast dc link voltage (or dc link current) control, which is a property not being offered by other types of converters.

Fast controllability of both ac and dc terminal voltages and currents, high availability due to the redundancy, bidirectional power flow, scalability to any voltage level, no filtering requirements, and high efficiency make the MMC a good candidate for the converter interfacing MVac with the future MVdc power networks.

## 1.4 Current and prospective applications of the MMC

### 1.4.1 HVdc power transfer

Thyristor-based LCCs are still dominating point-to-point HVdc power transmission, exceeding several giga-watts. Nevertheless, for multiterminal HVdc grids, with preferred black-start capability, the MMC set up to be the standard VSC solution over the last decade. Hitachi Energy, Siemens, Toshiba, and RXHK are some of the large providers of the MMC-based HVdc converters. Typical use cases are power transmission from offshore wind power plants to onshore substations, (undersea) cable interlinking of two power systems, long-distance power transmission, as well as interconnection of asynchronous grids. Illustrations of the typical use-cases of the MMC within the HVdc grids are presented in **Fig. 1.2**.

The first commercial use of the MMC technology in the HVdc power transmission was in Trans Bay project from Pittsburg to San Francisco, with rated power of 400 MW and bipolar dc grid voltage of ±200 kV. It was realized by Siemens in 2011. Contemporary MMC-based HVdc projects go as high as ±515 kV (NSL HVdc project [19]), and deliver as much as 2000 MW of power (ULTRANET – A-Nord [18]). If realized with the so-called full-bridge SMs, the MMC can offer a quick dc-fault clearance, thus eliminating the need for a solid-state dc circuit breaker. The very first commercialization of the MMC of such a type will be realized in ULTRANET–A-Nord project [18] in Germany, in 2023.

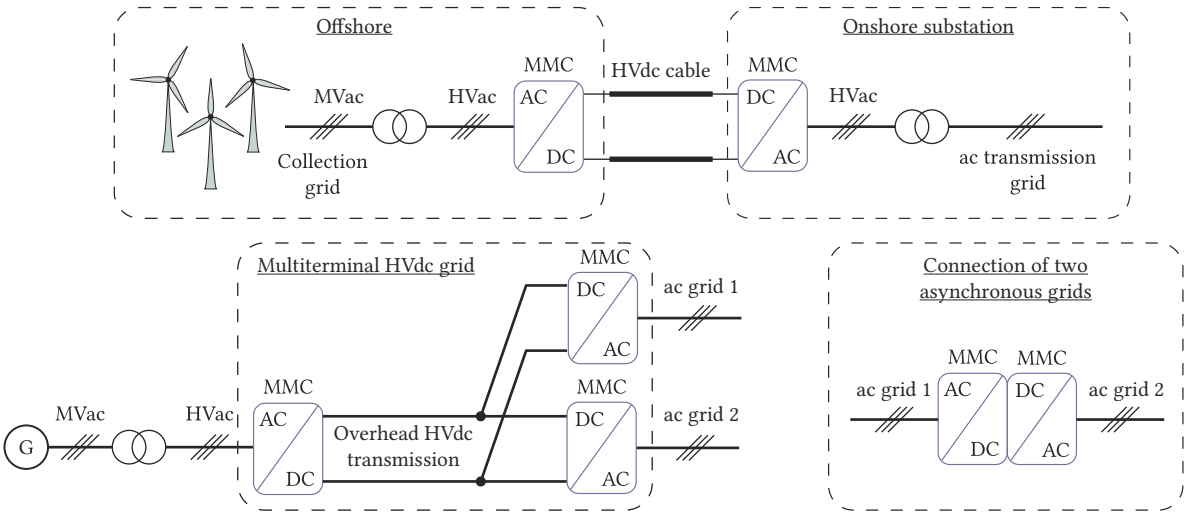


**Fig. 1.2** Typical use-cases of the MMC within the HVdc application: (top) Offshore to onshore power transmission using undersea HVdc cables; (bottom left) Multiterminal HVdc grid connecting multiple ac systems; (bottom right) back-to-back connection of two MMCs for interconnection of two asynchronous grids.

**Fig. 1.3** shows the offshore converter station of the BorWin3 HVdc project, realized by Siemens, as well as a valve hall of one of the *HVDC Light* projects, realized by Hitachi Energy.

### 1.4.2 MV variable-speed drives

Together with research activities in the HVdc domain, the application of the MMC in variable-frequency MV drives has been extensively studied [20]–[23].

Three-level NPC is a converter topology used by most of the medium-voltage drives suppliers [24]. Nevertheless, in order to reach higher voltage levels, either expensive semiconductors rated for higher blocking voltages are necessary, or the number of levels should be increased. Increase in the number of levels is coupled with an increase in the number of clamping diodes, resulting in a complex and expensive mechanical design of the low-inductive commutation paths [25]. Another

**Fig. 1.3** Photos of the contemporary HVDdc projects: (left) offshore converter station in BorWin3 HVdc project, realized using HB MMC by Siemens [18]; (right) MMC valve hall of an HVdc project realized by Hitachi Energy [19].

widely-used topology in medium-voltage drives is the cascaded H-bridge (CHB) inverter, with the SMs supplied from a transformer with multiple isolated secondary windings, each with a dedicated rectifier. While this topology can ensure to meet higher voltage levels and offers redundancy principle, a multi-winding transformer should be designed for each new configuration of the SMs.

MMC for drives applications offers several advantages, such as ease of scalability, high availability achieved through redundancy, and motor-friendly multilevel waveforms, among others. It benefits from the inexpensive low-voltage capacitors and switching devices, and has no scalability constraints, as the other two topologies. Besides lower power density, a weakness of the MMC topology is also a high capacitor voltage ripple in the low-frequency mode of operation, for loads with a constant torque characteristic [21]. Hence, they are suitable for loads with higher operating frequencies and quadratic torque characteristics.

Commercial electric drives based on the MMC topology are today manufactured by Siemens, Benshaw, and General Electric [26]–[28]. Examples of the MV drives, SINAMICS SH150 from Siemens and M2L Series from Benshaw, are shown in **Fig. 1.4**.

**Fig. 1.4** Commercially available MV drives based on the MMC topology: (left) Siemens SINAMICS SH150; (right) Benshaw M2L Series.

### 1.4.3 Pumped-hydro storage plants and railway inter-ties

Pumped-hydro storage plants are gaining importance with the ever increasing share of the intermittent sources of electrical energy, such as wind and solar. Converter-fed variable-frequency synchronous machines are a favourable choice for this application, and back-to-back connection of two active NPC converters used to be a preferred topology for interconnection of the grid and the machine [29].

With the introduction of the MMC arose the idea of using a so-called *indirect MMC* for interfacing the grid and the synchronous machine [30]. It represents a simple back-to-back (B2B) connection of two MMC units. Besides increased availability, ability of the MMC to meet any voltage level renders the machine-side power transformer unnecessary, thus improving the overall efficiency and reducing the footprint.

As the MMC suffers from the high voltage ripple in the SMs at low machine frequencies, variable speed operation is guaranteed only if the common-mode voltage and circulating currents are injected [21], [31], which might not be always permitted, and in general negatively influences converter efficiency and cost.

Modular multilevel matrix converter (M3C) is an ac-ac converter topology, belonging to the family

of the modular multilevel converters. It was introduced by *Ericksson et al.* in 2001 [32], before the standard ac-dc MMC. Despite being introduced as independent converter topologies, the employed control schemes of the two are to a great extent similar, and the M3C is often referred to as *direct MMC*.

It has been shown by [33], [34] that the direct MMC is better suited than the indirect MMC to variable speed operation with low nominal frequencies. It can better handle machine startup with the rated torque, has lower SM count, and better overload capability [29]. First 3PH - 3PH direct MMC for pumped-hydro storage plants was commissioned in Austria in 2020 by Hitachi Energy.

Besides pumped-hydro storage plants, the direct MMC proves to have superior performance in case of a 3PH (50 Hz) to single-phase (1PH) (16.7 Hz) railway interties [35]. Authors in [36] analyse the behaviour of the integrated gate-commutated thyristor (IGCT)-based 3PH-1PH direct MMC for railway interties, demonstrating the robustness of such a converter. It is commercially available, and offered by Siemens under the product line *Sitras SFC Plus* [37], and Hitachi Energy under the product line *Rail SFC Light* [38].

### 1.4.4 MVdc shipboard distribution

Shipboard power distribution systems based on dc are being conceived today both for commercial and military vessels. In case when the power consumption exceeds 20 MW, MVdc power distribution systems are favourable over the LVdc ones, with a recommended voltage range between 1 kV-35 kV [12]. Benefits of the dc shipboard distribution systems are, among others, the following:

- No need for synchronization of phase angles between different synchronous generators. This also permits using high speed generators, resulting in the reduced weight of the power system.
- Reduced resistive losses and no inductive voltage drop on the distribution grid.
- Easier integration of the energy storage elements, such as batteries and fuel cells, observed through improved efficiency and controllability of the power flows in transient and emergency situations.

Due to the need for an MV ac-dc converter as an interface between the generator and the distribution network, several authors propose the use of the MMC [39]–[41]. Besides increased reliability achieved through redundancy, the MMC can also block dc short circuits, and thus inherently provide a service of a solid-state dc breaker. Authors in [42] analyze a hybrid-MMC for shipboard electrical systems, as means for interconnecting the MVac generators with an MVdc distribution network, while integrating battery energy storage into the converter SMs. This topology allows uninterrupted operation of the converter and the storage system, regardless of the possible failures at either dc or ac grid.

To interface the shipboard MVdc distribution network and the other dc loads or energy storage, an isolating dc-dc converter is necessary. Several authors have addressed this issue by proposing the MMC-based dc-dc converter with isolating transformer [43]–[45]. Even though the dc-dc MMCs have been extensively analysed in the literature for other applications, such as HVdc, they are not of particular concern of this thesis. Within the context of the shipboard power conversion, the MMC has also been proposed by [46] for supplying the LV ac loads from the MVdc distribution network.

### 1.4.5 Integration of distributed renewable energy sources and storage systems

As wind turbines are growing in size and in rated power, reaching 14 MW to this date [47], there is a tendency of replacing the low-voltage generators for 690 V by the medium-voltage 6.6 kV permanent-magnet generators [48], [49].

No filtering requirements, scalability to higher voltage levels and high availability of MMC topologies make them particularly attractive for offshore wind applications, where the accessibility is reduced and the maintenance costs are high.

Depending on the type of a collection grid (ac or dc), ratio between the grid and the machine voltage, frequency range of the permanent-magnet synchronous generator (PMSG), and fault ride-through (FRT) capability, different MMC-based topologies are found to be optimal [48], [50], [51]. Authors in [48] provide a design process of an MMC with integrated ultracapacitors as energy storage elements, with the main focus on the FRT capability. Another proposal for the use of the M3C in wind power applications is for offshore-to-onshore fractional frequency power transmission [52].

As previously mentioned, when it comes to wind energy harvesting, the MMC is mostly used as an interface converter for the HVdc offshore power transfer.

Solar energy is equally penetrating the energy mix as does the wind. To provide a connection of a photo-voltaic (PV) plant to a distribution grid, without using a filter and a power transformer, the authors in [53] proposed the use of the MMC for grid connection of the solar power plant. Further investigation is conducted in [54], with a focus on applicable modulation methods. In both cases the MMC interfaces the PV plant connected to its dc terminals and ac grid.

Partial shading conditions can negatively influence the overall yield of a PV plant connected to dc terminals of an MMC. To fully utilize the potential of a PV power plant, authors in [55] proposed the MMC converter structure with PV strings connected to the MMC SMs dc terminals. In this case, grid-code compliant operation of a PV plant, with maximally possible power yield is ensured.

Power yield of the renewable energy sources, such as solar and wind, is generally varying throughout the day and year, and together with the varying power consumption of the end-users, deteriorates power quality of the grid. To alleviate the power-quality-related issues and fully utilize potentials of the renewable energy sources, energy storage systems are a possible solution [56].

With the wind and solar farms collection grids realized as MVdc grids, an MMC with distributed batteries is a good candidate for the connection to the MVac grid, while integrating LV batteries. It has been firstly proposed by [57], and later analysed in more detail by [42], [48], [58]–[60], as an interface converter between MV ac and dc grids. It allows omnidirectional power flow between the two grids and the energy storage units, as well as the reactive power compensation. Furthermore, in case of failure on either ac or dc grid, the MMC with integrated batteries can remain in operation and exchange the energy with the healthy grid [42], or store the excess energy during the fault ride-through [48]. Nevertheless, these proposals have mainly remained in the academic world thus far, without commercial deployments in the field.

## 1.5 Objectives of the thesis

Previous sections have briefly outlined current and prospective applications of the MMC. Behaviour of the MMC in all mentioned applications will depend upon requirements of a given application, and will mostly influence its terminal voltages and currents. Vast amount of research has been conducted thus far on the MMC internal as well as application-specific control and protection schemes, with the former being more general.

Given the great advantages offered by the MMC and related topologies, as well as considerable interest of both academia and industry in the MMC topology, the intention of the author of this thesis was to address some of the internal control problems, that are application independent, and thus applicable to the MMC and M3C serving various applications.

In addition to the theoretical studies, considerable effort was put in development of a laboratory MMC MV prototype, consisting of two MMC units, acting as an MVdc source.

Briefly, objectives of the thesis could be summarized as follows:

- While MMC offers many advantages over other converter topologies, presence of floating capacitors in the converter SMs necessitates advanced control schemes to ensure the capacitor voltages are stable and around predefined values. Different energy/voltage control schemes were presented in the literature, both for the MMC and the M3C. Control schemes were also evaluated under different scenarios, such as unbalanced grid conditions, failure of a SM, short circuit at the dc terminals, etc. General energy control approaches, applicable to various converter structures and using different degrees of freedom, are also available in literature. While most of the proposed solutions offer good static and dynamic behaviour of the controlled variables (voltages of the SMs capacitors), they either lack simplicity of implementation, or generality in terms of their application to various MMC-alike topologies. Therefore, the intention of the author was to systematically cover the energy control issue in the MMC, yielding intuitive and effective solutions, with a simple implementation and extensibility to other similar topologies, such as the M3C.

- One of the merits of the MMC is its high availability achieved through redundancy. As the events in the grids interconnected by the MMC can be various, the MMC should be capable of operating under faulty conditions. Energy content within the MMC arms should correspond to the energy references, in order to enable proper generation of the arm voltages. To meet the objective, terminal, as well as internal currents must be controlled in a way that ensures that the arm energies correspond to their references. Energy content within each arm should be controlled independently, thus allowing the greatest possible flexibility of the converter operation. Proposed control methods should be valid during normal as well as faulty conditions, such as grid unbalances and a SM failure. Therefore, the objective was that the proposed control methods can be readily used under both normal and faulty conditions, all while retaining the abovementioned merits.

- Low-voltage SMs design, manufacturing, testing and integration into the converter, was part of development activities of the MMC laboratory prototype. Cost of the equipment, as well as a high number of SMs in the MMC call for different layers of protection and supervision, which would minimize the risk of a great damage in case of undesired scenarios. Prior to deploying the SM into the converter prototype, a thorough testing of its local control and protection features

has to be performed. In addition, the SM should undergo the same conditions as those present in the real converter, to test its ability to handle electrical and thermal stresses identical to the ones found in the MMC under consideration. One of the objectives was to devise a test platform for thorough SM testing, which would allow to test the SMs under realistic operating conditions. Additionally, to further minimize the risks, the test platform should permit employing the control principles applied for the converter-level control, and verifying them using a minimal set of SMs prior to their deployment to the actual converter.

## 1.6 Outline of the thesis

This thesis is organized in seven distinctive chapters. A summary of the content of each chapter is provided in the following paragraphs:

- **Chapter 2** introduces the MMC converter operation and modelling to a reader. Basic equations, descriptions of the dynamics of terminal variables, internal control loops, capacitor voltage variations, and as well as the main control challenges are outlined in this chapter. In addition, basic equations of the M3C topology are covered, with the specific focus on the arm current, voltage and power components, necessary to supplement the conducted analyses.

- **Chapter 3** discusses the energy control of the MMC and derives two distinctive methods applicable in the MMC control. It outlines benefits and drawbacks of both methods, and provides mutual comparison. Implementation of the two energy control approaches is presented, and verified by high-fidelity simulation results.

- **Chapter 4** extends the derived energy control methods to the faulty conditions in the MMC, specifically to the unbalanced grid conditions, and to the case of a failed SM condition, with the objective of having uninterrupted operation of the MMC. It shows that the proposed control method can be equally used under faulty conditions, and meets all the objectives set.

- **Chapter 5** evaluates presented energy control methods for application in the M3C control. It shows that the control concept from **Chapter 4** can be extended to the M3C, resulting in a simple and intuitive approach for the M3C control under various operating conditions, including grid faults and no-load conditions. Its functionality is verified using the hardware-in-the-loop (HIL) simulator of the M3C, having the control architecture equivalent to the industrial grade converter.

- **Chapter 6** presents development of a test platform, used for testing hardware and software features of the MMC SMs. The platform was developed with the aid of a HIL system, where important test scenarios were verified, prior to being carried out on the physical SMs. The HIL system is based on the same control architecture, real-time simulator and arm model, as the HIL system used for the development and testing of the converter-level control. The test platform was primarily used to expose the SMs to the electrical and thermal stresses, equivalent to those in the real converter. Additionally, the platform was used to evaluate fidelity of the HIL system-based results, and thus de-risk development of the converter-level control.

- **Chapter 7** provides a summary of the conducted work, draws conclusions out of the research topics, and outlines some open questions that might be subject of future work.

## 1.7 List of publications

**Journal papers:**

$J_1$ **M. Utvić** and D. Dujić, "Generalized theory on direct arm energy control in modular multilevel converters," in CPSS Transactions on Power Electronics and Applications, vol. 5, no. 4, pp. 388-399, Dec. 2020, doi: 10.24295/CPSSTPEA.2020.00032.

$J_2$ **M. Utvić**, P. Bontemps and D. Dujić, "Direct Arm Energy Control of the Modular Multilevel Matrix Converter," in IEEE Access, vol. 11, pp. 1793-1805, 2023, doi: 10.1109/ACCESS.2023.3234013..

$J_3$ A. Christe, M. Petkovic, I. Polanco, **M. Utvic** and D. Dujic, "Auxiliary submodule power supply for a medium voltage modular multilevel converter," in CPSS Transactions on Power Electronics and Applications, vol. 4, no. 3, pp. 204-218, Sept. 2019, doi: 10.24295/CPSSTPEA.2019.00020.

$J_4$ S. Milovanovic, I. Polanco, **M. Utvic** and D. Dujic, "Flexible and Efficient MMC Digital Twin Realized With Small-Scale Real-Time Simulators," in IEEE Power Electronics Magazine, vol. 8, no. 2, pp. 24-33, June 2021, doi: 10.1109/MPEL.2021.3075803.

$J_5$ M. Basić, **M. Utvić** and D. Dujić, "Hybrid Modular Multilevel Converter Design and Control for Variable Speed Pumped Hydro Storage Plants," in IEEE Access, doi: 10.1109/ACCESS.2021.3118277.

**Conference papers:**

$C_1$ **M. Utvic**, I. P. Lobos and D. Dujic, "Low Voltage Modular Multilevel Converter Submodule for Medium Voltage Applications," PCIM Europe 2019; International Exhibition and Conference for Power Electronics, Intelligent Motion, Renewable Energy and Energy Management, 2019, pp. 1-8.

$C_2$ **M. Utvić**, S. Milovanović and D. Dujić, "Flexible Medium Voltage DC Source Utilizing Series Connected Modular Multilevel Converters," 2019 21st European Conference on Power Electronics and Applications (EPE '19 ECCE Europe), 2019, pp. 1-9, doi: 10.23919/EPE.2019.8915466.

$C_3$ **M. Utvic** and D. Dujic, "Direct Arm Energy Control in Modular Multilevel Converter Under Unbalanced Grid Conditions," 2020 International Symposium on Power Electronics, Electrical Drives, Automation and Motion (SPEEDAM), 2020, pp. 250-256, doi: 10.1109/SPEEDAM48782.2020.9161828.

# 2

# Modelling and Operating Principles of Modular Multilevel Converters

*To familiarize with basic operating principles and modelling of the MMC, the topology of the MMC is presented in this chapter along with its relevant terminal and internal variables. Operating range, fault-handling capability, and internal converter dynamics are also subject of the chapter. Influence of different methods of reference calculation on the converter performance is analysed, along with various multi-level modulation schemes. Due to the fact that some control methods presented in the thesis will be applied to the modular multilevel matrix converter, its basic operating principles will also be covered in this chapter.*

## 2.1 MMC topology: basic elements and properties

CHB converters have paved the way to a new breed of multilevel converters. Firstly proposed for MV motor drives [61], similar concept was later introduced for static synchronous compensator (STATCOM) application [62]. *Lesnicar and Marquardt* proposed the MMC - a new converter topology suitable for a high voltage and high power range [63]. The converter is originally conceived as an ac-dc converter for HVdc applications. Since there are many variations of the topology, a 3PH ac-dc MMC is referred to as *standard MMC* within this thesis, or simply MMC. In contrast, a 3PH ac-ac matrix MMC will be simply referred to as M3C.

In the standard MMC each phase of its ac terminals is connected to the dc terminals by two MMC arms, thus constituting a phase leg, as shown in **Fig. 2.1**. Arms in the original MMC topology featured series connection of HB SMs without an arm inductor, whereas the later publications [64]–[67] assumed an arm inductor as part of the arm.

Basic building block of the MMC is a SM. In principle, each SM consists of a floating dc capacitor and a switching module, typically realized as an HB or FB module **Fig. 2.1**. In case of an HB SM, the output voltage of an SM can be either zero, or equal to the capacitor voltage $V_C$. In case when the switching module is of FB type, three distinctive output voltage levels can be realized: $V_C$, 0, and $-V_C$. While many other SM types have been proposed in literature [68]–[71], the two abovementioned are most commonly analysed and applied due to their simplicity.

The number of SMs per arm is equal in all the arms, in order to guarantee symmetrical operation, and is labelled as $N$. Floating capacitors in the SMs are dynamically charged and discharged during operation, and it is one of the control objectives to ensure the voltages of all the capacitors are around their rated value. At the same time, this is one of the key advantages of the topology, as the capacitors do not need external power supply, like in the case of a CHB converter. Stacking a high number of

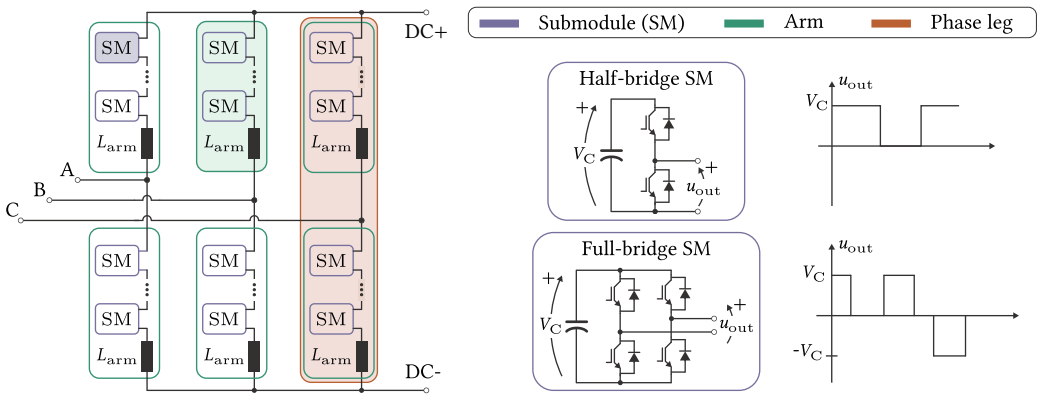


**Fig. 2.1** Schematic of a 3PH ac-dc modular multilevel converter (MMC). Building block of the converter is a submodule (SM), which is typically realized with a half-bridge (HB) or full-bridge (FB) switching module.

SMs in series results in a reduced rated voltage of the SM capacitors for a given application. As the rated voltage of a switching module within the SM is defined by the rated voltage of the SM capacitor, high number of SMs within an arm permits the use of commercially-available low-cost capacitors and semiconductors in the SMs, even for ultra-high voltage applications.

A stack of series-connected SMs can be perceived as a controllable multilevel voltage source, provided that the voltages of the individual SM capacitors are mutually balanced. Multilevel voltage waveforms at the converter terminals (c.f. **Fig. 2.2**) render terminal filters unnecessary and reduce the stress on the insulation caused by a high $dv/dt$. High number of SMs allows generating terminal voltage references with very low switching frequencies of individual SMs, making the converter highly efficient.

During operation, each SM can be in either of the three following states: *inserted*, *bypassed*, and *idle*. *Inserted* SM has its capacitor directly connected to the SM terminals, inserting to the arm either a positive (HB and FB), or a negative capacitor voltage (FB). When a SM is not expected to insert any voltage to the arm, it is simply *bypassed*, providing zero voltage at its terminals. Finally, in case of terminal or SM faults, switching commands to a SM can be suppressed, bringing the SM into a so-called *idle* state.

Owing to the fact that a SM can be inserted into the arm, or bypassed from it, redundancy principle

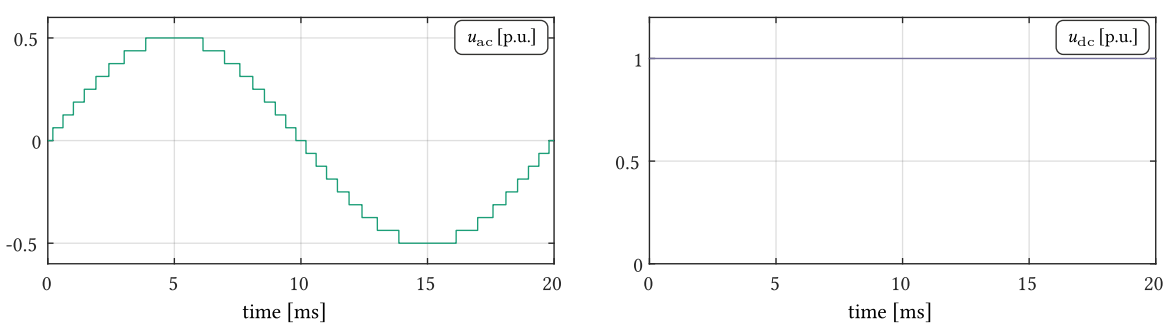


**Fig. 2.2** Idealized terminal voltages of an MMC converter with $N = 16$ SMs per arm, obtained using the nearest-level modulation: (left) ac terminal phase voltage; (right) dc terminal voltage. Voltage values are normalized with respect to the rated dc terminal voltage.

can be applied by having a redundant SM, resulting in improved availability of the converter. Namely, in case a fault is detected in a SM, affected SM is bypassed, whereas the redundant one takes over its duty, and the arm seamlessly continues synthesizing the voltage reference.

Modular design also drives down the manufacturing costs due to the economy of scale, and facilitates maintenance, as a faulty SM is simply replaced by a redundant one during operation, or with a new one during a scheduled maintenance.

## 2.2 Modelling of the MMC

To facilitate understanding of the MMC operation, certain nomenclature should be adopted, which will be utilized throughout the thesis. **Fig. 2.3** shows electrical schematic of the MMC topology, together with the relevant nomenclature.

A stack of SMs within an arm is equivalently represented with a voltage source $u_{\mathrm{x,y}}$, where $x$ denotes an arm connected to a positive (p) or negative (n) dc terminal, whereas $y$ corresponds to a phase of the ac terminal to which the arm is connected, $y = \{A, B, C\}$. The voltage of an equivalent voltage source $u_{\mathrm{x,y}}$ is a sum of the terminal voltages $u_{\mathrm{out}}^{\mathrm{x,y,z}}$ of the individual SMs (denoted by the superscript $z$) within the $xy$ arm. Taking into account a switching function $S_{\mathrm{x,y,z}}$ of an individual SM, and denoting capacitor voltages of the individual SMs as $v_{\mathrm{c}}^{\mathrm{x,y,z}}$, the equivalent arm voltage $u_{\mathrm{x,y}}$ can be expressed as:

$$u_{\mathrm{x,y}} = \sum_{z=1}^{N} u_{\mathrm{out}}^{\mathrm{x,y,z}} = \sum_{z=1}^{N} S_{\mathrm{x,y,z}} v_{\mathrm{c}}^{\mathrm{x,y,z}}, \quad \text{where} \quad S_{\mathrm{x,y,z}} = \begin{cases} \{0, 1\}, & \text{for half-bridge SMs} \\ \{-1, 0, 1\}, & \text{for full-bridge SMs} \end{cases} \tag{2.1}$$

Relationship (2.1) demonstrates that by controlling the switching functions of individual SMs, a stack of SMs behaves as a controllable voltage source, yielding a multilevel voltage waveform of a desired form.

To define terminal voltages, the mid-point of the dc terminal is chosen as a reference point (labelled as $N_{\mathrm{dc}}$ in **Fig. 2.3**), even though in some cases it might be physically unavailable. Nevertheless, the results of analyses do not depend on a chosen reference point, so theoretically, any point in the shown schematic could be chosen as the reference. Neutral point of the ac terminals is labelled as $N_{\mathrm{ac}}$, and generated ac terminal voltages are referred to this point. The voltage between the ac neutral point and the dc mid-point is referred to as *common-mode voltage*, labelled as $u_{\mathrm{CM}}$.

Following the same logic as for the arm voltages, arm currents are denoted as $i_{\mathrm{x,y}}$, and they can be decomposed into a common and differential components, as will be shown shortly. Owing to the fact that the topology is symmetrical with respect to its ac and dc terminals, to derive meaningful conclusions it is sufficient to analyse the quantities within a single phase leg. Writing Kirchoff's voltage equations for a positive and negative arm of a single phase yields:

$$\frac{u_{\mathrm{dc}}}{2} = u_{\mathrm{x,p}} + L_{\mathrm{arm}} \frac{di_{\mathrm{x,p}}}{dt} + u_{\mathrm{x}} + u_{\mathrm{CM}} \tag{2.2}$$

$$\frac{u_{\mathrm{dc}}}{2} = u_{\mathrm{x,n}} + L_{\mathrm{arm}} \frac{di_{\mathrm{x,n}}}{dt} - u_{\mathrm{x}} - u_{\mathrm{CM}} \tag{2.3}$$

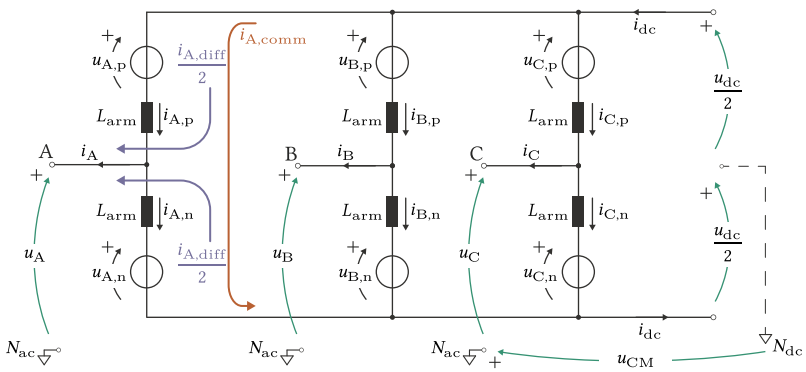


**Fig. 2.3** MMC topology with the relevant terminal and internal variables. Arm currents are expressed by their arm-common and arm-differential components. Common-mode voltage is defined as a voltage between the grid neutral point and dc terminal mid-point.

By subtracting the two equations, a relationship between the arm voltages and the ac terminal voltage can be obtained:

$$\underbrace{\frac{u_{x,n} - u_{x,p}}{2}}_{u_{x,diff}} = \frac{L_{arm}}{2}\frac{d}{dt}\Big(\underbrace{i_{x,p} - i_{x,n}}_{i_{x,diff}=i_x}\Big) + u_x + u_{CM} \quad \Longrightarrow \quad u_{x,diff} = \frac{L_{arm}}{2}\frac{di_x}{dt} + u_x + u_{CM} \tag{2.4}$$

Ac terminal current $i_x$ is determined by the difference between the positive and negative arm currents. Under balanced conditions, the two arms should equally contribute to the ac terminal current. This current component is referred to as arm-differential current component $i_{diff}$. It is shown by (2.4) that the ac terminal, or arm-differential current, can be controlled by controlling the arm-differential voltage $u_{diff}$. Conversely, in case when the MMC acts as a grid-forming converter, the ac terminal voltage $u_x$ can be controlled by means of the arm-differential voltage. Equivalent circuit of the MMC ac terminal and corresponding arm-differential quantities are depicted in **Fig. 2.4.a**.

On the other hand, should one sum up the equations (2.2)-(2.3), arm voltages can be related to the dc terminal values as:

$$\frac{u_{dc}}{2} = \underbrace{\frac{u_{x,p} + u_{x,n}}{2}}_{u_{x,comm}} + L_{arm}\frac{d}{dt}\Bigg(\underbrace{\frac{i_{x,p} + i_{x,n}}{2}}_{i_{x,comm}}\Bigg) \quad \Longrightarrow \quad \frac{u_{dc}}{2} = u_{x,comm} + L_{arm}\frac{di_{x,comm}}{dt} \tag{2.5}$$

Arm-common current component $i_{comm}$ is a mutual current component of two arms within a phase leg. It is thus not observed at the ac terminals, however a portion of this current constitutes the dc terminal current. In ideal conditions, dc terminal current is equally split among the three phase legs, therefore the arm-common current component is in ideal conditions equal to $i_{dc}/3$. Nevertheless, there may exist cases where the dc terminal current is unequally shared among the phase legs, as will be discussed within **Chapter 4**. To better comprehend the difference between the arm-common and arm-differential current components, one can refer to **Fig. 2.3**, where the two are shown in orange and purple, respectively.

Besides the dc current, the arm-common current can contain other current components, observable neither at the ac, nor at the dc terminals. Such current components are termed *circulating currents*,

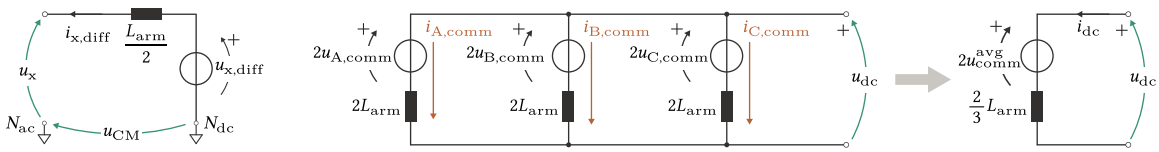


a) b)

**Fig. 2.4** Equivalent circuits for the: a) ac terminal current (voltage) control; b) circulating current and dc terminal current (voltage) control.

and can have parasitic nature, or can be intentionally introduced by the control algorithm. These current components will be further labelled as $i_{circ}$, as in (2.6). All arm-common current components that satisfy the condition (2.7) have circulating nature.

$$i_{x,comm} = i_{x,dc} + i_{x,circ} \tag{2.6}$$

$$i_{A,circ} + i_{B,circ} + i_{C,circ} = 0 \tag{2.7}$$

Based on (2.5), the arm-common current is controlled by the arm-common voltage component $u_{comm}$, as it is graphically shown in **Fig. 2.4.b**. By controlling the arm-common current in each phase leg, a portion of the dc terminal current of that respective phase is controlled. Such components of the three phases constitute the dc terminal current. Similarly to the ac quantities, in case when the MMC acts as a dc grid-forming converter, the dc terminal voltage can be controlled by the appropriate control of the arm-common voltages of the three phases. Equivalent circuit of the MMC, observed from its dc terminals is shown in **Fig. 2.4.b**. Equivalent voltage source, relevant for the dc terminal voltage/current control is obtained as an average of the three voltage sources in **Fig. 2.4.b**, as shown in (2.8). Similarly, equivalent inductance observed from the dc terminals is a parallel connection of the three inductances form **Fig. 2.4.b**, calculated as in (2.9).

$$u^{avg}_{comm} = \frac{u_{A,comm} + u_{B,comm} + u_{C,comm}}{3} \tag{2.8}$$

$$L_{eq} = \frac{2}{3} L_{arm} \tag{2.9}$$

From **Fig. 2.4** it can be concluded that all MMC-related quantities can be controlled independently one from another. While the ac terminal voltages/currents are controlled by means of the arm-differential voltage, dc terminal voltage/current and circulating currents are controlled by means of the arm-common voltage quantities.

Based on the previous discussion, arm voltages and currents can be expressed in terms of their common and differential components as in (2.10)-(2.13). Ideal waveforms of arm voltages and currents within a phase leg of an MMC are illustrated in **Fig. 2.5**.

$$u_{x,p} = u_{x,comm} - u_{x,diff} \tag{2.10}$$

$$u_{x,n} = u_{x,comm} + u_{x,diff} \tag{2.11}$$

$$i_{x,p} = i_{x,comm} + i_{x,diff}/2 \tag{2.12}$$

$$i_{x,n} = i_{x,comm} - i_{x,diff}/2 \tag{2.13}$$

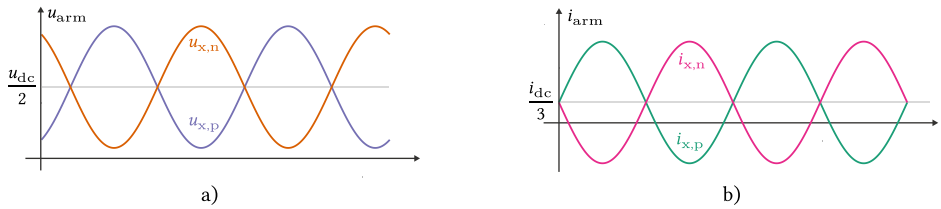


**Fig. 2.5** Ideal waveforms of arm quantities: a) positive and negative arm voltages; b) positive and negative arm currents.

Besides the fact that the available degrees of freedom permit independent control of the ac, dc and internal variables (circulating currents), these variables are not completely independent from each other. While the ac terminal current is coupled with the dc terminal current through the converter energy balance, further analysed in **Chapter 3** and **Chapter 4**, ac and dc terminal voltage capabilities are also mutually dependent. This dependence defines the operating region of the MMC, and is influenced by the number and type of the SMs employed, as well as by their rated voltage.

## 2.3 Operating range of the MMC

Given that a stack of SMs within an arm represents an equivalent voltage source, voltage generating capability of the arm is dependent upon the total voltage across the SMs within the arm, labelled as $V_{\mathrm{c}}^{\Sigma}$ in (2.14). Note that the phase and arm notation ($xy$) is omitted in the following analysis, based on the assumption that the voltage generating capabilities of the arms within an MMC are equal.

$$V_{\mathrm{c}}^{\Sigma} = \sum_{z=1}^{N} v_{\mathrm{c}}^{z} \tag{2.14}$$

Depending on a SM configuration, and the total arm voltage, different limits exist in terms of attainable dc and ac voltage at the MMC terminals. Based on the expression for the positive arm voltage (2.10), arm-voltage generating limits can be summarized as:

$$\left.\begin{array}{lcll} \max\left(u_{\mathrm{arm}}\right) \leq V_{\mathrm{c}}^{\Sigma} & \Longrightarrow & u_{\mathrm{comm}} + \hat{u}_{\mathrm{diff}} \leq V_{\mathrm{c}}^{\Sigma} & (2.15) \\ \min\left(u_{\mathrm{arm}}\right) \geq 0 & \Longrightarrow & u_{\mathrm{comm}} - \hat{u}_{\mathrm{diff}} \geq 0 & (2.16) \end{array}\right\} \text{HB arm}$$

$$\left.\begin{array}{lcll} \max\left(u_{\mathrm{arm}}\right) \leq V_{\mathrm{c}}^{\Sigma} & \Longrightarrow & u_{\mathrm{comm}} + \hat{u}_{\mathrm{diff}} \leq V_{\mathrm{c}}^{\Sigma} & (2.17) \\ \min\left(u_{\mathrm{arm}}\right) \geq -V_{\mathrm{c}}^{\Sigma} & \Longrightarrow & u_{\mathrm{comm}} - \hat{u}_{\mathrm{diff}} \geq -V_{\mathrm{c}}^{\Sigma} & (2.18) \end{array}\right\} \text{FB arm}$$

Constraints defined by (2.15)-(2.16) are applicable to an MMC with HB SMs, given the fact that HB SMs can produce only non-negative voltage at their terminals. On the other hand, FB SMs can produce voltage of both polarities at their terminals, therefore the arm voltage is constrained within $[-V_{\mathrm{c}}^{\Sigma}, V_{\mathrm{c}}^{\Sigma}]$, as indicated by (2.17)-(2.18). For this type of analysis, the inductive voltage drop can be neglected, so the arm-differential voltage becomes $u_{\mathrm{diff}} \approx u_{\mathrm{ac}}$, whereas the arm-common voltage equals $u_{\mathrm{comm}} \approx u_{\mathrm{dc}}/2$. Consequently, constraints (2.15)-(2.18) can be rewritten as:

$$\left.\begin{aligned} \frac{u_{\mathrm{dc}}}{2} + \hat{u}_{\mathrm{ac}} &\leq V_{\mathrm{c}}^{\Sigma} && (2.19) \\ \frac{u_{\mathrm{dc}}}{2} - \hat{u}_{\mathrm{ac}} &\geq 0 && (2.20) \end{aligned}\right\} \text{HB arm} \qquad \left.\begin{aligned} \frac{u_{\mathrm{dc}}}{2} + \hat{u}_{\mathrm{ac}} &\leq V_{\mathrm{c}}^{\Sigma} && (2.21) \\ \frac{u_{\mathrm{dc}}}{2} - \hat{u}_{\mathrm{ac}} &\geq -V_{\mathrm{c}}^{\Sigma} && (2.22) \end{aligned}\right\} \text{FB arm}$$

Defining dc and ac voltage modulation indices as in (2.23)-(2.24), conditions (2.19)-(2.22) can be rewritten as in (2.25)-(2.28). Note that the variable $\hat{u}_{\mathrm{ac}}$ in (2.24) is a non-negative magnitude of the ac terminal phase voltage $u_{\mathrm{ac}}$. Consequently, ac modulation index $m_{\mathrm{ac}}$ can take only positive values.

$$m_{\mathrm{dc}} = \frac{u_{\mathrm{dc}}}{2V_{\mathrm{c}}^{\Sigma}} \qquad (2.23) \qquad\qquad m_{\mathrm{ac}} = \frac{\hat{u}_{\mathrm{ac}}}{V_{\mathrm{c}}^{\Sigma}} \qquad (2.24)$$

$$\left.\begin{aligned} m_{\mathrm{ac}} &\leq 1 - m_{\mathrm{dc}} && (2.25) \\ m_{\mathrm{ac}} &\leq m_{\mathrm{dc}} && (2.26) \end{aligned}\right\} \text{HB arm} \qquad \left.\begin{aligned} m_{\mathrm{ac}} &\leq 1 - m_{\mathrm{dc}} && (2.27) \\ m_{\mathrm{ac}} &\leq 1 + m_{\mathrm{dc}} && (2.28) \end{aligned}\right\} \text{FB arm}$$

Constraints (2.25)-(2.28) are depicted in **Fig. 2.6.a**, together with the constrain $m_{\mathrm{ac}} \geq 0$. These constraints define achievable operating range for an HB-based MMC and FB-based MMC, shaded in green and purple, respectively. Ideal waveforms of the arm voltages for different operating points are depicted in **Fig. 2.6.b-c**. While HB-based MMC arms can generate only positive voltage (waveform B), FB-based arms are able to produce voltage of both polarities (waveforms C, D and E).

It can be concluded from **Fig. 2.6.a** that the ac modulation index $m_{\mathrm{ac}}$ can never exceed the dc modulation index $m_{\mathrm{dc}}$ for HB-based arms, and attains the highest value for $m_{\mathrm{ac}} = m_{\mathrm{dc}}$. In other words, magnitude of the ac phase voltage $\hat{u}_{\mathrm{ac}}$ is limited to $u_{\mathrm{dc}}/2$. This operating point is the point of best utilization of the arm voltage capacity, and in this case, the total arm voltage should be selected as $V_{\mathrm{c}}^{\Sigma} \geq u_{\mathrm{dc}}$.

However, some ac-dc conversion stages necessitate higher ac to dc voltage ratio, meaning that either a transformer should be used at the ac terminals, or a FB-based MMC should be utilized [72]. Waveforms C and E in **Fig. 2.6.c** are the examples where this ratio is higher than 1/2 in absolute terms. Apart from the cases where ac and dc voltages are unmatched, leading to the ac to dc voltage ratio higher than 1/2, operation under such conditions is also expected when the dc voltage is reduced on the HVdc transmission lines, to prevent flashovers during unfavourable atmospheric conditions [72].

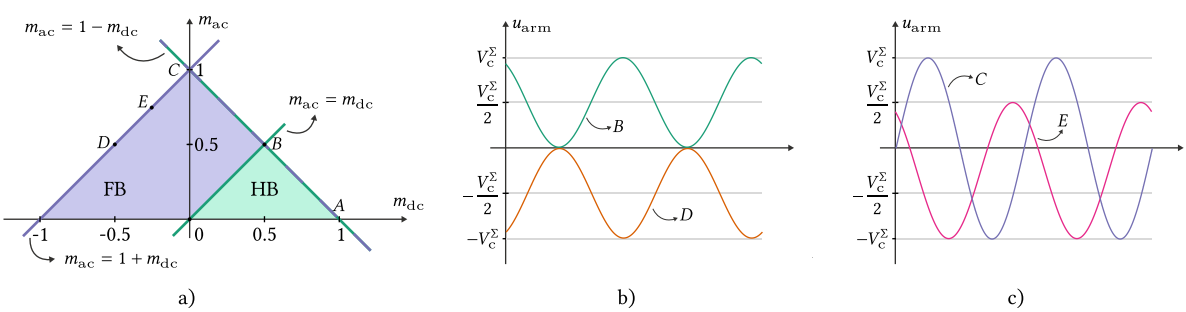


a) b) c)

**Fig. 2.6** a) Operating range of a HB-based and FB-based MMC, defined by the constraints from (2.25)-(2.28); b), c) ideal waveforms of the arm voltages for different operating points.

Another application with reduced dc link voltage is a B2B connection of two MMCs, proposed for supplying a synchronous machine in large pumped-hydro storage plants [30], [73]. For common-mode-free operation at low machine speeds, reduction of the dc link voltage is a necessary action to prevent excessive voltage ripple across the machine-side MMC SMs [31], [74], [75]. MMC-based active front-end (AFE) stage should remain in operation on the grid side, while allowing for the dc link voltage reduction. Operation of the AFE stage under such conditions is not possible with HB SMs, thus necessitating either a fully-FB solution, or a hybrid solution with a mix of HB and FB SMs.

In any case, each arm should be able to support half the dc terminal voltage as well as the ac terminal phase voltage. Some voltage reserve is also accounted for the current control purpose, as well as for the potential ac voltage swells.

## 2.4 Fault-blocking capability

Besides the differences in terms of voltage generating capability of the HB and FB-based MMC, they also differ in terms of their fault-blocking capabilities.

HB-based MMC can naturally block faults at the ac terminals, as illustrated in **Fig. 2.7.a**. In case of a line-to-line fault at the ac terminals, the inrush current is detected, and the active switches (IGBTs) are gated-off. The path of inrush currents naturally goes from the dc terminals to the ac terminals through the free-wheeling diodes and the SM capacitors. Given the fact that two arms are in the path, and each arm is charged to a voltage level of approximately $u_{dc}$, opposing voltage of the arms drives the inrush current to zero thus cutting-off the feeding path for the ac faults from the dc side. Depending on a type of the ac fault, an HB-based MMC can restore partial-power operation after the inrush current is suppressed.

In case of a dc pole-to-pole fault, once the inrush current is detected, the active switches are gated-off, so the fault current is supplied from the MMC ac terminals through a six-pulse rectifier (c.f. **Fig. 2.7.b**). As a result, an HB-based MMC is incapable of naturally blocking the dc terminal faults. In addition, an

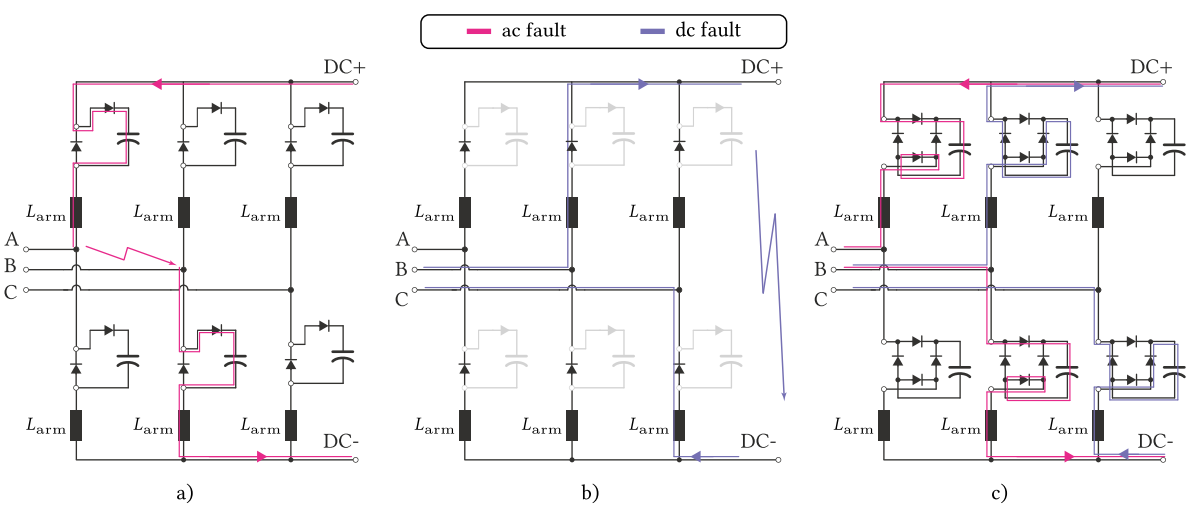


**Fig. 2.7** Equivalent circuits of the MMC under ac and dc faults: a) ac line-to-line fault at the HB-based MMC terminals; b) dc pole-to-pole fault at the HB-based MMC terminals; c) ac line-to-line (red) and dc pole-to-pole (blue) faults in the FB-based MMC.

HB-based MMC could not remain in operation under zero dc voltage, even if the inrush current was suppressed. Despite its higher efficiency and lower cost compared to a FB-based MMC, an HB-based one is not well suited for applications where the dc faults could happen regularly, such as in the dc distribution grids, and where converter might be expected to remain in operation on the ac side.

FB-based MMC behaves similarly during the ac faults as does the HB-based MMC. On the other hand, it has far more favourable behaviour under the dc faults, as illustrated in **Fig. 2.7.c**. Once the inrush current is detected, active switches are gated-off, making the inrush current path through the free-wheeling diodes and SM capacitors. The inrush current is driven by the line-to-line voltage, and it passes through two arms. Given the fact that each arm is charged to a voltage higher than the ac phase voltage, two arms on the inrush-current path oppose the line-to-line voltage, leading to a cut-off of the faulty current. Not only can a FB-based MMC block dc faults, but it can also remain in operation at the ac terminals, while its dc terminals are in fault, providing a STATCOM functionality. All the aforementioned benefits are penalized by higher losses, and more costly converter, which is the reason why all commercially-available MMCs up to this date were realized with HB SMs [18].

## 2.5 Energy dynamics of an MMC arm

Arm SM capacitors can be perceived as energy buffer elements, storing the energy received from the ac terminals and releasing the energy to the dc terminals, and vice versa. This energy exchange is taking place simultaneously, and is accompanied by energy pulsations originating from the single-phase nature of the SMs. To better understand the underlying process, arm energy dynamics should be expressed as a function of the terminal variables, i.e. voltages and currents.

For the sake of analysis, the equivalent switching frequency of an arm is assumed to be much greater than the fundamental frequency of the ac terminal voltage. Consequently, switching effects can be neglected, and an arm can be perceived as a single controllable voltage source, while all the SMs within an arm are assumed to have the same dynamics.

Arm energy is the energy stored within capacitors of a respective arm. The energy variation is governed by the arm power, i.e. a product of the voltage and current at the arm terminals. Arm power equations for two arms of a single phase leg can be expressed as:

$$p_{\mathrm{p,x}} = u_{\mathrm{p,x}} i_{\mathrm{p,x}} = (u_{\mathrm{dc}}/2 - u_{\mathrm{x}} - u_{\mathrm{CM}})(i_{\mathrm{dc,x}} + i_{\mathrm{x}}/2 + i_{\mathrm{circ,x}}) \tag{2.29}$$

$$p_{\mathrm{n,x}} = u_{\mathrm{n,x}} i_{\mathrm{n,x}} = (u_{\mathrm{dc}}/2 + u_{\mathrm{x}} + u_{\mathrm{CM}})(i_{\mathrm{dc,x}} - i_{\mathrm{x}}/2 + i_{\mathrm{circ,x}}) \tag{2.30}$$

Note that the arm voltage is expressed only as a function of its terminal components, whereas the additional voltage components, that exists due to the inductive and resistive voltage drop, are relatively minor compared to the terminal variables, and thus neglected.

Defining ac terminal variables as in (2.31)-(2.32), and replacing them into (2.29)-(2.30) yields (2.33)-(2.34). As a first step, the common-mode voltage $u_{\mathrm{CM}}$ and the circulating current $i_{\mathrm{circ,x}}$ are neglected in order to facilitate the analysis.

$$u_{\mathrm{x}} = \hat{u}_{\mathrm{x}} \sin\left(\omega_{\mathrm{g}} t\right) \tag{2.31} \qquad i_{\mathrm{x}} = \hat{i}_{\mathrm{x}} \sin\left(\omega_{\mathrm{g}} t + \phi_{\mathrm{x}}\right) \tag{2.32}$$

$$p_{\mathrm{p,x}} = \underbrace{\frac{u_{\mathrm{dc}} i_{\mathrm{dc,x}}}{2} - \frac{\hat{u}_{\mathrm{x}} \hat{i}_{\mathrm{x}} \cos(\phi_{\mathrm{x}})}{4}}_{\text{dc value}} + \underbrace{\frac{u_{\mathrm{dc}} \hat{i}_{\mathrm{x}}}{4} \sin\left(\omega_{\mathrm{g}} t + \phi_{\mathrm{x}}\right) - \hat{u}_{\mathrm{x}} i_{\mathrm{dc,x}} \sin\left(\omega_{\mathrm{g}} t\right)}_{\text{1st harmonic}} + \underbrace{\frac{\hat{u}_{\mathrm{x}} \hat{i}_{\mathrm{x}}}{4} \cos\left(2\omega_{\mathrm{g}} t + \phi_{\mathrm{x}}\right)}_{\text{2nd harmonic}} \tag{2.33}$$

$$p_{\mathrm{n,x}} = \underbrace{\frac{u_{\mathrm{dc}} i_{\mathrm{dc,x}}}{2} - \frac{\hat{u}_{\mathrm{x}} \hat{i}_{\mathrm{x}} \cos(\phi_{\mathrm{x}})}{4}}_{\text{dc value}} - \underbrace{\frac{u_{\mathrm{dc}} \hat{i}_{\mathrm{x}}}{4} \sin\left(\omega_{\mathrm{g}} t + \phi_{\mathrm{x}}\right) + \hat{u}_{\mathrm{x}} i_{\mathrm{dc,x}} \sin\left(\omega_{\mathrm{g}} t\right)}_{\text{1st harmonic}} + \underbrace{\frac{\hat{u}_{\mathrm{x}} \hat{i}_{\mathrm{x}}}{4} \cos\left(2\omega_{\mathrm{g}} t + \phi_{\mathrm{x}}\right)}_{\text{2nd harmonic}} \tag{2.34}$$

Expressions (2.33)-(2.34) represent the arm power components, which are composed of their dc and second harmonic component, that are equal in the two arms, as well as the first harmonic component, which is in counterphase in the two arms. Integrating (2.33)-(2.34), the expressions for the arm energies of a positive and negative arm are obtained (2.35)-(2.36). Arm energy is a reflection of the SM capacitor voltages, and thus should have a dominant constant term, corresponding to the average capacitor voltage. Additionally, due to the interaction between the terminal variables of different frequencies, fundamental and the second harmonic energy oscillations are also present.

$$w_{\mathrm{p,x}} = \underbrace{W_{\mathrm{p,x}}}_{\text{average value}} \underbrace{- \frac{u_{\mathrm{dc}} \hat{i}_{\mathrm{x}}}{4\omega_{\mathrm{g}}} \cos\left(\omega_{\mathrm{g}} t + \phi_{\mathrm{x}}\right) + \frac{\hat{u}_{\mathrm{x}} i_{\mathrm{dc,x}}}{\omega_{\mathrm{g}}} \cos\left(\omega_{\mathrm{g}} t\right)}_{\text{1st harmonic}} + \underbrace{\frac{\hat{u}_{\mathrm{x}} \hat{i}_{\mathrm{x}}}{8\omega_{\mathrm{g}}} \sin\left(2\omega_{\mathrm{g}} t + \phi_{\mathrm{x}}\right)}_{\text{2nd harmonic}} \tag{2.35}$$

$$w_{\mathrm{n,x}} = \underbrace{W_{\mathrm{n,x}}}_{\text{average value}} \underbrace{+ \frac{u_{\mathrm{dc}} \hat{i}_{\mathrm{x}}}{4\omega_{\mathrm{g}}} \cos\left(\omega_{\mathrm{g}} t + \phi_{\mathrm{x}}\right) - \frac{\hat{u}_{\mathrm{x}} i_{\mathrm{dc,x}}}{\omega_{\mathrm{g}}} \cos\left(\omega_{\mathrm{g}} t\right)}_{\text{1st harmonic}} + \underbrace{\frac{\hat{u}_{\mathrm{x}} \hat{i}_{\mathrm{x}}}{8\omega_{\mathrm{g}}} \sin\left(2\omega_{\mathrm{g}} t + \phi_{\mathrm{x}}\right)}_{\text{2nd harmonic}} \tag{2.36}$$

Average values of the arm energies $W_{\mathrm{p,x}}$ and $W_{\mathrm{n,x}}$ are controlled by the dc components of the respective arm powers. As the energies are a measure of the total voltage available within the arm SMs ($V_{\mathrm{c}}^{\Sigma}$), they should be thus maintained around predefined values, as a prerequisite for a proper converter operation. Techniques for the arm energy control will be covered in depth in **Chapter 3** and **Chapter 4**.

Oscillations in the arm energy are directly reflecting the oscillations in the SM voltages. Since the SMs should ideally have constant voltage, the oscillating terms are unwelcome, so they should be evaluated. Since the expressions for the energy oscillating terms are already derived, a relationship between the arm energy and the arm total voltage oscillations should be established.

### 2.5.1 Relationship between the arm energy and voltage

To allow for a proper operation of the converter, rated value of the total arm voltage ($V_{\mathrm{c,nom}}^{\Sigma}$) should conform the identities expressed by (2.19)-(2.22). The rated value is chosen during the design procedure of the converter, as well as the number of SMs per arm $N$, and the SM capacitance $C_{\mathrm{SM}}$. Assuming that the SMs within an arm are mutually balanced, i.e. they equally share the total arm voltage, the total energy stored within the arm is determined by:

$$w_{\mathrm{arm}} = \sum_{z=1}^{N} \frac{1}{2} C_{\mathrm{SM}} v_{\mathrm{c,z}}^2 = \frac{1}{2} N C_{\mathrm{SM}} v_{\mathrm{c}}^2 = \frac{1}{2} N C_{\mathrm{SM}} \left(\frac{v_{\mathrm{c}}^{\Sigma}}{N}\right)^2 = \frac{1}{2} \frac{C_{\mathrm{SM}}}{N} (v_{\mathrm{c}}^{\Sigma})^2 = \frac{1}{2} C_{\mathrm{arm}} (v_{\mathrm{c}}^{\Sigma})^2 \tag{2.37}$$

Equation (2.37) shows that, in terms of its energy content, an arm can be equivalently perceived as a single capacitor with the capacitance $C_{\text{arm}}$ and the voltage $v_{\text{c}}^{\Sigma}$. The arm capacitance is the equivalent capacitance of a series connection of $N$ capacitors, whereas the total arm voltage $v_{\text{c}}^{\Sigma}$ is a sum of the voltages across $N$ individual capacitors.

As shown by (2.35)-(2.36), apart from the constant terms, arm energies contain oscillating terms at the fundamental and second harmonic of the ac terminal frequency. Analogously, it can be assumed that the same components will be dominant in the total arm voltage. As a result, the total arm voltage $v_{\text{c}}^{\Sigma}$ can be expressed as:

$$v_{\text{c}}^{\Sigma} = \underbrace{V_{\text{c}}^{\Sigma}}_{\text{dc value}} + \underbrace{v_{\text{c,1st}}^{\Sigma}}_{\text{1st harmonic}} + \underbrace{v_{\text{c,2nd}}^{\Sigma}}_{\text{2nd harmonic}} \tag{2.38}$$

Replacing the expression for the total arm voltage (2.38) into (2.37), and assuming that the amplitudes of the oscillating terms are much smaller than the average arm voltage, yields:

$$\begin{aligned} w_{\text{arm}} = \frac{1}{2}C_{\text{arm}}(v_{\text{c}}^{\Sigma})^2 = & \frac{1}{2}C_{\text{arm}}\left(V_{\text{c}}^{\Sigma} + v_{\text{c,1st}}^{\Sigma} + v_{\text{c,2nd}}^{\Sigma}\right)^2 = \frac{1}{2}C_{\text{arm}}\Big(\left(V_{\text{c}}^{\Sigma}\right)^2 + \underbrace{\left(v_{\text{c,1st}}^{\Sigma}\right)^2}_{\approx 0} + \underbrace{\left(v_{\text{c,2nd}}^{\Sigma}\right)^2}_{\approx 0} + \ldots \\ & + 2V_{\text{c}}^{\Sigma}v_{\text{c,1st}}^{\Sigma} + 2V_{\text{c}}^{\Sigma}v_{\text{c,2nd}}^{\Sigma} + \underbrace{2v_{\text{c,1st}}^{\Sigma}v_{\text{c,2nd}}^{\Sigma}}_{\approx 0}\Big) \end{aligned} \tag{2.39}$$

The term $V_{\text{c}}^{\Sigma}$ has dc nature, whereas the terms $v_{\text{c,1st}}^{\Sigma}$ and $v_{\text{c,2nd}}^{\Sigma}$ are ac quantities. Consequently, from (2.39), three distinctive arm energy components can be identified:

$$W_{\text{arm}} \approx \frac{1}{2}C_{\text{arm}}\left(V_{\text{c}}^{\Sigma}\right)^2 \tag{2.40}$$

$$w_{\text{arm,1st}} \approx C_{\text{arm}}V_{\text{c}}^{\Sigma}v_{\text{c,1st}}^{\Sigma} \tag{2.41}$$

$$w_{\text{arm,2nd}} \approx C_{\text{arm}}V_{\text{c}}^{\Sigma}v_{\text{c,2nd}}^{\Sigma} \tag{2.42}$$

The three energy components from (2.40)-(2.42) correspond to the arm energy expressions from (2.35)-(2.36), and they also confirm the assumptions from (2.38).

It is shown in (2.40) that the average arm voltage $V_{\text{c}}^{\Sigma}$ can be controlled by controlling the average arm energy. On the other hand, the oscillating terms of the arm voltage, $v_{\text{c,1st}}$ and $v_{\text{c,2nd}}$, should be minimized so as to avoid overmodulation, and the resulting low-frequency harmonics. Those terms can be expressed as:

$$v_{\text{c,1st}}^{\Sigma} = \frac{1}{C_{\text{arm}}}\frac{w_{\text{arm,1st}}}{V_{\text{c}}^{\Sigma}} \tag{2.43}$$

$$v_{\text{c,2nd}}^{\Sigma} = \frac{1}{C_{\text{arm}}}\frac{w_{\text{arm,2nd}}}{V_{\text{c}}^{\Sigma}} \tag{2.44}$$

Energy pulsations are determined by the terminal voltages and currents, as shown in (2.35)-(2.36), and are an inevitable consequence of a single-phase nature of the converter SMs. Arm voltage oscillations

are reflections of the energy oscillations, and are inversely proportional to the SM capacitance value. Therefore, in order to maintain the voltage oscillations within a certain limit, appropriate value of the SM capacitance should be chosen. Unreasonably high values of the SM capacitance would result in a very small voltage ripple, however, the size and the cost of the converter would be prohibitively high.

### 2.5.2 Capacitor voltage ripple reduction

To minimize the SM (arm) voltage ripple, without employing unreasonably high capacitance values, energy oscillations should be reduced. Arm energy oscillation reduction can be achieved by reducing the power terms that cause these oscillations.

Fundamental frequency energy oscillations are in counterphase in the arms of the same phase leg (c.f. (2.35)-(2.36)), and are governed by the power term $p_{1\mathrm{st}}$ in (2.45). The power term in (2.45) is expressed for the positive arm only, as for the negative it differs only in sign.

$$p_{1\mathrm{st}} = \frac{u_{\mathrm{dc}}\hat{i}_{\mathrm{x}}}{4}\sin\big(\omega_{\mathrm{g}}t + \phi_{\mathrm{x}}\big) - \hat{u}_{\mathrm{x}} i_{\mathrm{dc,x}}\sin\big(\omega_{\mathrm{g}}t\big) \qquad (2.45)$$

$$p_{2\mathrm{nd}} = \frac{\hat{u}_{\mathrm{x}}\hat{i}_{\mathrm{x}}}{4}\cos\big(2\omega_{\mathrm{g}}t + \phi_{\mathrm{x}}\big) \qquad (2.46)$$

Second harmonic energy oscillations are common to the two arms of a single phase leg, and their dynamics is determined by the power term $p_{2\mathrm{nd}}$ in (2.46). Reduction of the existing power components can be achieved by introducing new power components in the total arm power. Circulating currents are internal MMC variables, and thus invisible at its terminals. As such, they can be utilized to produce additional power components, and suppress or reduce the energy oscillations. Additional power terms in the two arms, originating from the circulating currents, take the form as in (2.47)-(2.48).

$$\left.\begin{aligned} p_{\mathrm{p,x}}^{(\mathrm{circ})} &= u_{\mathrm{p,x}} i_{\mathrm{circ,x}} = \frac{u_{\mathrm{dc}}}{2} i_{\mathrm{circ,x}} - u_{\mathrm{x}} i_{\mathrm{circ,x}} && (2.47) \\ p_{\mathrm{n,x}}^{(\mathrm{circ})} &= u_{\mathrm{n,x}} i_{\mathrm{circ,x}} = \frac{u_{\mathrm{dc}}}{2} i_{\mathrm{circ,x}} + u_{\mathrm{x}} i_{\mathrm{circ,x}} && (2.48) \end{aligned}\right\} \implies \begin{aligned} p_{\mathrm{comm}}^{(\mathrm{circ})} &= \frac{u_{\mathrm{dc}}}{2} i_{\mathrm{circ,x}} && (2.49) \\ p_{\mathrm{diff}}^{(\mathrm{circ})} &= -u_{\mathrm{x}} i_{\mathrm{circ,x}} && (2.50) \end{aligned}$$

Arm power components in (2.47)-(2.48) have a common term $p_{\mathrm{comm}}^{(\mathrm{circ})}$, and a differential term $p_{\mathrm{diff}}^{(\mathrm{circ})}$. The two terms should ideally cancel the arm power terms from (2.45)-(2.46). The common term from (2.49) should cancel the second harmonic power component in (2.46), whereas the differential component from (2.50) should cancel the fundamental frequency power component in (2.45):

$$p_{\mathrm{comm}}^{(\mathrm{circ})} + p_{2\mathrm{nd}} = 0 \qquad \implies \qquad \frac{u_{\mathrm{dc}}}{2} i_{\mathrm{circ,x}} + \frac{\hat{u}_{\mathrm{x}}\hat{i}_{\mathrm{x}}}{4}\cos\big(2\omega_{\mathrm{g}}t + \phi_{\mathrm{x}}\big) = 0 \qquad (2.51)$$

$$p_{\mathrm{diff}}^{(\mathrm{circ})} + p_{1\mathrm{st}} = 0 \qquad \implies \qquad -u_{\mathrm{x}} i_{\mathrm{circ,x}} + \frac{u_{\mathrm{dc}}\hat{i}_{\mathrm{x}}}{2\omega_{\mathrm{g}}}\cos\big(\omega_{\mathrm{g}}t + \phi_{\mathrm{x}}\big) - \frac{\hat{u}_{\mathrm{x}} i_{\mathrm{dc,x}}}{\omega_{\mathrm{g}}}\cos\big(\omega_{\mathrm{g}}t\big) = 0 \qquad (2.52)$$

As the $i_{\mathrm{circ,x}}$ cannot conform both conditions, two straightforward solutions are that the current is chosen to cancel either the common term, or the differential term. Authors in [35] proposed injection of the second harmonic circulating current that would completely suppress the second harmonic

energy oscillations. From (2.51), and using the definitions of the modulation indices $m_{\mathrm{dc}}$ and $m_{\mathrm{ac}}$, the circulating current takes the form:

$$i_{\mathrm{circ,x}} = -\frac{m_{\mathrm{ac}}}{m_{\mathrm{dc}}}\frac{\hat{i}_{\mathrm{x}}}{4}\cos\left(2\omega_{\mathrm{g}}t + \phi_{\mathrm{x}}\right) \tag{2.53}$$

Obtained circulating current is at double the fundamental frequency, and while it completely suppresses the second harmonic pulsations, it also interacts with the ac voltage component $u_{\mathrm{x}}$, creating a fundamental and third harmonic power components, shown in (2.54). These power components create an additional first and third arm-energy harmonics, expressed by (2.55).

$$\begin{aligned}\Delta p_{\mathrm{arm}}^{(\mathrm{circ})} &= -\mathrm{u_x} i_{\mathrm{circ,x}} = m_{\mathrm{ac}} V_{\mathrm{c}}^{\Sigma}\sin\left(\omega_{\mathrm{g}}t\right)\frac{m_{\mathrm{ac}}}{m_{\mathrm{dc}}}\frac{\hat{i}_{\mathrm{x}}}{4}\cos\left(2\omega_{\mathrm{g}}t + \phi_{\mathrm{x}}\right)\\ &= -\frac{m_{\mathrm{ac}}^2}{m_{\mathrm{dc}}}\frac{\hat{i}_{\mathrm{x}}}{8}V_{\mathrm{c}}^{\Sigma}\Big(\sin\left(\omega_{\mathrm{g}}t + \phi_{\mathrm{x}}\right) - \sin\left(3\omega_{\mathrm{g}}t + \phi_{\mathrm{x}}\right)\Big)\end{aligned} \tag{2.54}$$

$$\Delta w_{\mathrm{arm}}^{(\mathrm{circ})} = \underbrace{\frac{m_{\mathrm{ac}}^2}{m_{\mathrm{dc}}}\frac{\hat{i}_{\mathrm{x}}}{8}\frac{V_{\mathrm{c}}^{\Sigma}}{\omega_{\mathrm{g}}}\cos\left(\omega_{\mathrm{g}}t + \phi_{\mathrm{x}}\right)}_{\Delta w_{\mathrm{1st}}^{\mathrm{ind}}} - \underbrace{\frac{m_{\mathrm{ac}}^2}{m_{\mathrm{dc}}}\frac{\hat{i}_{\mathrm{x}}}{24}\frac{V_{\mathrm{c}}^{\Sigma}}{\omega_{\mathrm{g}}}\cos\left(3\omega_{\mathrm{g}}t + \phi_{\mathrm{x}}\right)}_{\Delta w_{\mathrm{3rd}}^{\mathrm{ind}}} \tag{2.55}$$

Induced first harmonic $\Delta w_{\mathrm{1st}}^{\mathrm{ind}}$ from (2.54) adds up to the naturally present first harmonic of arm energy (2.35). The difference between the original and the resulting first harmonic of the arm energy is denoted as $\Delta w_{\mathrm{1st}}^{\mathrm{ind,eff}}$, and is visualized in **Fig. 2.8.a**, as a function of the ac modulation index $m_{\mathrm{ac}}$ and grid current phase angle $\phi_{\mathrm{x}}$. It can be concluded that, besides the complete suppression of the arm energy second harmonic, the magnitude of the first harmonic is also reduced. On the other hand, third harmonic of the arm energy is introduced, which does not exist in normal conditions.

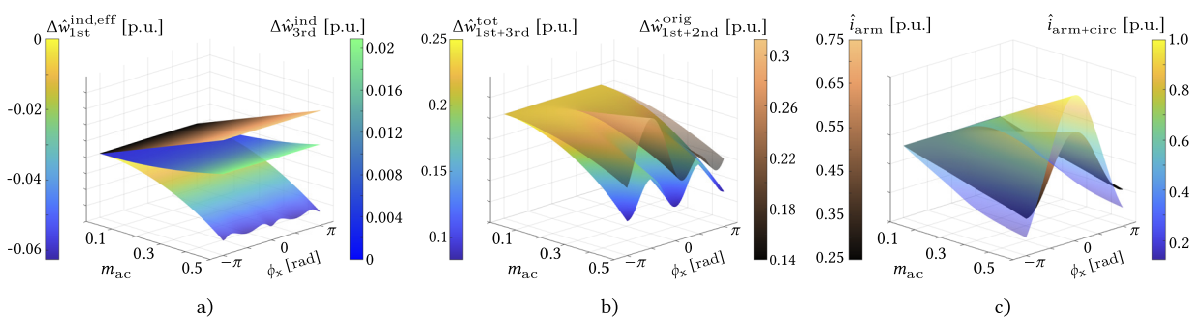


**Fig. 2.8** Effects of the second harmonic energy mitigation on other energy oscillation components: a) magnitude of the natural second harmonic energy component (brown), magnitude of the induced third harmonic energy component (blue-green), magnitude of the effective induced first harmonic energy component (yellow-blue); b) comparison between the total energy magnitude in the natural case (brown), and when the circulating current is injected (yellow-blue); c) comparison of the arm current magnitudes without (brown) and with (yellow-blue) circulating current injection. Note that the plots assumed normalized values of the currents, voltages and energies, while the dc modulation index is assumed to be $m_{\mathrm{dc}} = 0.5$.

To visualize the overall benefits of the second harmonic circulating current injection according to (2.53), the magnitude of the total original arm energy oscillations is compared with the magnitude of the total resulting arm energy oscillations in **Fig. 2.8.b**. It is obvious that the circulating current injection, proposed by [35], results in reduced overall arm energy oscillations. Nevertheless, the arm current is increased (c.f. **Fig. 2.8.c**), and so are the converter losses.

As the first-harmonic arm energy oscillations are dominant, injection of the circulating current with the aim of suppressing them might yield better results. Second harmonic circulating current is calculated according to (2.52), and it takes the following form:

$$i_{\mathrm{circ}} = \hat{i}_{\mathrm{circ}} \cos\left(2\omega_{\mathrm{g}} t + \phi_{\mathrm{c}}\right) \tag{2.56}$$

$$\phi_{\mathrm{c}} = \operatorname{atan}\left(\frac{2m_{\mathrm{dc}}^2 \tan\phi_{\mathrm{x}}}{2m_{\mathrm{dc}}^2 - m_{\mathrm{ac}}^2}\right) \tag{2.57}$$

$$\hat{i}_{\mathrm{circ}} = -\hat{i}_{\mathrm{g}} \frac{m_{\mathrm{dc}}}{m_{\mathrm{ac}}} \frac{\sin\phi_{\mathrm{x}}}{\sin\phi_{\mathrm{c}}} \tag{2.58}$$

The injected current interacts with the arm-differential voltage $u_{\mathrm{x}}$, resulting in a complete suppression of the first-harmonic energy oscillations. Additionally, this interaction generates the third harmonic power component $\Delta p_{3\mathrm{rd}}^{\mathrm{ind}}$, shown in (2.59). The circulating current also interacts with the arm-common voltage component, which is approximately equal to $u_{\mathrm{dc}}/2$, resulting in a parasitic second-harmonic power oscillations $\Delta p_{2\mathrm{nd}}^{\mathrm{ind}}$, given in (2.60). The two parasitic power terms create corresponding energy oscillations $\Delta w_{3\mathrm{rd}}^{\mathrm{ind}}$ and $\Delta w_{2\mathrm{nd}}^{\mathrm{ind}}$.

$$\Delta p_{3\mathrm{rd}}^{\mathrm{ind}} = -\frac{m_{\mathrm{ac}}}{2} \hat{i}_{\mathrm{circ}} V_{\mathrm{c}}^{\Sigma} \sin\left(3\omega_{\mathrm{g}} t + \phi_{\mathrm{c}}\right) \quad \Longrightarrow \quad \Delta w_{3\mathrm{rd}}^{\mathrm{ind}} = \frac{m_{\mathrm{ac}}}{6\omega_{\mathrm{g}}} \hat{i}_{\mathrm{circ}} V_{\mathrm{c}}^{\Sigma} \cos\left(3\omega_{\mathrm{g}} t + \phi_{\mathrm{c}}\right) \tag{2.59}$$

$$\Delta p_{2\mathrm{nd}}^{\mathrm{ind}} = m_{\mathrm{dc}} \hat{i}_{\mathrm{circ}} V_{\mathrm{c}}^{\Sigma} \cos\left(2\omega_{\mathrm{g}} t + \phi_{\mathrm{c}}\right) \quad \Longrightarrow \quad \Delta w_{2\mathrm{nd}}^{\mathrm{ind}} = \frac{m_{\mathrm{dc}}}{2\omega_{\mathrm{g}}} \hat{i}_{\mathrm{circ}} V_{\mathrm{c}}^{\Sigma} \sin\left(2\omega_{\mathrm{g}} t + \phi_{\mathrm{c}}\right) \tag{2.60}$$

To comprehend the benefits and disadvantages of such an approach, oscillating terms of the arm energy were mutually compared in **Fig. 2.9**. While the induced third-harmonic energy term $\Delta w_{3\mathrm{rd}}^{\mathrm{ind}}$ is relatively minor with respect to the suppressed first harmonic, the induced second-harmonic energy term $\Delta w_{2\mathrm{nd}}^{\mathrm{ind}}$ have comparable, or even higher magnitude than the first harmonic that is suppressed. **Fig. 2.9.b** compares the magnitude of the total energy oscillations prior and after the first harmonic compensation. It shows that the compensation might be advantageous for high ac modulation indices ($m_{\mathrm{ac}} > 0.4$) and for negative grid current phase angles ($\phi_{\mathrm{x}} < 0$). Nevertheless, introduced circulating current component heavily increases the arm current (c.f. **Fig. 2.9.c**), making this approach unjustified.

Therefore, instead of suppressing only the second harmonic of the arm energy oscillations, many authors opt for a holistic approach focussing on reducing the overall peak-to-peak energy ripple within an arm [76], [77]. For this purpose, not only the second, but also the fourth harmonic circulating current is injected [78], resulting from an optimization algorithm. A trade-off between the voltage oscillation reduction and the arm current increase is usually found using cost functions with variable weight factors [76].

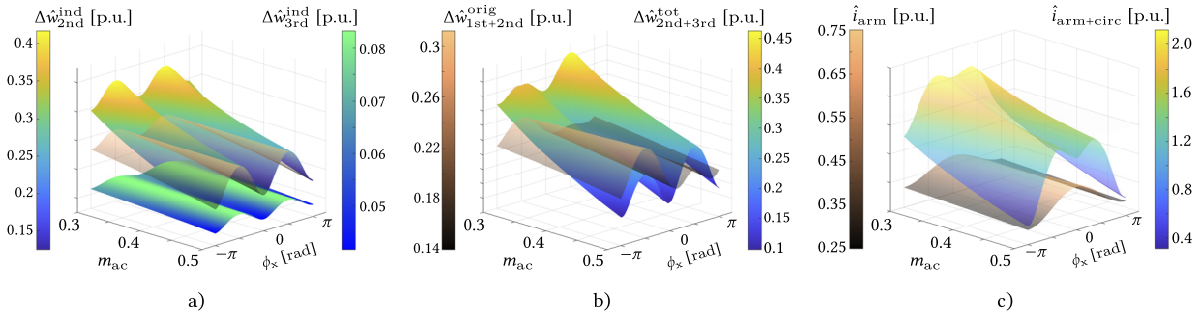


**Fig. 2.9** Effects of the first harmonic energy mitigation on the other energy oscillation components: a) magnitude of the natural first harmonic energy component (brown), magnitude of the induced third harmonic energy component (blue-green), magnitude of the induced second harmonic energy component (yellow-blue); b) comparison between the total energy magnitude in the natural case (brown), and when the circulating current is injected (yellow-blue); c) comparison of the arm current magnitudes without (brown) and with (yellow-blue) circulating current injection. Note that the plots assumed normalized values of the currents, voltages and energies, while the dc modulation index is assumed to be $m_{\text{dc}} = 0.5$.

### 2.5.3 Low-frequency operation of the MMC

Although not initially conceived for application in electric drives, some of superior features of the MMC, such as low filtering requirements, redundancy, and scalability to any voltage level, made it a good candidate for this type of application. As frequency-controlled drives should support wide operating frequency range, low-frequency operating points can be challenging for the MMC.

To facilitate the discussion, the arm energy equation (2.35) is rewritten:

$$w_{\text{p,x}} = W_{\text{p,x}} - \frac{u_{\text{dc}}\hat{i}_{\text{x}}}{4\omega_{\text{g}}}\cos\big(\omega_{\text{g}}t + \phi_{\text{x}}\big) + \frac{\hat{u}_{\text{x}}i_{\text{dc,x}}}{\omega_{\text{g}}}\cos\big(\omega_{\text{g}}t\big) + \frac{\hat{u}_{\text{x}}\hat{i}_{\text{x}}}{8\omega_{\text{g}}}\sin\big(2\omega_{\text{g}}t + \phi_{\text{x}}\big) \tag{2.61}$$

Regardless of the motor control method being applied, the ratio between the magnitude and frequency of the voltage supplied to the motor remains more or less constant. The principal reason is to preserve the flux of the machine at the rated value, and thus maximize efficiency. Analysing the terms in (2.61), one can conclude that the second term increases its magnitude with the frequency decrease. The other oscillating terms have their magnitudes independent of the frequency, due to the constant $u/f$ ratio.

This increase in energy ripple negatively affects voltage generating capability, reducing the available arm voltage when the dominant oscillating term exhibits its minimum, but also leading to the overvoltages in the SM capacitors, when it hits the maximum. Therefore, this scenario should be avoided, and different methods are available for mitigating this term.

The authors in [21] were the first to address the issue by proposing the injection of the common-mode voltage component and the circulating current, defined as in (2.62)-(2.63). The power and energy components originating from this interaction are given by (2.64)-(2.65).

$$u_{\text{CM}} = \hat{u}_{\text{CM}}\sin(\omega_{\text{cm}}t) \tag{2.62}$$

$$i_{\text{circ,cm}} = \hat{i}_{\text{circ,CM}}\cos\big((\omega_{\text{cm}} - \omega_{\text{g}})t - \phi_{\text{cm}}\big) \tag{2.63}$$

$$\Delta p_{\mathrm{CM}} = -u_{\mathrm{CM}} i_{\mathrm{circ,CM}} = -\frac{\hat{u}_{\mathrm{CM}} \hat{i}_{\mathrm{circ,CM}}}{2} \sin\Big((2\omega_{\mathrm{cm}} - \omega_{\mathrm{g}})t - \phi_{\mathrm{cm}}\Big) - \frac{\hat{u}_{\mathrm{CM}} \hat{i}_{\mathrm{circ,CM}}}{2} \sin\Big(\omega_{\mathrm{g}} t + \phi_{\mathrm{cm}}\Big) \quad (2.64)$$

$$\Delta w_{\mathrm{CM}} = \underbrace{\frac{\hat{u}_{\mathrm{CM}} \hat{i}_{\mathrm{circ,CM}}}{2(2\omega_{\mathrm{cm}} - \omega_{\mathrm{g}})} \cos\Big((2\omega_{\mathrm{cm}} - \omega_{\mathrm{g}})t - \phi_{\mathrm{cm}}\Big)}_{\text{HF term}} + \underbrace{\frac{\hat{u}_{\mathrm{CM}} \hat{i}_{\mathrm{circ,CM}}}{2\omega_{\mathrm{g}}} \cos\Big(\omega_{\mathrm{g}} t + \phi_{\mathrm{cm}}\Big)}_{\text{LF term}} \quad (2.65)$$

The low-frequency term in (2.65) should suppress the second term in (2.61). On the other hand, interaction between the common-mode voltage and the circulating current introduces the oscillating term at the angular frequency $2\omega_{\mathrm{cm}} - \omega_{\mathrm{g}}$, with the magnitude inversely proportional to the chosen common-mode frequency $\omega_{\mathrm{cm}}$. Consequently, it is desirable to have the common-mode voltage at the highest possible frequency, in order to minimize the oscillating term. This approach was also analysed in [79], whereas the references [80]–[82] use a square-wave common-mode voltage, with a square-wave [80], [82] or sinusoidal [81] circulating currents, or triangular common-mode and circulating currents [83].

The second term in (2.61) can be reduced if the ratio between the peak-current and the frequency is kept constant through the rotor-flux optimization, as suggested by [21]. This method is applicable to the loads with a quadratic torque characteristic, and results in a reduced range where the injection of the common-mode voltage and circulating current is applied.

Disadvantages of the proposed method are detrimental effects of the common-mode voltage on the machine bearings, as well as the increased converter losses due to the circulating current injection. The former is particularly pronounced in retrofit applications, where the machine is designed to be grid-connected and thus does not support any or very little common-mode voltage [31], [73]. In that case a solution is to reduce the dc link voltage in the B2B connection of two MMCs supplying the machine. To achieve such regimes, either a FB or hybrid MMC is necessary as the AFE stage [31], [74], [75].

Which one of the aforementioned methods for voltage ripple reduction in low-frequency mode of operation will be applied, depends on the application and the associated trade-offs.

## 2.6 Modulation

So far, we have assumed that a stack of SMs within an arm acts as an ideal controllable voltage source, able to generate a multilevel voltage waveform. In fact, the number of SMs per arm is finite, and each SM contributes a discrete voltage value, i.e. $V_{\mathrm{out}} \in \{-V_{\mathrm{c}}, 0, V_{\mathrm{c}}\}$. The arm voltage reference is obtained from the control algorithms, further explained in **Chapter 3** and **Chapter 4**, and the role of the modulator is to reproduce these references to the best possible extent, given the available arm voltage $v_{\mathrm{c}}^{\Sigma}$.

### 2.6.1 Generation of the insertion index

The insertion index is defined as the ratio between the arm voltage reference, and the total available arm voltage $v_{\mathrm{c}}^{\Sigma}$. Depending on the information used for the total available arm voltage $v_{\mathrm{c}}^{\Sigma}$, there are different approaches for the insertion index generation.

**Direct voltage control** is the method where the average value of the total available arm voltage is used for the insertion indices generation. For the positive and negative arm of the same phase leg, the insertion indices are calculated as in (2.66)-(2.67), where $u_{\mathrm{p}}^{*}$ and $u_{\mathrm{n}}^{*}$ are the arm-voltage references for the positive and negative arm. Note that the phase notation is omitted, as it is not relevant for the discussion. Calculated insertion indices represent a relative number of SMs that is to be inserted in order to generated the reference voltage.

$$n_{\mathrm{p}} = \frac{u_{\mathrm{p}}^{*}}{V_{\mathrm{c}}^{\Sigma}} \tag{2.66}$$

$$n_{\mathrm{n}} = \frac{u_{\mathrm{n}}^{*}}{V_{\mathrm{c}}^{\Sigma}} \tag{2.67}$$

This method is computationally very simple, as it does not require instantaneous information about the SMs voltages. Additionally, it has been shown in [84] that the converter is inherently stable when this method is applied, meaning that the converter total energy is equally distributed among its arms. However, this method introduces parasitic voltage components, briefly analysed hereupon.

We have already seen that the arm voltage can be decomposed into a common and differential component. Consequently, arm voltage references can be written as in (2.68)-(2.69). Also, the total arm voltage $v_{\mathrm{c}}^{\Sigma}$ is shown to consists of the average value, as well as the first and the second harmonic oscillating components, as expressed in (2.70)-(2.71).

$$u_{\mathrm{p}}^{*} = u_{\mathrm{comm}}^{*} - u_{\mathrm{diff}}^{*} \tag{2.68}$$

$$u_{\mathrm{n}}^{*} = u_{\mathrm{comm}}^{*} + u_{\mathrm{diff}}^{*} \tag{2.69}$$

$$v_{\mathrm{c,p}}^{\Sigma} = V_{\mathrm{c,p}}^{\Sigma} - v_{\mathrm{1st}}^{\Sigma} + v_{\mathrm{2nd}}^{\Sigma} \tag{2.70}$$

$$v_{\mathrm{c,n}}^{\Sigma} = V_{\mathrm{c,n}}^{\Sigma} + v_{\mathrm{1st}}^{\Sigma} + v_{\mathrm{2nd}}^{\Sigma} \tag{2.71}$$

Neglecting the computational and actuator delays, and adopting the definitions from (2.66)-(2.71), actual arm voltages are computed as:

$$u_{\mathrm{p}} = n_{\mathrm{p}} v_{\mathrm{c,p}}^{\Sigma} = \frac{u_{\mathrm{comm}}^{*} - u_{\mathrm{diff}}^{*}}{V_{\mathrm{c}}^{\Sigma}} \left( V_{\mathrm{c,p}}^{\Sigma} - v_{\mathrm{1st}}^{\Sigma} + v_{\mathrm{2nd}}^{\Sigma} \right) \tag{2.72}$$

$$u_{\mathrm{n}} = n_{\mathrm{n}} v_{\mathrm{c,n}}^{\Sigma} = \frac{u_{\mathrm{comm}}^{*} + u_{\mathrm{diff}}^{*}}{V_{\mathrm{c}}^{\Sigma}} \left( V_{\mathrm{c,n}}^{\Sigma} + v_{\mathrm{1st}}^{\Sigma} + v_{\mathrm{2nd}}^{\Sigma} \right) \tag{2.73}$$

Assuming that the total average arm voltages are equal in the two arms $V_{\mathrm{c,p}}^{\Sigma} = V_{\mathrm{c,n}}^{\Sigma} = V_{\mathrm{c}}^{\Sigma}$, arm-common and arm-differential voltages can be computed accordingly:

$$\begin{aligned} u_{\mathrm{comm}} &= \frac{u_{\mathrm{p}} + u_{\mathrm{n}}}{2} = u_{\mathrm{comm}}^{*} \left( \frac{V_{\mathrm{c}}^{\Sigma} + v_{\mathrm{2nd}}^{\Sigma}}{V_{\mathrm{c}}^{\Sigma}} \right) + u_{\mathrm{diff}}^{*} \frac{v_{\mathrm{1st}}^{*}}{V_{\mathrm{c}}^{\Sigma}} = u_{\mathrm{comm}}^{*} + u_{\mathrm{comm}}^{*} \frac{v_{\mathrm{2nd}}^{\Sigma}}{V_{\mathrm{c}}^{\Sigma}} + u_{\mathrm{diff}}^{*} \frac{v_{\mathrm{1st}}^{\Sigma}}{V_{\mathrm{c}}^{\Sigma}} \\ &= u_{\mathrm{comm}}^{*} + \Delta u_{\mathrm{dc,comm}} + \Delta u_{\mathrm{2nd,comm}} \end{aligned} \tag{2.74}$$

$$u_{\text{diff}} = \frac{u_{\text{n}} - u_{\text{p}}}{2} = u^*_{\text{diff}}\left(\frac{V^\Sigma_{\text{c}} + v^\Sigma_{\text{2nd}}}{V^\Sigma_{\text{c}}}\right) + u^*_{\text{comm}}\frac{v^*_{\text{1st}}}{V^\Sigma_{\text{c}}} = u^*_{\text{diff}} + u^*_{\text{diff}}\frac{v^\Sigma_{\text{2nd}}}{V^\Sigma_{\text{c}}} + u^*_{\text{comm}}\frac{v^\Sigma_{\text{1st}}}{V^\Sigma_{\text{c}}}$$
$$= u^*_{\text{diff}} + \Delta u_{\text{1st,diff}} + \Delta u_{\text{3rd,diff}} \tag{2.75}$$

The arm-common voltage reference $u^*_{\text{comm}}$ is in steady state approximately equal to $u_{\text{dc}}/2$, yet due to the presence of the oscillating terms in the available arm voltage $v^\Sigma_{\text{c}}$, the realized arm-common voltage $u_{\text{comm}}$ contains parasitic components, as shown in (2.74). Parasitic dc and second harmonic voltage component appear, causing a parasitic dc and second harmonic arm-common currents. While dc component is closed-loop regulated by the available arm-current controller, parasitic second harmonic current necessitates a dedicated controller that would suppress this term. Otherwise, it appears as a parasitic second harmonic circulating current, reducing the converter efficiency, and further increasing the oscillating terms of the SM voltage [67], [85].

The arm-differential voltage controls the arm-differential (ac terminal) current component. Besides the reference voltage $u^*_{\text{diff}}$, realized arm-differential voltage $u_{\text{diff}}$ contains parasitic first and third harmonic voltage components, shown in (2.75). The first harmonic voltage component $\Delta u_{\text{1st,diff}}$ creates a parasitic first harmonic ac terminal current, which is successfully suppressed by the ac current controller. The third harmonic parasitic component $\Delta u_{\text{3rd,diff}}$ is in phase in all three phase legs, thus creating undesirable common-mode voltage component.

Direct voltage control also has certain drawbacks when it comes to operation under unbalanced grid conditions. Namely, a product of the negative-sequence grid voltage and the positive sequence grid current, as well as the product of the positive-sequence grid voltage and negative sequence grid current yield zero sequence power components at double the fundamental frequency. In other words, the induced second harmonic power oscillations in three phases are equal in magnitude and phase. When the direct voltage control is applied, these power terms are not supplied by the MMC arms, but by the dc terminals, thus inducing a double the fundamental frequency current component at the dc terminals [86].

**Closed-loop voltage control** is another insertion index generation method, where the instantaneous values of the arm voltages are used, as in (2.76)-(2.77), as opposed to the average values used in the direct voltage control. This method poses more burden on communication, and is marginally stable, as opposed to the asymptotically stable direct voltage control [67], [85]. To balance the total converter energy among the arms, dedicated arm energy controllers are needed as part of the control structure. On the other hand, there are no parasitic voltage components, as can be seen from (2.78)-(2.79).

$$n_{\text{p}} = \frac{u^*_{\text{p}}}{v^\Sigma_{\text{c}}} \tag{2.76}$$

$$n_{\text{n}} = \frac{u^*_{\text{n}}}{v^\Sigma_{\text{c}}} \tag{2.77}$$

$$u_{\text{comm}} = \frac{u_{\text{p}} + u_{\text{n}}}{2} = \frac{n_{\text{p}}v^\Sigma_{\text{c,p}} + n_{\text{n}}v^\Sigma_{\text{c,n}}}{2} = \frac{1}{2}\left(\frac{u^*_{\text{comm}} - u^*_{\text{diff}}}{v^\Sigma_{\text{c,p}}}v^\Sigma_{\text{c,p}} + \frac{u^*_{\text{comm}} + u^*_{\text{diff}}}{v^\Sigma_{\text{c,n}}}v^\Sigma_{\text{c,n}}\right) = u^*_{\text{comm}} \tag{2.78}$$

$$u_{\text{diff}} = \frac{u_{\text{n}} - u_{\text{p}}}{2} = \frac{n_{\text{n}}v^\Sigma_{\text{c,n}} - n_{\text{p}}v^\Sigma_{\text{c,p}}}{2} = \frac{1}{2}\left(\frac{u^*_{\text{comm}} + u^*_{\text{diff}}}{v^\Sigma_{\text{c,n}}}v^\Sigma_{\text{c,n}} - \frac{u^*_{\text{comm}} - u^*_{\text{diff}}}{v^\Sigma_{\text{c,p}}}v^\Sigma_{\text{c,p}}\right) = u^*_{\text{diff}} \tag{2.79}$$

**Open-loop voltage control** method, proposed by [85], [87] is based on the similar principle of obtaining the insertion indices as in the closed-loop control method, apart from the fact that the instantaneous total arm voltages are not measured, but estimated. The authors argue that in such a manner the communication burden can be significantly reduced, and the need for voltage sensing devices can be eliminated. The stability analysis [85] shows that this method is asymptotically stable.

Due to the fact that the SM voltage is measured for protection reasons, and is readily available both to the local SM controller, as well as to the central converter controller through communication channels, all the analyses conducted within this thesis will assume closed-loop voltage control. The converter prototype, developed within the laboratory, briefly described in **Chapter 6**, also utilizes this control approach.

Up until this point, only the averaged model of the MMC arm was considered. It was assumed that the stack of SMs realizes the commanded arm voltage in a continuous manner, devoid of any parasitic components, as in the case of the closed-loop voltage control. Nevertheless, the number of SMs within an arm is finite, and so are the available voltage levels. Therefore, to produce a desired voltage waveform, an appropriate pulse-width modulation (PWM) technique should be adopted.

### 2.6.2 PWM techniques

The purpose of a PWM is to generate an ac voltage, whose average over a switching period is equal to the reference. While the PWM in two-level converters means switching the output ac voltage between the positive and negative dc terminal voltage, multilevel converters permit more degrees of freedom in choosing the number of voltage levels and duration of the pulses.

Modulation techniques decide when the switching event should take place and how long it should last. Different modulation methods, already studied for other types of more mature converters, have been investigated for the MMC. In the following paragraphs, some of the most prominent methods will be covered, outlining their advantages and disadvantages.

**The phase-shifted carrier (PSC) modulation** has been extensively studied for the MMC in [88]–[93]. It relies on $N$ mutually-shifted carriers, with each one being assigned to a single SM. The phase shift between carriers results in increased apparent switching frequency, and multilevel voltage waveform, as illustrated in **Fig. 2.10.a**.

Spectral analysis of the generated arm voltage shows that apart from the desired dc and fundamental ac component, components around ($N f_{\text{carr}},\ 2N f_{\text{carr}}, ...$) appear in the spectrum [89], [90]. Additional spectral components increase the total harmonic distortion (THD) of the generated voltage, and necessitate filters. Given the fact that the inductances in the grid have low pass nature, higher frequency content becomes less of a problem. Therefore, the product $N f_{\text{carr}}$ should be chosen such that the obtained voltage conforms the grid code requirements. On the other hand, the carrier frequency $f_{\text{carr}}$ is equal to the switching frequency of a single module in the PSC modulation, so there is a trade-off between the low THD and low switching losses.

Two arms constitute a phase leg, and therefore, spectral components of both arms influence the overall spectral content seen from the dc and ac terminals. As the two arms have different voltage references, the resulting high-frequency spectral content will differ as well. Introducing a phase-shift of $\beta = \pi$ between the upper and lower arm carriers, a so-called $(N + 1)$-level modulation is achieved, and the high frequency spectra seen from the dc terminals is minimized. Otherwise, if the high frequency

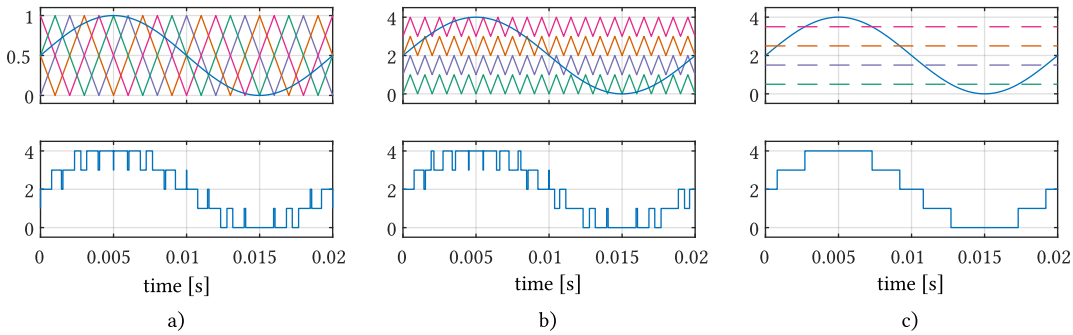


**Fig. 2.10** Examples of different modulation methods used for generating the reference arm voltage with $N = 4$ SMs per arm: a) PSC modulation method, with phase shift among carriers of $\Delta\theta = 2\pi/N$, and carrier frequency $f_{\text{carr}} = 250\,\text{Hz}$; b) Phase-disposition (PD) modulation method with carrier frequency $f_{\text{carr}} = 1000\,\text{Hz}$; c) Nearest-level (NL) modulation method.

spectrum observed from the ac terminals is to be minimized, the displacement angles between the positive arm and negative arm carriers should be as follows:

$$\beta = \begin{cases} 0, & N \text{ is odd} \\ \pi/N, & N \text{ is even} \end{cases} \tag{2.80}$$

Under such conditions, the number of voltage levels at the ac side is artificially increased, leading to the so-called $(2N + 1)$-level modulation [90], [93]. High-frequency harmonic spectrum of the ac terminal voltages is reduced, but increased of the dc terminal voltage. The choice between the two types is subject to the constraints of a specific application.

Voltage oscillations in the SMs as a consequence of the converter dynamics have been already studied in the previous sections. Nevertheless, the used model assumed continuous arm voltage, instead of a stack of dynamically switched SMs. As a consequence of switching, SM voltages contain high frequency ripple components, located around multiples of the carrier frequency $f_{\text{carr}}$. These components are inversely proportional to the number of SMs within the arm ($N$), but only up to some extent, where this dependence saturates, and the increase in $N$ has no further influence on the high frequency voltage spectra in the SMs.

PSC modulation method shows good results in mitigating all the frequency content up to the higher frequencies, determined by the carrier frequency. Another good feature of this modulation method is the fact that each SM has a dedicated carrier, and thus a constant switching frequency, resulting in equal loading among the SMs. In addition, the convenience of having a dedicated carrier to each SM can be utilized to realize a distributed control scheme, as will be detailed in **Chapter 6**. Note that although the carriers can be assigned to individual SMs, this might not always be the case. Namely, due to the possible differences in the SM voltages, inserting or bypassing one SM instead of other might be advantageous for preserving the voltage balance. Therefore, PSC method might just provide the adequate switching references, while the decision on which SMs are inserted/bypassed can be made by a sorting algorithm.

**Level-shifted carrier (LSC) modulation** techniques represent a group of multi-carrier modulation techniques, where the individual carriers are shifted with respect to one another in a vertical manner.

Namely, assuming an arm with $N$ SMs, $N$ individual carriers are created, and "stacked" on top of one another, as illustrated in **Fig. 2.10.b**. The reference insertion index $n_{x,y}$ is multiplied by the number of carriers $N$, thus constituting a reference for this modulation scheme. By comparing the reference with the "stack" of carriers, switching signals are obtained, as illustrated in **Fig. 2.10.b**.

The simplest form the the LSC modulation is the phase-disposition (PD) technique, where all $N$ stacked carriers are in-phase, as was in the example illustrated in **Fig. 2.10.b**. Other LSC modulation methods include *phase opposition disposition (POD)*, and *alternative phase opposition disposition (APOD)*, with latter producing the same output voltage as in the case of PSC modulation [91], [94]. One should note that in order to produce voltage waveforms with the same apparent switching frequency, carrier frequency should be selected as $N$ times higher than in the case of the PSC modulation.

Unlike the PSC, where each carrier could be assigned to a specific SM, switching frequency of the SMs with LSCs would be uneven, resulting in uneven thermal stress and unbalanced voltages among the SMs. Consequently, the intersection of the reference signal with the carriers determines just the switching events, whereas the choice of a SM to be inserted/bypassed is left to a sorting algorithm.

Compared to the PSC modulation method, where the harmonic spectrum is grouped around the multiples of carrier frequencies ($N f_{car}, 2N f_{car}, ...$), the frequency content of the arm voltage in case of PD and POD is dispersed up to the low frequencies [91]. Although the THD of the LSC methods might be lower compared to the PSC method [91] for a higher number of SMs, the presence of low frequency harmonics imposes higher overall filtering requirements. In addition, comparison between the PSC and the two LSC methods shows that the capacitor voltage ripple caused by modulation effects is the lowest in case of the PSC modulation (the same as APOD) [91].

**Nearest-level (NL) modulation** method relies on inserting the amount of SMs that would produce the voltage closest to the reference value. This is achieved by defining $N$ voltage levels that would represent the boundaries of specific regions, defined by $L_k$ in (2.81). If the reference voltage is within the range $[L_k, L_{k+1}]$, the number of SMs to be inserted is equal to $k$. The principle of the NL modulation has been illustrated in **Fig. 2.10.c**, where the assumed number of SMs is $N = 4$. Because of its characteristic shape, it is also referred to as *staircase modulation*.

$$L_k = \frac{V_c^{\Sigma}}{N}\left(0.5 + k\right) \qquad \text{, where } k = 1..N \tag{2.81}$$

The frequency with which the reference voltage is sampled, and compared with the predefined boundaries, is called *sampling frequency* and has major influence on performance of the method, along with the number of SMs [95]. It is shown that the dominant harmonics in the spectrum of the arm voltage are those around sampling frequency and its multiples, thereby creating an equivalence between the sampling frequency in the NL modulation and the carrier frequency in the PSC modulation. The value of this frequency should be chosen as high as possible, in order to have more precise sampling of the reference, and thus fully utilize all the available voltage levels. Nevertheless, above certain sampling frequency, further reduction of the sampling period does not bring any benefits, and the quality of the voltage waveform is solely dependent on the number of SMs [95].

Besides harmonic components around multiples of the sampling frequency, spectrum of the arm voltage also contains low frequency harmonics, which become pronounced as the number of available

voltage levels decreases [96]. Consequently, for an MMC with a low number of SMs per arm, the NL modulation is not as suitable as is the PSC modulation, with a sufficiently high carrier frequency. In contrast, if the number of SMs per arm is high, NL modulation becomes favourable over the PSC, due to simplicity of implementation, whereas the THD of the two methods becomes very similar.

Unlike PSC modulation, the NL modulation cannot have pre-assigned SMs that would be inserted/bypassed during the transition from one level to another. This is a consequence of the asymmetry between the lower and higher levels in terms of insertion period, which would eventually result in imbalance between the SMs [94]. Therefore, this modulation scheme necessitates a centralized voltage balancing algorithm, based on SMs sorting.

**Programmable modulation** methods are those modulation methods where the switching instants of the SMs are predetermined as a result of different criteria.

*Selective harmonic elimination (SHE)* is a modulation method inherited from the thyristor-based converters, that can be applied in the MMC with low number of SMs [97]. As the name indicates, the switching instants of the SMs are precalculated, with the objective of eliminating certain low-frequency harmonics. Precalculated values of the switching angles are stored in a form of look-up table for different values of modulation indices. As the method determines only the switching events, and not the particular SMs to be inserted/bypassed, it is applied in conjunction with a centralized voltage balancing algorithm.

More advanced programmable methods are *optimized pulse patterns (OPPs)* [98], [99], where the switching events are precalculated in a similar fashion as for the SHE. Nevertheless, the objective of these modulation methods is often multidimensional, meaning that several parameters are taken into consideration, such as total demand distortion (TDD), converter losses (switching frequency), dynamic performance, etc. The switching frequency in thus modulated converter can be as low as fundamental frequency [98], [99], all while conforming with the grid codes.

It is noteworthy that the PSCs modulation, unlike LSC and NL methods, can also meet grid code requirements and provide superior dynamic behaviour with a low number of SMs per arm. However, this comes at the expense of an increased switching frequency, and thus converter losses. Due to that fact, and due to the possibility of assigning carriers to individual SMs, the PSC modulation method has been adopted as the modulation method used in the work presented in this thesis.

## 2.7 M3C: Topology properties and basic operating principles

Focus of the thesis will be mainly on control methods and development of the standard MMC. Arm-energy control methods, presented in **Chapter 3** and **Chapter 4**, are developed for the standard MMC, yet they are general in a sense that they can be equally applied to different variants of the MMC family of converters, including the M3C. Therefore, it is important to familiarize with the basic operating principles of the M3C, in order to facilitate the discussion on energy control in **Chapter 5**.

This topology was proposed by *Erickson and Al-Naseem* [32] for interconnection of two asynchronous ac systems. It was proposed even before the standard MMC, and as the first proposal of the MMC, it also lacked arm inductors, unlike later publications [33], [100], [101]. The layout of a 3PH ac-ac M3C topology is given in **Fig. 2.11**, where two 3PH systems, labelled as *ABC* and *RST*, are interfaced by an M3C.

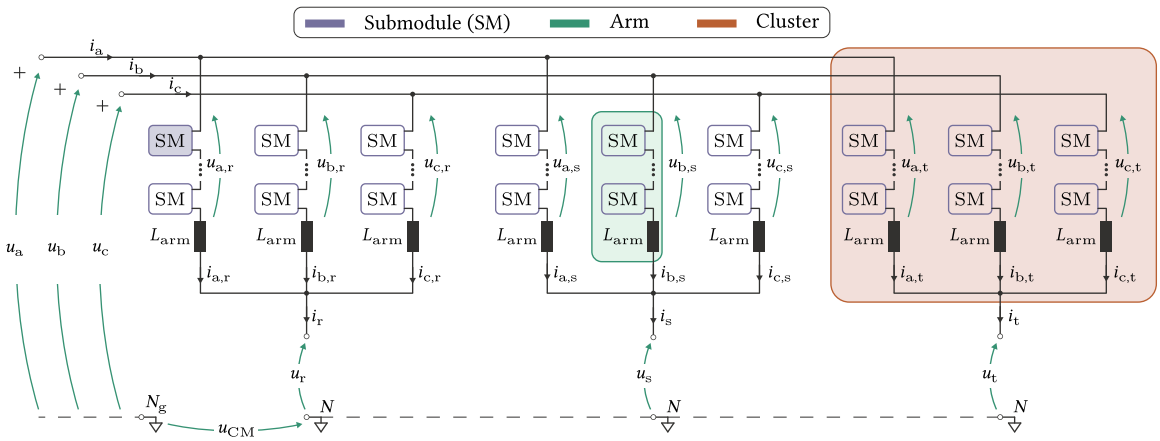


**Fig. 2.11** Layout of a 3PH ac-ac M3C topology, together with labelling of relevant converter variables (voltages and currents).

Like in the standard MMC, each terminal of the *ABC* system is interconnected to a terminal of the *RST* system via an arm, consisting of a stack of series-connected SMs and an arm inductor. Unlike the standard MMC, a SM has to provide a bipolar voltage at its terminals, so it is typically realized with a FB switching module. The role of the arm inductor is to permit independent switching in each arm, and allow for circulating current control within the converter. Like in the MMC, a stack of SMs acts as a controllable multilevel voltage source.

From **Fig. 2.11**, one can observe that three arms connected to three *ABC* terminals are connected in star configuration, which is referred to as a *cluster* within this thesis. Neutral point of such a cluster is connected to an *RST* terminal. As a result, three such clusters can be identified in the M3C topology. Note that the topology is symmetrical regardless from which terminals it is observed. Namely, one could identify a cluster of three arms connected to three different *RST* terminals, connected in star configuration, with the neutral point connected to one of the *ABC* terminals. Neutral points of the systems *ABC* and *RST* are labelled as $N_g$ and $N$, respectively, whereas the voltage difference between the two neutrals is referred to as *common-mode voltage*, and is labelled as $u_{CM}$.

The fact that three phase-voltages in both systems are symmetrical in normal conditions, and that the topology itself is symmetrical, permits us to draw useful conclusions on the M3C operation just by observing a single arm. Therefore, adopting a generic form, where $x = \{A, B, C\}$, and $y = \{R, S, T\}$, and applying Kirchoff's voltage equation for the arm *xy* yields:

$$u_{x,y} = u_x - u_y - u_{CM} - L_{arm}\frac{di_{x,y}}{dt} \tag{2.82}$$

Observing **Fig. 2.11**, and identifying clusters of arms connected to a single terminal, one can assume that the terminal current is equally split among the arms forming that cluster. Therefore, arm current can be expressed in terms of terminal currents as:

$$i_{x,y} = \frac{i_x}{3} + \frac{i_y}{3} \tag{2.83}$$

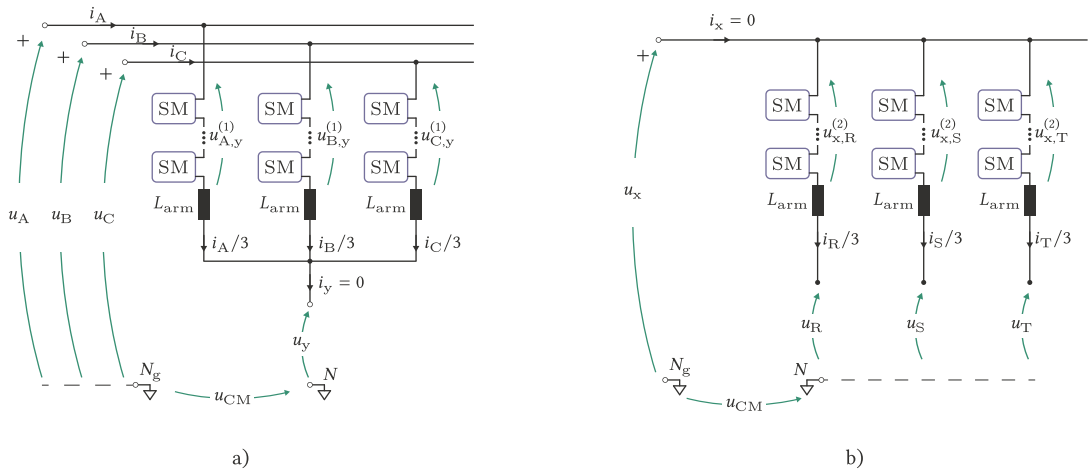


**Fig. 2.12** Decoupled control of the terminal variables: a) *ABC* terminal current control, not influencing the *RST* terminal current; b) *RST* terminal current control not influencing the *ABC* terminal current.

Assuming that the ac systems *ABC* and *RST* are of different frequencies, control of the terminal variables is decoupled one from another, decomposing the arm voltage from (2.82) into two independent terms:

$$u^{(1)}_{x,y} = u_x - \frac{L_{arm}}{3}\frac{di_x}{dt} \tag{2.84}$$

$$u^{(2)}_{x,y} = -u_y - u_{CM} - \frac{L_{arm}}{3}\frac{di_y}{dt} \tag{2.85}$$

The arm-voltage consists of two components: $u^{(1)}_{x,y}$, which is in charge of the $x = \{A, B, C\}$ current/voltage control, and $u^{(2)}_{x,y}$, which controls the $y = \{R, S, T\}$ terminal current/voltage. To demonstrate that the two systems can be really decoupled, as assumed, we will at first observe a cluster of arms connected to one of the $y = \{R, S, T\}$ terminals, as illustrated in **Fig. 2.12.a**. Arm voltages and currents are assumed to have only the components related to the $x = \{A, B, C\}$ terminal, i.e. $u^{(1)}_{x,y}$ and $i_x/3$. Under the assumption that the *ABC* system current is deprived of a zero-sequence component, the three arm currents sum-up to zero, thus yielding $i_y = 0$. Under this condition, and with equal arm inductances, terminal voltage $u_y$ can be calculated as a mean value of the three voltages applied to the star. Taking into account the definition from (2.84), this sum takes the form:

$$u_y + u_{CM} = \frac{(u_A - u^{(1)}_{A,y}) + (u_B - u^{(1)}_{B,y}) + (u_C - u^{(1)}_{C,y})}{3} = \frac{L_{arm}}{3}\frac{d(i_A + i_B + i_C)}{dt} = 0 \tag{2.86}$$

The last expression shows that the arm-voltage components $u^{(1)}_{x,y}$ are decoupled from the $y$ terminal voltage. In addition, provided that there is no path for zero-sequence currents, three arm-current components originating from the *ABC* terminals also sum-up to zero, and thus do not appear at *RTS* terminals. Therefore, the voltage term $u^{(1)}_{x,y}$ solely influence the $x$ terminal current component control, as assumed previously in (2.84).

On the other hand, should one observe a cluster of arms connected to the same $x = \{A, B, C\}$ terminal, and observing only the arm components related to $y = \{R, S, T\}$ terminals, an equivalent circuit can

be expressed as in **Fig. 2.12.b**. As there is no path for zero-sequence currents, the three *RST* terminal currents sum-up to zero, yielding $i_x = 0$. Similarly to the previous case, the terminal voltage $u_x$ can be calculated as a mean value of the three voltages applied to the star. Taking into account the definition from (2.85), this sum takes the following form:

$$u_x = \frac{(u_R + u_{CM} + u_{x,R}^{(2)}) + (u_S + u_{CM} + u_{x,S}^{(2)}) + (u_T + u_{CM} + u_{x,T}^{(2)})}{3} = \frac{L_{arm}}{3}\frac{d(i_R + i_S + i_T)}{dt} = 0 \quad (2.87)$$

The last expression confirms that the arm-voltage components $u_{x,y}^{(2)}$ have no influence on the $x = \{A, B, C\}$ terminal voltages $u_x$. In addition, due to the absence of the zero-sequence current path, the three arm-current components originating from the *RST* terminals also sum-up to zero, and do not appear at *ABC* terminals. As a result, we can conclude that the two assumptions about an independent control of the terminal voltages and currents, expressed in (2.84)-(2.85), are valid, and will be utilized in the upcoming analyses.

As the SMs in the M3C are equipped with floating capacitors, their energy content is dynamically changed and dependent upon the arm-power components. To understand interactions between the arm quantities, and the consequences it has on the M3C operation, the following notation will be adopted, focusing on a single arm *xy*. Please note that, as in the case of the MMC, switching effects are neglected, and arm voltage is assumed to be a continuous variable.

$$u_x = \hat{u}_x \sin(\omega_x t) \quad (2.88) \qquad i_x = \hat{i}_x \sin(\omega_x t + \phi_x) \quad (2.89)$$

$$u_y = \hat{u}_y \sin\big(\omega_y t + \Theta_y\big) \quad (2.90) \qquad i_y = \hat{i}_y \sin\big(\omega_y t + \Theta_y + \phi_y\big) \quad (2.91)$$

Based on the definitions of terminal variables (2.88)-(2.91), arm voltage (2.82) and current (2.83), and neglecting the inductive voltage drop and the common-mode voltage $u_{CM}$, the arm power is calculated as follows:

$$\begin{aligned} p_{xy} = u_{x,y} i_{x,y} = &\big(u_x - u_y\big)\big(i_x/3 + i_y/3\big) = \underbrace{\frac{\hat{u}_x \hat{i}_x}{6}\cos(\phi_x)}_{\text{dc value}} - \frac{\hat{u}_x \hat{i}_x}{6}\cos(2\omega_x t + \phi_x) + \ldots \\ &+ \underbrace{\frac{\hat{u}_x \hat{i}_y}{6}\cos\big((\omega_x - \omega_y)t - \Theta_y - \phi_y\big)}_{\text{LF component}} - \frac{\hat{u}_x \hat{i}_y}{6}\cos\big((\omega_x + \omega_y)t + \Theta_y + \phi_y\big) + \ldots \\ &- \underbrace{\frac{\hat{u}_y \hat{i}_y}{6}\cos\big(\phi_y\big)}_{\text{dc value}} + \frac{\hat{u}_y \hat{i}_y}{6}\cos\big(2\omega_y t + 2\Theta_y + \phi_y\big) + \ldots \\ &- \underbrace{\frac{\hat{u}_y \hat{i}_x}{6}\cos\big((\omega_x - \omega_y)t - \Theta_y + \phi_x\big)}_{\text{LF component}} + \frac{\hat{u}_y \hat{i}_x}{6}\cos\big((\omega_x + \omega_y)t + \Theta_y + \phi_x\big) \end{aligned} \quad (2.92)$$

Observing (2.92), it can be concluded that the arm power component has two dc values, stemming from the active power delivered from the *ABC* system, and delivered to the *RST* system. These terms

will be utilized for the arm energy control, further explained in **Chapter 5**. Two power terms at the angular frequency $\omega_x - \omega_y$ are also present and have a significant influence on the operation of the M3C. Namely, in case when the angular frequency of the *RST* system $\omega_y$ approaches the angular frequency of the *ABC* system $\omega_x$, amplitude of the voltage oscillation at the angular frequency $\omega_x - \omega_y$ increases significantly, leading to an unstable operation of the converter. Unless circulating currents are injected to compensate these terms [102], operation of the M3C interfacing two systems of similar frequencies is prohibited. Even in case when the circulating currents are injected, voltage ripple is still higher than in the case of an equivalent MMC [34], while the arm current is significantly increased. On the other hand, the standard MMC experiences a similar problem when operating at low frequencies.

Various studies have been conducted on operation of the M3C [33], [100]–[102], and its comparison with the standard MMC for drives applications [33], [34]. It has been concluded that the standard MMC is well suited for drives which operate nominally at higher frequencies, and with a quadratic torque characteristic, such as pumps, fans and blowers. On the other hand, M3C is well suited for low-speed gearless drives with a constant torque characteristic, such as mills, conveyors and extruders [34].

## 2.8 Summary

In this chapter, modelling of the standard and matrix MMC was performed. Key variables, governing the MMC operation were identified. The operating range of the converter voltage was defined, as a function of the the submodule ratings, number of submodules and their type. Fault-handling capabilities of the converter with different submodule types were discussed. Equations describing energy oscillations within the converter arms were derived, and directly related to the voltage oscillations within the submodules. Remedies for reducing the voltage oscillations were presented for the standard operation, as well as the low-output-frequency operation. Different methods for insertion index generation were discussed, as well as various multi-level modulation methods, typically employed in the MMC control. Finally, topology and basic operating principles of the M3C were presented, together with the equations describing terminal and internal variables. All the theory presented in this chapter serves as a basis for further theoretical analyses in the thesis.

# 3

# Methods for the Arm Energy Control in the MMC

*The energy content within the arms should correspond to their respective energy references, in order to enable proper generation of the arm voltages. To meet the objective, terminal, as well as internal currents must be controlled in a way that ensures that the arm energies correspond to their references. The energy content within each arm should be controlled independently, thus allowing the greatest possible flexibility of the converter operation. In addition, these control actions should not alter the terminal variables. Finally, the arm energy control method should be intuitive and simple to implement, while providing satisfactory results under different operating conditions. In this chapter, energy control mechanisms are identified, and different methods for their realization are proposed. The proposed control methods are evaluated under different conditions, compared mutually, as well as with other control methods.*

## 3.1 Motivation

To generate desired arm-voltage waveforms, the average value of the total voltage within an MMC arm should be greater than the maximal value of the arm-voltage reference. It has been shown in **Fig. 2.6** that the highest utilization of the HB SMs is achieved when $m_{\mathrm{ac}} = m_{\mathrm{dc}} = 0.5$. In that case, the total available arm voltage should be $V_{\mathrm{c}}^{\Sigma} \geq u_{\mathrm{dc}}$. Nevertheless, in order not to loose generality, the average value of the arm voltage will be simply denoted as $V_{\mathrm{c}}^{\Sigma}$, without presumptions regarding its value.

The average value of the total voltage available within an arm $V_{\mathrm{c}}^{\Sigma}$ is related to the energy content of the arm capacitors by the relationship (2.40), repeated here:

$$W_{\mathrm{arm}} = \frac{1}{2} C_{\mathrm{arm}} \left( V_{\mathrm{c}}^{\Sigma} \right)^2 \tag{3.1}$$

By controlling the average arm-power quantities, the average arm energy can be controlled, and so the average arm voltage $V_{\mathrm{c}}^{\Sigma}$. In other words, to maintain the arm voltage around its current value, the net-zero power flow into the arm should be achieved.

Repeating the equations (2.33)-(2.34), shows that in order to have a zero-net power flow into an arm, the dc power terms should cancel each other. Oscillating components that exist in the arm power do not contribute to the average arm energy, and are thus disregarded.

$$p_{\mathrm{x,p}} = \underbrace{\frac{u_{\mathrm{dc}} i_{\mathrm{dc,x}}}{2} - \frac{\hat{u}_{\mathrm{ac}} \hat{i}_{\mathrm{ac}} \cos(\phi_{\mathrm{ac}})}{4}}_{\text{dc value}} \tag{3.2}$$

$$p_{\mathrm{x,n}} = \underbrace{\frac{u_{\mathrm{dc}} i_{\mathrm{dc,x}}}{2} - \frac{\hat{u}_{\mathrm{ac}} \hat{i}_{\mathrm{ac}} \cos(\phi_{\mathrm{ac}})}{4}}_{\text{dc value}} \tag{3.3}$$

From the above two equations, we can conclude that the average power terms in the two arms of a same phase leg $x$ are identical, and dependent upon the terminal variables. Assuming symmetrical conditions, i.e. dc current equally distributed among the arms ($i_{\mathrm{dc,x}} = i_{\mathrm{dc}}/3$), and symmetrical ac terminal currents, summing the power terms from (3.2) and (3.3) across all the arms of the converter yields:

$$p_{\Sigma} = \sum_{\substack{x=A,B,C \\ y=p,n}} \left( \frac{u_{\mathrm{dc}}}{2} \frac{i_{\mathrm{dc,x}}}{3} - \frac{\hat{u}_{\mathrm{ac}} \hat{i}_{\mathrm{ac}} \cos(\phi_{\mathrm{ac}})}{4} \right) = \underbrace{u_{\mathrm{dc}} i_{\mathrm{dc}}}_{P_{\mathrm{dc}}} - \underbrace{\frac{3}{2} \hat{u}_{\mathrm{ac}} \hat{i}_{\mathrm{ac}} \cos(\phi_{\mathrm{ac}})}_{P_{\mathrm{ac}}} \tag{3.4}$$

Therefore, to maintain an energy equilibrium in each arm of the converter under symmetrical conditions, it is sufficient to maintain a balance between the ac terminal active power and the dc terminal power. Additionally, if the total converter energy is to be changed, i.e. the capacitor voltage in all the SMs, it is sufficient to manipulate the power difference between the total ac and dc power, and it will equally reflect in all the arms.

Note that in the previous analysis the converter power losses were neglected. Therefore, at equilibrium state, the power difference will be equal to the converter power losses. Nevertheless, even when it is accounted for the converter power losses, and the converter is kept at its equilibrium energy state, the total converter energy might not be equally distributed among the converter arms, due to different effects.

### 3.1.1 Sources of energy imbalances

There are several factors that might cause asymmetries among the arm energies, and that require further explanation.

Electrical parameters of the arms might differ to some extent, and thus cause an energy imbalance. To understand the imbalances caused by asymmetries in the arm parameters, we will briefly analyse those caused by the asymmetries in the arm capacitance, inductance and the parasitic resistance.

To facilitate understanding, it will be assumed that the converter works in the inverter mode of operation, i.e. generates an adequate ac voltage at its ac terminals, and draws the active power from the dc terminals. Power drawn from the dc terminals should correspond to the active ac power, augmented for the total power losses inside the converter.

**The arm capacitance asymmetry** occurs when the the equivalent capacitance $C_{\mathrm{arm}}$ differs among the arms of a converter. The equivalent capacitance of an arm is the capacitance of a series connection of all the SM capacitors within the arm:

$$\frac{1}{C_{\mathrm{arm}}} = \sum_{z=1}^{N} \frac{1}{C_{\mathrm{z}}} \tag{3.5}$$

Two types of asymmetries can occur. The first asymmetry type occurs when the equivalent arm capacitances within one phase leg are higher or lower with respect to the ones in another phase

leg. Under dynamic conditions, when the dc power does not match the power reference, there will be a surplus (or deficiency) of a power delivered to the converter, which is absorbed (or released) by the SM capacitors. This integral of power will represent the excess energy stored in (or drawn from) the SM capacitors, and the energy is equally distributed to all arms under symmetric conditions. In case when the total capacitance within a phase leg is different from the other two, equal energy distribution yields unequal voltage distribution among the phase-legs.

The second type of asymmetry occurs when the arm capacitances differ within a phase leg. During transient conditions, when there is a non-zero power flow to (from) the phase leg, although the excess power will be equally split among the two arms, the arm with a lower arm capacitance will charge (discharge) more compared to the other arm within the phase leg. As a result, a voltage imbalance between the arms appears.

**The arm inductance asymmetry** also provokes energy imbalance between the arms, and it might cause some parasitic current components at the MMC terminals [103]. To understand the underlying processes, a single phase leg of an MMC is depicted in **Fig. 3.1.a**, using the averaged arm model, and assuming unequal inductances in the two arms, denoted as $L_p$ and $L_n$.

Writing the Kirchoff's voltage law equations for the two arms yields:

$$\frac{u_{dc}}{2} = u_{ac} + R_p i_p + L_p \frac{di_p}{dt} + u_p \tag{3.6}$$

$$\frac{u_{dc}}{2} = -u_{ac} + R_n i_n + L_n \frac{di_n}{dt} + u_n \tag{3.7}$$

Defining the sum and differential inductances as $L_\Sigma = L_p + L_n$ and $L_\Delta = L_p - L_n$, and similarly the sum and differential arm resistances, arm-common and arm-differential equations are obtained from (3.6)-(3.7) as:

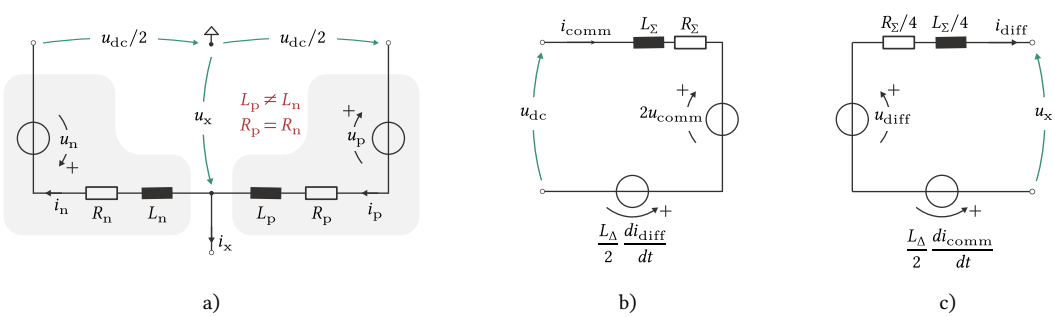


**Fig. 3.1** a) Representation of an MMC phase leg, with idealized voltage sources, and asymmetric arm parameters; b) Equivalent circuit for the arm-common current control considering inductance mismatches among the arms; c) Equivalent circuit for the arm-differential current control considering inductance mismatches among the arms.

$$\begin{aligned} u_{\mathrm{dc}} =& \underbrace{u_{\mathrm{p}} + u_{\mathrm{n}}}_{2u_{\mathrm{comm}}} + R_{\mathrm{p}}\Big(i_{\mathrm{comm}} + \frac{i_{\mathrm{diff}}}{2}\Big) + L_{\mathrm{p}}\frac{d(i_{\mathrm{comm}} + i_{\mathrm{diff}}/2)}{dt} + \ldots \\ &+ R_{\mathrm{n}}\Big(i_{\mathrm{comm}} - \frac{i_{\mathrm{diff}}}{2}\Big) + L_{\mathrm{n}}\frac{d(i_{\mathrm{comm}} - i_{\mathrm{diff}}/2)}{dt} \\ =& 2u_{\mathrm{comm}} + R_{\Sigma}i_{\mathrm{comm}} + L_{\Sigma}\frac{di_{\mathrm{comm}}}{dt} + \frac{R_{\Delta}}{2}i_{\mathrm{diff}} + \frac{L_{\Delta}}{2}\frac{di_{\mathrm{diff}}}{dt} \end{aligned} \tag{3.8}$$

$$\begin{aligned} u_{\mathrm{ac}} =& \underbrace{\frac{u_{\mathrm{n}} - u_{\mathrm{p}}}{2}}_{u_{\mathrm{diff}}} + \frac{R_{\mathrm{n}}}{2}(i_{\mathrm{comm}} - \frac{i_{\mathrm{diff}}}{2}) + \frac{L_{\mathrm{n}}}{2}\frac{d(i_{\mathrm{comm}} - \frac{i_{\mathrm{diff}}}{2})}{dt} - \frac{R_{\mathrm{p}}}{2}(i_{\mathrm{comm}} + i_{\mathrm{diff}}/2) + \ldots \\ &- \frac{R_{\mathrm{n}}}{2}(i_{\mathrm{comm}} - \frac{i_{\mathrm{diff}}}{2}) - \frac{L_{\mathrm{p}}}{2}\frac{d(i_{\mathrm{comm}} + \frac{i_{\mathrm{diff}}}{2})}{dt} \\ =& u_{\mathrm{diff}} - \frac{R_{\Sigma}}{4}i_{\mathrm{diff}} - \frac{L_{\Sigma}}{4}\frac{di_{\mathrm{diff}}}{dt} - \frac{R_{\Delta}}{2}i_{\mathrm{comm}} - \frac{L_{\Delta}}{2}\frac{di_{\mathrm{comm}}}{dt} \end{aligned} \tag{3.9}$$

The equation (3.8) shows correlation between the arm-common voltage and the arm current. It reveals that under the asymmetry among the arm inductors, a parasitic ac voltage component appears, proportional to the time-derivative of the ac terminal current $i_{\mathrm{diff}}$, and the arm inductance difference $L_{\Delta}$, as shown in **Fig. 3.1.b**. This voltage component will drive a parasitic fundamental-frequency arm-common current component. As the arm inductance differences $L_{\Delta}$ might have arbitrary values in the three phase legs, so do the induced fundamental-frequency arm-common currents. Therefore, their sum over the three-phase legs is not equal to zero, and thus appears at the MMC dc terminals as the oscillating component. Therefore, it is necessary to have a dedicated controller tuned to suppress this parasitic arm-common current term.

On the other hand, the equation (3.9) reveals that a parasitic voltage component appears in the arm-differential circuitry (c.f. **Fig. 3.1.c**), proportional to the derivative of the arm-common current $i_{\mathrm{comm}}$, and the arm inductance difference $L_{\Delta}$. While the derivative of the arm-differential current is the oscillating term at the fundamental frequency, the derivative of the arm-common current oscillates at double the fundamental frequency in case when the direct voltage control is applied, thus appearing at the ac terminals. In addition, the second harmonic arm-common current component is not symmetrical among the three phases, thus appearing at the dc terminals as well. Though a dedicated controller for this current component is needed in the direct voltage control scheme, such a problem is not present in the closed-loop voltage control.

Nevertheless, even in case of the closed-loop voltage control, parasitic fundamental-frequency arm-common current appears as a result of asymmetry, and interacts with the arm voltage components, resulting in non-zero average power components. To understand the effects of such a current on the arm energy content, induced arm-common current component can assume the following form:

$$\Delta v_{\mathrm{comm}}^{(\mathrm{ac})} = -\frac{L_{\Delta}}{2}\frac{di_{\mathrm{diff}}}{dt} = -\frac{\omega_{\mathrm{g}}L_{\Delta}\hat{i}_{\mathrm{ac}}}{2}\cos\left(\omega_{\mathrm{g}}t + \phi\right) \quad \Longrightarrow \quad \Delta i_{\mathrm{comm}}^{(\mathrm{ac})} = \frac{L_{\Delta}\hat{i}_{\mathrm{ac}}}{2L_{\Sigma}}\sin\left(\omega_{\mathrm{g}}t + \phi\right) \tag{3.10}$$

Interaction of such a current with the arm-voltage components in the positive and negative arm yields the following power terms:

$$\frac{dW_{\mathrm{p}}}{dt} = \left(\frac{u_{\mathrm{dc}}}{2} - \hat{u}_{\mathrm{ac}} \sin\left(\omega_{\mathrm{g}} t\right)\right) \frac{L_{\Delta} \hat{i}_{\mathrm{ac}}}{2L_{\Sigma}} \sin\left(\omega_{\mathrm{g}} t + \phi\right) \tag{3.11}$$

$$\frac{dW_{\mathrm{n}}}{dt} = \left(\frac{u_{\mathrm{dc}}}{2} + \hat{u}_{\mathrm{ac}} \sin\left(\omega_{\mathrm{g}} t\right)\right) \frac{L_{\Delta} \hat{i}_{\mathrm{ac}}}{2L_{\Sigma}} \sin\left(\omega_{\mathrm{g}} t + \phi\right) \tag{3.12}$$

Only the arm-differential energy term has a non-zero average over a fundamental period, which is equal to:

$$\frac{dW_{\Delta}}{dt} = -\frac{\hat{u}_{\mathrm{ac}} \hat{i}_{\mathrm{ac}} L_{\Delta} \cos\left(\phi\right)}{4L_{\Sigma}} \tag{3.13}$$

The last equation shows that this current component creates an energy imbalance between the arms within a phase leg. As discussed earlier, it can be suppressed by a dedicated controller. However, even temporary existence of the parasitic fundamental-frequency arm-common current component creates an energy imbalance between the arms within a phase leg, thus necessitating a dedicated energy controller that would maintain the arm-differential energy $W_{\Delta}$ around its reference value.

Note that in previous analysis the arm resistance was neglected, as it does not have profound effect on the outcomes of the analysis. Nevertheless, difference in the parasitic arm resistance may also cause an energy imbalance, which will be clarified hereupon.

**The arm resistance asymmetry** is the most likely to occur, as the arm-resistance is a parasitic term, combining the parasitic resistances of the semiconductors in the SMs, the arm inductor resistance, as well as the resistances of the busbars and connections. Differences in cooling, layout and manufacturing may cause the parasitic resistance terms to differ among the converter arms, which may provoke different effects in the MMC.

Equations (3.8) - (3.9) show the dependence of the arm-common and arm-differential currents on the respective voltages. Assuming symmetric arm inductors in this analysis ($L_{\Delta} = 0$), a parasitic voltage term appears in the arm-common equivalent circuitry, proportional to the asymmetry in the arm resistances, and the arm-differential current, as illustrated in **Fig. 3.2.b**. On the other hand, arm-differential equivalent circuitry (c.f. **Fig. 3.2.c**) reveals that the asymmetry in the arm resistances results in parasitic dc voltage component, creating a parasitic dc current at the ac terminals [103].

Nevertheless, the parasitic resistances are typically small, and significantly lower than the arm impedances, rendering these parasitic current components negligible. Nevertheless, the asymmetry in the parasitic resistances can contribute to the energy imbalances among the MMC arms. The first type of imbalance may occur among the phase legs, if the parasitic resistances are different among the phases. Namely, the dc current drawn from the dc terminals corresponds to the power requirements at the ac terminals, augmented for the total converter power losses. Assuming symmetrical conditions, the dc current is equally split among the phase-legs. While the active power consumption at the ac terminals might be balanced, different parasitic resistances would cause different power losses among the phase legs. As a result, phase legs with lower resistance will experience lower losses, resulting in increased energy content in their SMs, whereas those with higher resistance would have their energy content reduced.

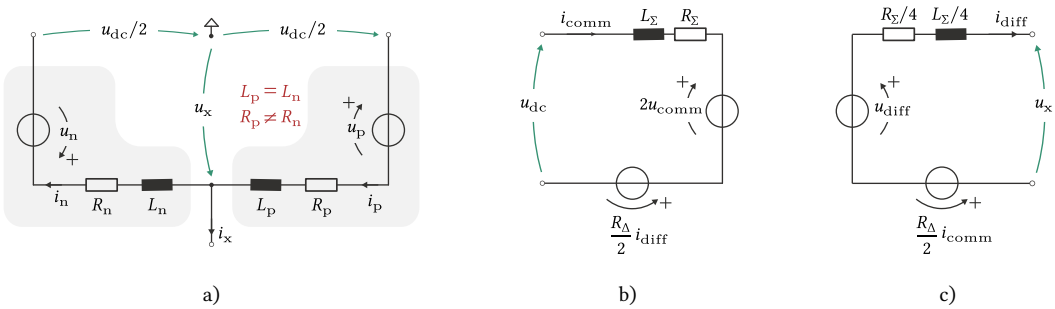


**Fig. 3.2** a) Representation of an MMC phase leg, with idealized voltage sources, and asymmetric arm parameters; b) Equivalent circuit for the arm-common current control considering resistance mismatches among the arms; c) Equivalent circuit for the arm-differential current control considering resistance mismatches among the arms.

Another type of energy imbalance might occur within a phase leg, when the parasitic resistances of the two arms differ. In such a case, while the power received from the dc terminals and released to a corresponding ac terminal are equal for the two arms (c.f. (3.2)-(3.3)), the difference in their power losses causes the arm with lower losses to surcharge, and the other with higher losses to discharge.

**Unbalanced grid conditions** are yet another source of energy imbalance within the converter. Namely, taking as an example a single-phase-to-ground fault, affected phase will experience a sudden voltage drop at the MMC terminals. While the grid-current control will ensure that the ac terminal currents remain symmetrical after the transient, the active power delivered to the affected phase will be generally smaller compared to the remaining phases. Consequently, under equal dc power distribution among the phases, the total energy in the affected phase leg will increase, in contrast to the other two phases. Even if the dc power is distributed among the phases proportionally to the active power delivered to the ac terminals, a power difference during transients might have already caused an energy imbalance in the affected phase.

As a result, besides dc power redistribution among the phases according the the ac phase power outputs, an energy controller maintaining the energy content within each phase leg is also necessary, to support operation under unbalanced grid conditions.

**Failed SM operation** is an operating mode where the energy imbalance among the arms can be a desired scenario. Namely, redundant SMs can be installed to provide uninterrupted operation during a fault of a SM. There are different schemes how the redundancy is employed.

One possible scheme is a so-called ”cold reserve” [104], [105], where the redundant SMs are kept bypassed during normal operation, and inserted into the circuitry only when a SM fails. The drawback of this approach is that the ”cold” SM has to be charged prior to being inserted, and this process might last prohibitively long.

Another scheme is the so-called ”hot reserve” or ”spinning reserve”, where redundant SMs are used along with the regular ones during normal operation. In case of a fault of a SM, faulty SM is bypassed, whereas the affected arm continues its operation with the remaining SMs. Although operating with an asymmetric number of SMs per arm, the last scheme can guarantee normal operation, provided that the total voltage available in the affected arm is sufficiently high to generate the reference voltage [104]. In case where the increase in the SM voltage reference is permitted, the total arm voltage is

preserved by increasing the voltages of individual SMs. Otherwise, the neutral-point shift approach is applied. Nevertheless, in both cases the arm energy reference is changed, due to the change in the number of SMs.

Previous discussion has shown that the energy content in the arms might change due to the tolerances in arm parameters, as well as during transients or unbalanced grid conditions. The energy imbalance can also be intentionally produced in case of a failed SM.

In the previous chapter, different methods for insertion index generation were discussed, together with the implications they have on the generated arm voltage. It has also been mentioned that the *direct voltage control* method maintains the arm energies inherently balanced, in contrast to the *closed-loop voltage control* method, which necessitates dedicated energy controllers for this purpose.

### 3.1.2 Internal dynamics of the direct-voltage-controlled converter

The direct voltage control method is the simplest control method, as its modulation indices are generated without the need of measured arm voltages, and more importantly- it does not require dedicated energy controllers to keep the converter arm energies balanced, as it was empirically proved in [67].

A formal proof of the self-balancing capability, along with the discussion regarding the process dynamics and different factors that have a decisive influence over it, is provided in **Appendix A**.

To summarize the conclusions, the total arm voltages are defined as in (3.14)-(3.15), where $V^{\Sigma}_{\mathrm{c,p,ref}}$ and $V^{\Sigma}_{\mathrm{c,n,ref}}$ are reference arm voltages, whereas $\Delta V^{\Sigma}_{\mathrm{c,p}}$ and $\Delta V^{\Sigma}_{\mathrm{c,n}}$ are mean arm voltage deviations from the reference values.

$$V^{\Sigma}_{\mathrm{c,p}} = V^{\Sigma}_{\mathrm{c,p,ref}} + \Delta V^{\Sigma}_{\mathrm{c,p}} \tag{3.14}$$

$$V^{\Sigma}_{\mathrm{c,n}} = V^{\Sigma}_{\mathrm{c,n,ref}} + \Delta V^{\Sigma}_{\mathrm{c,n}} \tag{3.15}$$

After a derivation process, detailed in **Appendix A**, and introducing a sum deviation term $\Delta V^{\Sigma}_{\mathrm{c},\Sigma} = \Delta V^{\Sigma}_{\mathrm{c,p}} + \Delta V^{\Sigma}_{\mathrm{c,n}}$, and delta deviation term $\Delta V^{\Sigma}_{\mathrm{c},\Delta} = \Delta V^{\Sigma}_{\mathrm{c,p}} - \Delta V^{\Sigma}_{\mathrm{c,n}}$, the dynamic behaviour of the two terms is described by the following equations in Laplace's domain:

$$\Delta V^{\Sigma}_{\mathrm{c},\Sigma}(s)\left(s^2 C_{\mathrm{arm}} L_{\mathrm{arm}} + sC_{\mathrm{arm}}\left(R_{\mathrm{arm}} + K_{\mathrm{p}}\right) + \left(m^2_{\mathrm{dc}} + \frac{m^2_{\mathrm{ac}}}{2}\right)\right) = 0 \tag{3.16}$$

$$\Delta V^{\Sigma}_{\mathrm{c},\Delta}(s)\left(s^2 C_{\mathrm{arm}} L_{\mathrm{arm}} + sC_{\mathrm{arm}}\left(R_{\mathrm{arm}} + K_{\mathrm{p}}\right) + \left(m^2_{\mathrm{dc}} + \frac{m^2_{\mathrm{ac}}}{2}\right)\right) = 0 \tag{3.17}$$

These equations show that whatever the deviation, the arm voltages will naturally converge towards the setpoints $V^{\Sigma}_{\mathrm{c,p,ref}}$ and $V^{\Sigma}_{\mathrm{c,n,ref}}$. Although the convergence is guaranteed, it is dependent on the arm parameters and control gains, and is some cases might be very slow.

Despite the ease of implementation, and natural self-balancing property, it has already been shown that a variety of undesired effects follows the direct voltage control, which are completely avoided if the closed-loop voltage control is applied.

### 3.1.3 Internal dynamics of a closed-loop voltage-controlled converter

Motivated by the appearance of the parasitic second harmonic current in the direct-voltage-control scheme, the authors in [67] proposed the closed-loop voltage control concept. They have also shown that the control concept is marginally stable, and requires additional energy controllers to stabilize the system.

To understand these principles, we shall start with the insertion index definition, which is the major difference with respect to the direct voltage control scheme. Insertion indices in the closed-loop voltage-controlled converter are determined by dividing the arm voltage reference with the instantaneous value of the total arm voltage:

$$n_{\mathrm{p}} = \frac{u_{\mathrm{p}}^{*}}{v_{\mathrm{c,p}}^{\Sigma}} = \frac{u_{\mathrm{comm}}^{*} - u_{\mathrm{diff}}^{*}}{v_{\mathrm{c,p}}^{\Sigma}} \tag{3.18}$$

$$n_{\mathrm{n}} = \frac{u_{\mathrm{n}}^{*}}{v_{\mathrm{c,n}}^{\Sigma}} = \frac{u_{\mathrm{comm}}^{*} + u_{\mathrm{diff}}^{*}}{v_{\mathrm{c,n}}^{\Sigma}} \tag{3.19}$$

Consequently, generated arm-common and arm-differential voltages correspond to their references, as shown in (3.20)-(3.21). As a result, no parasitic current components appear neither in the arm-common, nor in the arm-differential current.

$$u_{\mathrm{comm}} = \frac{u_{\mathrm{p}} + u_{\mathrm{n}}}{2} = \frac{1}{2}\left(\frac{u_{\mathrm{comm}}^{*} - u_{\mathrm{diff}}^{*}}{v_{\mathrm{c,p}}^{\Sigma}} v_{\mathrm{c,p}}^{\Sigma} + \frac{u_{\mathrm{comm}}^{*} + u_{\mathrm{diff}}^{*}}{v_{\mathrm{c,n}}^{\Sigma}} v_{\mathrm{c,n}}^{\Sigma}\right) = u_{\mathrm{comm}}^{*} \tag{3.20}$$

$$u_{\mathrm{comm}} = \frac{u_{\mathrm{n}} - u_{\mathrm{p}}}{2} = \frac{1}{2}\left(\frac{u_{\mathrm{comm}}^{*} + u_{\mathrm{diff}}^{*}}{v_{\mathrm{c,n}}^{\Sigma}} v_{\mathrm{c,n}}^{\Sigma} + \frac{u_{\mathrm{comm}}^{*} - u_{\mathrm{diff}}^{*}}{v_{\mathrm{c,p}}^{\Sigma}} v_{\mathrm{c,p}}^{\Sigma}\right) = u_{\mathrm{diff}}^{*} \tag{3.21}$$

Neglecting the voltage terms originating from the current control (inductive and resistive voltage drops), arm power equations for the positive and negative arm take the following form:

$$\frac{dW_{\mathrm{p}}}{dt} = p_{\mathrm{p}} = u_{\mathrm{p}} i_{\mathrm{p}} = \left(\frac{u_{\mathrm{dc}}}{2} - \hat{u}_{\mathrm{ac}} \sin\left(\omega_{\mathrm{g}} t\right)\right)\left(\frac{i_{\mathrm{dc}}}{3} + \frac{\hat{i}_{\mathrm{ac}}}{2} \sin\left(\omega_{\mathrm{g}} t + \phi\right)\right) \tag{3.22}$$

$$\frac{dW_{\mathrm{n}}}{dt} = p_{\mathrm{n}} = u_{\mathrm{n}} i_{\mathrm{n}} = \left(\frac{u_{\mathrm{dc}}}{2} + \hat{u}_{\mathrm{ac}} \sin\left(\omega_{\mathrm{g}} t\right)\right)\left(\frac{i_{\mathrm{dc}}}{3} - \frac{\hat{i}_{\mathrm{ac}}}{2} \sin\left(\omega_{\mathrm{g}} t + \phi\right)\right) \tag{3.23}$$

Adding and subtracting the equations (3.22)-(3.23) yields:

$$\begin{aligned} \frac{dW_{\Sigma}}{dt} &= \frac{u_{\mathrm{dc}} i_{\mathrm{dc}}}{3} - \hat{u}_{\mathrm{ac}} \sin\left(\omega_{\mathrm{g}} t\right) \frac{\hat{i}_{\mathrm{ac}}}{2} \sin\left(\omega_{\mathrm{g}} t + \phi\right) \\ &= \frac{u_{\mathrm{dc}} i_{\mathrm{dc}}}{3} - \frac{\hat{u}_{\mathrm{ac}} \hat{i}_{\mathrm{ac}} \cos\left(\phi\right)}{4} + \frac{\hat{u}_{\mathrm{ac}} \hat{i}_{\mathrm{ac}} \cos\left(2\omega_{\mathrm{g}} t + \phi\right)}{4} \end{aligned} \tag{3.24}$$

$$\frac{dW_{\Delta}}{dt} = \frac{u_{\mathrm{dc}} \hat{i}_{\mathrm{ac}} \sin\left(\omega_{\mathrm{g}} t + \phi\right)}{2} - \frac{2\hat{u}_{\mathrm{ac}} i_{\mathrm{dc}} \sin\left(\omega_{\mathrm{g}} t\right)}{3} \tag{3.25}$$

Provided that the ac and dc power balance condition is satisfied, the first two terms in (3.24) cancel each other out, and the equations (3.24)-(3.25) take the following form:

$$\frac{dW_\Sigma}{dt} = \frac{\hat{u}_{\mathrm{ac}}\hat{i}_{\mathrm{ac}}\cos\left(2\omega_{\mathrm{g}}t+\phi\right)}{4} \tag{3.26}$$

$$\frac{dW_\Delta}{dt} = \frac{u_{\mathrm{dc}}\hat{i}_{\mathrm{ac}}\sin\left(\omega_{\mathrm{g}}t+\phi\right)}{2} - \frac{2\hat{u}_{\mathrm{ac}}i_{\mathrm{dc}}\sin\left(\omega_{\mathrm{g}}t\right)}{3} \tag{3.27}$$

The last two equations contain only the oscillating terms, giving a conclusion that the system is at the boundary of stability. Namely, in case of any deviation of the arm-sum energy $W_\Sigma$ or arm-delta energy $W_\Delta$, the system does not return to the nominal operating point on its own. Therefore, to stabilize the system, two controllers should be added, as demonstrated by the following equations:

$$\frac{dW_\Sigma}{dt} = \frac{\hat{u}_{\mathrm{ac}}\hat{i}_{\mathrm{ac}}\cos\left(2\omega_{\mathrm{g}}t+\phi\right)}{4} + K_{\mathrm{p},\Sigma}\Big(W_\Sigma^* - W_\Sigma\Big) \tag{3.28}$$

$$\frac{dW_\Delta}{dt} = \frac{u_{\mathrm{dc}}\hat{i}_{\mathrm{ac}}\sin\left(\omega_{\mathrm{g}}t+\phi\right)}{2} - \frac{2\hat{u}_{\mathrm{ac}}i_{\mathrm{dc}}\sin\left(\omega_{\mathrm{g}}t\right)}{3} + K_{\mathrm{p},\Delta}\Big(W_\Delta^* - W_\Delta\Big) \tag{3.29}$$

Neglecting the oscillating terms, and applying Laplace transformation onto (3.28)-(3.29) yields:

$$W_\Sigma(s) = W_\Sigma^*(s)\frac{K_{\mathrm{p},\Sigma}}{s+K_{\mathrm{p},\Sigma}} \tag{3.30}$$

$$W_\Delta(s) = W_\Delta^*(s)\frac{K_{\mathrm{p},\Delta}}{s+K_{\mathrm{p},\Delta}} \tag{3.31}$$

Therefore, the two energy controllers not only stabilize the system, but can also drive the arm-sum $W_\Sigma$ and arm-delta $W_\Delta$ energies to the arbitrary references. The question that naturally arises is how the two control actions are achieved, and how do they correlate to the terminal and internal voltages and currents of the MMC. Therefore, the subject of this chapter is to investigate different methods for the arm-energy control.

## 3.2 Arm-Energy Control Mechanisms

In the previous chapter, it was shown that the arm energies consists of a dc term and oscillating components at fundamental and double the fundamental frequency. As the dc value of the arm energy corresponds to the average value of the total arm voltage $V_{\mathrm{c}}^{\Sigma}$, the energy content within each arm should be maintained around predefined value to ensure proper operation of the converter.

It was shown by (3.28)-(3.31) that by addition of two energy controllers for the arm-sum $W_\Sigma$ and arm-differential $W_\Delta$ energy in each phase, the arm-sum and arm-differential energies can be controlled to arbitrary values. As a result, individual arm energies within a respective phase can also be controlled to arbitrary values:

$$W_{\mathrm{p}}(s) = \frac{W_{\Sigma}(s) + W_{\Delta}(s)}{2} \tag{3.32}$$

$$W_{\mathrm{n}}(s) = \frac{W_{\Sigma}(s) - W_{\Delta}(s)}{2} \tag{3.33}$$

Mean arm energies are governed by the mean arm-power components, and it is necessary to identify power components that would realize the arm-energy control tasks, as proposed in (3.28)-(3.29). We have already seen that when the closed-loop voltage control scheme is applied, average power components equal zero, thus making this control scheme incapable of achieving the energy control tasks. One should recall that during the analysis, it was assumed that the arm voltages and currents consist only of the ac and dc terminal components. Nevertheless, as it has been shown in **Chapter 2**, a common-mode voltage $u_{\mathrm{cm}}$ can be also injected at the ac terminals, if permitted, and the circulating currents can be produced within the MMC arms, without affecting its terminals. These components can be utilized to produce non-zero mean arm-power components that would execute the arm-energy control tasks.

To understand how these components interact with the other arm voltage and current quantities, arm power equations are repeated here for a single phase leg, assuming symmetrical conditions.

$$p_{\mathrm{p}} = u_{\mathrm{p}} i_{\mathrm{p}} = \left(\frac{u_{\mathrm{dc}}}{2} - \hat{u}_{\mathrm{ac}} \sin\left(\omega_{\mathrm{g}} t\right) - u_{\mathrm{cm}}\right)\left(\frac{i_{\mathrm{dc}}}{3} + \frac{\hat{i}_{\mathrm{ac}}}{2} \sin\left(\omega_{\mathrm{g}} t + \phi\right) + i_{\mathrm{circ}}\right) \tag{3.34}$$

$$p_{\mathrm{n}} = u_{\mathrm{n}} i_{\mathrm{n}} = \left(\frac{u_{\mathrm{dc}}}{2} + \hat{u}_{\mathrm{ac}} \sin\left(\omega_{\mathrm{g}} t\right) + u_{\mathrm{cm}}\right)\left(\frac{i_{\mathrm{dc}}}{3} - \frac{\hat{i}_{\mathrm{ac}}}{2} \sin\left(\omega_{\mathrm{g}} t + \phi\right) + i_{\mathrm{circ}}\right) \tag{3.35}$$

Common-mode voltage $u_{\mathrm{cm}}$ and arm-circulating current $i_{\mathrm{circ}}$ are degrees of freedom, and can theoretically take any form. A product of two ac components has non-zero average only in case when the two components are of the same frequency. Therefore, the common-mode voltage and circulating current should be chosen such that their frequency components correspond to those of the other terms in (3.34)-(3.35). Therefore, we can assume that the two variables have the following form:

$$u_{\mathrm{cm}} = \hat{u}_{\mathrm{cm1}} \sin\left(\omega_{\mathrm{g}} t + \phi_{\mathrm{cm1}}\right) + \hat{u}_{\mathrm{cm2}} \sin\left(\omega_{\mathrm{cm}} t + \phi_{\mathrm{cm2}}\right) \tag{3.36}$$

$$i_{\mathrm{circ}} = i_{\mathrm{circ,dc}} + i_{\mathrm{circ,ac1}} \sin\left(\omega_{\mathrm{g}} t + \phi_{\mathrm{circ1}}\right) + i_{\mathrm{circ,ac2}} \sin\left(\omega_{\mathrm{cm}} t + \phi_{\mathrm{circ2}}\right) \tag{3.37}$$

The choice of frequency components in (3.36)-(3.37) should be further clarified. The common-mode voltage was chosen such that it might contain a fundamental frequency component, in order to interract with the grid current component $i_{\mathrm{ac}}$, and another arbitrarily chosen component at the angular frequency $\omega_{\mathrm{cm}}$. It might also interact with the dc current component, but the reason why only the $\omega_{\mathrm{g}}$ is chosen is the fact that all the control requirements will be satisfied with the interaction with the grid current. Namely, while the dc current cannot exist without the corresponding grid current, grid current can exist even if the dc current is equal to zero, when the MMC is providing STATCOM functionality. Therefore, as the interaction of the common-mode voltage with the dc and grid current would give the same effects, it is more reasonable to have the common-mode voltage at the angular frequency $\omega_{\mathrm{g}}$. Regarding the circulating current, it is assumed that the circulating current might have all the components as the arm voltages.

Multiplying all the terms in (3.34)-(3.35) and retaining only those that could have non-zero average values, the equations (3.38)-(3.39) are obtained.

$$\begin{aligned} p_{\mathrm{p}} =& \frac{u_{\mathrm{dc}} i_{\mathrm{dc}}}{6} - \frac{\hat{u}_{\mathrm{ac}} \hat{i}_{\mathrm{ac}} \cos\left(\phi\right)}{4} + \frac{u_{\mathrm{dc}} i_{\mathrm{circ,dc}}}{2} - \frac{\hat{u}_{\mathrm{ac}} \hat{i}_{\mathrm{circ,ac1}} \cos\left(\phi_{\mathrm{circ,ac1}}\right)}{2} + \ldots \\ & - \frac{\hat{u}_{\mathrm{cm1}} \hat{i}_{\mathrm{ac}} \cos\left(\phi_{\mathrm{cm1}} - \phi\right)}{4} - \frac{\hat{u}_{\mathrm{cm2}} \hat{i}_{\mathrm{circ,ac2}} \cos\left(\phi_{\mathrm{cm2}} - \phi_{\mathrm{circ,ac2}}\right)}{4} \end{aligned} \tag{3.38}$$

$$\begin{aligned} p_{\mathrm{n}} =& \frac{u_{\mathrm{dc}} i_{\mathrm{dc}}}{6} - \frac{\hat{u}_{\mathrm{ac}} \hat{i}_{\mathrm{ac}} \cos\left(\phi\right)}{4} + \frac{u_{\mathrm{dc}} i_{\mathrm{circ,dc}}}{2} + \frac{\hat{u}_{\mathrm{ac}} \hat{i}_{\mathrm{circ,ac1}} \cos\left(\phi_{\mathrm{circ,ac1}}\right)}{2} + \ldots \\ & - \frac{\hat{u}_{\mathrm{cm1}} \hat{i}_{\mathrm{ac}} \cos\left(\phi_{\mathrm{cm1}} - \phi\right)}{4} + \frac{\hat{u}_{\mathrm{cm2}} \hat{i}_{\mathrm{circ,ac2}} \cos\left(\phi_{\mathrm{cm2}} - \phi_{\mathrm{circ,ac2}}\right)}{4} \end{aligned} \tag{3.39}$$

The fact that the positive-arm power and negative-arm power contain the same terms, yet some with the opposite signs, couples the control of the positive and negative arm energies, thus making it impossible to control them independently. Nevertheless, by summing and subtracting the equations (3.38)-(3.39), arm-common $p_{\Sigma}$ and arm-differential $p_{\Delta}$ power terms are obtained, which are completely decoupled from one another.

$$p_{\Sigma} = p_{\mathrm{p}} + p_{\mathrm{n}} = \frac{u_{\mathrm{dc}} i_{\mathrm{dc}}}{3} - \frac{\hat{u}_{\mathrm{ac}} \hat{i}_{\mathrm{ac}} \cos\left(\phi\right)}{2} + u_{\mathrm{dc}} i_{\mathrm{circ,dc}} - \frac{\hat{u}_{\mathrm{cm1}} \hat{i}_{\mathrm{ac}} \cos\left(\phi_{\mathrm{cm1}} - \phi\right)}{2} \tag{3.40}$$

$$p_{\Delta} = p_{\mathrm{p}} - p_{\mathrm{n}} = -\hat{u}_{\mathrm{ac}} \hat{i}_{\mathrm{circ,ac1}} \cos\left(\phi_{\mathrm{circ1}}\right) - \frac{\hat{u}_{\mathrm{cm2}} \hat{i}_{\mathrm{circ,ac2}} \cos\left(\phi_{\mathrm{cm2}} - \phi_{\mathrm{circ2}}\right)}{2} \tag{3.41}$$

The arm-sum $p_{\Sigma}$ and arm-differential $p_{\Delta}$ power components are derivatives of the arm-sum $W_{\Sigma}$ and arm-differential $W_{\Delta}$ energies, respectively. As such, these two power components represent the means for controlling the sum and differential arm energies, and thus the positive and negative arm energy.

As there are several terms that can be used to achieve a desired control function, each control mechanism should be examined in more detail. As the arm-differential and arm-sum control methods are decoupled from one another, they can be separately analysed. Arm-differential energy control is analysed first, as some of the principles derived for this control action are used later in the arm-sum energy control.

## 3.3 Arm-Differential Energy Control

To start with, the equation (3.41) is repeated in (3.42), where two power terms can be identified. The first power terms is based on interaction of the arm-differential voltage $u_{\mathrm{diff}}$ and the intentionally-produced circulating current $i_{\mathrm{circ,ac1}}$. The second term is a product of interaction of the common-mode voltage $u_{\mathrm{cm}}$, with the intentionally produced circulating currents $i_{\mathrm{circ,ac2}}$.

$$p_{\Delta} = -\hat{u}_{\mathrm{ac}} \hat{i}_{\mathrm{circ,ac1}} \cos\left(\phi_{\mathrm{circ,ac1}}\right) - \frac{\hat{u}_{\mathrm{cm2}} \hat{i}_{\mathrm{circ,ac2}} \cos\left(\phi_{\mathrm{cm2}} - \phi_{\mathrm{circ,ac2}}\right)}{2} \tag{3.42}$$

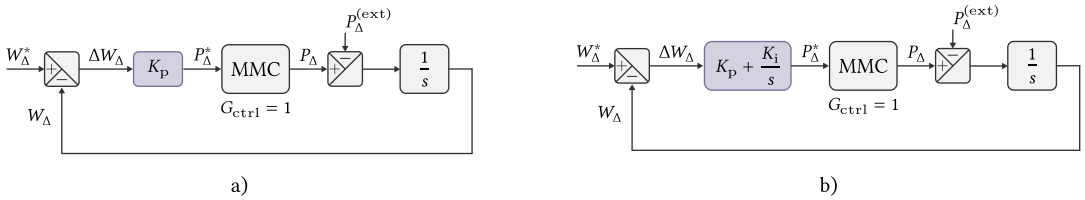


**Fig. 3.3** Equivalent model of the arm-differential control assuming a) P control structure; b) PI control structure.

While the arm-differential voltage is available in most of the operating modes, the common-mode voltage might not always be available. Even in case when the common-mode voltage is injected, it magnitude is typically significantly lower compared to the arm-differential voltage. In case of a third-harmonic injection method, this ratio equals 1:6. Therefore, to produce the same power component, the second term in (3.42) would require significantly higher circulating current component, than it would be the case with the first term. Consequently, unless in case of a severe short circuit close to the MMC ac terminals happens, the first term will be utilized for arm-differential energy control in most of the cases, and hence be the subject of the forthcoming discussion.

### 3.3.1 Choice of controller structure

The arm-differential energy controller was introduced in the equation (3.29), and by neglecting the oscillating terms, the time derivative of the arm-differential energy $W_\Delta$ is determined by:

$$\frac{dW_\Delta}{dt} = K_{p,\Delta}\left(W_\Delta^* - W_\Delta\right) \tag{3.43}$$

Therefore, the output of the arm-differential energy controller described by (3.43) is the arm-differential power reference. Structure of the arm-differential energy controller is shown in **Fig. 3.3.a**. The basic control structure assumes only the proportional gain, yet in certain cases it might not be sufficient. For example, in case of the arm-inductance asymmetry, a parasitic fundamental-frequency arm-common current component will appear, and by interacting with the arm-differential voltage create the arm-differential power component. If this current component is not compensated for, it will result in a constant arm-differential power term $P_\Delta^{(ext)}$, modelled as a disturbance in **Fig. 3.3.a**.

From the equivalent model from **Fig. 3.3.a**, the arm-differential energy error $\Delta W_\Delta$ can be obtained as a function of the arm-differential energy reference $W_\Delta^*$ and the external disturbance $P_\Delta^{(ext)}$ as:

$$\Delta W_\Delta(s) = \frac{s}{s + K_p} W_\Delta^*(s) + \frac{1}{s + K_p} P_\Delta^{(ext)}(s) \tag{3.44}$$

Assuming the arm-differential energy reference and external disturbance are two constants, that can be described by Heaviside step function, and applying the final-value theorem, yields the steady-state value of the arm-differential energy error:

$$\Delta W_\Delta(t \to \infty) = \lim_{s \to 0} s\, \Delta W_\Delta(s) = \lim_{s \to 0} s \left( \frac{s}{s + K_p} \frac{W_\Delta^*}{s} + \frac{1}{s + K_p} \frac{P_\Delta^{(ext)}}{s} \right) = \frac{P_\Delta^{(ext)}}{K_p} \tag{3.45}$$

The last expression shows that in presence of a constant external disturbance, proportional only control structure is incapable of achieving zero steady-state error in tracking the arm-differential energy reference.

On the other hand, if the controller assumed proportional-integral (PI) control structure, as illustrated in **Fig. 3.3.b**, the arm-differential energy error $\Delta W_\Delta$ now takes the following form in s-domain:

$$\Delta W_\Delta(s) = \frac{s^2}{s^2 + sK_\mathrm{p} + K_\mathrm{i}} W_\Delta^*(s) + \frac{s}{s^2 + sK_\mathrm{p} + K_\mathrm{i}} P_\Delta^{(\mathrm{ext})}(s) \tag{3.46}$$

Applying the final-value theorem, the steady state error in presence of a constant external disturbance becomes zero:

$$\Delta W_\Delta(t \to \infty) = \lim_{s \to 0} s\, \Delta W_\Delta(s) = \lim_{s \to 0} s \left( \frac{s^2}{s^2 + sK_\mathrm{p} + K_\mathrm{i}} \frac{W_\Delta^*}{s} + \frac{s}{s^2 + sK_\mathrm{p} + K_\mathrm{i}} \frac{P_\Delta^{(\mathrm{ext})}}{s} \right) = 0 \tag{3.47}$$

Therefore, due to various effects that might be a constant disturbance for the arm-differential energy control, PI controller structure is adopted, as it ensures zero steady-state error.

### 3.3.2 Arm-differential energy control mechanism

While the controller structure is defined, it still remains an open question how the arm-differential power reference ($P_\Delta^*$ in **Fig. 3.3**) is realized. In **Fig. 3.3**, the internal control structure that realizes the reference arm-differential power is represented by a block named *MMC*, which has a unity gain, i.e. ensures that $P_\Delta = P_\Delta^*$. Recalling the equation (3.42), and considering only the first power term, arm-differential power in phase $x$ can be expressed as in (3.48), where $\hat{u}_\mathrm{x}$ is the magnitude of the arm-differential voltage in the phase, $\hat{i}_{\Delta,\mathrm{x}}$ is the magnitude of the circulating current introduced for the arm-differential control, and $\phi_{\Delta,\mathrm{x}}$ is a phase shift between the voltage and the current. Circulating current and phase shift are labelled slightly differently with respect to (3.42) for convenience reasons.

$$P_{\Delta,\mathrm{x}} = -\hat{u}_{\mathrm{diff,x}} \hat{i}_{\Delta,\mathrm{x}} \cos\left(\phi_{\Delta,\mathrm{x}}\right) \tag{3.48}$$

The arm-differential voltage magnitude $\hat{u}_{\mathrm{diff,x}}$ is readily available variable in the controller, and is equal among all phases under symmetric conditions. The remaining variables, the circulating current magnitude and the phase shift, are two degrees of freedom that should be carefully selected.

By setting the circulating currents in phase with the respective arm-differential voltages, circulating currents with the lowest magnitudes are obtained from the arm-differential power references:

$$\hat{i}_{\Delta,\mathrm{a}}^* = \frac{P_{\Delta,\mathrm{a}}^*}{\hat{u}_{\mathrm{diff,a}}} \tag{3.49} \qquad \hat{i}_{\Delta,\mathrm{b}}^* = \frac{P_{\Delta,\mathrm{b}}^*}{\hat{u}_{\mathrm{diff,b}}} \tag{3.50} \qquad \hat{i}_{\Delta,\mathrm{c}}^* = \frac{P_{\Delta,\mathrm{c}}^*}{\hat{u}_{\mathrm{diff,c}}} \tag{3.51}$$

While the arm-differential voltage magnitudes are equal in all three phases under balanced conditions, arm-differential power references have in general arbitrary values. Consequently, calculated circulating current magnitudes $\hat{i}_{\Delta,\mathrm{x}}^*$ have different values among the phases. Based on the initial assumption

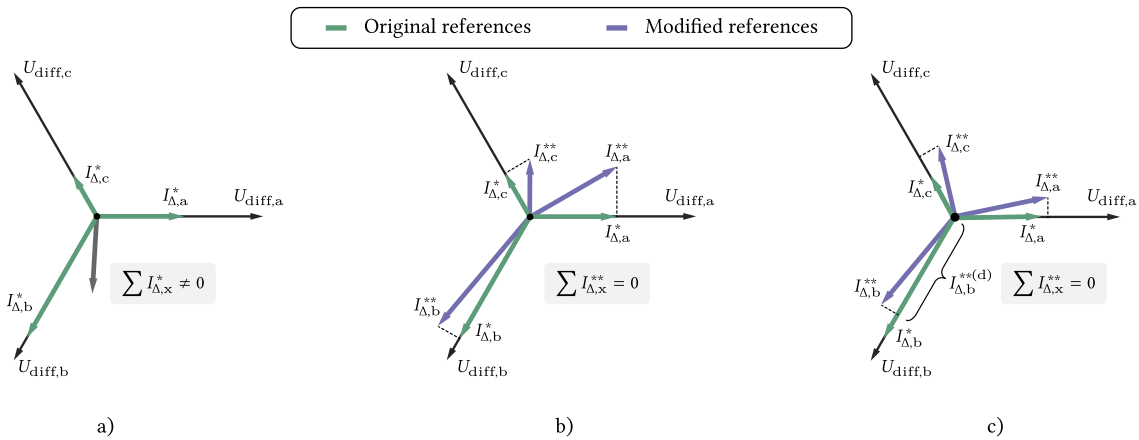


**Fig. 3.4** Phasors of the arm-differential voltage references $U_{\mathrm{diff,x}}$ and circulating currents $I^*_{\Delta,x}$ for arm-differential energy control: a) Original set of circulating current reference phasors; b) original and modified circulating current reference phasors - Method I; c) original and modified circulating current reference phasors - Method II.

that the circulating currents are controlled to be in phase with the respective arm-differential voltages, their sum across three phases is in general different from zero. This is illustrated in **Fig. 3.4.a**.

While many authors use the abovementioned principle to control the arm-differential energies, many of them fail to recognize the issue of a non-zero sum of the circulating current references, as in [67], [103], [105]–[108]. Generating references in this manner would result in an ac current component penetrating the dc terminals, which should be avoided.

Several other authors [109]–[117] deal with the issue using different approaches.

Authors in [109] propose a solution where the circulating current references are obtained by transforming the original references into the positive and negative sequence rotating reference frames, and controlling currents independently in the two frames. The same approach is used in [112]. Although derived using a different approach, the solution proposed by [114] results in the same circulating current references, obtained in the two rotating reference frames. Authors in [110] propose a generalized method for a class of modular multilevel converters, resulting in a transformation matrix that is used to multiply the original set of references. Nevertheless, interpretation of the results from [110] might be tedious, and requires the use of advanced mathematical tools [118], [119]. The reference [111] uses two rotating reference frames at fundamental and double the fundamental frequencies to control the arm energies and suppress the voltage ripple in the SMs. While the proposed method ensures that the circulating currents remain within the converter, it cannot guarantee a control of arm-differential energies to arbitrary values. Authors in [113], [115] propose an arm-differential energy control method based on positive and negative sequence circulating currents. Although it can ensure that the circulating currents remain within the converter, as well as an arbitrary arm-differential energy reference tracking, it requires decomposition into the two sequences, as well as the positive sequence voltage extraction during unbalanced grid conditions. The authors in [116], [117] present a generalized energy control method, applicable to the class of MMCs. The set of circulating currents is obtained as a result of optimization with respect to the RMS value of the current. According to the authors [116], resulting currents have the same form as in the case of method [114].

The upcoming analyses will investigate different methods for obtaining the circulating currents for the

arm-differential energy control task. Its aim is to explore the degrees of freedom, and find effective, yet simple solutions to the problem. Proposed methods do not require use of multiple rotating reference frames, neither advanced mathematical tools for its understanding and implementation. In addition, the methods derived within the thesis can be effortlessly extended to different types of MMC topologies, such as a multiphase MMC, M3C or the MMC with paralleled arms [120], and are equally applicable under unbalanced grid conditions.

Based on the equations (3.49)-(3.51), arm-common current references for the differential energy control ($i^*_{\Delta,x}$) are calculated, keeping in mind that they should be synchronized with the respective arm-differential voltages. However, as the illustration in **Fig. 3.4.a** shows, the sum of the three arm-common currents is not necessarily equal to zero, due to the arbitrary arm-differential power references $P^*_{\Delta,x}$. Additionally, during unbalanced conditions, arm-differential voltages are asymmetrical, yielding asymmetrical current references $i^*_{\Delta,x}$, even if theoretically arm-differential power references are equal among the phases. Therefore, there exists a need for the arm-differential current modification.

**Fig. 3.4.b** and **Fig. 3.4.c** show two possibilities that are analysed in this chapter. Phasors of the original current references (green) and symmetrical arm-differential voltages (black) are shown, together with the phasors of the modified current references (purple).

The first approach assumes that the active power obtained by interaction of an arm-common current and a corresponding arm-differential voltage should remain equal in case of both original and modified current references. In other words, by modifying the current references, arm-differential power references $P^*_{\Delta,x}$ should be respected. In addition, modified references should sum-up to zero, so as not to appear at the MMC dc terminals. This method is referred to as *Method I* within this thesis.

The second approach identifies a set of modified current references that have the lowest deviation from the original set of references, and still sum-up to zero. As a consequence, it does not ensure the arm-differential power reference tracking, yet due to the low deviation of the generated currents from the original references, realized power components are close to the references. The motivation is to generate the lowest possible circulating currents that satisfy the zero-sum condition, while enabling arm-differential energy control. This method is further referred to as *Method II*.

### 3.3.3 Current modification - Method I

To obtain a set of currents that would produce required arm-differential power components while summing-up to zero, we will start by defining the time domain expressions for the original and modified current references:

$$i^*_{\Delta,a} = \hat{i}^*_{\Delta,a} \sin\left(\omega_g t\right) \tag{3.52}$$

$$i^*_{\Delta,b} = \hat{i}^*_{\Delta,b} \sin\left(\omega_g t - \frac{2\pi}{3}\right) \tag{3.53}$$

$$i^*_{\Delta,c} = \hat{i}^*_{\Delta,c} \sin\left(\omega_g t + \frac{2\pi}{3}\right) \tag{3.54}$$

$$i^{**}_{\Delta,a} = \hat{i}^{**}_{\Delta,a} \sin\left(\omega_g t + \phi_{\Delta,a}\right) \tag{3.55}$$

$$i^{**}_{\Delta,b} = \hat{i}^{**}_{\Delta,b} \sin\left(\omega_g t - \frac{2\pi}{3} + \phi_{\Delta,b}\right) \tag{3.56}$$

$$i^{**}_{\Delta,c} = \hat{i}^{**}_{\Delta,c} \sin\left(\omega_g t + \frac{2\pi}{3} + \phi_{\Delta,c}\right) \tag{3.57}$$

Magnitudes of the original set of current references $\hat{i}^*_{\Delta,x}$ are obtained from (3.49)-(3.51), whereas their

phases are aligned to the associated arm-differential voltages, as illustrated in **Fig. 3.5.a**. Note that during the analysis it is assumed that the grid phase voltages and currents are symmetrical, and so are the arm-differential voltages. Arm-energy control under unbalanced grid conditions is subject of **Chapter 4**.

On the other hand, modified current references, expressed by (3.55)-(3.57) have three magnitudes $\hat{i}^{**}_{\Delta,\mathrm{x}}$ and three phase angles $\phi_{\Delta,\mathrm{x}}$ that can in general take arbitrary values. Therefore, at initial stage, there are six degrees of freedom in choosing the modified current references.

Nevertheless, the ultimate criterion that the modified references should comply with is that their sum should be equal to zero, as expressed by (3.58).

$$\hat{i}^{**}_{\Delta,\mathrm{a}} \sin\left(\omega_{\mathrm{g}} t + \phi_{\Delta,\mathrm{a}}\right) + \hat{i}^{**}_{\Delta,\mathrm{b}} \sin\left(\omega_{\mathrm{g}} t - \frac{2\pi}{3} + \phi_{\Delta,\mathrm{b}}\right) + \hat{i}^{**}_{\Delta,\mathrm{c}} \sin\left(\omega_{\mathrm{g}} t + \frac{2\pi}{3} + \phi_{\Delta,\mathrm{c}}\right) = 0 \tag{3.58}$$

This constraint can be further decomposed into the sine and cosine terms, which should both be equal to zero:

$$\sin\left(\omega_{\mathrm{g}} t\right)\left(\hat{i}^{**}_{\Delta,\mathrm{a}} \cos\left(\phi_{\Delta,\mathrm{a}}\right) + \hat{i}^{**}_{\Delta,\mathrm{b}} \cos\left(\phi_{\Delta,\mathrm{b}} - \frac{2\pi}{3}\right) + \hat{i}^{**}_{\Delta,\mathrm{c}} \cos\left(\phi_{\Delta,\mathrm{c}} + \frac{2\pi}{3}\right)\right) = 0 \tag{3.59}$$

$$\cos\left(\omega_{\mathrm{g}} t\right)\left(\hat{i}^{**}_{\Delta,\mathrm{a}} \sin\left(\phi_{\Delta,\mathrm{a}}\right) + \hat{i}^{**}_{\Delta,\mathrm{b}} \sin\left(\phi_{\Delta,\mathrm{b}} - \frac{2\pi}{3}\right) + \hat{i}^{**}_{\Delta,\mathrm{c}} \sin\left(\phi_{\Delta,\mathrm{c}} + \frac{2\pi}{3}\right)\right) = 0 \tag{3.60}$$

Equations (3.59)-(3.60) are two constraints that are imposed on the degrees of freedom, and as such reduce the degrees of freedom from six to four. Denoting the projections of the modified current references to the axes of the respective voltages as in (3.61), the two constraints (3.59)-(3.60) can be expressed as in (3.62)-(3.63).

$$\hat{i}^{(d)}_{\Delta,\mathrm{x}} = \hat{i}^{**}_{\Delta,\mathrm{x}} \cos\left(\phi_{\Delta,\mathrm{x}}\right) \tag{3.61}$$

$$\sqrt{3}\hat{i}^{(d)}_{\Delta,\mathrm{b}} \tan\left(\phi_{\Delta,\mathrm{b}}\right) = \hat{i}^{(d)}_{\Delta,\mathrm{a}}\left(\sqrt{3}\tan\left(\phi_{\Delta,\mathrm{a}}\right) - 1\right) - \hat{i}^{(d)}_{\Delta,\mathrm{b}} + 2\hat{i}^{(d)}_{\Delta,\mathrm{c}} \tag{3.62}$$

$$\sqrt{3}\hat{i}^{(d)}_{\Delta,\mathrm{c}} \tan\left(\phi_{\Delta,\mathrm{c}}\right) = \hat{i}^{(d)}_{\Delta,\mathrm{a}}\left(\sqrt{3}\tan\left(\phi_{\Delta,\mathrm{a}}\right) + 1\right) - 2\hat{i}^{(d)}_{\Delta,\mathrm{b}} + \hat{i}^{(d)}_{\Delta,\mathrm{c}} \tag{3.63}$$

The two conditions (3.62)-(3.63) are valid for both *Method I* and *Method II*, as both methods have to ensure the zero-sum of the currents.

What *Method I* aims to ensure is that the arm-differential power references are preserved with the employed current modification. This is achieved if the projections of the modified current references on the corresponding voltage axes ($\hat{i}^{(d)}_{\Delta,\mathrm{x}}$) are equal to the original current references $\hat{i}^{*}_{\Delta,\mathrm{x}}$, as illustrated in **Fig. 3.5.a**.

$$\hat{i}^{**}_{\Delta,\mathrm{a}} \cos\left(\phi_{\Delta,\mathrm{a}}\right) = \hat{i}^{(d)}_{\Delta,\mathrm{a}} = \hat{i}^{*}_{\Delta,\mathrm{a}} \tag{3.64}$$

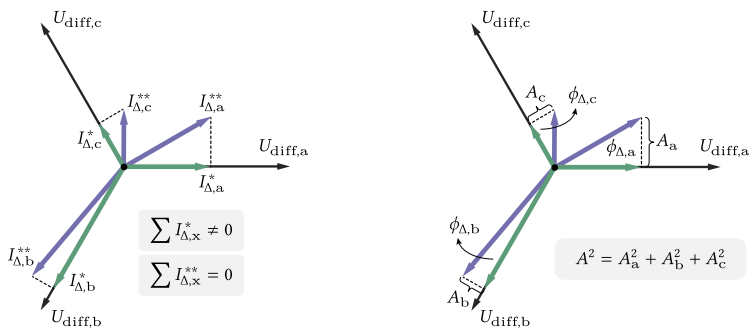


a) b)

**Fig. 3.5** Phasors of the original and modified current references, for *Method I* of the arm-differential energy control: a) Projections of the modified current references to the respective voltage axes are equal to the original references, thus preserving power references; b) Criterion used to find an optimal solution, by minimizing the deviation of the modified references with respect to the original ones.

$$\hat{i}^{**}_{\Delta,\text{b}} \cos\left(\phi_{\Delta,\text{b}}\right) = \hat{i}^{(d)}_{\Delta,\text{b}} = \hat{i}^{*}_{\Delta,\text{b}} \tag{3.65}$$

$$\hat{i}^{**}_{\Delta,\text{c}} \cos\left(\phi_{\Delta,\text{c}}\right) = \hat{i}^{(d)}_{\Delta,\text{c}} = \hat{i}^{*}_{\Delta,\text{c}} \tag{3.66}$$

As a result, the constraints (3.62)-(3.63) can be now expressed as a function of a single unknown variable - $\tan(\phi_{\Delta,\text{a}})$:

$$\sqrt{3}\hat{i}^{*}_{\Delta,\text{b}} \tan\left(\phi_{\Delta,\text{b}}\right) = \hat{i}^{*}_{\Delta,\text{a}}\left(\sqrt{3}\tan\left(\phi_{\Delta,\text{a}}\right) - 1\right) - \hat{i}^{*}_{\Delta,\text{b}} + 2\hat{i}^{*}_{\Delta,\text{c}} \tag{3.67}$$

$$\sqrt{3}\hat{i}^{*}_{\Delta,\text{c}} \tan\left(\phi_{\Delta,\text{c}}\right) = \hat{i}^{*}_{\Delta,\text{a}}\left(\sqrt{3}\tan\left(\phi_{\Delta,\text{a}}\right) + 1\right) - 2\hat{i}^{*}_{\Delta,\text{b}} + \hat{i}^{*}_{\Delta,\text{c}} \tag{3.68}$$

With the three additional constraints (3.64)-(3.66), the number of degrees of freedom is further reduced from four to one. The two phase angles ($\phi_{\Delta,\text{b}}$ and $\phi_{\Delta,\text{c}}$) as well as the three current magnitudes ($\hat{i}^{**}_{\Delta,\text{a}}$, $\hat{i}^{**}_{\Delta,\text{b}}$, and $\hat{i}^{**}_{\Delta,\text{c}}$) are implicitly defined by (3.64)-(3.68), leaving the variable $\phi_{\Delta,\text{a}}$ the only degree of freedom.

In general, this degree of freedom can be arbitrarily set (for example $\tan(\phi_{\Delta,\text{a}}) = 0$), rendering the system fully determined. Nevertheless, the objective is to use the remaining degree of freedom so as to minimize the magnitudes of the newly obtained current references. Given the fact that the original current references represent the lowest circulating currents that would attain the arm-differential power references, it is of interest that the modified current references have the least possible deviation from the original ones. This would ensure that the magnitudes of the modified references are the least possible, under given constraints.

To do so, a criterion function $A^2$ is defined as in **Fig. 3.5.b**, representing the sum of the squared deviations of the modified references from their original values:

$$A^2 = A_\text{a}^2 + A_\text{b}^2 + A_\text{c}^2 = \left(\hat{i}^{*}_{\Delta,\text{a}} \tan(\phi_{\Delta,\text{a}})\right)^2 + \left(\hat{i}^{*}_{\Delta,\text{b}} \tan(\phi_{\Delta,\text{b}})\right)^2 + \left(\hat{i}^{*}_{\Delta,\text{c}} \tan(\phi_{\Delta,\text{c}})\right)^2 \tag{3.69}$$

Incorporating the equations (3.67)-(3.68) into (3.69), and finding the solutions for the equation:

$$\frac{\partial A^2}{\partial \tan(\phi_{\Delta,\mathrm{a}})} = 0 \tag{3.70}$$

yields the three phase angles ($\phi_{\Delta,\mathrm{a}}$, $\phi_{\Delta,\mathrm{b}}$, and $\phi_{\Delta,\mathrm{c}}$) that would ensure the minimal deviation of the modified references with respect to the original ones, while preserving the arm-differential power references and ensuring a zero sum of the currents.

$$\tan(\phi_{\Delta,\mathrm{a}}) = \frac{\hat{i}^*_{\Delta,\mathrm{b}} - \hat{i}^*_{\Delta,\mathrm{c}}}{\sqrt{3}\hat{i}^*_{\Delta,\mathrm{a}}} \quad (3.71) \qquad \tan(\phi_{\Delta,\mathrm{b}}) = \frac{\hat{i}^*_{\Delta,\mathrm{c}} - \hat{i}^*_{\Delta,\mathrm{a}}}{\sqrt{3}\hat{i}^*_{\Delta,\mathrm{b}}} \quad (3.72) \qquad \tan(\phi_{\Delta,\mathrm{c}}) = \frac{\hat{i}^*_{\Delta,\mathrm{a}} - \hat{i}^*_{\Delta,\mathrm{b}}}{\sqrt{3}\hat{i}^*_{\Delta,\mathrm{c}}} \quad (3.73)$$

Recalling the initially assumed time-domain expressions for the modified current references (3.55)-(3.57), they can be now expressed as:

$$\begin{aligned} i^{**}_{\Delta,\mathrm{a}}(t) &= \hat{i}^{**}_{\Delta,\mathrm{a}} \sin\left(\omega_\mathrm{g} t + \phi_{\Delta,\mathrm{a}}\right) = \hat{i}^{**}_{\Delta,\mathrm{a}} \cos\left(\phi_{\Delta,\mathrm{a}}\right) \sin\left(\omega_\mathrm{g} t\right) + \hat{i}^{**}_{\Delta,\mathrm{a}} \sin\left(\phi_{\Delta,\mathrm{a}}\right) \cos\left(\omega_\mathrm{g} t\right) \\ &= \hat{i}^*_{\Delta,\mathrm{a}} \sin\left(\omega_\mathrm{g} t\right) + \hat{i}^*_{\Delta,\mathrm{a}} \tan(\phi_{\Delta,\mathrm{a}}) \cos\left(\omega_\mathrm{g} t\right) \\ &= \underbrace{\hat{i}^*_{\Delta,\mathrm{a}} \sin\left(\omega_\mathrm{g} t\right)}_{\text{original reference}} + \frac{1}{\sqrt{3}}\left(\hat{i}^*_{\Delta,\mathrm{b}} - \hat{i}^*_{\Delta,\mathrm{c}}\right) \cos\left(\omega_\mathrm{g} t\right) \end{aligned} \tag{3.74}$$

$$\begin{aligned} i^{**}_{\Delta,\mathrm{b}}(t) &= \hat{i}^{**}_{\Delta,\mathrm{b}} \sin\left(\omega_\mathrm{g} t - \frac{2\pi}{3} + \phi_{\Delta,\mathrm{b}}\right) = \hat{i}^{**}_{\Delta,\mathrm{b}} \cos\left(\phi_{\Delta,\mathrm{b}}\right) \sin\left(\omega_\mathrm{g} t - \frac{2\pi}{3}\right) + \hat{i}^{**}_{\Delta,\mathrm{b}} \sin\left(\phi_{\Delta,\mathrm{b}}\right) \cos\left(\omega_\mathrm{g} t - \frac{2\pi}{3}\right) \\ &= \hat{i}^*_{\Delta,\mathrm{b}} \sin\left(\omega_\mathrm{g} t - \frac{2\pi}{3}\right) + \hat{i}^*_{\Delta,\mathrm{b}} \tan(\phi_{\Delta,\mathrm{b}}) \cos\left(\omega_\mathrm{g} t - \frac{2\pi}{3}\right) \\ &= \underbrace{\hat{i}^*_{\Delta,\mathrm{b}} \sin\left(\omega_\mathrm{g} t - \frac{2\pi}{3}\right)}_{\text{original reference}} + \frac{1}{\sqrt{3}}\left(\hat{i}^*_{\Delta,\mathrm{c}} - \hat{i}^*_{\Delta,\mathrm{a}}\right) \cos\left(\omega_\mathrm{g} t - \frac{2\pi}{3}\right) \end{aligned} \tag{3.75}$$

$$\begin{aligned} i^{**}_{\Delta,\mathrm{c}}(t) &= \hat{i}^{**}_{\Delta,\mathrm{c}} \sin\left(\omega_\mathrm{g} t + \frac{2\pi}{3} + \phi_{\Delta,\mathrm{c}}\right) = \hat{i}^{**}_{\Delta,\mathrm{c}} \cos\left(\phi_{\Delta,\mathrm{c}}\right) \sin\left(\omega_\mathrm{g} t + \frac{2\pi}{3}\right) + \hat{i}^{**}_{\Delta,\mathrm{c}} \sin\left(\phi_{\Delta,\mathrm{c}}\right) \cos\left(\omega_\mathrm{g} t + \frac{2\pi}{3}\right) \\ &= \hat{i}^*_{\Delta,\mathrm{c}} \sin\left(\omega_\mathrm{g} t + \frac{2\pi}{3}\right) + \hat{i}^*_{\Delta,\mathrm{c}} \tan(\phi_{\Delta,\mathrm{c}}) \cos\left(\omega_\mathrm{g} t + \frac{2\pi}{3}\right) \\ &= \underbrace{\hat{i}^*_{\Delta,\mathrm{c}} \sin\left(\omega_\mathrm{g} t + \frac{2\pi}{3}\right)}_{\text{original reference}} + \frac{1}{\sqrt{3}}\left(\hat{i}^*_{\Delta,\mathrm{a}} - \hat{i}^*_{\Delta,\mathrm{b}}\right) \cos\left(\omega_\mathrm{g} t + \frac{2\pi}{3}\right) \end{aligned} \tag{3.76}$$

Sine terms in (3.74)-(3.76) are identical to the original arm current references, defined in (3.52) - (3.54), which are in-phase with the arm-differential voltages. In addition, in-quadrature sinusoidal components are also present in the modified references, and the question is how those can be generated. By denoting the sine terms of the three arm-differential phase voltages as:

$$A = \sin\left(\omega_g t\right) \quad (3.77) \qquad B = \sin\left(\omega_g t - \frac{2\pi}{3}\right) \quad (3.78) \qquad C = \sin\left(\omega_g t + \frac{2\pi}{3}\right) \quad (3.79)$$

time-domain expressions for the modified current references can be obtained as:

$$i^{**}_{\Delta,a}(t) = \hat{i}^{*}_{\Delta,a} A + \frac{1}{3}\left(\hat{i}^{*}_{\Delta,b} - \hat{i}^{*}_{\Delta,c}\right)\left(C - B\right) \tag{3.80}$$

$$i^{**}_{\Delta,b}(t) = \hat{i}^{*}_{\Delta,b} B + \frac{1}{3}\left(\hat{i}^{*}_{\Delta,c} - \hat{i}^{*}_{\Delta,a}\right)\left(A - C\right) \tag{3.81}$$

$$i^{**}_{\Delta,c}(t) = \hat{i}^{*}_{\Delta,a} C + \frac{1}{3}\left(\hat{i}^{*}_{\Delta,a} - \hat{i}^{*}_{\Delta,b}\right)\left(B - A\right) \tag{3.82}$$

Implementation of *Method I* of the arm-current modification is illustrated in **Fig. 3.6**. As it can be observed, the additional currents are generated by a simple multiplication of the normalized arm-differential voltages and original current references by the matrix denoted as $K_1$. Thus obtained current components are summed with the original references, yielding the final circulating current references for the arm-differential energy control.

Compared with the other methods that aim to modify the current references, based on current decomposition into the positive and negative sequence rotating reference frames, this method offers a straightforward implementation, devoid of the need for sequence decomposition. On the other hand, by comparing the original and modified references of the proposed method and the method presented in [109], as it is done in **Tab. 3.1** using exemplary phasors, it can be concluded that both methods yield the same modified references. Nevertheless, the implementation of the *Method I* is significantly simpler compared to the method presented in [109].

Thus obtained current references $i^{**}_{\Delta,x}$ sum-up to zero, while preserving the original power references. The modified current references from **Fig. 3.6** are further fed to the current controller, which should be able to track the references.

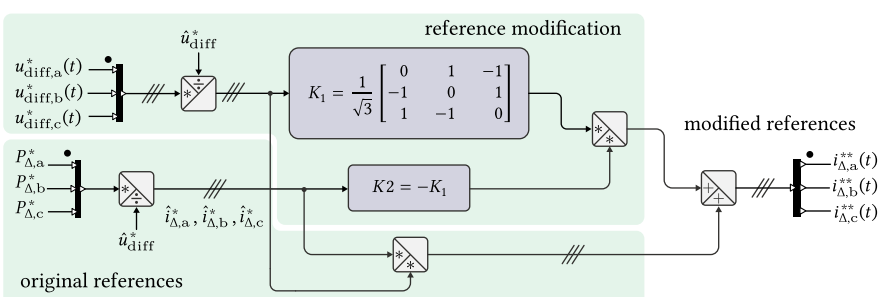


**Fig. 3.6** Implementation of the reference current modification for the arm-differential energy control. Modification part involves multiplication of the normalized arm-differential voltages with the matrix $K1$, as well as the multiplication of the original current reference magnitudes with the same matrix. Finally, the product of the two is added to the original references.

**Tab. 3.1** Comparison between the modified current reference phasors

| | Original phasors | Modified phasors (Method I) | Modified phasors (Method [109]) |
|---|---|---|---|
| Phase a | $I^{*}_{\Delta,\mathrm{a}} = 0.6\underline{/0^{\circ}}$ p.u. | $I^{**}_{\Delta,\mathrm{a}} = 0.6928\underline{/-30^{\circ}}$ p.u. | $I^{**}_{\Delta,\mathrm{a}} = 0.6928\underline{/-30^{\circ}}$ p.u. |
| Phase b | $I^{*}_{\Delta,\mathrm{b}} = 0.2\underline{/-120^{\circ}}$ p.u. | $I^{**}_{\Delta,\mathrm{b}} = 0.2309\underline{/-90^{\circ}}$ p.u. | $I^{**}_{\Delta,\mathrm{b}} = 0.2309\underline{/-90^{\circ}}$ p.u. |
| Phase c | $I^{*}_{\Delta,\mathrm{c}} = 0.8\underline{/120^{\circ}}$ p.u. | $I^{**}_{\Delta,\mathrm{c}} = 0.8327\underline{/136,1^{\circ}}$ p.u. | $I^{**}_{\Delta,\mathrm{c}} = 0.8327\underline{/136,1^{\circ}}$ p.u. |

### 3.3.4 Current modification - Method II

In the previous discussion it was shown that the circulating current references can be modified in such a way that they sum-up to zero and remain unobserved at both converter terminals. In addition, reference modification achieved by *Method I* preserves the arm-differential power references, obtained from the energy controller. To achieve so, additional in-quadrature current components are generated as shown in **Fig. 3.6**, thus increasing the overall circulating current magnitudes.

Another approach that can be used in modifying the original current references is illustrated in **Fig. 3.7.a**. It aims to minimize deviation of the modified current references from the original ones, all while conforming to the zero-sum criterion. As indicated before, it is referred to as *Method II* within the thesis.

To obtain a set of references with the minimum deviation with respect to the original ones, a similar process to the one applied for *Method I* is used. A deviation function $A^2$ was created, representing the sum of the squares of particular deviations, as illustrated in **Fig. 3.7.b**. Denoting projections of the modified current references to the corresponding voltage axes as $\hat{i}^{(\mathrm{d})}_{\Delta,\mathrm{x}}$ (c.f. **Fig. 3.7.a**), the criterion function can be expressed as:

$$\begin{aligned} A^2 = A^2_{\mathrm{a}} + A^2_{\mathrm{b}} + A^2_{\mathrm{c}} =& \left(\hat{i}^{*}_{\Delta,\mathrm{a}} - \hat{i}^{(\mathrm{d})}_{\Delta,\mathrm{a}}\right)^2 + \left(\hat{i}^{(\mathrm{d})}_{\Delta,\mathrm{a}} \tan\left(\phi_{\Delta,\mathrm{a}}\right)\right)^2 + \left(\hat{i}^{*}_{\Delta,\mathrm{b}} - \hat{i}^{(\mathrm{d})}_{\Delta,\mathrm{b}}\right)^2 + \left(\hat{i}^{(\mathrm{d})}_{\Delta,\mathrm{b}} \tan\left(\phi_{\Delta,\mathrm{b}}\right)\right)^2 + \ldots \\ &+ \left(\hat{i}^{*}_{\Delta,\mathrm{c}} - \hat{i}^{(\mathrm{d})}_{\Delta,\mathrm{c}}\right)^2 + \left(\hat{i}^{(\mathrm{d})}_{\Delta,\mathrm{c}} \tan\left(\phi_{\Delta,\mathrm{c}}\right)\right)^2 \end{aligned} \tag{3.83}$$

The three modified reference projections - $\hat{i}^{(\mathrm{d})}_{\Delta,\mathrm{a}}$, $\hat{i}^{(\mathrm{d})}_{\Delta,\mathrm{b}}$, $\hat{i}^{(\mathrm{d})}_{\Delta,\mathrm{c}}$ - as well as the three phase angles - $\phi_{\Delta,\mathrm{a}}$, $\phi_{\Delta,\mathrm{b}}$, $\phi_{\Delta,\mathrm{c}}$ - are six degrees of freedom in selecting the modified references. Nevertheless, one should recall that the ultimate objective of the reference modification is to obtain a zero-sum of the modified references. Therefore, as for the *Method I*, this constraint can be expressed in terms of equations (3.62)-(3.63), repeated hereafter:

$$\sqrt{3}\hat{i}^{(\mathrm{d})}_{\Delta,\mathrm{b}} \tan\left(\phi_{\Delta,\mathrm{b}}\right) = \hat{i}^{(\mathrm{d})}_{\Delta,\mathrm{a}}\left(\sqrt{3}\tan\left(\phi_{\Delta,\mathrm{a}}\right) - 1\right) - \hat{i}^{(\mathrm{d})}_{\Delta,\mathrm{b}} + 2\hat{i}^{(\mathrm{d})}_{\Delta,\mathrm{c}} \tag{3.84}$$

$$\sqrt{3}\hat{i}^{(\mathrm{d})}_{\Delta,\mathrm{c}} \tan\left(\phi_{\Delta,\mathrm{c}}\right) = \hat{i}^{(\mathrm{d})}_{\Delta,\mathrm{a}}\left(\sqrt{3}\tan\left(\phi_{\Delta,\mathrm{a}}\right) + 1\right) - 2\hat{i}^{(\mathrm{d})}_{\Delta,\mathrm{b}} + \hat{i}^{(\mathrm{d})}_{\Delta,\mathrm{c}} \tag{3.85}$$

The two constraints implicitly define the two phase angles - $\phi_{\Delta,\mathrm{b}}$, $\phi_{\Delta,\mathrm{c}}$ - thus reducing the degrees of

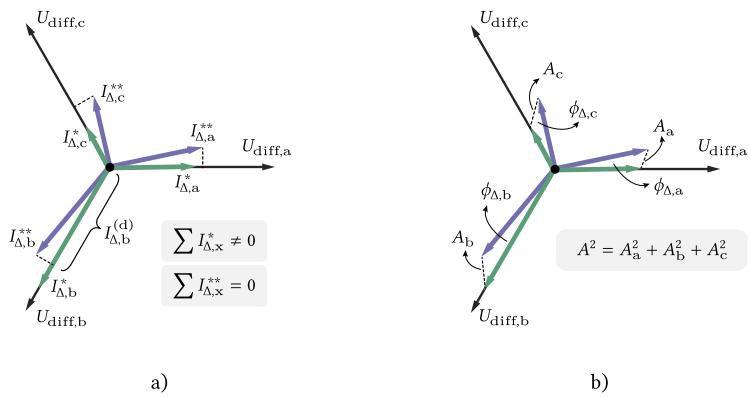


**Fig. 3.7** Phasors of the original and modified current references, for *Method II* of the arm-differential energy control: a) Projections of the modified current references to the respective voltage axes are different from the original references, yet the modified references should the least deviate from the original ones; b) Criterion used to find an optimal solution, by minimizing the deviation of the modified references with respect to the original ones.

freedom from six to four. Combining the expression (3.83) with (3.84)-(3.85), the criterion function can be expressed as a function of the remaining four degrees of freedom:

$$A^2 = f\Big(\tan\left(\phi_{\Delta,\mathrm{a}}\right), \hat{i}^{(\mathrm{d})}_{\Delta,\mathrm{a}}, \hat{i}^{(\mathrm{d})}_{\Delta,\mathrm{b}}, \hat{i}^{(\mathrm{d})}_{\Delta,\mathrm{c}}\Big) \tag{3.86}$$

Full expression is omitted here for the sake of brevity. Finding a minimum of the function of four variables provides a unique solution for the available degrees of freedom:

$$\hat{i}^{(\mathrm{d})}_{\Delta,\mathrm{a}} = \frac{4\hat{i}^{*}_{\Delta,\mathrm{a}} + \hat{i}^{*}_{\Delta,\mathrm{b}} + \hat{i}^{*}_{\Delta,\mathrm{c}}}{6} \tag{3.87}$$

$$\hat{i}^{(\mathrm{d})}_{\Delta,\mathrm{b}} = \frac{\hat{i}^{*}_{\Delta,\mathrm{a}} + 4\hat{i}^{*}_{\Delta,\mathrm{b}} + \hat{i}^{*}_{\Delta,\mathrm{c}}}{6} \tag{3.88}$$

$$\hat{i}^{(\mathrm{d})}_{\Delta,\mathrm{c}} = \frac{\hat{i}^{*}_{\Delta,\mathrm{a}} + \hat{i}^{*}_{\Delta,\mathrm{b}} + 4\hat{i}^{*}_{\Delta,\mathrm{c}}}{6} \tag{3.89}$$

$$\tan\left(\phi_{\Delta,\mathrm{a}}\right) = \frac{\sqrt{3}\left(\hat{i}^{*}_{\Delta,\mathrm{b}} - \hat{i}^{*}_{\Delta,\mathrm{c}}\right)}{4\hat{i}^{*}_{\Delta,\mathrm{a}} + \hat{i}^{*}_{\Delta,\mathrm{b}} + \hat{i}^{*}_{\Delta,\mathrm{c}}} \tag{3.90}$$

Incorporating the solutions (3.87)-(3.90) into the two constraints (3.84)-(3.85), expressions for the two remaining phase angles - $\phi_{\Delta,\mathrm{b}}$, $\phi_{\Delta,\mathrm{c}}$ - can be obtained as:

$$\tan\left(\phi_{\Delta,\mathrm{b}}\right) = \frac{\sqrt{3}\left(\hat{i}^{*}_{\Delta,\mathrm{c}} - \hat{i}^{*}_{\Delta,\mathrm{a}}\right)}{\hat{i}^{*}_{\Delta,\mathrm{a}} + 4\hat{i}^{*}_{\Delta,\mathrm{b}} + \hat{i}^{*}_{\Delta,\mathrm{c}}} \tag{3.91}$$

$$\tan\left(\phi_{\Delta,\mathrm{c}}\right) = \frac{\sqrt{3}\left(\hat{i}^{*}_{\Delta,\mathrm{a}} - \hat{i}^{*}_{\Delta,\mathrm{b}}\right)}{\hat{i}^{*}_{\Delta,\mathrm{a}} + \hat{i}^{*}_{\Delta,\mathrm{b}} + 4\hat{i}^{*}_{\Delta,\mathrm{c}}} \tag{3.92}$$

Once all the degrees of freedom are defined, we can obtain the time-domain expressions for the modified current references. Recalling their definitions, they can be expressed as:

$$\begin{aligned}
i^{**}_{\Delta,\mathrm{a}}(t) &= \hat{i}^{**}_{\Delta,\mathrm{a}} \sin\left(\omega_\mathrm{g} t + \phi_{\Delta,\mathrm{a}}\right) = \hat{i}^{**}_{\Delta,\mathrm{a}} \cos\left(\phi_{\Delta,\mathrm{a}}\right) \sin\left(\omega_\mathrm{g} t\right) + \hat{i}^{**}_{\Delta,\mathrm{a}} \sin\left(\phi_{\Delta,\mathrm{a}}\right) \cos\left(\omega_\mathrm{g} t\right) \\
&= \hat{i}^{(\mathrm{d})}_{\Delta,\mathrm{a}} \sin\left(\omega_\mathrm{g} t\right) + \hat{i}^{(\mathrm{d})}_{\Delta,\mathrm{a}} \tan\left(\phi_{\Delta,\mathrm{a}}\right) \cos\left(\omega_\mathrm{g} t\right) \\
&= \frac{2}{3}\hat{i}^{*}_{\Delta,\mathrm{a}} \sin\left(\omega_\mathrm{g} t\right) - \frac{1}{3}\hat{i}^{*}_{\Delta,\mathrm{b}} \sin\left(\omega_\mathrm{g} t - \frac{2\pi}{3}\right) - \frac{1}{3}\hat{i}^{*}_{\Delta,\mathrm{c}} \sin\left(\omega_\mathrm{g} t + \frac{2\pi}{3}\right) \\
&= \underbrace{\hat{i}^{*}_{\Delta,\mathrm{a}} A}_{\substack{\text{original}\\ \text{reference}}} - \frac{1}{3}\left(\hat{i}^{*}_{\Delta,\mathrm{a}} A + \hat{i}^{*}_{\Delta,\mathrm{b}} B + \hat{i}^{*}_{\Delta,\mathrm{c}} C\right)
\end{aligned} \tag{3.93}$$

$$\begin{aligned}
i^{**}_{\Delta,\mathrm{b}}(t) &= \hat{i}^{**}_{\Delta,\mathrm{b}} \sin\left(\omega_\mathrm{g} t - \frac{2\pi}{3} + \phi_{\Delta,\mathrm{b}}\right) = \hat{i}^{**}_{\Delta,\mathrm{b}} \cos\left(\phi_{\Delta,\mathrm{b}}\right) \sin\left(\omega_\mathrm{g} t - \frac{2\pi}{3}\right) + \hat{i}^{**}_{\Delta,\mathrm{b}} \sin\left(\phi_{\Delta,\mathrm{b}}\right) \cos\left(\omega_\mathrm{g} t - \frac{2\pi}{3}\right) \\
&= \hat{i}^{(\mathrm{d})}_{\Delta,\mathrm{b}} \sin\left(\omega_\mathrm{g} t - \frac{2\pi}{3}\right) + \hat{i}^{(\mathrm{d})}_{\Delta,\mathrm{b}} \tan\left(\phi_{\Delta,\mathrm{b}}\right) \cos\left(\omega_\mathrm{g} t - \frac{2\pi}{3}\right) \\
&= \frac{2}{3}\hat{i}^{*}_{\Delta,\mathrm{b}} \sin\left(\omega_\mathrm{g} t - \frac{2\pi}{3}\right) - \frac{1}{3}\hat{i}^{*}_{\Delta,\mathrm{a}} \sin\left(\omega_\mathrm{g} t\right) - \frac{1}{3}\hat{i}^{*}_{\Delta,\mathrm{c}} \sin\left(\omega_\mathrm{g} t + \frac{2\pi}{3}\right) \\
&= \underbrace{\hat{i}^{*}_{\Delta,\mathrm{b}} B}_{\substack{\text{original}\\ \text{reference}}} - \frac{1}{3}\left(\hat{i}^{*}_{\Delta,\mathrm{a}} A + \hat{i}^{*}_{\Delta,\mathrm{b}} B + \hat{i}^{*}_{\Delta,\mathrm{c}} C\right)
\end{aligned} \tag{3.94}$$

$$\begin{aligned}
i^{**}_{\Delta,\mathrm{c}}(t) &= \hat{i}^{**}_{\Delta,\mathrm{c}} \sin\left(\omega_\mathrm{g} t + \frac{2\pi}{3} + \phi_{\Delta,\mathrm{c}}\right) = \hat{i}^{**}_{\Delta,\mathrm{c}} \cos\left(\phi_{\Delta,\mathrm{c}}\right) \sin\left(\omega_\mathrm{g} t + \frac{2\pi}{3}\right) + \hat{i}^{**}_{\Delta,\mathrm{c}} \sin\left(\phi_{\Delta,\mathrm{c}}\right) \cos\left(\omega_\mathrm{g} t + \frac{2\pi}{3}\right) \\
&= \hat{i}^{(\mathrm{d})}_{\Delta,\mathrm{c}} \sin\left(\omega_\mathrm{g} t + \frac{2\pi}{3}\right) + \hat{i}^{(\mathrm{d})}_{\Delta,\mathrm{c}} \tan\left(\phi_{\Delta,\mathrm{c}}\right) \cos\left(\omega_\mathrm{g} t + \frac{2\pi}{3}\right) \\
&= \frac{2}{3}\hat{i}^{*}_{\Delta,\mathrm{c}} \sin\left(\omega_\mathrm{g} t + \frac{2\pi}{3}\right) - \frac{1}{3}\hat{i}^{*}_{\Delta,\mathrm{a}} \sin\left(\omega_\mathrm{g} t\right) - \frac{1}{3}\hat{i}^{*}_{\Delta,\mathrm{b}} \sin\left(\omega_\mathrm{g} t - \frac{2\pi}{3}\right) \\
&= \underbrace{\hat{i}^{*}_{\Delta,\mathrm{c}} C}_{\substack{\text{original}\\ \text{reference}}} - \frac{1}{3}\left(\hat{i}^{*}_{\Delta,\mathrm{a}} A + \hat{i}^{*}_{\Delta,\mathrm{b}} B + \hat{i}^{*}_{\Delta,\mathrm{c}} C\right)
\end{aligned} \tag{3.95}$$

Implementation of *Method II* is shown in **Fig. 3.8**. Original current references are obtained by multiplying the normalized arm-differential voltage references $u^{*}_{\mathrm{diff,x}}$ with the magnitudes of the circulating current references $\hat{i}^{*}_{\Delta,\mathrm{x}}$. They are further modified by multiplying with the matrix $K$, which is equivalent to subtraction of the average value of the three references from each one.

The final result of the analysis could have also been obtained by analysing the space vector of the original set of current references. In general, there could be $n$ phases, where the resulting space vector can be represented by $n$ linearly-independent vectors. One such a vector can be chosen as a vector representing an average value of $n$ original vectors, representing the zero component. As the sum

of the current references should be equal to zero, the closest possible approximation of the original space vector is obtained by a simple subtraction of the zero component. The resulting space vector preserves all the other $n-1$ linearly-independent components, thus representing the best possible approximation of the original.

An example of these theoretical considerations is illustrated in **Fig. 3.9** for a 3PH system, where the original set of current references constitute a space vector $\vec{I}^*$, presented in $\alpha\beta 0$ reference frame. The modified space vector $\vec{I}^{**}$ is obtained when the zero component $\vec{I}_0^*$ is subtracted from the original space vector, whereas the original $\alpha$ and $\beta$ components remain unaltered.

It can be shown that the obtained results are generic, and can be applied to an MMC with an arbitrary number of phases. Namely, in order to obtain circulating current components with the lowest deviation from the original set of references, the general approach for *Method II* can be expressed as in (3.96), where $k$ represents the number of phases.

$$i_{\Delta,\mathrm{x}}^{**} = i_{\Delta,\mathrm{x}}^{*} - \frac{1}{k}\sum_{x=1}^{k} i_{\Delta,\mathrm{x}}^{*} \tag{3.96}$$

Since the modified current references obtained by *Method II* have the lowest possible deviation from the original references, their magnitudes will generally be lower compared to currents obtained by *Method I*. On the other hand, although the arm-differential power components generated from such currents will be close to the references, they will not completely preserve the power references yielded by the arm-differential energy controller. As a consequence, the settling time for the arm-differential energy control might be longer for *Method II* compared to *Method I*.

A choice between the two presented methods is the choice between faster energy control response and lower circulating current magnitudes. Both methods are equally applicable under unbalanced grid conditions, as will be shown in **Chapter 4** as well as in case of SM failure.

To achieve a full control over the arm energies, the arm-sum energy control mechanism shall also be incorporated.

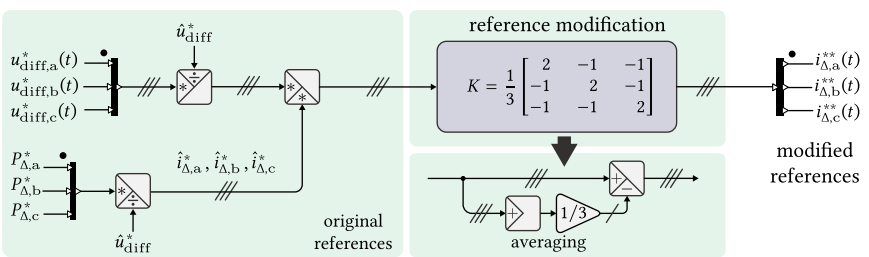


**Fig. 3.8** Implementation of the reference current modification for the arm-differential energy control, using *Method II*. Modification part involves multiplication of the original references with the matrix K, which is equivalent to the subtraction of the average value of the three references from the originals.

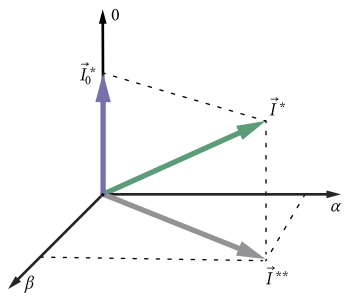


**Fig. 3.9** Graphical representation of the effects imposed by application of *MethodII* to the space vector of the original current references. The vector deprived from the zero component is the best possible approximation of the original vector under the zero-sum constraint.

## 3.4 Arm-Sum Energy Control Method

Arm-sum energy control is achieved through the arm-sum power $p_\Sigma$ control. Recalling the equation for the arm-sum power (3.40), repeated in (3.97), the key terms can be identified:

$$p_\Sigma = \frac{u_{\mathrm{dc}} i_{\mathrm{dc}}}{3} - \frac{\hat{u}_{\mathrm{ac}} \hat{i}_{\mathrm{ac}} \cos(\phi)}{2} + u_{\mathrm{dc}} i_{\mathrm{circ,dc}} - \frac{\hat{u}_{\mathrm{cm1}} \hat{i}_{\mathrm{ac}} \cos(\phi_{\mathrm{cm1}} - \phi)}{2} \tag{3.97}$$

During normal operation, only the first two terms exist, and they normally cancel out each other, due to the active power balance maintained between the ac and dc terminals. It should be noted that for the moment only symmetric grid conditions are considered, whereas the arm-sum energy control under grid asymmetries is the subject of the following chapter.

Regardless of the active power balance, arm-sum energies might still diverge from their references, due to various reasons mentioned at the beginning of this chapter. Therefore, a control action is needed to ensure the arm-sum energy convergence towards the reference. During the following analyses, it will be assumed that the dc terminal voltage is always available.

From the terminal point of view, an MMC can generally be controlled in two distinctive modes - inverter mode and rectifier mode. In the inverter mode, the MMC is assumed to be connected to a dc grid, which is supplying power to the ac grid. In such a case, the MMC terminal control aims to follow the active and reactive power references towards the ac grid, whereas the active power is drawn from the dc terminals. In case when the MMC operates in the rectifier mode of operation, it generates a necessary dc voltage at its terminals, where the necessary dc power is supplied from the ac terminals. Therefore, to achieve the energy balance within the converter phase legs, either ac or dc current is controlled.

### 3.4.1 Inverter mode of operation

Neglecting the power term originating from the common-mode voltage in 3.97, the expression for the arm-sum power can be simplified as:

$$p_\Sigma = \frac{u_{\mathrm{dc}} i_{\mathrm{dc}}}{3} - \frac{\hat{u}_{\mathrm{ac}} \hat{i}_{\mathrm{ac}} \cos(\phi)}{2} + u_{\mathrm{dc}} i_{\mathrm{circ,dc}} \tag{3.98}$$

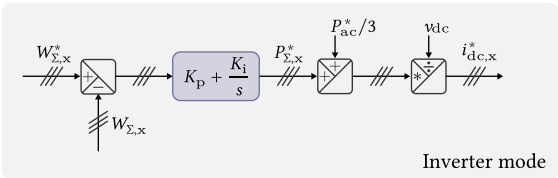


**Fig. 3.10** Arm-sum energy control for the inverter mode of operation, shown for three phases simultaneously. Symmetrical ac grid conditions are assumed. Final references are dc arm currents, that in sum constitute the dc terminal current.

In the inverter mode of operation, the ac terminal currents are controlled such that the ac power references are respected, whereas the dc currents are controlled to maintain the total energy balance within the converter.

**Fig. 3.10** shows how the arm-sum energy control is executed in the inverter mode of operation. The difference between the first two terms in (3.98) is used to generate the power references from the controller. As the ac power reference is provided from a higher control level, the dc power reference per phase is obtained as a sum of the ac power and the controller power request. Finally, the arm-common dc current components of the respective phases are obtained, which in sum constitute the dc terminal power.

### 3.4.2 Rectifier mode of operation

In this mode of operation, the dc voltage (current) reference is provided from a higher hierarchy, whereas the ac terminal active power is controlled to ensure the energy balance of the converter.

In the inverter mode of operation, different power requirements per phase leg could have been satisfied with the different dc arm-common currents, which would in sum constitute the total dc current. However, in case of the rectifier mode of operation, dc current is determined by the load, and must not be influenced for internal control purpose. On the other hand, ac currents should be symmetrical, amd thus cannot account for different power requirements among the phase legs.

To settle this problem, additional dc circulating currents are injected into the converter arms, with the aim of generating necessary power references from the energy controllers. From (3.98), utilizing the circulating dc currents, arm-sum energy can be controlled by the power:

$$p_\Sigma = u_{dc} i_{circ,dc} \tag{3.99}$$

**Fig. 3.11** shows the arm sum-energy control block diagram. Three energy controllers for each phase leg output three arm-sum power references $P^{**}_{\Sigma,x}$. Sum of the three references and the total power delivered to the dc terminals $P_{dc}$ constitutes the ac terminal active power reference $P^*_{ac}$. This control action preserves the total energy balance in the converter.

Power references of the individual legs are converted to the dc current references $i^{**}_{\Sigma,x}$. Due to the fact that three energy controllers in general yield different power requirements, sum of the three dc current references is generally different than zero, and thus would appear at the dc terminals. This is not acceptable in the rectifier mode of operation, where the dc terminal voltage and currents should be determined solely by application requirements, and not by the internal control actions.

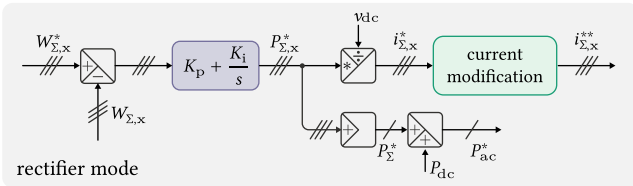


**Fig. 3.11** Arm-sum energy control for the rectifier mode of operation, shown for three phases simultaneously. Symmetrical ac grid conditions are assumed. Output of the arm-sum energy control are the ac power reference $P^*_{ac}$ and dc circulating current references $i^*_{\Sigma,x}$.

To mitigate this issue, current modification is needed, so that the three current references sum-up to zero. This is illustrated in **Fig. 3.12**, where three arbitrary dc current references are shown. As in the case of the arm-differential energy control, the current references should be modified such that they sum-up to zero, and have the least possible deviation from the original references.

Criterion function $A^2$ is created, and a minimum is found as a function of two variables, and the resulting modified current references are:

$$i^{**}_{\Sigma,a} = \frac{2}{3} i^*_{\Sigma,a} - \frac{1}{3} i^*_{\Sigma,b} - \frac{1}{3} i^*_{\Sigma,a} \tag{3.100}$$

$$i^{**}_{\Sigma,b} = \frac{2}{3} i^*_{\Sigma,b} - \frac{1}{3} i^*_{\Sigma,a} - \frac{1}{3} i^*_{\Sigma,c} \tag{3.101}$$

$$i^{**}_{\Sigma,c} = \frac{2}{3} i^*_{\Sigma,c} - \frac{1}{3} i^*_{\Sigma,a} - \frac{1}{3} i^*_{\Sigma,b} \tag{3.102}$$

As in the case of *Method II* of arm-differential energy control, modified current references are obtained by subtracting the zero sequence component from the original references. In such a way, it is ensured that the dc currents generated for the the arm-sum energy control do not alter the dc terminal current. Observing **Fig. 3.11**, one can also note that the zero sequence component of the power references in the arm-sum energy control ($P^*_{\Sigma,0}$) is also respected, through the ac terminal power reference $P^*_{ac}$.

The derived arm-sum energy control method can be generalized for an MMC with an arbitrary number of phase legs, or an arbitrary number of paralleled arms [121]. In both cases, modified current references can be obtained by subtracting the zero-sequence component from the original references:

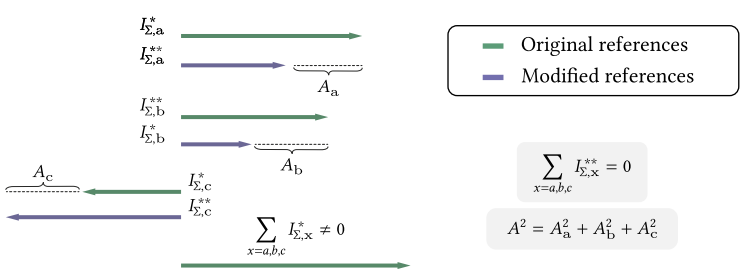


**Fig. 3.12** Modification criterion for the arm-common currents used in arm-sum energy control in the rectifier mode of operation.

$$i_{\Sigma,\mathrm{x}}^{**} = i_{\Sigma,\mathrm{x}}^{*} - \frac{1}{k}\sum_{x=1}^{k} i_{\Sigma,\mathrm{x}}^{*} \tag{3.103}$$

Previous discussions presented two methods for the arm-differential and one method for the arm-sum energy control. Compared to the other control methods that can be found in the literature, presented methods are characterized by their simplicity, intuitiveness, and generality. Their applicability under faulty conditions are evaluated in the **Chapter 4**, whereas the same principles are applied for the M3C energy control, as will be presented in **Chapter 5**.

## 3.5 Arm energies filtering techniques

Once the novel energy control methods are presented, to be able to understand the whole control structure, and to properly tune the energy controllers, energy measurement and filtering techniques should be analysed.

Due to the decoupled relationship between the arm-sum $W_\Sigma$ and arm-differential $W_\Delta$ energy control mechanisms, the two are controlled independently from one another, as shown in previous sections.

While it is of interest to control only the average terms of the arm-sum and arm-differential energies, they both contain oscillating terms at different frequencies, as it was already derived in **Chapter 2**. Equations (2.35)-(2.36) do not take into account existence of a common-mode voltage, which would, if present, necessarily interact with the arm currents and create oscillations in the arm energy.

These oscillations should be filtered out from the measured arm energies, in order to be used in the arm energy control structures. As a first step, dominant frequencies at which the oscillations occur should be identified. Recalling the arm voltage and current definitions, neglecting the inductive and resistive voltage drops, and defining the common-mode voltage as in (3.104), the two arm energies are determined as in (3.105)-(3.106).

$$u_{\mathrm{cm}} = \hat{u}_{\mathrm{cm}} \sin\left(3\omega_{\mathrm{g}} t + \phi_{\mathrm{cm}}\right) \tag{3.104}$$

$$\begin{aligned}
w_{\mathrm{p}} = \int_t^{t+T} p_{\mathrm{p}} dt &= \int_t^{t+T} \left(\frac{u_{\mathrm{dc}}}{2} - \hat{u}_{\mathrm{x}} \sin\left(\omega_{\mathrm{g}} t\right) - \hat{u}_{\mathrm{cm}} \sin\left(3\omega_{\mathrm{g}} t + \phi_{\mathrm{cm}}\right)\right)\left(\frac{i_{\mathrm{dc}}}{3} + \frac{\hat{i}_{\mathrm{x}}}{2} \sin\left(\omega_{\mathrm{g}} t + \phi\right)\right) \\
&= \int_t^{t+T} \Bigg( \underbrace{\frac{u_{\mathrm{dc}} i_{\mathrm{dc}}}{6} - \frac{\hat{u}_{\mathrm{x}} \hat{i}_{\mathrm{x}} \cos\left(\phi\right)}{4}}_{=0} + \frac{u_{\mathrm{dc}} \hat{i}_{\mathrm{x}}}{4} \sin\left(\omega_{\mathrm{g}} t + \phi\right) - \frac{\hat{u}_{\mathrm{x}} i_{\mathrm{dc}}}{3} \sin\left(\omega_{\mathrm{g}} t\right) \\
&\quad + \frac{\hat{u}_{\mathrm{x}} \hat{i}_{\mathrm{x}}}{4} \cos\left(2\omega_{\mathrm{g}} t + \phi\right) - \frac{\hat{u}_{\mathrm{cm}} i_{\mathrm{dc}}}{3} \sin\left(3\omega_{\mathrm{g}} t + \phi_{\mathrm{cm}}\right) \\
&\quad - \frac{\hat{u}_{\mathrm{cm}} \hat{i}_{\mathrm{x}}}{4} \cos\left(2\omega_{\mathrm{g}} t + \phi_{\mathrm{cm}} - \phi\right) + \frac{\hat{u}_{\mathrm{cm}} \hat{i}_{\mathrm{x}}}{4} \cos\left(4\omega_{\mathrm{g}} t + \phi_{\mathrm{cm}} + \phi\right) \Bigg) dt
\end{aligned} \tag{3.105}$$

$$
\begin{aligned}
w_{\mathrm{n}} = \int_t^{t+T} p_{\mathrm{n}} dt &= \int_t^{t+T} \left( \frac{u_{\mathrm{dc}}}{2} + \hat{u}_{\mathrm{x}} \sin\left(\omega_{\mathrm{g}} t\right) + \hat{u}_{\mathrm{cm}} \sin\left(3\omega_{\mathrm{g}} t + \phi_{\mathrm{cm}}\right) \right) \left( \frac{i_{\mathrm{dc}}}{3} - \frac{\hat{i}_{\mathrm{x}}}{2} \sin\left(\omega_{\mathrm{g}} t + \phi\right) \right) \\
&= \int_t^{t+T} \Bigg( \underbrace{\frac{u_{\mathrm{dc}} i_{\mathrm{dc}}}{6} - \frac{\hat{u}_{\mathrm{x}} \hat{i}_{\mathrm{x}} \cos\left(\phi\right)}{4}}_{=0} - \frac{u_{\mathrm{dc}} \hat{i}_{\mathrm{x}}}{4} \sin\left(\omega_{\mathrm{g}} t + \phi\right) + \frac{\hat{u}_{\mathrm{x}} i_{\mathrm{dc}}}{3} \sin\left(\omega_{\mathrm{g}} t\right) \\
&\quad + \frac{\hat{u}_{\mathrm{x}} \hat{i}_{\mathrm{x}}}{4} \cos\left(2\omega_{\mathrm{g}} t + \phi\right) + \frac{\hat{u}_{\mathrm{cm}} i_{\mathrm{dc}}}{3} \sin\left(3\omega_{\mathrm{g}} t + \phi_{\mathrm{cm}}\right) \\
&\quad - \frac{\hat{u}_{\mathrm{cm}} \hat{i}_{\mathrm{x}}}{4} \cos\left(2\omega_{\mathrm{g}} t + \phi_{\mathrm{cm}} - \phi\right) + \frac{\hat{u}_{\mathrm{cm}} \hat{i}_{\mathrm{x}}}{4} \cos\left(4\omega_{\mathrm{g}} t + \phi_{\mathrm{cm}} + \phi\right) \Bigg) dt
\end{aligned}
\tag{3.106}
$$

Integrating the expressions (3.105)-(3.106), followed by summing and subtracting them, arm-sum and arm-differential energies can be thus expressed as:

$$
w_{\Sigma} = \frac{\hat{u}_{\mathrm{x}} \hat{i}_{\mathrm{x}}}{4\omega_{\mathrm{g}}} \sin\left(2\omega_{\mathrm{g}} t + \phi\right) - \frac{\hat{u}_{\mathrm{cm}} \hat{i}_{\mathrm{x}}}{4\omega_{\mathrm{g}}} \sin\left(2\omega_{\mathrm{g}} t + \phi_{\mathrm{cm}} - \phi\right) + \frac{\hat{u}_{\mathrm{cm}} \hat{i}_{\mathrm{x}}}{8\omega_{\mathrm{g}}} \sin\left(4\omega_{\mathrm{g}} t + \phi_{\mathrm{cm}} + \phi\right) \tag{3.107}
$$

$$
w_{\Delta} = - \frac{u_{\mathrm{dc}} \hat{i}_{\mathrm{x}}}{2\omega_{\mathrm{g}}} \cos\left(\omega_{\mathrm{g}} t + \phi\right) + \frac{2\hat{u}_{\mathrm{x}} i_{\mathrm{dc}}}{3\omega_{\mathrm{g}}} \cos\left(\omega_{\mathrm{g}} t\right) + \frac{2\hat{u}_{\mathrm{cm}} i_{\mathrm{dc}}}{9\omega_{\mathrm{g}}} \cos\left(3\omega_{\mathrm{g}} t + \phi_{\mathrm{cm}}\right) \tag{3.108}
$$

Arm-sum energy contains the second harmonic and fourth harmonic components. The first term in (3.107) exists in normal operation, whereas the other two terms are a consequence of a common-mode voltage component at triple the fundamental frequency. The common-mode voltage component is typically injected to increase the ac voltage generation capability, and besides the third harmonic, it can contain other multiples of three of the fundamental frequency, as in min-max (or space-vector) modulation. Nevertheless, the third harmonic component of the common-mode voltage is dominant and in case when it is only injected, its magnitude is equal to 1/6 of the fundamental ac voltage magnitude. Consequently, by comparing the first and the third term in (3.107) it is concluded that the fourth harmonic energy component has twelve times lower amplitude compared to the second harmonic energy pulsation in normal conditions. Therefore, it will be predominantly important to eliminate the second harmonic component from the arm-sum energy.

Arm-differential energy component, on the other hand, contains a first harmonic component that exists in normal operation, as well as the additional first and third harmonic components, stemming from the common-mode voltage. Again, comparing the magnitudes of the first and the third term in (3.108), it can be concluded that the ratio of the two is 1/36. Therefore, it is of particular interest to eliminate the first harmonic energy pulsations from the arm-differential energy.

As the dc value of both arm-sum and arm-differential energies is of interest, it can be obtained applying either low-pass or notch filters to the measured energies. As the filtering influences the achievable bandwidth of the energy controllers, it is necessary to assess both options.

### 3.5.1 Low-pass filters

Low-pass filters (LPFs) have nearly unity gain for frequencies lower than the cutoff frequency, whereas they attenuate signals at higher frequencies. First-order LPF has the simplest form, shown in (3.109). Second-order LPFs are used to increase the attenuation of the high-frequency signals, compared to the first-order LPF. Conversely, they can be perceived as filters that have a wider unity gain area than the first-order counterparts, for a given attenuation at a specific frequency. While they can be realized in many different ways, a second-order Butterworth filter is used as an example, with a transfer function given in (3.110).

$$G_a(s) = \frac{\omega_c}{s + \omega_c} \tag{3.109}$$

$$G_a(s) = \frac{\omega_c^2}{s^2 + 2\xi\omega_c s + \omega_c^2} \tag{3.110}$$

The choice of a corner frequency $f_c$ determines the frequency range that will be passed through a filter. Analysing the arm-sum and arm-differential energies, it was concluded that the dominant frequency components appear at the fundamental frequency (50 Hz) in the arm-differential energy, and double the fundamental frequency in the arm-sum energy. Therefore, if the LPFs are to be used to obtain the average arm-sum and arm-differential energies, they should be tuned such that they greatly attenuate the dominant frequency components.

Comparison between the magnitude and phase characteristics of the two filters, with the corner frequencies selected as $f_c = 10$ Hz and $f_c = 20$ Hz, are provided in **Fig. 3.13.a-b**.

The filters with the corner frequency selected as $f_c = 10$ Hz are intended to be used for the fundamental frequency component suppression in the arm-differential energy. **Fig. 3.13.a** shows the difference between the two filters in terms of attenuation at the fundamental frequency. It is evident that the second-order filter introduces five-fold higher attenuation at the fundamental frequency, compared to its first-order counterpart. Therefore, it can be adopted as an obvious choice for the arm-differential

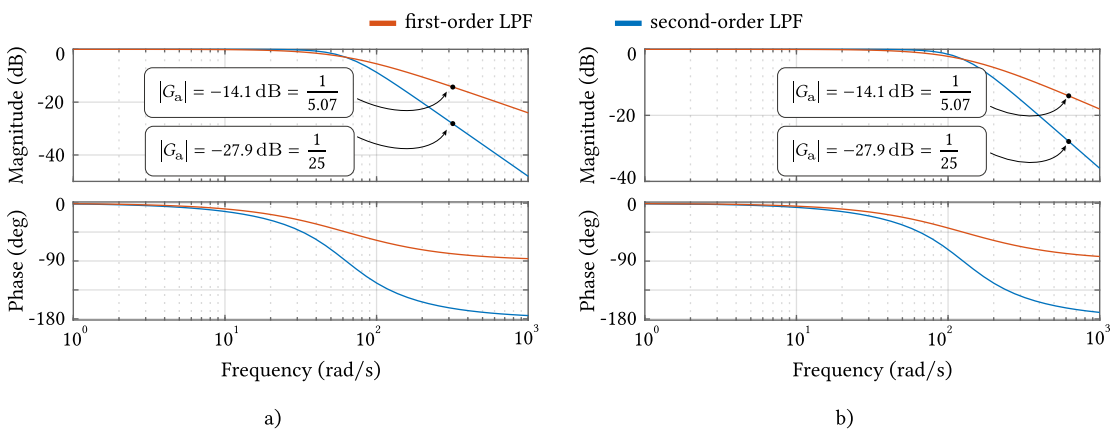


**Fig. 3.13** a) Magnitude and phase characteristics of the first and second-order filters, tuned for the corner frequency of $f_c = 10$ Hz. In case of the second-order filter, the relative damping is chosen as $\xi = 1/\sqrt{2}$. Actual damping is examined at the fundamental frequency. b) Magnitude and phase characteristics of the first and second-order filters, tuned for the corner frequency of $f_c = 20$ Hz. In case of the second-order filter, the relative damping is chosen as $\xi = 1/\sqrt{2}$. Actual damping is examined at double the fundamental frequency.

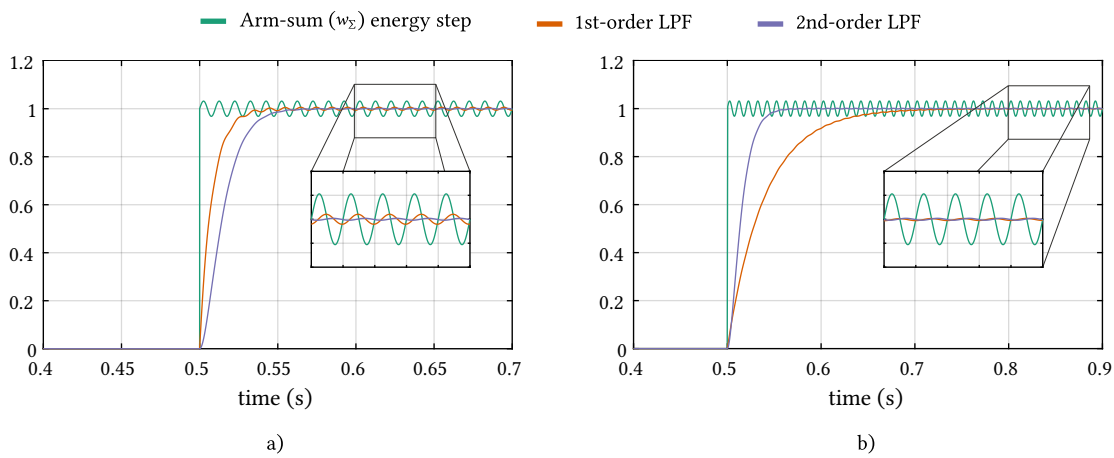


**Fig. 3.14** Responses of arm-sum energy filters on energy step change: a) First and second-order LPFs both tuned at $f_c = 20\,\text{Hz}$, aiming to suppress the dominant second harmonic component. To make a comparison easier, the relative damping of the second-order filter was set to $\xi = 1$. The first-order filter has lower rise time, but a five times higher steady-state oscillating component. b) The responses of two LPF are compared for the first-order filter cutoff frequency of $f_{c,1} = 4\,\text{Hz}$, and the second-order filter cutoff frequency is retained. The same steady-state oscillation suppression is achieved, yet with a higher response time of a first-order LPF.

energy filtering.

On the other hand, LPFs tuned at $f_c = 20\,\text{Hz}$ are intended to suppress the oscillations at double the fundamental frequency. Since the corner frequency is increased two-fold, examination at double the fundamental frequency reveals that the resulting attenuation will be the same as in the previously analysed case. As a result, the two corner frequencies can be adopted for LPFs used in arm-energy filtering.

Analysis of the phase characteristics of the two types of filters shows that the second-order filter introduces a larger phase delay at frequencies higher than the cutoff frequency. This should be taken into account during the design of the energy controller, as it might lead to instability if unreasonably high control gains are adopted.

To observe the difference between the two filters, both in dynamic and steady-state conditions, a simulation of an arm-sum $w_\Sigma$ energy step is conducted. The arm-sum energy is normalized with respect to its rated value, and the second harmonic energy oscillations are included. The simulated arm-sum energy is filtered by both first-order and second-order LPFs, and the results are presented in **Fig. 3.14**.

To make the comparison easier, the relative-damping of the second-order filter was assumed to be equal to $\xi = 1$. From **Fig. 3.14.a** can be concluded that when the two LPFs are tuned for the same corner frequency, the dynamic response of the first-order filter is generally faster, yet at the expense of a higher steady-state oscillating component. The difference between the steady-state oscillating terms is well in accordance with the conclusions drawn from **Fig. 3.13**.

As it is of interest to suppress the oscillating term to a greatest reasonable extent, the first-order filter cutoff frequency is reduced five-fold, in order to have the same attenuation in steady-state as the second-order filter tuned at $f_c = 20\,\text{Hz}$. The responses to the step change in in the arm-sum energy are presented in **Fig. 3.14.b**. While the steady-state oscillating terms are suppressed to nearly the same

extent, dynamic response of the first-order filter becomes rather slow compared to its second-order counterpart.

As a result, it can be concluded that the second-order filters are better suited for filtering out the undesired harmonic components from the measured arm energies. Further increase in the cutoff frequency is possible, and would yield a faster dynamic response, but at the expense of lower attenuation of the oscillating components. For example, increasing the cutoff frequencies by 50 % results in the second-order filter attenuation reduction from 1/25 to 1/11. Further increase by 100 % from the original values would result in attenuation of approximately 1/6.

Note that the arm-sum energy step does not represent a real scenario, as the energy in the converter cannot change abruptly. Nevertheless, it used in the simulation to compare the behaviour of the two filters. Although the filters are examined for a cutoff frequency of 20 Hz, while suppressing double the fundamental frequency, the same conclusions can be drawn if a cutoff frequency is chosen differently, such as to suppress the fundamental frequency oscillations in the arm-differential energy.

Also note that the arm-sum and arm-differential energies might contain the third and fourth harmonic components, which were not accounted for in the analysis. However, besides their magnitudes being naturally lower, attenuation of the LPFs at higher frequencies only gets higher.

### 3.5.2 Notch filter

Band-stop or notch filters are types of filters used to suppress frequency components around some resonant frequency, while leaving unattenuated the rest of the spectrum. In case of both arm-sum and arm-differential energies, frequency components to be attenuated are known in advance, and thus notch filters can be employed.

A transfer function of a notch filter in Laplace domain is typically represented as:

$$G_{\mathrm{a}}(s) = \frac{s^2 + \omega_{\mathrm{c}}^2}{s^2 + 2\xi\omega_{\mathrm{c}}s + \omega_{\mathrm{c}}^2} \tag{3.111}$$

where $\omega_{\mathrm{c}}$ represents a frequency component to be filtered out (or rejected), whereas the parameter $\xi$ defines the width of the rejection region.

To understand the influence of the parameter $\xi$ on the filter frequency characteristics, magnitude and phase characteristics of a notch filter, tuned to suppress a frequency component at $f_{\mathrm{c}} = 100\,\mathrm{Hz}$, are plotted in **Fig. 3.15.a** for different values of the parameter $\xi$.

Magnitude characteristics reveal that the parameter $\xi$ defines the selectivity of the filter, i.e. a range of frequencies that will be attenuated. For the smallest chosen value of $\xi$, the notch filter also introduces the smallest phase deviation for a large range of frequencies. Thus, from the perspective of frequency characteristics, the lowest chosen value of $\xi$ seems to be the most favourable.

Dynamic response of the notch filter to the arm-sum energy step change is shown in **Fig. 3.15.b**. On the same figure, the second-order LPF response was shown for the sake of comparison. It can be observed that the notch filter with the lowest value of $\xi$ quickly attains the final value, but the settling time is prolonged due to the oscillations at the central frequency. On the other hand, responses of the notch filters with higher values of the parameter $\xi$, are more attenuated, and converge towards the steady-state value quickly.

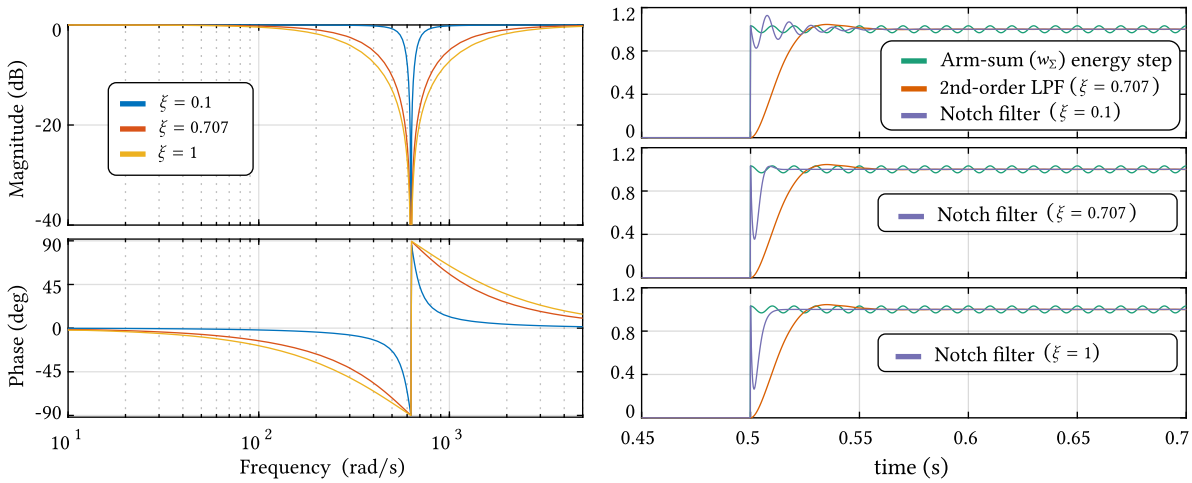


**Fig. 3.15** (left) Magnitude and phase frequency characteristics of a notch filter with a central rejection frequency $f_c = 100\,\text{Hz}$ ($\omega_c \approx 628\,\text{rad}\,\text{s}^{-1}$), and different values of the parameter $\xi$; (right) Comparison of a dynamic response of a second-order LPF and notch filters with different values of $\xi$, to a step change of the arm-sum energy at their input.

Compared to the response of the second-order LPF, notch filters show faster response for any of the chosen value of $\xi$. Consequently, notch filters will introduce smaller equivalent delays in the arm energy control structure. As such, they are a preferable solution for filtering in the arm energy control structure.

Although a notch filter with smaller value of $\xi$ reaches the setpoint faster, filters with a higher value of $\xi$ might better suit the application, as they do not introduce oscillations into the feedback signal. Therefore, in the following analysis, notch filters with a value of $\xi = \sqrt{2}/2$ will be used to suppress desired frequency components.

A notch filter with a central frequency of $f_c = 100\,\text{Hz}$ was subject of the analysis, nevertheless, the same conclusions apply to a notch filter tuned at any central frequency. For the arm-differential energy filtering, a dominant frequency component is at the fundamental grid frequency. Besides, when the common-mode voltage component is injected, a third harmonic and fourth harmonic components appear in the arm-differential and arm-sum energies, respectfully.

Block diagram of the energy measurement and filtering process in the MMC is provided in **Fig. 3.16**.

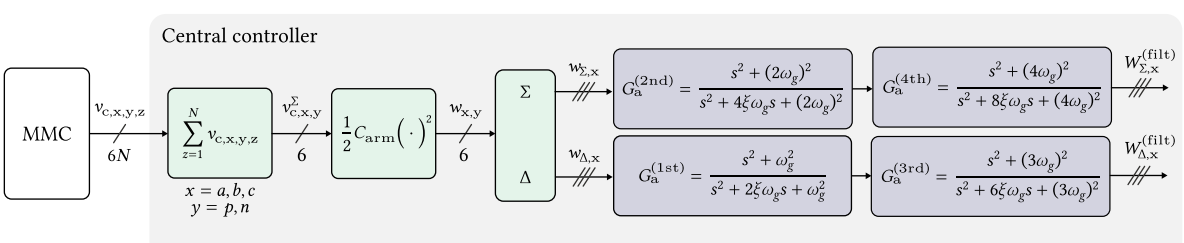


**Fig. 3.16** Block diagram of the energy measurement and filtering: SM voltages $v_{c,x,y,z}$ are communicated from the SMs to the central controller, where the six arm energies $w_{x,y}$ are calculated and converted to the arm-sum $w_\Sigma$ and arm-differential $w_\Delta$ energies, which are further filtered using the appropriate notch filters.

Assuming that the voltage measurement is available on each SM, measured values are communicated to the central controller, where the total arm voltages in all six arms are calculated. These are further converted to the equivalent arm energies $w_{\mathrm{x,y}}$, from which the sum and differential components are calculated for each phase. These components are further filtered using notch, according to the previous discussion. Finally, filtered arm-sum $w_{\Sigma}^{(\mathrm{filt})}$ and arm-differential $w_{\Delta}^{(\mathrm{filt})}$ energies, are fed to the $\Sigma$ and $\Delta$ energy controllers as the feedback variables.

## 3.6 Energy control parameters

As discussed earlier within this chapter, both arm-sum and arm-differential energy controllers should have a PI structure. Although the two control methods are decoupled from each other and based on different mechanisms, their control structures have similar form.

A block diagram showing the energy control structure is presented in **Fig. 3.17**, using the arm-sum energy control as an example. Note that the same conclusions would as well apply for the arm-differential energy.

The objective is to model all relevant parts of the system, in order to obtain an equivalent transfer function, that will be used to tune the controller's parameters. As the energy control occurs in the central controller, which communicates with all the SMs, it is executed with certain period, labelled as $T_{\mathrm{ctrl}}$. The output of the energy controller are power references, which are further converted to the current references, based on the previous discussion. Thus generated modified references $I_{\Sigma,\mathrm{x}}^{**}$ are further fed to the current controller structure, which eventually makes the converter currents follow their references.

SM voltages (or energies) are communicated to the main controller, where the communication latency is modelled by a transport delay of $T_{\mathrm{COMM}}$. Finally, arm-sum energies are filtered in the central controller using notch filters, and their outputs are fed back to the control structure as feedback variables.

To be able to properly tune the controllers, each block in the block diagram shown in **Fig. 3.17** should be modelled. Even though the main controller is a digital controller, with a discrete time step of $T_{\mathrm{CTRL}}$, modelling will be performed in $s$-domain for a sake of simplicity.

**Fig. 3.18** shows a block diagram, representing the arm-sum energy control structure from **Fig. 3.17**, modelled in $s$-domain. It can be observed that the output of the energy controller converted to the modified current references $I_{\Sigma,\mathrm{x}}^{**}$, making an assumption that the current modification block ($G_{\mathrm{cm}}$) does not induce significant magnitude change. Further, controller time step is modelled as a transport

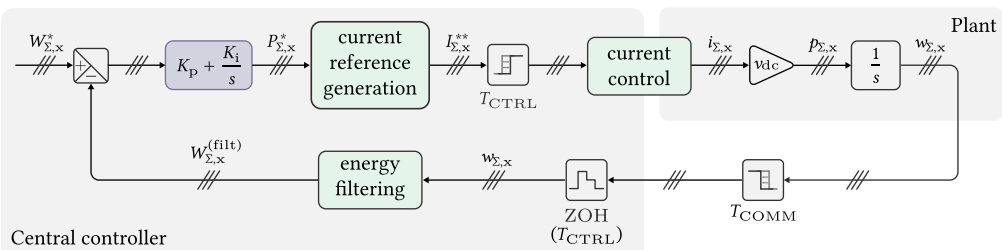


**Fig. 3.17** Block diagram of a complete arm-sum energy control structure.

delay of $T_{\mathrm{CTRL}}$, whereas the current control loop is equivalently modelled with a first-order transfer function. While the current control loop might be represented more accurately using a second-order transfer function, for the sake of analysing the slower, outer loops, such as the energy control loop, the first-order transfer function is a good approximation. Note that the parameter $\omega_{\mathrm{c}}$ represents the bandwidth of the current control loop.

The plant (leg capacitance) is represented by an integrator. Realized arm-common currents $i_{\Sigma,\mathrm{x}}$ interact with the dc terminal voltage $v_{\mathrm{dc}}$ yielding the arm-sum power. Integral of such a power represents the arm-sum energy.

Communication delay is represented as a transport delay of $T_{\mathrm{COMM}}$, whereas the sampling of the energies by a central controller introduces an additional transport delay of of $T_{\mathrm{CTRL}}/2$.

Finally, a notch filter employed in the arm-sum energy filtering is modelled by an equivalent first-order transfer function, with the same characteristics within the frequency range of interest. Due to the fact that the current control loop is subordinate to the energy control, and that it has expected bandwidth of $f_{\mathrm{cc}} = 500\,\mathrm{Hz}$, it is reasonable to have an order of magnitude slower outer loop. Therefore, for the selected frequency range, a first-order transfer function can be a good approximation of a notch filter.

**Fig. 3.19.a** shows frequency characteristics of a notch filter with the central frequency $f_{\mathrm{c,2nd}} = 100\,\mathrm{Hz}$, and the parameter $\xi = \sqrt{2}/2$. In addition, frequency characteristics of a first-order transfer function, with a bandwidth frequency $f_{\mathrm{bw,1st}} = 60\,\mathrm{Hz}$, are shown on the same plots. The two transfer functions have almost identical magnitude and phase characteristics for the frequency range $\omega < 300\,\mathrm{rad/s}$ ($f < 48\,\mathrm{Hz}$). Consequently, for the notch filter with a central frequency of $f_{\mathrm{c,2nd}} = 100\,\mathrm{Hz}$, the equivalent first-order transfer function bandwidth can be selected as:

$$\omega_{\mathrm{f,2nd}} = 2\pi f_{\mathrm{bw,1st}} = 120\pi\ \mathrm{rad/s} \tag{3.112}$$

Similarly, **Fig. 3.19.a** shows frequency characteristics of a notch filter tuned to suppress the fourth harmonic, i.e. with a central frequency $f_{\mathrm{c,4th}} = 200\,\mathrm{Hz}$. It is shown that a first order transfer function with a bandwidth frequency $f_{\mathrm{bw,1st}} = 120\,\mathrm{Hz}$ represents a good approximation of the notch filter.

As the two filters (second harmonic and fourth harmonic) are cascaded (c.f. **Fig. 3.17**) the equivalent transfer function of the two represents a product of their particular first-order transfer functions:

$$G_{\mathrm{f,eq}} = \frac{\omega_{\mathrm{f,2nd}}}{s + \omega_{\mathrm{f,2nd}}} \frac{\omega_{\mathrm{f,4th}}}{s + \omega_{\mathrm{f,4th}}} \approx \frac{\omega_{\mathrm{f,eq}}}{s + \omega_{\mathrm{f,eq}}} \tag{3.113}$$

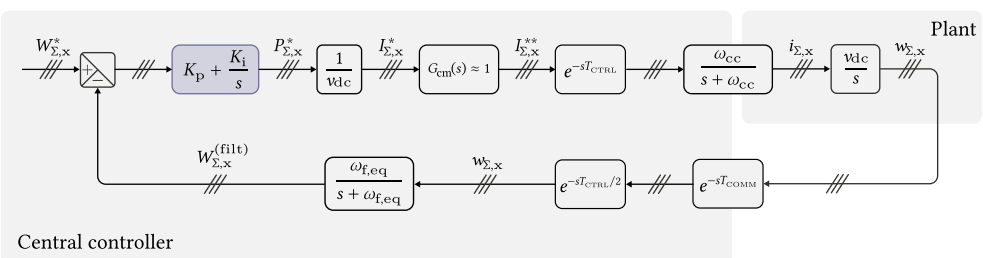


**Fig. 3.18** Block diagram of a complete arm-sum energy control structure, where individual blocks are modelled by the appropriate s-domain transfer functions.

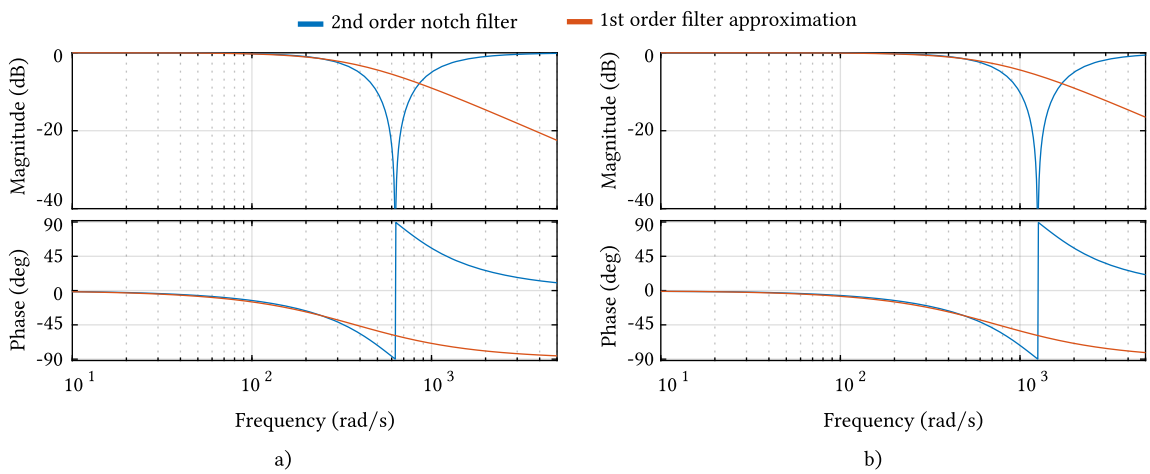


**Fig. 3.19** Magnitude and phase characteristics of a second-order notch filter and its first-order equivalent: a) notch filter with a central frequency set as $f_c = 100\,\text{Hz}$, and $\xi = \sqrt{2}/2$; first-order equivalent has the bandwidth frequency set as $f_{\text{bw,1st}} = 60\,\text{Hz}$; b) notch filter with a central frequency set as $f_c = 200\,\text{Hz}$, and $\xi = \sqrt{2}/2$; first-order equivalent has the bandwidth frequency set as $f_{\text{bw,1st}} = 120\,\text{Hz}$.

$$\omega_{\text{f,eq}} = \frac{\omega_{\text{f,2nd}}\omega_{\text{f,4th}}}{\omega_{\text{f,2nd}} + \omega_{\text{f,4th}}} = \frac{2}{3}\omega_{\text{f,2nd}} = 80\pi\ \text{rad/s} \tag{3.114}$$

Similar conclusions can be drawn for the arm-differential energy filters, suppressing the fundamental and third harmonic. In such a case, equivalent angular frequency of the first-order filter approximation equals:

$$\omega_{\text{f,eq}} = \frac{\omega_{\text{f,1st}}\omega_{\text{f,3rd}}}{\omega_{\text{f,1st}} + \omega_{\text{f,3rd}}} = \frac{3}{4}\omega_{\text{f,1st}} = 45\pi\ \text{rad/s} \tag{3.115}$$

Once all the parts of the energy control structure are modelled, parameters of the controller can be selected. To simplify the analysis, all transport delays will be combined into a single delay of $T_{\text{D}}$, whereas the transfer function of the current control and energy filtering are approximated by a single first-order transfer function, with an angular frequency:

$$\omega_{\text{eq}} = \frac{\omega_{\text{cc}}\omega_{\text{f,eq}}}{\omega_{\text{cc}} + \omega_{\text{f,eq}}} \tag{3.116}$$

A simplified block diagram of the arm-sum energy control is presented in **Fig. 3.20**. The bandwidth of the control structure is determined by the proportional gain, so theoretically higher proportional gains would yield higher bandwidth in the energy control. Nevertheless, due to the delays in the system and a low-pass nature of certain subsystems, too high values of the proportional gain might render the system unstable.

Therefore, to chose a proper value of the proportional gain, the integral part is neglected in the first analysis. Open-loop transfer function of the system shown in **Fig. 3.20** takes the following form:

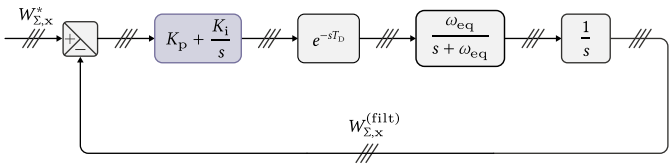


**Fig. 3.20** Simplified block diagram of the arm-sum energy control. All the transport delays are combined into a single delay $T_\mathrm{D}$, whereas the energy filters and the current control are approximated with an equivalent first-order transfer function.

$$G_\mathrm{ol}(s) = \frac{K_\mathrm{p}}{s}\frac{\omega_\mathrm{eq}}{s+\omega_\mathrm{eq}}e^{-sT_\mathrm{D}} \tag{3.117}$$

Gain crossover frequency $\omega_\mathrm{gc}$ is a frequency at which the magnitude characteristic of an open-loop transfer function reaches unity (or 0 dB). Phase margin is a parameter used to evaluate stability of a given system, and is typically defined as in (3.119), where $\phi_\mathrm{Gol}$ is phase lag introduced by the open-loop transfer function $G_\mathrm{ol}(s)$ at the gain crossover frequency $\omega_\mathrm{gc}$.

$$\left|G_\mathrm{ol}(j\omega_\mathrm{gc})\right| = 1 \tag{3.118}$$

$$\phi_\mathrm{PM} = \pi - \phi_\mathrm{Gol} \tag{3.119}$$

As a compromise between stability of the system and a high bandwidth, a phase margin is recommended to be within the range $\phi_\mathrm{PM} \in [30^\circ, 60^\circ]$. In this work, the target phase margin is chosen as $\phi_\mathrm{PM} = 45^\circ$. To evaluate the phase lag introduced by the open-loop transfer function around the gain crossover frequency, the open-loop transfer function can be expressed as:

$$G_\mathrm{ol}(s) = \frac{K_\mathrm{p}}{j\omega_\mathrm{gc}}\frac{1}{1+\frac{j\omega_\mathrm{gc}}{\omega_\mathrm{eq}}}e^{-j\omega_\mathrm{gc}T_\mathrm{D}} \tag{3.120}$$

As a result, the phase lag of the open-loop transfer function can be obtained as in (3.121), whereas the phase margin is given by (3.122). Defining the target phase margin as $\phi_\mathrm{PM} = \pi/4$, the expression (3.122) becomes (3.123).

$$\phi_\mathrm{Gol} = \frac{\pi}{2} + \omega_\mathrm{gc}T_\mathrm{D} + \mathrm{atan}\left(\frac{\omega_\mathrm{gc}}{\omega_\mathrm{eq}}\right) \tag{3.121}$$

$$\phi_\mathrm{PM} = \frac{\pi}{2} - \omega_\mathrm{gc}T_\mathrm{D} - \mathrm{atan}\left(\frac{\omega_\mathrm{gc}}{\omega_\mathrm{eq}}\right) \tag{3.122}$$

$$\omega_\mathrm{gc}T_\mathrm{D} + \mathrm{atan}\left(\frac{\omega_\mathrm{gc}}{\omega_\mathrm{eq}}\right) = \frac{\pi}{4} \tag{3.123}$$

From (3.123) the gain crossover frequency can be obtained. Two parameters have an influence on its value, and those are the total transport delay in the system $T_\mathrm{D}$, and the equivalent angular frequency $\omega_\mathrm{eq}$. While the former is explicitly defined as a sum of the delays in **Fig. 3.17**, the latter is a combination of the current control bandwidth $\omega_\mathrm{cc}$ and the equivalent angular frequency of an employed filter $\omega_\mathrm{f,eq}$, defined in (3.114)-(3.115).

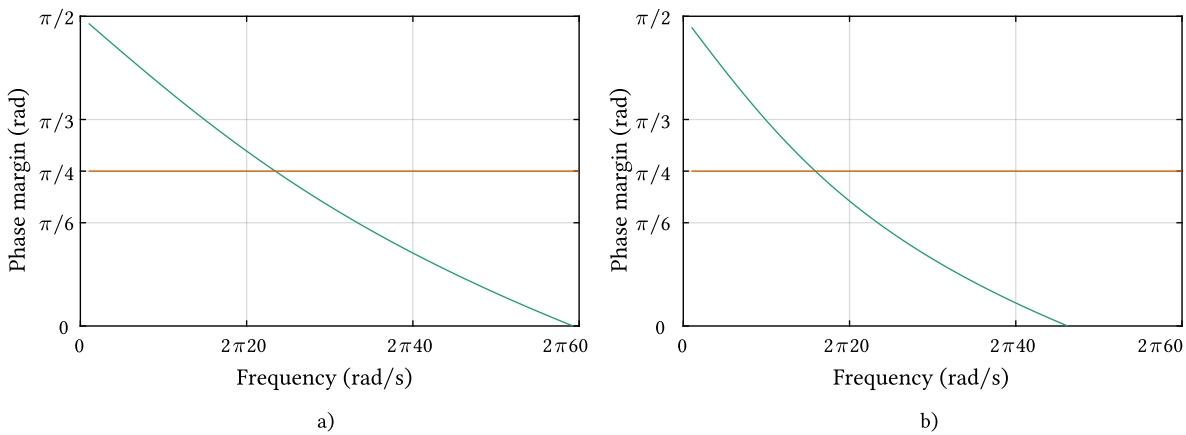


**Fig. 3.21** Evaluation of a phase margin as a function of frequency: a) phase margin for the arm-sum energy control; b) phase margin for the arm-differential energy control.

In case of an energy controller, sampling period is chosen as ten times the control period of the subordinate current control, i.e. $T_{\mathrm{CTRL}} = 1.25\,\mathrm{ms}$. Neglecting the communication delays, the total transport delay of the energy control system is approximately $T_{\mathrm{D}} = 1.87\,\mathrm{ms}$.

To obtain a gain crossover frequency, a phase margin is plotted in **Fig. 3.21** for both arm-sum and arm-delta energy control, accounting for different filter delays. They assume the use of cascaded filter structure (2nd + 4th order / 1st + 3rd order), and reveal that the gain crossover frequency can be selected as $\omega_{\mathrm{gc}} = 2\pi 23\,\mathrm{rad/s}$ for the arm-sum energy control, whereas the gain crossover frequency for the arm-differential energy control equals $\omega_{\mathrm{gc}} = 2\pi 16\,\mathrm{rad/s}$.

Once the gain crossover frequency is determined, one can find a value of the proportional gain, based on the definition from (3.118).

$$\left|G_{\mathrm{ol}}(j\omega_{\mathrm{gc}})\right| = \frac{K_{\mathrm{p}}}{|j\omega_{\mathrm{gc}}|}\left|\frac{\omega_{\mathrm{eq}}}{j\omega_{\mathrm{gc}} + \omega_{\mathrm{eq}}}\right| \underbrace{\left|e^{-j\omega_{\mathrm{gc}}T_{\mathrm{D}}}\right|}_{=1} = 1 \quad \Longrightarrow \quad K_{\mathrm{p}} = \omega_{\mathrm{gc}}\sqrt{1 + \left(\frac{\omega_{\mathrm{gc}}}{\omega_{\mathrm{eq}}}\right)^2} \tag{3.124}$$

Once the proportional gain is determined, the integral gain can be determined, either based on a desired response, or using some of the common tuning techniques, such as symmetrical optimum. To obtain a closed-loop transfer function of the system, the open-loop transfer function should be further simplified.

Since the frequency range of interest is rather low, and the transport delay $T_{\mathrm{D}}$ is in a millisecond range, it can be well approximated as in (3.125). Then the open-loop transfer function can be expressed as in (3.126), where $T_{\mathrm{eq}} = 1/\omega_{\mathrm{eq}}$.

$$e^{-sT_{\mathrm{D}}} \approx \frac{1}{1 + sT_{\mathrm{D}}} \tag{3.125}$$

$$G_{\mathrm{ol}}(s) = \frac{sK_{\mathrm{p}} + K_{\mathrm{i}}}{s^2}\frac{1}{1 + sT_{\mathrm{eq}}}\frac{1}{1 + sT_{\mathrm{D}}} \approx \frac{sK_{\mathrm{p}} + K_{\mathrm{i}}}{s^2}\frac{1}{1 + s\underbrace{(T_{\mathrm{D}} + T_{\mathrm{eq}})}_{T_{\mathrm{tot}}}} = \frac{sK_{\mathrm{p}} + K_{\mathrm{i}}}{s^2}\frac{1}{1 + sT_{\mathrm{tot}}} \tag{3.126}$$

Consequently, closed-loop transfer function of the energy control system takes the following form:

$$G_{\mathrm{cl}}(s) = \frac{G_{\mathrm{ol}}(s)}{1 + G_{\mathrm{ol}}(s)} = \frac{sK_{\mathrm{p}} + K_{\mathrm{i}}}{s^3 T_{\mathrm{tot}} + s^2 + sK_{\mathrm{p}} + K_{\mathrm{i}}} \tag{3.127}$$

As the closed-loop transfer function is of third order, whereas the two controller gains are available for tuning, independent pole placement cannot be achieved. Since the proportional gain has been already determined using the phase margin rule, one way to select the integral gain can be according to the symmetrical optimum rule, which is expressed in (3.128). It is noteworthy that the proportional gain could have been selected based on the symmetrical optimum, in which case it would take the value as in (3.129).

$$K_{\mathrm{i}}^{(\mathrm{SO})} = \frac{K_{\mathrm{p}}^2}{2} \tag{3.128}$$

$$K_{\mathrm{p}}^{(\mathrm{SO})} = \frac{1}{2T_{\mathrm{tot}}} \tag{3.129}$$

Step responses of the transfer function (3.127) for two sets of control gains are shown in **Fig. 3.22**. Selecting the proportional gain according to the phase-margin rule, as in (3.124), combined with the integral gain based on symmetrical optimum, as in (3.128), yields quick, yet oscillatory response with low settling time. If the proportional gain is retained, whereas the integral gain is reduced, the response becomes satisfactory. In comparison with the response when the control gains are chosen according to the symmetrical optimum criterion, the overshoot is similar, yet the dynamic response is faster.

As a result, control gains are adopted according to the **Tab. 3.2**. Similar analysis can be conducted for the arm-differential energy control, where the only difference is the equivalent transfer function of the filter, as described in (3.114)-(3.115).

**Tab. 3.2** Comparison between different energy controller gains for the arm-sum and arm-differential energy control. The gains are calculated assuming the current control bandwidth $\omega_{\mathrm{cc}} = 2\pi 500\,\mathrm{rad/s}$, and the total transport time delay $T_{\mathrm{D}} = 1.87\,\mathrm{ms}$. Assumed filtering bandwidth angular frequencies are given in (3.114)-(3.115)

| | $K_{\mathrm{p}}^{(\mathrm{PM})}$ | $K_{\mathrm{i}}^{(\mathrm{PM})}$ | $K_{\mathrm{p}}^{(\mathrm{SO})}$ | $K_{\mathrm{p}}^{(\mathrm{SO})}$ | $K_{\mathrm{p}}$ selected | $K_{\mathrm{i}}$ selected |
|---|---|---|---|---|---|---|
| $W_{\Sigma}$ control | 170.11 | 14469 | 81 | 3281 | 170.11 | 5787 |
| $W_{\Delta}$ control | 125.25 | 7843 | 53.96 | 1455 | 125.25 | 3137 |

Values of the control gains for both arm-sum and arm-differential energy control are provided in the **Tab. 3.2**. Both phase-margin and symmetrical optimum-based gains are provided, as well as the finally selected gains. It can be observed that the gains in the arm-differential control are generally lower, which is a consequence of the lower achievable bandwidth compared to the arm-sum energy control. This difference is also observed in the step responses provided in **Fig. 3.22**.

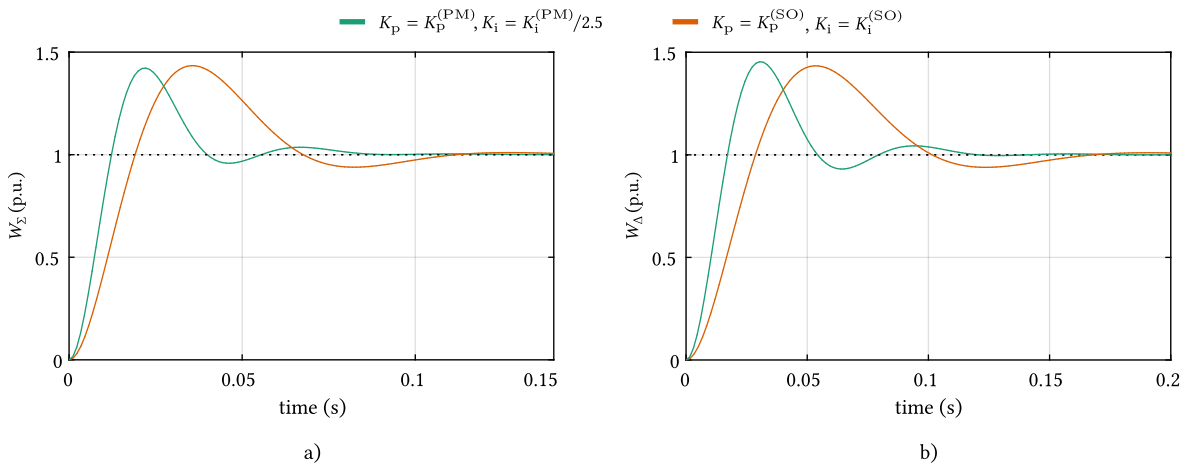


**Fig. 3.22** Step response of the energy control system, described by (3.127) for two sets of control gains: a) arm-sum energy step response; b) arm-differential energy step response.

## 3.7 Evaluation of the Proposed Control Methods

### 3.7.1 Arm-sum energy control evaluation

In the previous sections, the arm-sum energy control method was presented for two operating modes of the MMC: the inverter and the rectifier mode. In the inverter mode of operation, the principal objective of the MMC is to serve the ac grid, delivering required active and reactive power. In the rectifier mode, the MMC acts as a medium/high voltage/current source converter, ensuring that the reference dc voltage/current is being fully respected.

**Tab. 3.3** Physical and control parameters of the simulated MMC converter. Simulated converter represents a genuine replica of the physical MMC prototype developed in the laboratory.

| Parameter | Label | Value |
|---|---|---|
| Line-line voltage | $U_n$ | 3.3 kV |
| DC terminal voltage | $U_{dc}$ | 5 kV |
| Rated power | $S_n$ | 250 kVA |
| Grid frequency | $f_g$ | 50 Hz |
| No. of SMs per arm | $N$ | 8 |
| SM capacitance (tolerance ±5%) | $C_{SM}$ | 2.25 mF |
| Arm inductance (tolerance ±10%) | $L_{arm}$ | 2.5 mH |
| Arm resistance | $R_{arm}$ | 400 mΩ |
| IGBT switching frequency | $f_{SW}$ | 1 kHz |
| Inner-loop control period | $T_{CTRL}^{(i)}$ | 125 µs |
| Outer-loop control period | $T_{CTRL}^{(o)}$ | 1 ms |

From the energy control perspective, the difference between the two modes of operation is that for

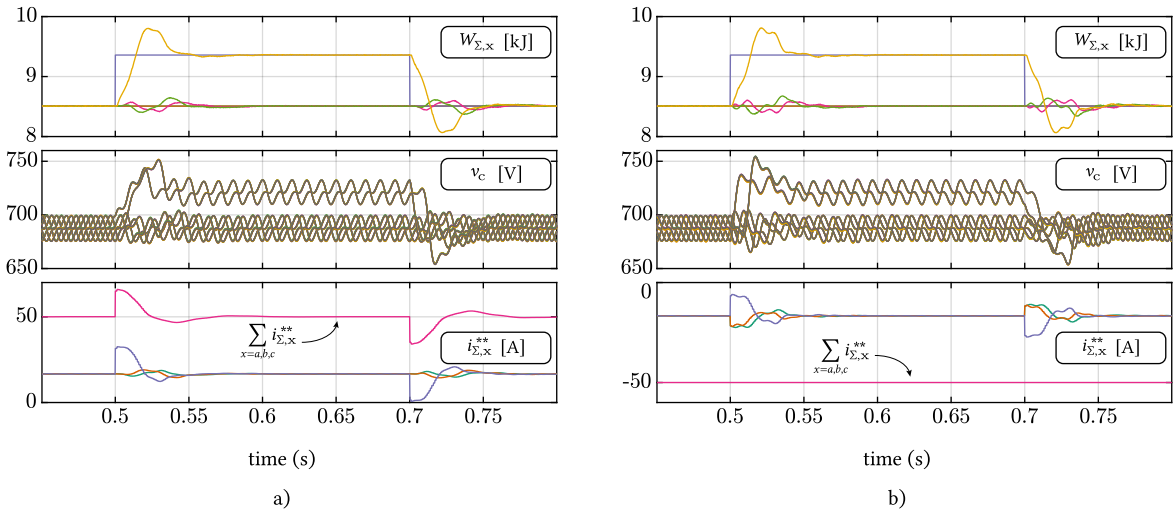


**Fig. 3.23** Step response of the arm-sum energy control system, for the two modes of operation: a) inverter mode of operation; b) rectifier mode of operation. The top figure shows the arm-sum energy reference and filtered arm-sum energies in three phases. The middle figure shows the SM voltages, whereas the bottom graph shows the arm-common currents.

the inverter mode, the MMC can freely draw current from the dc terminals, while respecting the active and reactive ac power references, whereas in the rectifier mode, the dc terminal current must not be altered for the reasons of the arm-sum energy control.

To evaluate the behaviour of the presented control method for both modes of operation, a high-fidelity model of the MMC converter, with parameters presented in **Tab. 3.3**, is created in PLECS. The model accounts for component tolerances, control algorithms are executed in finite time steps, and all effects relevant to the analyses are captured by the simulations. Energy controllers are implemented in discrete form using the forward-Euler discretization method, with the controller gains set according to **Tab. 3.2**. The PSC modulation was used to generate the switching signals of the individual SMs.

**Fig. 3.23** shows the behaviour of the arm-sum energies during the reference step change. **Fig. 3.23.a** illustrates the behaviour during the inverter mode of operation, whereas the energy step response for the rectifier mode of operation is shown in **Fig. 3.23.b**. The figure shows that the energy references in both modes of operation are reached after approximately 40 ms, which corresponds to the expected settling time from the theoretical analyses. In addition, it can be seen that the energy control in the inverter mode of operation relies on drawing the current from the dc terminals, whereas in the case of rectifier mode of operation, the dc current reference remains constant.

In practice, the current references from the energy controllers should be limited, so as not to create an excessive current stress on the semiconductors. To evaluate the performance of the energy controller under the limitations, the arm-sum current references, issued for the purpose of energy control, are limited to 10 A per phase, which represents around 60% of the rated dc current.

Behaviour of the arm-sum energy control under current reference limitation is shown in **Fig. 3.24**. It can be observed that while the arm-sum current references remain within predefined limits, settling time is slightly prolonged. Nevertheless, this has no major influence on the overall performance.

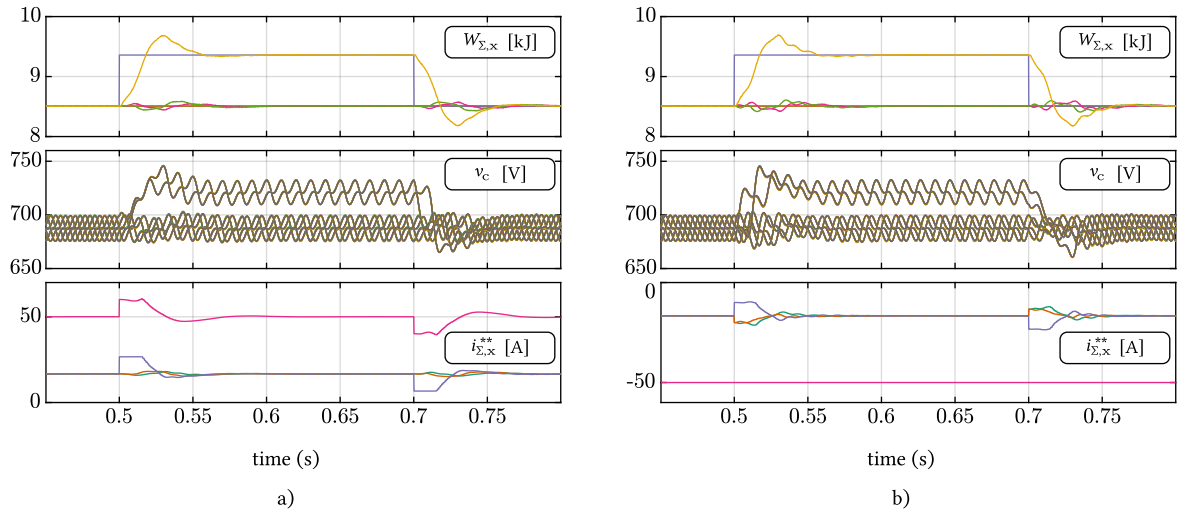


**Fig. 3.24** Step response of the arm-sum energy control system, with limited current references: a) inverter mode of operation; b) rectifier mode of operation.

### 3.7.2 Arm-differential energy control evaluation

Throughout this chapter, two methods for the arm-delta energy control were presented. Both methods are based on injection of the fundamental frequency components into the arm-common currents, while they differ in terms of implementation and performance.

The same simulation model in PLECS was used to confirm the performance of the presented control methods, and for their mutual comparison. **Fig. 3.25** shows the behavior of the arm-delta energy control structure for the step change in the delta energy reference. Both methods ensure short settling times, within approximately 60 ms, corresponding to the theoretical analyses presented in this chapter.

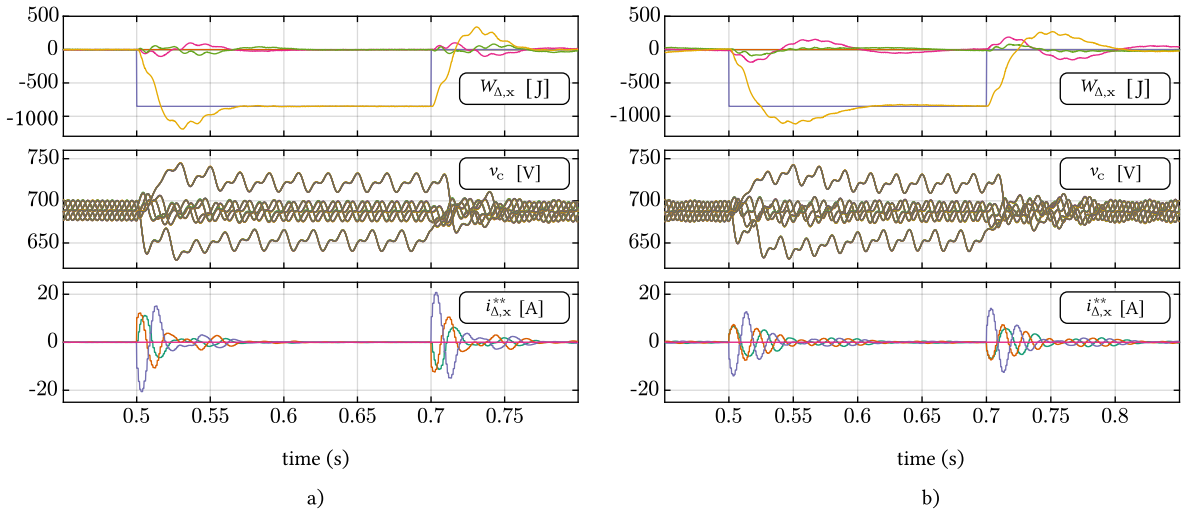


**Fig. 3.25** Step response of the arm-differential energy control system, for the two proposed methods: a) *Method I*; b) *Method II*. The top figure shows the arm-differential energy reference and filtered arm-differential energies in the three phases. The middle figure shows the SM voltages, whereas the bottom graph shows the arm-common currents.

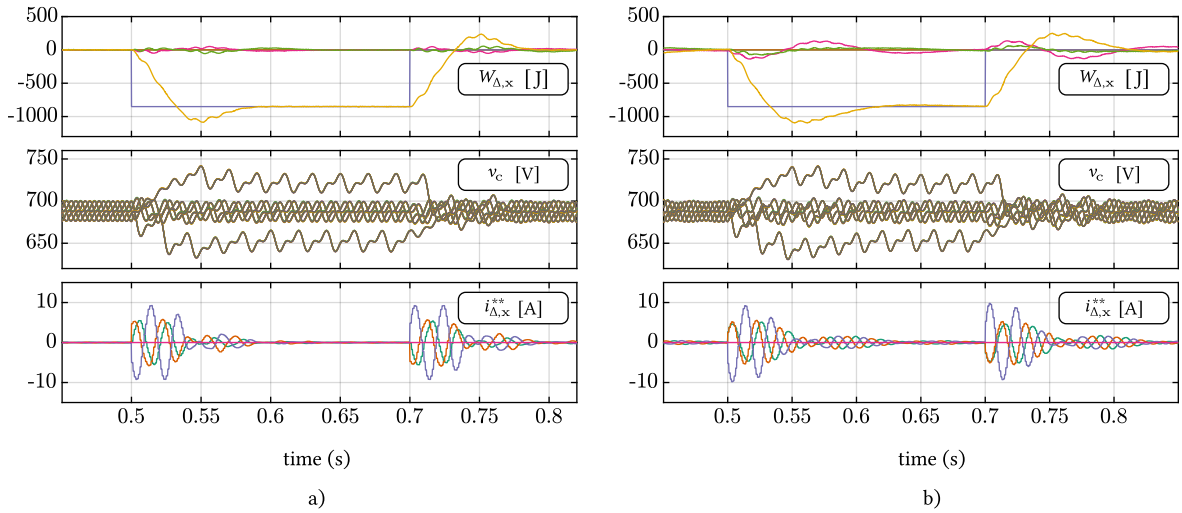


**Fig. 3.26** Step response of the arm-differential energy control system, for the two proposed methods, with the arm-common current limitation: a) *Method I*; b) *Method II*. The top figure shows the arm-differential energy reference and filtered arm-differential energies in the three phases. The middle figure shows the SM voltages, whereas the bottom graph shows the arm-common currents, with amplitudes limited to 10 A.

**Fig. 3.25.a** figure shows the fundamental frequency arm-common current references, generated by the *Method I* of the arm-delta energy control, whereas the current references generated using *Method II* are shown in **Fig. 3.25.b**. It can be observed that the *Method I* yields in general current references with the higher magnitudes, compared to *Method II*. On the other hand, the settling time for the *Method I* is slightly shorter, due to the fact that the power references are fully preserved with this method.

What can also be observed for the two methods is that the sum of the current references does not contain fundamental-frequency components, which was the objective of the current reference modification.

As in the case of the arm-sum energy control, arm-differential energy references can also be limited, in order to reduce the current stress on the semiconductors. To evaluate performance of the control methods under reference limitations, the simulations are repeated, where the maximum current reference was limited to 10 A. The results of a step response to the arm-differential energy reference are shown in **Fig. 3.26** for both *Method I* and *Method II*. While the settling time is slightly prolonged, both methods ensure energy reference tracking without interference with the dc terminal current.

### 3.7.3 Direct arm energy control

The arm-sum and the arm-differential energy control are two decoupled mechanisms that can ensure an arbitrary control of the arms energy content. While the previous results demonstrate their validity, the upcoming results aim to show their mutual action, while controlling the arm energies to arbitrary levels. In addition, it is beneficial to observe their influence on the other internal and terminal variables.

To start with, the converter was simulated for the inverter mode of operation. Ideal dc voltage source is assumed at its dc terminals, whereas a symmetrical ac grid voltage was present at its ac terminals.

The converter was operating at nominal power with a unity power factor until the time $t = 0.85$ s, when the active power flow was reversed. At $t = 0.5$ s energy references in the positive arm of phase b, and negative arm of phase c, were increased by 10%, and returned to its nominal value at $t = 0.7$ s. As it can be seen on the plots, the energies settled within approximately 60 ms, with the change only in the dc and circulating currents. Ac terminal currents were not affected by the energy control actions, which was a prerequisite for the inverter mode of operation.

After power reversal at $t = 0.85$ s, arm energy references were changed again, now in a slightly different manner. Namely, the energy reference in the positive arm of the b phase was increased by 10%, whereas the reference of the negative arm in c phase was decreased by the same amount. Consequently, the total energy requirements of the converter remained constant, and the control mechanisms needed to ensure the energy redistribution within the converter. From **Fig. 3.27**, it can be seen that the settling times are similar as before, whereas the dc and ac terminal currents are not at all influenced. Only the internal circulating currents ensure the energy redistribution within the converter.

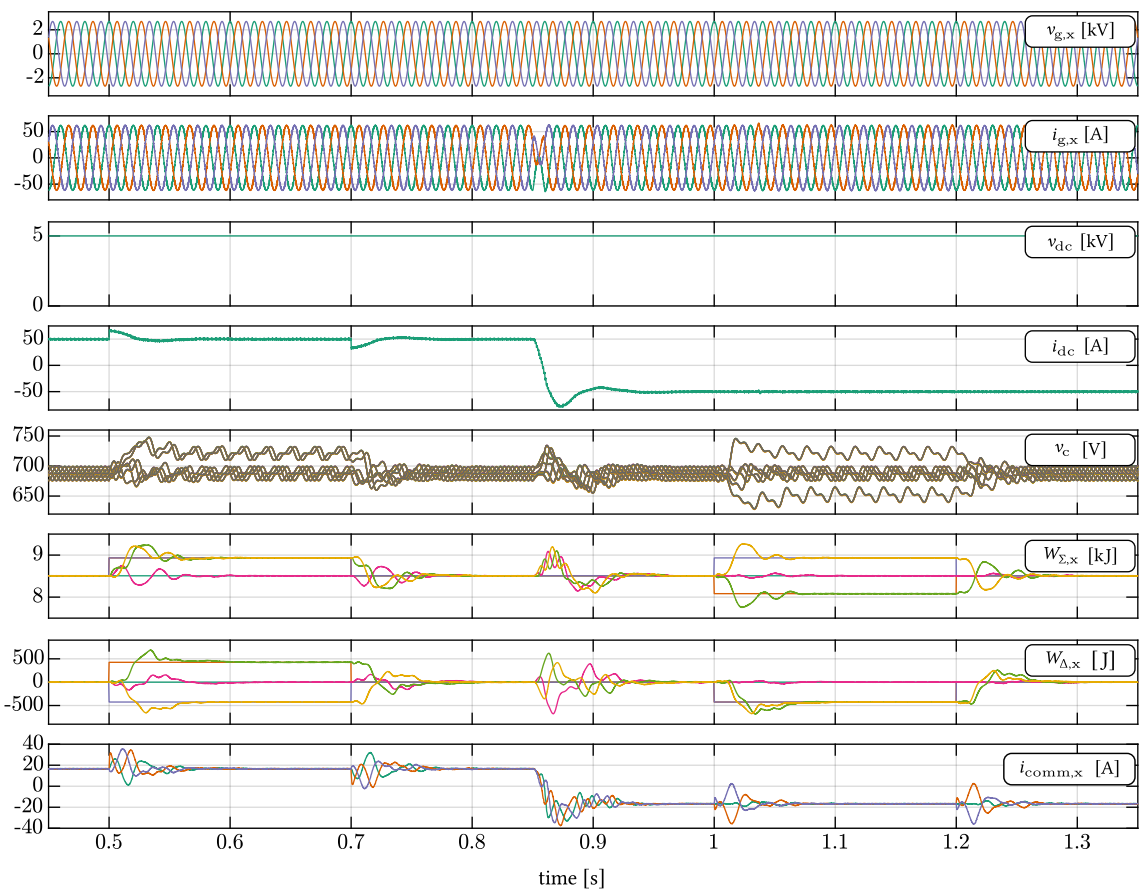


**Fig. 3.27** Simulation results showing the performance of the energy controllers in the inverter mode of operation, with arbitrary energy reference changes and the power reversal. Top two plots show the grid voltages and currents, while the following two show the dc terminal voltage and current. Voltages of the individual SMs are shown in the middle, followed by the arm-sum and arm-differential energy references and measured values. The final plot shows the arm-common currents in all three phase legs.

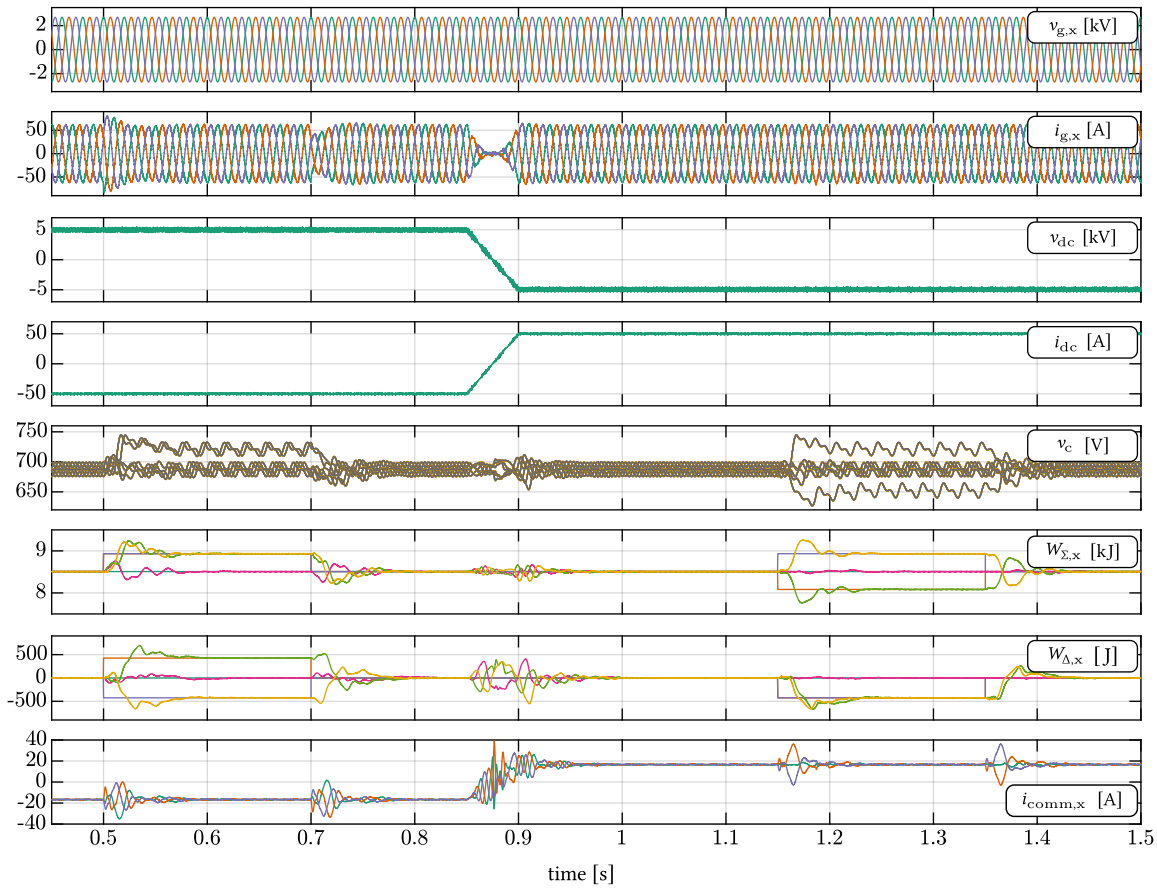


**Fig. 3.28** Simulation results showing the performance of the energy controllers in the rectifier mode of operation, with arbitrary energy reference changes and the dc terminal voltage reversal. A passive load is connected between the dc terminals.

Rectifier mode of operation assumes that the converter is connected to a stiff ac grid, and provides a dc terminal voltage/current according to the reference. In the analyzed case, the MMC acted as a dc voltage source, whereas the dc terminal current was influenced by the passive/active load connected to the dc terminals. Compared to the inverter mode of operation, the rectifier mode is more restrictive, as the dc terminal currents must not be influenced by the internal energy control actions, nor is the asymmetry in the grid currents permitted.

The first evaluation was performed assuming a passive load connected to the dc terminals, with the power consumption equivalent to the rated converter power. Reactive grid power was assumed to be equal to zero. Results of the simulations are shown in **Fig. 3.28**.

Similarly to the previous case, the energy references are increased in two arms, which resulted in the arm-sum and arm-differential energy references change. Settling time for the energy control is around 60 ms, which corresponds to the results achieved during the inverter mode of operation. The dc terminal current was not influenced, which was the ultimate objective of the proposed control methods. On the other hand, ac terminal currents exhibit a small change, which is a consequence of the temporarily increased active power reference. Nevertheless, the ac terminal current remain symmetrical.

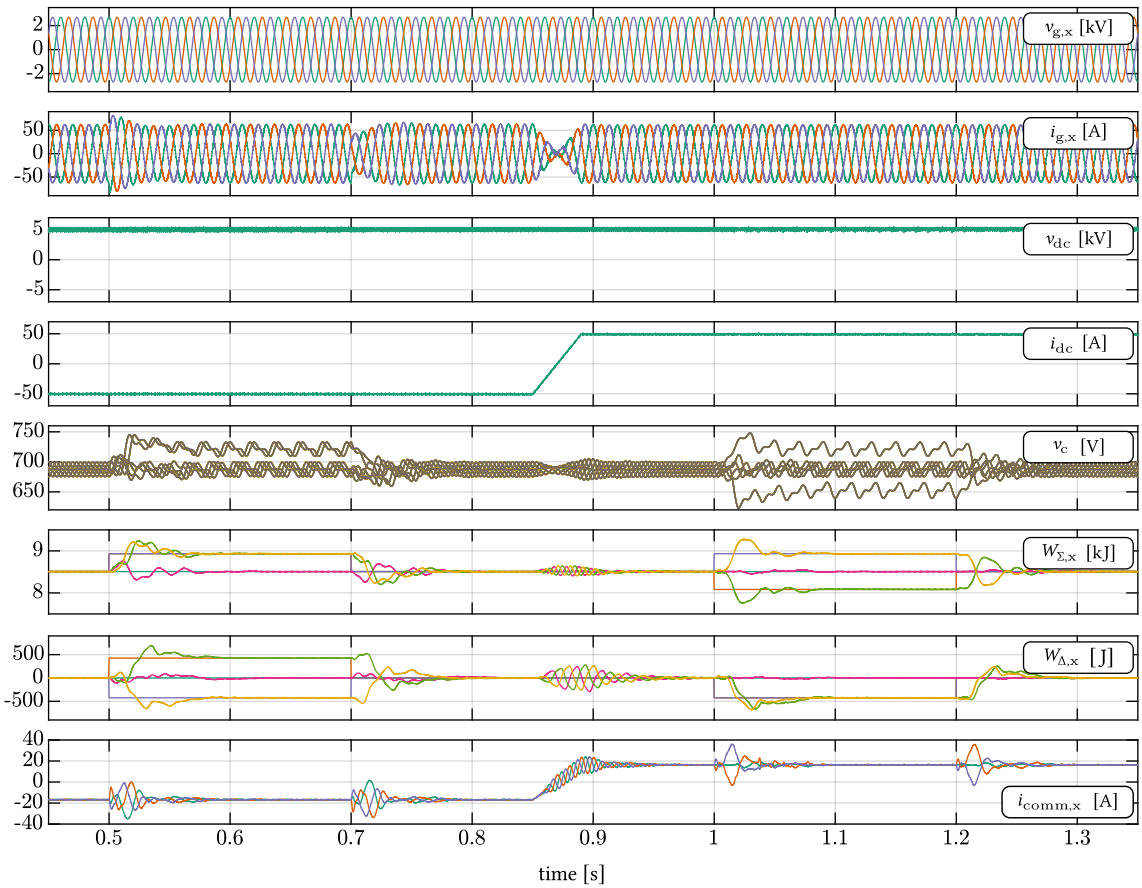


**Fig. 3.29** Simulation results showing the performance of the energy controllers in the rectifier mode of operation, with arbitrary energy reference changes and the dc power reversal. An active load is connected between the dc terminals.

At $t = 0.85$ second, the dc terminal voltage is reversed, followed by energy references step changes at $t = 1.15$ s. Again, energy references are changed in such a way that the total converter energy remains constant. Consequently, neither dc nor ac terminal currents are influenced during the transition.

The same scenarios are repeated assuming an active load connected to the dc terminals of the converter, in order to test the energy control capabilities during the power reversal in the rectifier mode of operation.

Results of the simulations are plotted in **Fig. 3.29**, for the same scenarios as in the previous two figures. Again, the results are almost identical, and energy control methods succeeds in ensuring tracking the arbitrary energy references, while conforming with the constraints regarding the interaction with the terminal currents.

It is noteworthy that in all the three previous simulations, *Method I* is used as the arm-differential control method, whereas the arm-sum control method is dependent upon the converter operating mode.

### 3.7.4 Effect of the current modification on the reference space vector

To observe the effects of the current modification methods applied in the arm-differential and arm-sum energy control, space vector of the original current reference is plotted in $\alpha\beta 0$ reference frame, along with the space vectors of the modified references.

**Fig. 3.30.a** shows the space vector of the original current reference, together with the space vectors of the modified current references, using the two presented methods. It can be concluded that both methods ensure that the zero component of the original reference is not present, which ensures that the ac circulating currents do not appear at the dc terminals. The other conclusion is that the $\alpha\beta$ components of the current reference are also modified in case of *Method I*, whereas those components are preserved in case of *Method II*. The difference comes from the fact that *Method I* ensures that the power references are preserved, resulting in the $\alpha\beta$ components modification, whereas *Method II* ensures the lowest deviation from the original current references, under the zero-sum constraint, which is achieved by the zero component subtraction.

**Fig. 3.30.b** shows the results of the reference current modification in case of arm-sum energy control. Since this method corresponds to the *Method II* in the arm-differential energy control, the conclusions are similar. The lowest deviation from the original current vector is achieved when only the zero component is reduced.

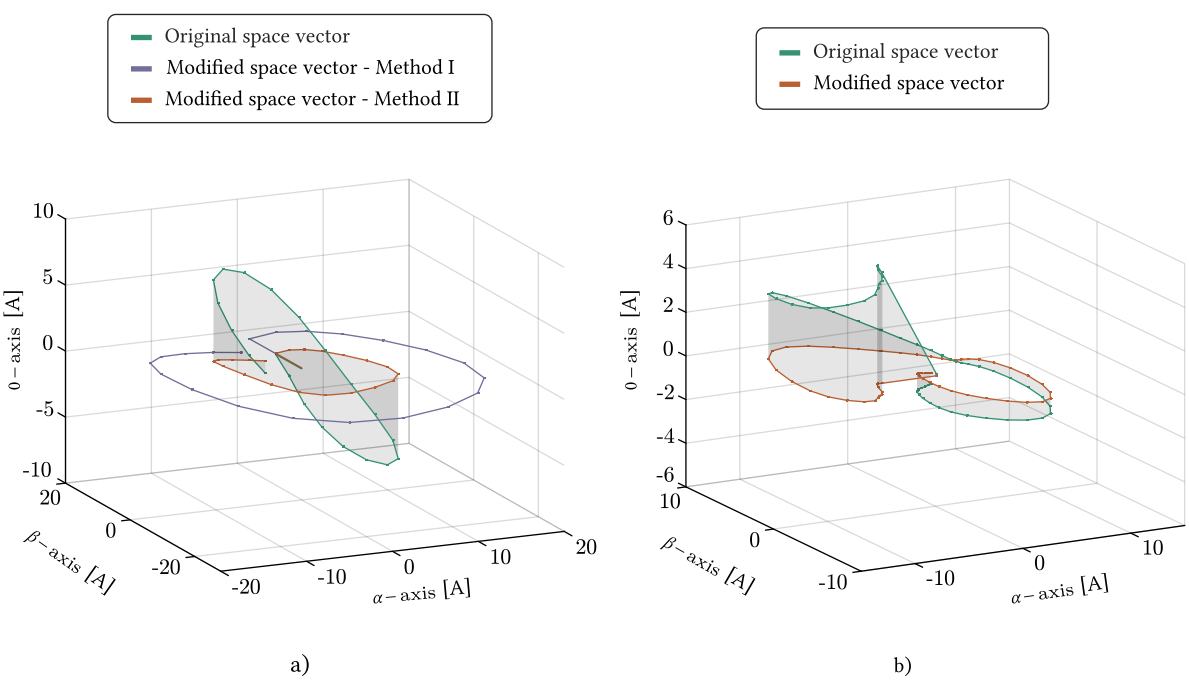


**Fig. 3.30** Space vectors of the original and modified current references: a) arm-differential energy control; b) arm-sum energy control.

## 3.8 Summary

The problem of energy control was introduced in this chapter, and control mechanisms were identified. Control structure was presented, along with the relevant parts of the system. Two control actions, that ensure an arbitrary arm energy control, are identified and analyzed.

Arm-differential energy control is achieved by introduction of a fundamental frequency current components in the arm-common currents. To prevent these current components from appearing at the dc terminals of the converter, two current modification methods are presented within this chapter. Theoretical foundation of the two methods was presented, as well as the way of implementation inside the control structure. Both methods are characterized by an intuitive approach and a simple implementation. Evaluation results show that both methods manage to achieve the objectives, and confirm theoretical considerations presented in the chapter.

Arm-sum energy control was presented as a second mechanism that, together with the arm-differential control, ensures an arbitrary control of the arm energies. Two mechanisms for this control were presented, applicable for the inverter and rectifier modes of operation. Finally, both methods are evaluated independently, as well as in conjunction with the arm-differential energy control.

Apart from their simple implementation, and good performance, the presented control methods are also applicable under faulty conditions, such as grid asymmetries and a SM failure, which is the subject of the following chapter. Moreover, the conclusions derived from this chapter can be easily adapted for the energy control of the other converters from the MMC family, such as multiphase MMC, and the M3C. Energy control of the M3C, applying the principles presented within this chapter, will be analysed in **Chapter 5**.

# 4
# Arm Energy Control Under Faulty Conditions

*The energy content within the MMC arms should correspond to the energy references, in order to enable proper generation of the arm voltages. To meet the objective, terminal, as well as internal currents must be controlled in a way that ensures that the arm energies correspond to their references. Energy content within each arm should be controlled independently, thus allowing the greatest possible flexibility of the converter operation. In addition, these control actions should not alter the terminal variables. Finally, the arm energy control method should be intuitive and simple to implement, while providing satisfactory results under different operating conditions. In this chapter, energy control mechanisms will be identified, and different methods for their realization will be proposed. Proposed control methods will be evaluated under faulty conditions, such as grid unbalance and a SM failure. Finally, presented methods will be compared mutually, as well as with other control methods.*

## 4.1 Motivation

One of the merits of the MMC is its high availability achieved through redundancy. As the events in the grids interconnected by the MMC can be various, the MMC should be capable of operating under faulty conditions. Two types of faulty conditions will be analyzed within this chapter: unbalanced grid conditions and a failure of a SM within an arm.

Researchers have been already dealing with the topic of energy control in the MMC under unbalanced grid conditions. Authors of [122] use a similar approach to the conventional horizontal and vertical energy balancing in $\alpha\beta$ domain. Regarding the horizontal energy control, they provide an improvement over the existing methods in terms of feeding forward the products of interaction of the grid voltages and currents of different sequences. The authors, however, provide a solution only for the inverter mode of operation. In terms of delta energy control, the authors use circulating currents aligned with the grid phase voltages, together with the zero-sequence subtraction. This approach corresponds to the approach offered by *Method II*, where the only aim was to control the currents such that they do not appear at the dc terminals, without considering the influence of such an approach on the active power references. In addition, they assume equal voltage magnitudes in the three phases, which yields incorrect current references under unbalanced grid conditions. Moreover, while they use per unit values of the phase voltages, they do not show how such values are obtained under unbalanced grid conditions.

Authors in [123] identify relationships between voltages and currents, in terms of the arm-sum, arm-differential and the total power components. They decompose all the terminal and internal variables into the positive and negative sequence components, and analyze their mutual interactions. The authors propose an independent use of positive-sequence voltage balancing with the negative

sequence circulating currents in cases when the positive sequence voltage is dominant, and vice-versa in cases when the negative sequence voltages are dominant. They identify a problem with the delta energy control in cases when the positive and negative sequence voltages have similar values, where the coupling happens and can render the control unstable. In such a case, they inject a zero-sequence second-harmonic common-mode voltage, as well as the second harmonic circulating currents. Besides the need to inject such components, the problem with the proposed approach is that it uses exclusively one system of voltages (positive or negative), and only one system of currents. Thus it does not fully benefit from the available grid voltages, resulting in a higher arm currents for the same arm-differential power requirements.

Researchers from [124] propose an improvement in the transient response of the energy control under unbalanced grid conditions. The approach is similar to the approach used by [123] in terms of horizontal (arm-sum) energy control, and is based on extraction of the positive and negative voltage and current components. This has an equivalent effect as the per-phase feed-forward power terms in the control proposed in this thesis. The arm-differential energy control is based on introduction of the circulating current components at the positive and negative sequence, that would interact with the grid voltage components. As there is a degree of freedom left, it has been used such that the positive sequence circulating currents are aligned with the positive sequence voltage. While it helps to make the system deterministic, and reduce the positive-sequence current amplitude, this doesn't ensure that the overall current amplitudes are minimal.

The control methods proposed in the previous chapter are evaluated for being used under faulty conditions. The control methods applied under such conditions should satisfy the following requirements:

- Proposed energy control methods should remain valid under unbalanced grid conditions, without significant changes in the control implementation.
- The internal currents, generated for the purpose of the energy control, should still not disturb the terminal currents.
- Magnitudes of such internal currents should be kept as low as possible.
- In case of a failure of a SM, the energy control should ensure that the converter continues its operation without affecting the terminal variables.

Therefore, to investigate whether and to what extent the two presented control methods are applicable under faulty conditions, theoretical studies are conducted. Additionally, theoretical conclusions are confirmed by high-fidelity simulations.

## 4.2 Energy control under grid unbalances

Proposed control methods were derived assuming a symmetrical system of grid voltages. While this is the case under balanced grid conditions, grid voltages are not symmetrical under grid faults.

### 4.2.1 Symmetrical components

Asymmetrical voltages in the three-phase system under grid faults can be decomposed into three symmetrical systems: a direct (positive), inverse (negative) and zero-sequence system. These are in

the literature often referred to as symmetrical components.

The direct sequence of the voltages is the only sequence present under balanced grid conditions, therefore, it is the desired sequence of three-phase voltages and currents. Within this chapter, it will be denoted with the superscript "+", and it is defined as:

$$u_a^+ = \hat{u}^+ \sin(\omega t) \tag{4.1}$$
$$u_b^+ = \hat{u}^+ \sin(\omega t - 2\pi/3) \tag{4.2}$$
$$u_c^+ = \hat{u}^+ \sin(\omega t + 2\pi/3) \tag{4.3}$$

In contrast, voltages of the inverse sequence are defined as in (4.4)-(4.6), and the equivalent space-vector of such a three-phase system rotates in the opposite direction with respect to the direct sequence, hence the name.

$$u_a^- = \hat{u}^- \sin(\omega t + \phi^-) \tag{4.4}$$
$$u_b^- = \hat{u}^- \sin(\omega t + \phi^- + 2\pi/3) \tag{4.5}$$
$$u_c^- = \hat{u}^- \sin(\omega t + \phi^- - 2\pi/3) \tag{4.6}$$

Zero sequence components represent those components that have the same magnitude and phase in all three phases. Therefore, the zero sequence component can be defined as:

$$u_a^0 = u_b^0 = u_c^0 = \hat{u}^0 \sin\left(\omega t + \phi^0\right) \tag{4.7}$$

Visualization of the grid voltages in case of a generic grid unbalance is provided in **Fig. 4.1**. One can observe that the phase voltages are asymmetrical in general case, but in the three systems, components in phases are mutually symmetrical.

This fact provides an opportunity for extension of the energy control methods from symmetrical to asymmetrical grid conditions. The following sections will provide an in-depth analysis of the application of the presented control methods to unbalanced grid conditions.

As both the arm-sum and the arm-differential energy control are dependent upon grid conditions, both methods deserve a thorough analysis. Nevertheless, as the arm-differential energy control is dependent only on the grid voltages, the analysis will start by analysing this control scheme.

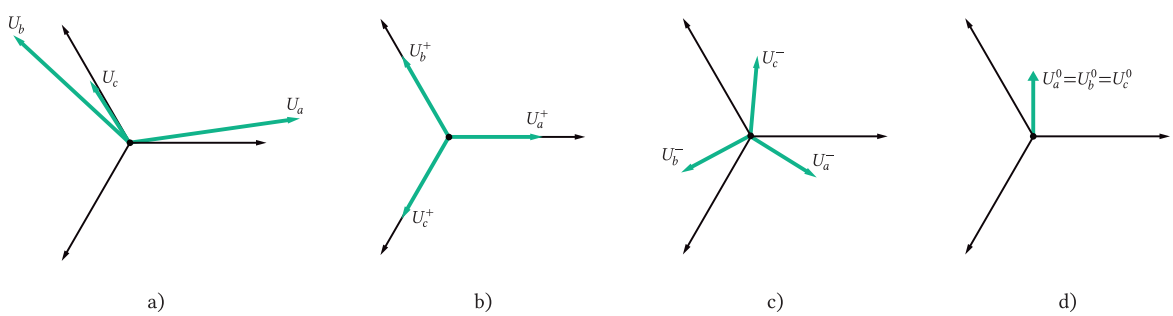


**Fig. 4.1** Phasors of phase voltages under a grid unbalance: a) total phase voltage phasors in a general asymmetric case; b) direct-sequence components; c) inverse-sequence components; d) zero-sequence components.

### 4.2.2 Arm-differential energy control

Two control schemes for the arm-differential energy control have been presented in the previous chapter. Given the fact than only symmetrical voltage components were considered during their derivation, it is expected that the performance of the methods change during the unbalanced grid conditions.

The following paragraphs aim to explore the influence that the unbalanced grid conditions have on the performance of the arm-differential energy control algorithms.

#### 4.2.2.1 Method I

This method was developed to generate the arm-common current references that satisfy the following two conditions:

- they produce the exact arm-differential power components as requested by the arm-differential energy controllers
- their sum equals zero, thus making them invisible at the converter dc terminals.

Current references that satisfy these conditions were presented in (3.80)-(3.82), and they are repeated here:

$$i^{**}_{\Delta,\mathrm{a}}(t) = \hat{i}^{*}_{\Delta,\mathrm{a}} A + \frac{1}{3}\left(\hat{i}^{*}_{\Delta,\mathrm{b}} - \hat{i}^{*}_{\Delta,\mathrm{c}}\right)\left(C - B\right) \tag{4.8}$$

$$i^{**}_{\Delta,\mathrm{b}}(t) = \hat{i}^{*}_{\Delta,\mathrm{b}} B + \frac{1}{3}\left(\hat{i}^{*}_{\Delta,\mathrm{c}} - \hat{i}^{*}_{\Delta,\mathrm{a}}\right)\left(A - C\right) \tag{4.9}$$

$$i^{**}_{\Delta,\mathrm{c}}(t) = \hat{i}^{*}_{\Delta,\mathrm{a}} C + \frac{1}{3}\left(\hat{i}^{*}_{\Delta,\mathrm{a}} - \hat{i}^{*}_{\Delta,\mathrm{b}}\right)\left(B - A\right) \tag{4.10}$$

While there is a possibility to follow a similar procedure as in the previous chapter, and obtain current references valid under unbalanced grid conditions, the analytical derivation of this method based on the approach used for balanced conditions would be extremely demanding. Therefore, an alternative approach is adopted here: the grid voltages will be observed through their symmetrical components, and arm-differential energy balancing will be analysed for each component independently, followed by their superposition at the end of the process.

**Direct-sequence components**

During this analysis, it can be assumed that only the direct sequence voltage components exist in the grid voltages. According to the definition of the symmetrical components provided in (4.1)-(4.3), variables A, B and C take the following form:

$$A^{+} = \frac{u_a^{+}}{\hat{u}^{+}} = \sin(\omega t) \tag{4.11}$$

$$B^{+} = \frac{u_b^{+}}{\hat{u}^{+}} = \sin(\omega t - 2\pi/3) \tag{4.12}$$

$$C^{+} = \frac{u_c^{+}}{\hat{u}^{+}} = \sin(\omega t + 2\pi/3) \tag{4.13}$$

Arm-differential power references requested by energy controllers in particular phases should be realized by all available voltage sequences, i.e. direct, inverse and zero, to maximally utilize the available components and thus minimize the currents. Therefore, the arm-differential power realized by the direct-sequence voltage should correspond to the fraction of the total arm-differential power reference, proportional to the ratio of the positive sequence voltage with the total voltage:

$$P_{\Delta,\mathrm{x}}^{*(+)} = P_{\Delta,\mathrm{x}}^{*} \frac{\hat{u}^{+}}{\hat{u}_{\mathrm{x}}} \tag{4.14}$$

Direct-sequence arm-common current magnitudes are obtained by dividing the respective power references by the direct-sequence voltage magnitude:

$$\hat{i}_{\Delta,\mathrm{a}}^{*(+)} = \frac{P_{\Delta,\mathrm{a}}^{*(+)}}{\hat{u}^{+}} = \frac{P_{\Delta,\mathrm{a}}^{*} \frac{\hat{u}^{+}}{\hat{u}_{\mathrm{a}}}}{\hat{u}^{+}} = \frac{P_{\Delta,\mathrm{a}}^{*}}{\hat{u}_{\mathrm{a}}} = \hat{i}_{\Delta,\mathrm{a}}^{*} \tag{4.15}$$

$$\hat{i}_{\Delta,\mathrm{b}}^{*(+)} = \frac{P_{\Delta,\mathrm{b}}^{*}}{\hat{u}_{\mathrm{b}}} = \hat{i}_{\Delta,\mathrm{b}}^{*} \tag{4.16}$$

$$\hat{i}_{\Delta,\mathrm{c}}^{*(+)} = \frac{P_{\Delta,\mathrm{c}}^{*}}{\hat{u}_{\mathrm{c}}} = \hat{i}_{\Delta,\mathrm{c}}^{*} \tag{4.17}$$

Note that in previous equations voltages $\hat{u}_{\mathrm{a}}$, $\hat{u}_{\mathrm{b}}$, and $\hat{u}_{\mathrm{c}}$ represent magnitudes of the voltages in individual phases. Further, direct-sequence arm-common current references are obtained by multiplying current magnitudes with per unit values of the direct-sequence voltages:

$$i_{\Delta,\mathrm{a}}^{*(+)} = \hat{i}_{\Delta,\mathrm{a}}^{*} A^{+} = \hat{i}_{\Delta,\mathrm{a}}^{*} \sin(\omega t) \tag{4.18}$$

$$i_{\Delta,\mathrm{b}}^{*(+)} = \hat{i}_{\Delta,\mathrm{b}}^{*} B^{+} = \hat{i}_{\Delta,\mathrm{b}}^{*} \sin(\omega t - 2\pi/3) \tag{4.19}$$

$$i_{\Delta,\mathrm{c}}^{*(+)} = \hat{i}_{\Delta,\mathrm{c}}^{*} C^{+} = \hat{i}_{\Delta,\mathrm{c}}^{*} \sin(\omega t + 2\pi/3) \tag{4.20}$$

As the magnitudes of the three arm-common current references have different values (c.f. (4.15)-(4.17)), they should be modified in order to satisfy the two aforementioned criteria. As the direct-sequence voltage components are present during the balanced grid conditions, the same conclusions apply as for the balanced grid conditions. Therefore, modified current references are obtained as:

$$i_{\Delta,\mathrm{a}}^{**(+)} = \hat{i}_{\Delta,\mathrm{a}}^{*} A^{+} + \frac{1}{3}\left(\hat{i}_{\Delta,\mathrm{b}}^{*} - \hat{i}_{\Delta,\mathrm{c}}^{*}\right) \underbrace{\left(C^{+} - B^{+}\right)}_{A_{\mathrm{q}}^{+}} \tag{4.21}$$

$$i_{\Delta,\mathrm{b}}^{**(+)} = \hat{i}_{\Delta,\mathrm{b}}^{*} B^{+} + \frac{1}{3}\left(\hat{i}_{\Delta,\mathrm{c}}^{*} - \hat{i}_{\Delta,\mathrm{a}}^{*}\right) \underbrace{\left(A^{+} - C^{+}\right)}_{B_{\mathrm{q}}^{+}} \tag{4.22}$$

$$i_{\Delta,\mathrm{c}}^{**(+)} = \hat{i}_{\Delta,\mathrm{c}}^{*} C^{+} + \frac{1}{3}\left(\hat{i}_{\Delta,\mathrm{a}}^{*} - \hat{i}_{\Delta,\mathrm{b}}^{*}\right) \underbrace{\left(B^{+} - A^{+}\right)}_{C_{\mathrm{q}}^{+}} \tag{4.23}$$

The modification of the direct-sequence arm-common current components is identical to the modification performed under balanced grid conditions. In fact, the performed modification results in introduction of an additional current component in each phase, which is in quadrature with the original current component (hence the subscript "q"). In such a way, no fundamental-frequency component appears in the dc link.

**Inverse-sequence components**

Following the same procedure as for the direct-sequence voltages, relative inverse-sequence voltages can be defined as:

$$A^{-} = \frac{u_a^{-}}{\hat{u}^{-}} = \sin(\omega t) \tag{4.24}$$

$$B^{-} = \frac{u_b^{-}}{\hat{u}^{-}} = \sin(\omega t + 2\pi/3) \tag{4.25}$$

$$C^{-} = \frac{u_c^{-}}{\hat{u}^{-}} = \sin(\omega t - 2\pi/3) \tag{4.26}$$

Similarly to the case of direct-sequence components, the arm-differential power generated by the inverse-sequence components should be a fraction of the arm-differential power reference, proportional to the ratio of the inverse-sequence and the total phase voltage magnitude:

$$P_{\Delta,\mathrm{x}}^{*(-)} = P_{\Delta,\mathrm{x}}^{*} \frac{\hat{u}^{-}}{\hat{u}_{\mathrm{x}}} \tag{4.27}$$

Inverse-sequence arm-common current magnitudes are obtained by dividing the respective power references by the inverse-sequence voltage magnitude:

$$\hat{i}_{\Delta,\mathrm{a}}^{*(-)} = \frac{P_{\Delta,\mathrm{a}}^{*(-)}}{\hat{u}^{-}} = \frac{P_{\Delta,\mathrm{a}}^{*} \frac{\hat{u}^{-}}{\hat{u}_{\mathrm{a}}}}{\hat{u}^{-}} = \frac{P_{\Delta,\mathrm{a}}^{*}}{\hat{u}_{\mathrm{a}}} = \hat{i}_{\Delta,\mathrm{a}}^{*} \tag{4.28}$$

$$\hat{i}_{\Delta,\mathrm{b}}^{*(-)} = \frac{P_{\Delta,\mathrm{b}}^{*}}{\hat{u}_{\mathrm{b}}} = \hat{i}_{\Delta,\mathrm{b}}^{*} \tag{4.29}$$

$$\hat{i}_{\Delta,\mathrm{c}}^{*(-)} = \frac{2P_{\Delta,\mathrm{c}}^{*}}{\hat{u}_{\mathrm{c}}} = \hat{i}_{\Delta,\mathrm{c}}^{*} \tag{4.30}$$

Note that the magnitudes of the direct and inverse-sequence arm-common currents are the same in each phase, which is a consequence of the arm-differential power reference distribution proportionally to the voltage magnitude of the respective sequence.

As a result, inverse-sequence arm-common current references are obtained by multiplying current magnitudes with per unit values of the inverse-sequence voltages:

$$i_{\Delta,\mathrm{a}}^{*(-)} = \hat{i}_{\Delta,\mathrm{a}}^{*} A^{-} = \hat{i}_{\Delta,\mathrm{a}}^{*} \sin(\omega t + \phi^{-}) \tag{4.31}$$

$$i_{\Delta,\mathrm{b}}^{*(-)} = \hat{i}_{\Delta,\mathrm{b}}^{*} B^{-} = \hat{i}_{\Delta,\mathrm{b}}^{*} \sin(\omega t + \phi^{-} + 2\pi/3) \tag{4.32}$$

$$i_{\Delta,\mathrm{c}}^{*(-)} = \hat{i}_{\Delta,\mathrm{c}}^{*} C^{-} = \hat{i}_{\Delta,\mathrm{c}}^{*} \sin(\omega t + \phi^{-} - 2\pi/3) \tag{4.33}$$

Based on the definition of the inverse-sequence components in (4.4)-(4.6), it can be observed that the fundamental difference between the inverse and the direct-sequence components is that the phases B and C are reversed. This practically means that in order to obtain the same in-quadrature components with respect to the original negative-sequence currents, the difference between the negative-sequence voltages ($A^{-}$, $B^{-}$, $C^{-}$) should have reversed sign, as in the following equations:

$$i_{\Delta,\mathrm{a}}^{**(-)} = \hat{i}_{\Delta,\mathrm{a}}^{*} A^{-} + \frac{1}{3}\left(\hat{i}_{\Delta,\mathrm{b}}^{*} - \hat{i}_{\Delta,\mathrm{c}}^{*}\right) \underbrace{\left(B^{-} - C^{-}\right)}_{A_{\mathrm{q}}^{-}} \tag{4.34}$$

$$i_{\Delta,\mathrm{b}}^{**(-)} = \hat{i}_{\Delta,\mathrm{b}}^{*} B^{-} + \frac{1}{3}\left(\hat{i}_{\Delta,\mathrm{c}}^{*} - \hat{i}_{\Delta,\mathrm{a}}^{*}\right) \underbrace{\left(C^{-} - A^{-}\right)}_{B_{\mathrm{q}}^{-}} \tag{4.35}$$

$$i_{\Delta,\mathrm{c}}^{**(-)} = \hat{i}_{\Delta,\mathrm{c}}^{*} C^{-} + \frac{1}{3}\left(\hat{i}_{\Delta,\mathrm{a}}^{*} - \hat{i}_{\Delta,\mathrm{b}}^{*}\right) \underbrace{\left(A^{-} - B^{-}\right)}_{C_{\mathrm{q}}^{-}} \tag{4.36}$$

One can note that in-quadrature current components for the negative-sequence references could have been created in the same manner as for the positive references. It would only result in having in-quadrature components that are advancing (c.f. **Fig. 4.2.c**) rather than lagging (c.f. **Fig. 4.2.b**) with respect to the original reference. In such a case, the power product of the negative-sequence current references and the negative-sequence voltages would still correspond to the desired power references. Current references obtained in this manner take the following form:

$$i_{\Delta,\mathrm{a}}^{**(-)} = \hat{i}_{\Delta,\mathrm{a}}^{*(-)} A^{-} + \frac{1}{3}\left(\hat{i}_{\Delta,\mathrm{b}}^{*(-)} - \hat{i}_{\Delta,\mathrm{c}}^{*(-)}\right) \underbrace{\left(C^{-} - B^{-}\right)}_{-A_{\mathrm{q}}^{-}} \tag{4.37}$$

$$i_{\Delta,\mathrm{b}}^{**(-)} = \hat{i}_{\Delta,\mathrm{b}}^{*(-)} B^{-} + \frac{1}{3}\left(\hat{i}_{\Delta,\mathrm{c}}^{*(-)} - \hat{i}_{\Delta,\mathrm{a}}^{*(-)}\right) \underbrace{\left(A^{-} - C^{-}\right)}_{-B_{\mathrm{q}}^{-}} \tag{4.38}$$

$$i_{\Delta,\mathrm{c}}^{**(-)} = \hat{i}_{\Delta,\mathrm{c}}^{*(-)} C^{-} + \frac{1}{3}\left(\hat{i}_{\Delta,\mathrm{a}}^{*(-)} - \hat{i}_{\Delta,\mathrm{b}}^{*(-)}\right) \underbrace{\left(B^{-} - A^{-}\right)}_{-C_{\mathrm{q}}^{-}} \tag{4.39}$$

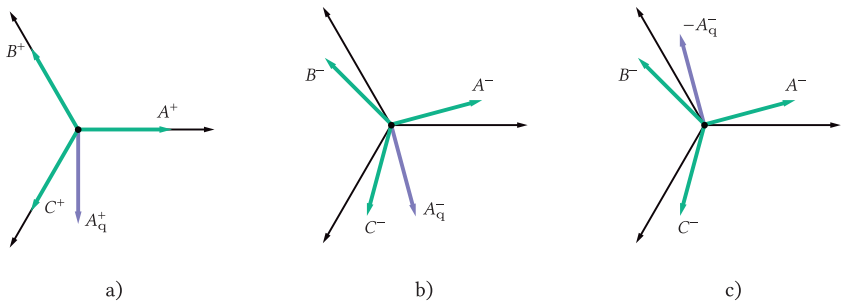


**Fig. 4.2** Illustration of in-quadrature voltage phasors of: a) direct-sequence voltage components; b) inverse-sequence voltage components with "lagging" in-quadrature phasor; c) inverse-sequence voltage components with "advancing" in-quadrature phasor.

Although the two approaches seem to have similar effects, the real comparison in terms of generated power and the sum of the current references when both sequences are considered reveals the differences.

#### 4.2.2.2 Mutual influence of direct and inverse components

Before analysing the influence of the zero-sequence components, the inverse-sequence current references should be superimposed onto the direct-sequence ones.

As the two methods of the inverse-sequence reference modification have been presented, their summation with the modified positive-sequence references yields different results.

The Method I introduced in **Chapter 3** is in general based on modification of the original current references such that in-quadrature components are generated so as not to produce an active power with the corresponding phase voltages. Additionally, these components ensure that the sum of the three arm-common current references is equal to zero.

To minimize the arm-common current references, the original current references are in-phase with the respective phase voltages. Additional current references should be in-quadrature with the original ones to avoid parasitic power terms. Exemplary phasors of the original and in-quadrature components are shown in **Fig. 4.3**. It can be seen that in-quadrature phasors are rotated for a quarter of the period in negative direction with respect to the original phasors. This can be mathematically expressed as in ((4.40)), where $\underline{U}_x$ represents an original phasor, whereas $\underline{U}_{x,q}$ represents its in-quadrature counterpart.

$$\underline{U}_{x,q} = e^{-j\frac{\pi}{2}}\underline{U}_x \tag{4.40}$$

Applying ((4.40)) to a phasor that can be decomposed into its direct, inverse and zero-sequence components, in-quadrature phasor takes the following form:

$$\underline{A}_q = e^{-j\frac{\pi}{2}}\underline{A} = e^{-j\frac{\pi}{2}}\left(\underline{A}^+ + \underline{A}^- + \underline{A}^0\right) = \underline{A}_q^+ + \underline{A}_q^- + \underline{A}_q^0 \tag{4.41}$$

Results from ((4.41)) show that the phase shift applied to the original phasor results in the same phase shift of its components, irrespectively of their sequence. This is visually represented in **Fig. 4.3**, and

corresponds to the method of the inverse-sequence in-quadrature signal generation described by (4.34)-(4.36), and graphically represented in **Fig. 4.2.b**.

A simple addition of the currents from (4.21)-(4.23) and (4.34)-(4.36) yields (4.42)-(4.44). As the current references have the same magnitudes for both the direct and the inverse sequences in a particular phase, no distinction was made between the two.

$$i_{\Delta,\mathrm{a}}^{**(+/-)} = \hat{i}_{\Delta,\mathrm{a}}^{*}\left(A^{+} + A^{-}\right) + \frac{1}{3}\left(\hat{i}_{\Delta,\mathrm{b}}^{*} - \hat{i}_{\Delta,\mathrm{c}}^{*}\right)\left(C^{+} - B^{+} + B^{-} - C^{-}\right) \tag{4.42}$$

$$i_{\Delta,\mathrm{b}}^{**(+/-)} = \hat{i}_{\Delta,\mathrm{b}}^{*}\left(B^{+} + B^{-}\right) + \frac{1}{3}\left(\hat{i}_{\Delta,\mathrm{c}}^{*} - \hat{i}_{\Delta,\mathrm{a}}^{*}\right)\left(A^{+} - C^{+} + C^{-} - A^{-}\right) \tag{4.43}$$

$$i_{\Delta,\mathrm{c}}^{**(+/-)} = \hat{i}_{\Delta,\mathrm{c}}^{*}\left(C^{+} + C^{-}\right) + \frac{1}{3}\left(\hat{i}_{\Delta,\mathrm{a}}^{*} - \hat{i}_{\Delta,\mathrm{b}}^{*}\right)\left(B^{+} - A^{+} + A^{-} - B^{-}\right) \tag{4.44}$$

From the graphical analysis of the components, it is obvious that the generation of modified references where in-quadrature components in all the sequences are phase shifted in the same direction yields no parasitic power terms. However, summing up the modified current references from (4.42)-(4.44) reveals that the sum of the three modified current references equals:

$$i_{\Delta,\mathrm{dc}}^{**} = i_{\Delta,\mathrm{a}}^{**(+/-)} + i_{\Delta,\mathrm{b}}^{**(+/-)} + i_{\Delta,\mathrm{c}}^{**(+/-)} = 2\left(\hat{i}_{\Delta,\mathrm{a}}^{*}A^{-} + \hat{i}_{\Delta,\mathrm{b}}^{*}B^{-} + \hat{i}_{\Delta,\mathrm{c}}^{*}C^{-}\right) \neq 0 \tag{4.45}$$

As it can be seen, the sum of the three modified current references that preserve the power reference do not sum-up to zero, which is one of the two main objectives of the modification.

On the other hand, omitting the formal proof, it can be shown that if the inverse-sequence reference modification obtained by (4.37)-(4.39) is used, the sum of the current references is equal to zero, however, the resulting arm-differential power in the three phases corresponds to:

$$\begin{aligned} P_{\Delta,\mathrm{a}} &= 2u_{\mathrm{diff,a}} i_{\Delta,\mathrm{a}}^{**} \\ &= \left(\hat{i}_{\Delta,\mathrm{a}}^{*}\left(A^{+} + A^{-}\right) + \frac{1}{3}\left(\hat{i}_{\Delta,\mathrm{b}}^{*} - \hat{i}_{\Delta,\mathrm{c}}^{*}\right)\left(C^{+} - B^{+} - B^{-} + C^{-}\right)\right)\hat{u}_{\mathrm{diff,a}}\left(A^{+} + A^{-}\right) \\ &= \underbrace{\frac{\hat{i}_{\Delta,\mathrm{a}}^{*}\hat{u}_{\mathrm{diff,a}}}{2}}_{P_{\Delta,\mathrm{a}}^{*}} + \frac{2\sqrt{3}\hat{u}_{\mathrm{diff,a}}}{3}\left(\hat{i}_{\Delta,\mathrm{b}}^{*} - \hat{i}_{\Delta,\mathrm{c}}^{*}\right)\sin\phi^{-} \end{aligned} \tag{4.46}$$

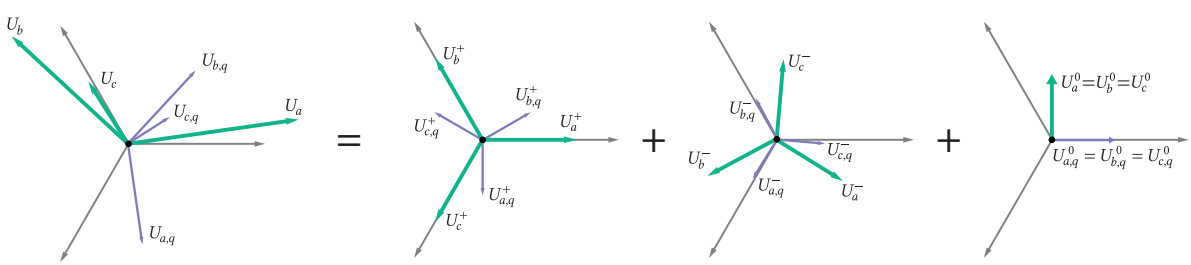


**Fig. 4.3** Decomposition of asymmetrical grid voltage phasors and respective in-quadrature voltages into the direct, inverse and zero sequence components.

$$
\begin{aligned}
P_{\Delta,\mathrm{b}} &= i^{**}_{\Delta,\mathrm{b}} u_{\mathrm{diff,b}} \\
&= \left(\hat{i}^{*}_{\Delta,\mathrm{b}}\left(B^{+}+B^{-}\right)+\frac{1}{3}\left(\hat{i}^{*}_{\Delta,\mathrm{c}}-\hat{i}^{*}_{\Delta,\mathrm{a}}\right)\left(A^{+}-C^{+}-C^{-}+A^{-}\right)\right)\hat{u}_{\mathrm{diff,b}}\left(B^{+}+B^{-}\right) \\
&= \underbrace{\frac{\hat{i}^{*}_{\Delta,\mathrm{b}}\hat{u}_{\mathrm{diff,b}}}{2}}_{P^{*}_{\Delta,\mathrm{b}}}+\frac{2\sqrt{3}\hat{u}_{\mathrm{diff,b}}}{3}\left(\hat{i}^{*}_{\Delta,\mathrm{c}}-\hat{i}^{*}_{\Delta,\mathrm{a}}\right)\sin\phi^{-}
\end{aligned}
\tag{4.47}
$$

$$
\begin{aligned}
P_{\Delta,\mathrm{c}} &= i^{**}_{\Delta,\mathrm{c}} u_{\mathrm{diff,c}} \\
&= \left(\hat{i}^{*}_{\Delta,\mathrm{c}}\left(C^{+}+C^{-}\right)+\frac{1}{3}\left(\hat{i}^{*}_{\Delta,\mathrm{a}}-\hat{i}^{*}_{\Delta,\mathrm{b}}\right)\left(B^{+}-A^{+}-A^{-}+B^{-}\right)\right)\hat{u}_{\mathrm{diff,c}}\left(C^{+}+C^{-}\right) \\
&= \underbrace{\frac{\hat{i}^{*}_{\Delta,\mathrm{c}}\hat{u}_{\mathrm{diff,c}}}{2}}_{P^{*}_{\Delta,\mathrm{c}}}+\frac{2\sqrt{3}\hat{u}_{\mathrm{diff,c}}}{3}\left(\hat{i}^{*}_{\Delta,\mathrm{a}}-\hat{i}^{*}_{\Delta,\mathrm{b}}\right)\sin\phi^{-}
\end{aligned}
\tag{4.48}
$$

It is obvious from (4.46)-(4.48) that the current modification method that ensures zero-sum at the dc terminals results in parasitic arm-differential power terms. The major problem is that in some cases these terms can take values significantly higher than the required power references, making the system unstable. To counteract these parasitic power terms, authors in [123] inject a second-harmonic common-mode voltage at the ac terminals and the second harmonic arm-common currents. While the approach ensures stability of the control system, it is inconvenient, as it requires increased voltage and current capacity of the converter, and does not fully benefit from all the voltage grid sequences, as explained in introductory section of this chapter.

Previous analyses show that the extension of the *Method I* to unbalanced grid conditions is troublesome due to the cross-coupling between the positive and negative sequences. Ensuring zero-sum of the introduced arm-common currents results in parasitic power terms which might lead to instability, whereas ensuring that generated power terms correspond to the reference values leads to the non-zero sum of the arm-common current components.

An analytical solution that ensures both conditions is possible to obtain, with the form that is similar to what was already presented in (4.42)-(4.44), with the only difference in coefficients that multiply in-quadrature components:

$$
i^{**}_{\Delta,\mathrm{a}}(t) = \hat{i}^{*}_{\Delta,\mathrm{a}} A + k_{\mathrm{A}} A_{\mathrm{q}} \tag{4.49}
$$

$$
i^{**}_{\Delta,\mathrm{b}}(t) = \hat{i}^{*}_{\Delta,\mathrm{b}} B + k_{\mathrm{B}} B_{\mathrm{q}} \tag{4.50}
$$

$$
i^{**}_{\Delta,\mathrm{c}}(t) = \hat{i}^{*}_{\Delta,\mathrm{c}} C + k_{\mathrm{C}} C_{\mathrm{q}} \tag{4.51}
$$

In cases when zero-sequence components are not present in the grid voltage, coefficients $k_{\mathrm{A}}$, $k_{\mathrm{B}}$, and $k_{\mathrm{C}}$ can be determined in such a way that the obtained arm-differential power components correspond to the references. However, these coefficients are not anymore dependent only upon the power references, but also include sine and cosine terms of the phase disposition angle $\phi^{-}$ between the

two sequences. Additionally, if the zero-sequence component is present in the grid voltages, the power references cannot be completely tracked while ensuring the zero-sum constraint. Moreover, calculation of the coefficients $k_A$, $k_B$, and $k_C$ becomes even more complex, making this approach extremely complicated for implementation. Consequently, *Method I* might not be the best candidate for the energy control under unbalanced grid conditions.

#### 4.2.2.3 Method II

Although a formal derivation of this method for the arm-differential current generation was conducted in previous chapter, conclusions can be summarized as follows:

- To ensure the arm-differential energy control, arm-common current references should be aligned with respective phase voltages to ensure minimal current amplitudes for a given power.
- As the current references have arbitrary values in phases, they should be modified to respect the zero-sum condition.
- *Method II* proposes a current modification that ensure minimal deviation from the original current (and thus power) references while respecting the zero-sum constraints.
- It is based on extraction of the zero-sequence component from the three generated current references.

While the conclusion was derived for arbitrary current references under balanced grid conditions, it is applicable irrespectively of the grid conditions, for any set of vectors. Therefore, formal derivation for unbalanced grid conditions will be omitted, and only the reasoning with the vectors (phasors) will be used.

To do so, an arbitrary set of three phase voltages, also used in the previous analysis, is shown in **Fig. 4.4.a**. This set is composed of direct, inverse, and zero-sequence symmetrical components, as illustrated in **Fig. 4.2**.

Following the reasoning behind the *Method II*, normalized voltages are obtained for each phase (c.f. **Fig. 4.4.b**), and the current references for the arm-differential energy control are multiplied by such voltages, in order to ensure minimal phase displacement between the currents and voltages, and thus minimal current amplitudes for the given power references. This step is illustrated in **Fig. 4.4.c**, and can be analytically described as:

$$i^*_{\Delta,\mathrm{a}}(t) = \hat{i}^*_{\Delta,\mathrm{a}} A \tag{4.52}$$

$$i^*_{\Delta,\mathrm{b}}(t) = \hat{i}^*_{\Delta,\mathrm{b}} B \tag{4.53}$$

$$i^*_{\Delta,\mathrm{c}}(t) = \hat{i}^*_{\Delta,\mathrm{c}} C \tag{4.54}$$

As the three current references do not sum up to zero (orange phasor in **Fig. 4.4.c**) it is necessary to modify them. Subtracting the zero-sequence component from the three phasors, results in modified phasors that represent the closest possible approximation of the original ones under the zero-sum constraint. Resulting phasors are illustrated in **Fig. 4.4.d**. Modified currents produce arm-differential

power components that are the closest possible approximation of the original power references, while the modified references sum up to zero.

The benefit of this method of arm-differential energy control is that it does not require decomposition of the grid voltages and arm currents into the direct, inverse and zero sequences. The analytical form of the current modification is as follows:

$$i^{**}_{\Delta,\mathrm{a}}(t) = \hat{i}^{*}_{\Delta,\mathrm{a}}A - \frac{1}{3}\left(\hat{i}^{*}_{\Delta,\mathrm{a}}A + \hat{i}^{*}_{\Delta,\mathrm{b}}B + \hat{i}^{*}_{\Delta,\mathrm{c}}C\right) \tag{4.55}$$

$$i^{**}_{\Delta,\mathrm{b}}(t) = \hat{i}^{*}_{\Delta,\mathrm{b}}B - \frac{1}{3}\left(\hat{i}^{*}_{\Delta,\mathrm{a}}A + \hat{i}^{*}_{\Delta,\mathrm{b}}B + \hat{i}^{*}_{\Delta,\mathrm{c}}C\right) \tag{4.56}$$

$$i^{**}_{\Delta,\mathrm{c}}(t) = \hat{i}^{*}_{\Delta,\mathrm{c}}C - \frac{1}{3}\left(\hat{i}^{*}_{\Delta,\mathrm{a}}A + \hat{i}^{*}_{\Delta,\mathrm{b}}B + \hat{i}^{*}_{\Delta,\mathrm{c}}C\right) \tag{4.57}$$

The modification of the current references has the same form as for the case when only the direct-sequence component is considered, which was presented in the previous chapter. The only difference with respect to symmetrical grid conditions is how normalized grid voltages are obtained.

For symmetrical grid conditions the amplitude of the grid voltage is equal among phases, and thus the normalized voltages can be effortlessly obtained by dividing the real-time grid voltage references with the magnitude.

In case of asymmetrical grid conditions, magnitudes of the phase voltages have arbitrary values, and to obtain them, the approach based on second-order generalized integrator (SOGI), presented in [125], is used. This approach uses SOGI to create in-quadrature voltage components, which is further used to calculate voltage magnitude in each particular phase, using the identity (4.58). Instantaneous value of the voltage of a particular phase is denoted as $u_{\mathrm{x}}$, whereas its in-quadrature component is labelled as $qu_{\mathrm{x}}$.

$$\hat{u}_{\mathrm{x}} = \sqrt{u_{\mathrm{x}}^2 + qu_{\mathrm{x}}^2} \tag{4.58}$$

Illustration of a SOGI-based phase voltage magnitude extraction is provided in **Fig. 4.5**, where $\omega_{\mathrm{FLL}}$ is

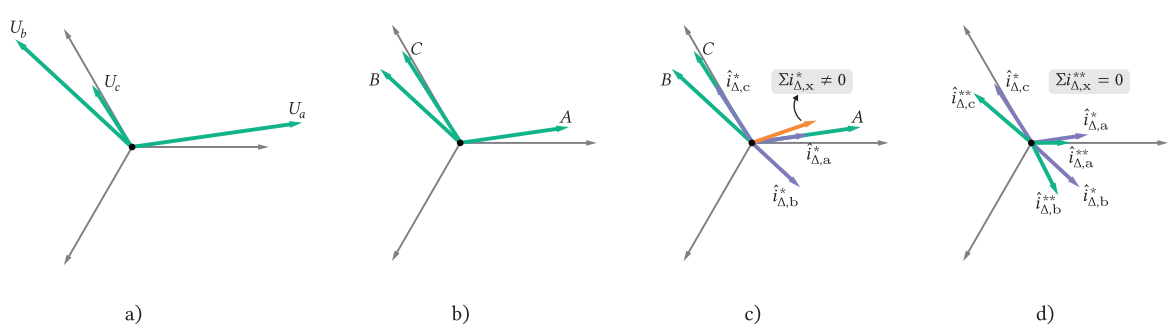


**Fig. 4.4** Illustration of the arm-common current generation process: a) phasors of three asymmetrical phase voltages; b) normalized asymmetrical phase voltage phasors ; c) arm-common current references aligned with respective phase voltages; d) modified arm-common current references, summing up to zero.

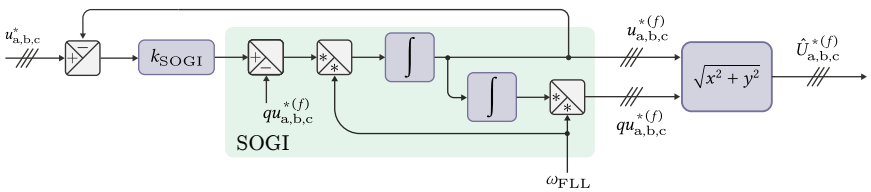


**Fig. 4.5** Phase voltage magnitude calculation using in-quadrature signal generation based on SOGI.

an estimated angular frequency of the grid voltages using the frequency-locked loop (FLL) technique [125] on the voltages measured at the point of common coupling (PCC), as will be described later.

Inputs to the magnitude extraction subsystem are the arm-differential voltage references in particular phases, as the arm-common current components for Δ energy control need to be aligned with these voltages. With phase voltage magnitudes calculated, magnitudes of the arm-common current references are calculated as:

$$\hat{i}^*_{\Delta,a} = -\frac{P^*_{\Delta,a}}{\hat{u}^*_{diff,a}} \tag{4.59}$$

$$\hat{i}^*_{\Delta,b} = -\frac{P^*_{\Delta,b}}{\hat{u}^*_{diff,b}} \tag{4.60}$$

$$\hat{i}^*_{\Delta,c} = -\frac{P^*_{\Delta,c}}{\hat{u}^*_{diff,c}} \tag{4.61}$$

Further, normalized phase voltage references are obtained as:

$$A = \frac{u^*_{diff,a}}{\hat{u}^*_{diff,a}} \tag{4.62}$$

$$B = \frac{u^*_{diff,b}}{\hat{u}^*_{diff,b}} \tag{4.63}$$

$$C = \frac{u^*_{diff,c}}{\hat{u}^*_{diff,c}} \tag{4.64}$$

Finally, instantaneous values of the modified arm-common current references for Δ energy control are obtained using (4.55)-(4.57).

### 4.2.3 Complete energy control scheme

Illustration of the complete arm energy control scheme, enhanced for the operation under unbalanced grid conditions is shown in **Fig. 4.6**.

The figure shows that the arm energies are calculated from the respective arm capacitor voltages, and further computed arm-sum and arm-differential energies ($W_\Sigma$ and $W_\Delta$). Computed energies are further filtered using notch filters tuned at appropriate frequencies.

Energy controllers are realized as PI controllers, due to existence of parasitic power terms during unbalanced grid conditions. They yield power references, which enter their corresponding reference generation blocks.

The current reference generation for the arm-sum energy control differs for the inverter and rectifier mode of operation, as already discussed in previous chapter. The difference with respect to symmetrical conditions is that the ac phase power components are not equally shared among phases, so individual active power components are fed-forward. Due to the fact that the single-phase active power contains a second-harmonic oscillating term, it needs to be filtered out.

In case of the rectifier mode of operation, the current reference generation does not differ from the case shown for the symmetrical grid conditions.

Concerning the current reference generation for the arm-differential energy control, the real difference from the *Method II* presented for the balanced grid conditions is in SOGI-based phase voltage

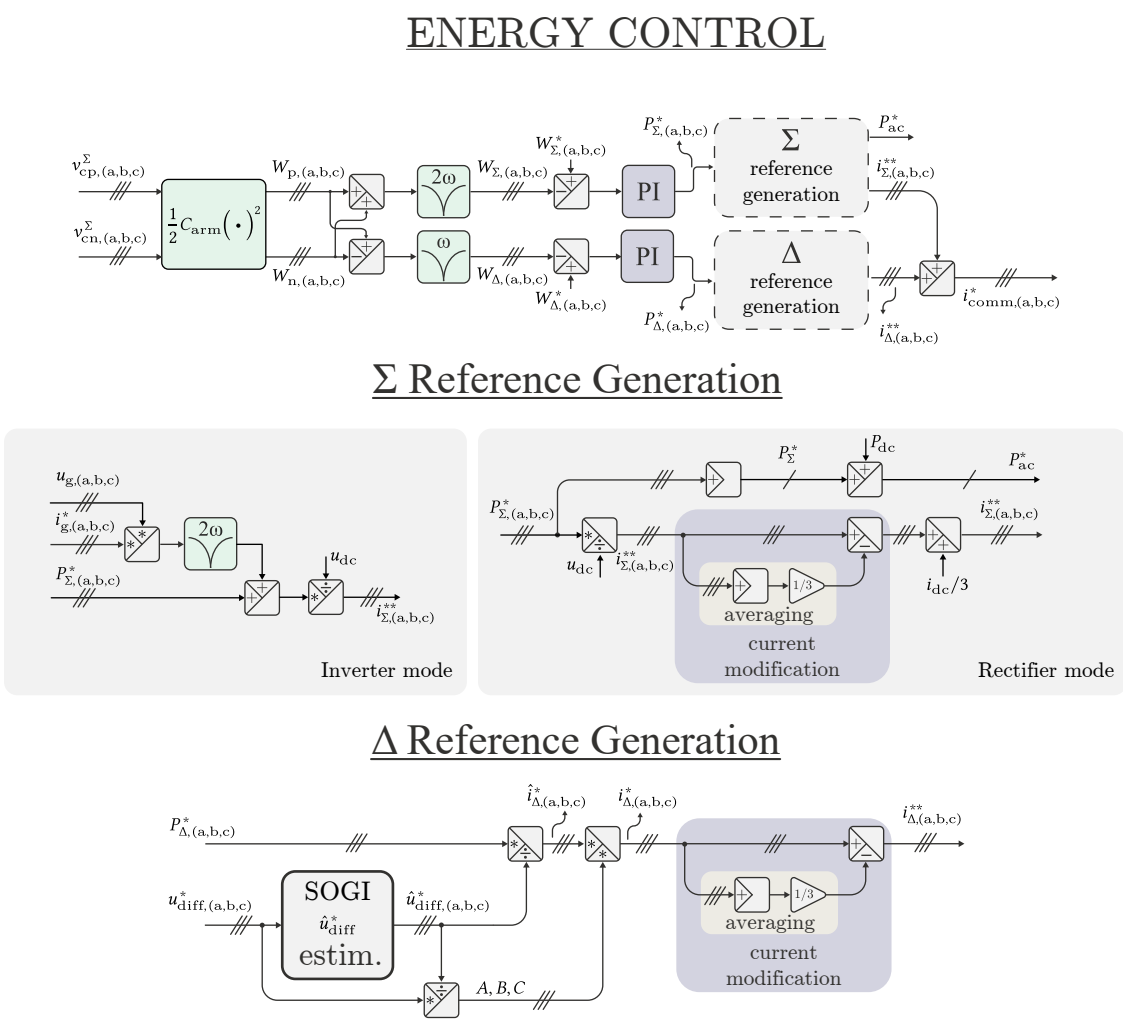


**Fig. 4.6** Illustration of the complete energy control scheme applicable in case of unbalanced grid conditions. One should note that this scheme is equally valid under balanced conditions, and is not subject to switchover with previously-presented scheme.

magnitude calculation. This permits to generate more accurate power references compared to the case when the voltage amplitudes are assumed equal in all three phases, without a significant increase in complexity.

### 4.2.4 Performance evaluation

To evaluate performance of the presented control schemes under unbalanced conditions, a high-fidelity simulation model of a 3PH MMC is created in PLECS.

Energy controllers are realized as discrete controllers, with the execution period ten times higher than the fast-loop (current control) execution period (equal to 125 µs). In all the analysed cases symmetrical components under grid unbalances are assumed to be: 0.5 p.u. for the positive, 0.35 p.u. for the negative, and 0.15 p.u. for the zero sequence.

Results for the inverter mode of operation are shown in **Fig. 4.7**-**Fig. 4.10**. The two figures show the grid voltages and currents during the unbalanced grid conditions, along with the dc terminal voltage and current, individual SM voltages, arm-sum and arm-differential energies, as well as the arm-common currents.

Results in **Fig. 4.7** show the moment when the imbalance in the grid occurs ($t = 0.5$ s), and the behaviour of the MMC at its terminals and internally during the imbalance.

As it can be witnessed, the phase currents remain symmetrical despite the asymmetry in the phase voltages. Their amplitude increases in order to deliver the same active power to the grid as prior to the grid fault. This is an assumption made during this test case, although the scenario might be different in reality. Nevertheless, it does not influence validity of the presented results.

The inverter configuration of the MMC assumes that it is connected to the stiff dc voltage grid, therefore grid conditions do not have influence over the terminal dc voltage. In contrast, the dc current drawn from the dc grid is freely controlled to match the power (energy) needs of the converter during transients. Nevertheless, the inverter configuration does not pose limits to the dc current, except that it should not contain any fundamental frequency components and its harmonics.

Further, individual capacitor voltages of all the arms are plotted, showing that the capacitor voltages remain balanced during the unbalance event, proving a good behaviour of the energy control system. Nevertheless, capacitor voltage oscillations increase, which is expected behavior, as capacitor voltages now buffer the zero-sequence $2^{\text{nd}}$ harmonic power oscillations stemming from the grid, not allowing it to appear on the dc side (typical problem in two-level inverters).

During the unbalance event, arm-sum and arm-differential energies remain around their references. Small transient effects can be noticed, originating from the transient in the energies, but also from the transients in the applied notch filters. To respond to the transients in the respective energies, arm-common currents become unbalanced among the phase legs, reflecting different active power needs of individual phases. In addition, an oscillating component is present in the arm-common current until the affected energies settle to their reference values.

At the time instant $t = 0.8$ s energy references are changed in different arms, resulting in the energy reference changes in both arm-sum and arm-differential energies. The results show that the applied energy control scheme ensures that the arbitrary energy references in the arms are followed, despite adverse grid conditions. Compared to the energy reference tracking during balanced grid conditions,

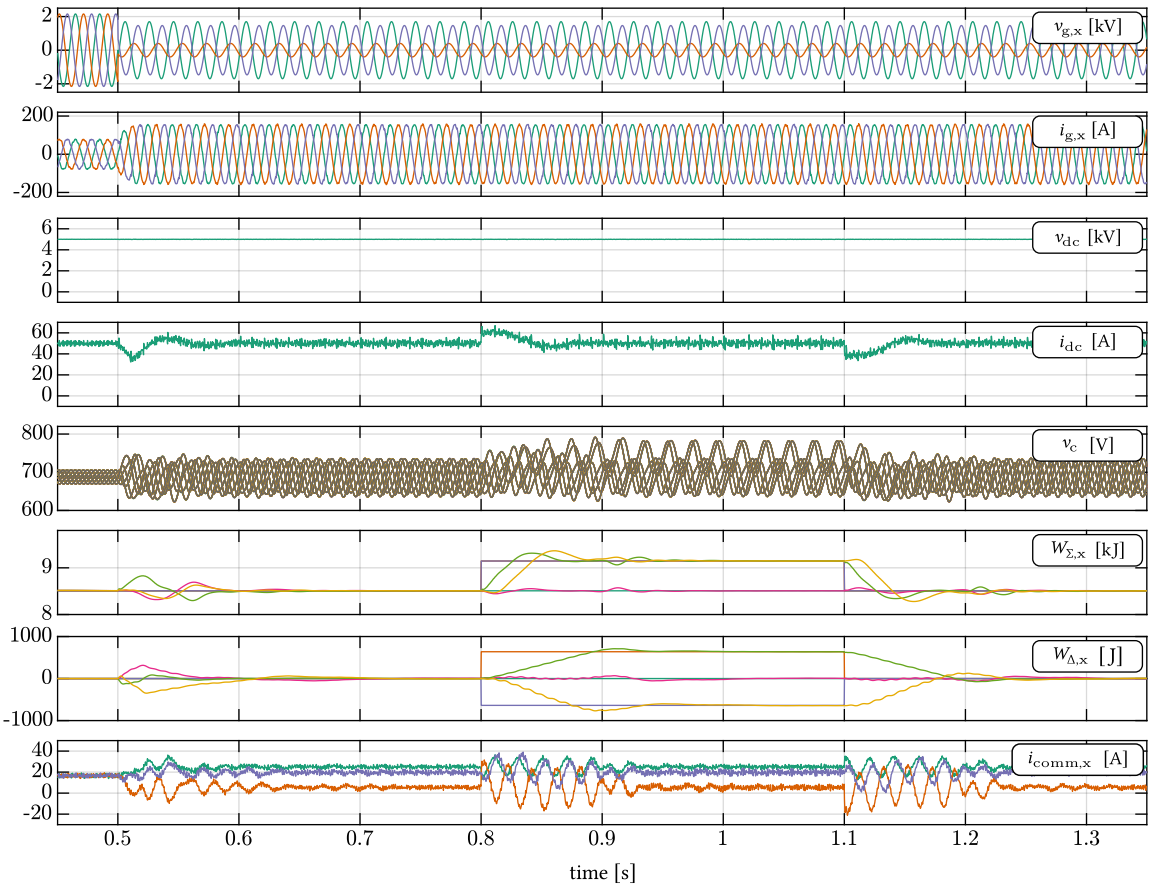


**Fig. 4.7** Behavior of the energy control scheme during a short circuit on the grid side of the converter, for the inverter mode of operation. Top two graphs show phase voltages $u_{g,x}$ and currents $i_{g,x}$, followed by the dc voltage $u_{dc}$ and current $i_{dc}$. Individual SM voltages $v_c$ are shown in the fifth plot from the top, followed by the arm-sum $W_{\Sigma,x}$ and arm-differential $W_{\Delta,x}$ energies and respective references. The final plot shows arm-common currents $i_{comm,x}$ in the three phase legs.

the response in the arm-sum energies is slightly slower. This can be explained by the slower response of the arm-sum energy filter, which is tuned to have higher suppression of the $2^{nd}$ harmonic component (due to its higher value during grid unbalances), yet at the expense of a slightly slower response.

Arm-differential energies do also track their references within the time interval of 100 ms . However, due to the fact that for this control action the arm-differential power is realized by the interaction of the arm-differential voltages and arm-common currents, the amplitudes of the latter are limited in order to avoid high arm-common current references during severe short circuits in the grid. This explains a rather slow response with a constant slope. Arm-common currents change during transients according to the references from the energy controllers.

**Fig. 4.8** and **Fig. 4.9** illustrate the behaviour of the energy control schemes under unbalanced conditions, focusing on arm-sum and differential energies, arm voltages, and respective arm-common current components.

Observing the arm-sum energy control behaviour in **Fig. 4.8** shows that the arm-common currents during the transient slightly change their average values in order to redistribute the arm-sum energies

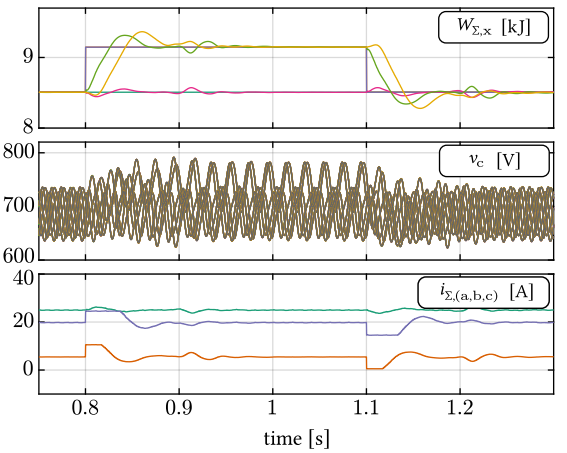


**Fig. 4.8** Effects of the arm-sum energy control during unbalanced grid conditions, for the inverter mode of operation.

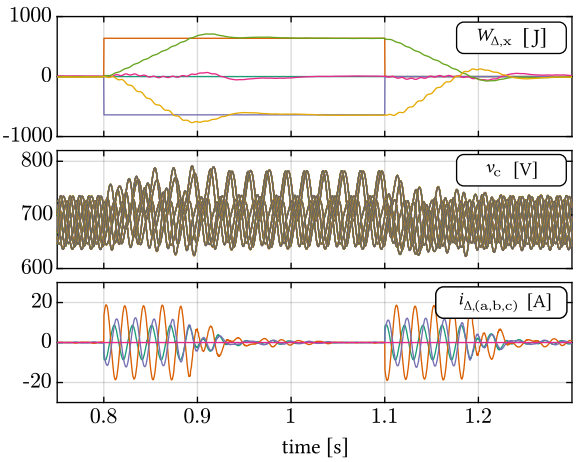


**Fig. 4.9** Effects of the arm-differential energy control during unbalanced grid conditions, for the inverter mode of operation.

between the phase legs. However, their steady-state values remain the same as prior to the transient, and reflect the ac average power requirements of individual phases.

On the other hand, **Fig. 4.9** shows the behaviour of the arm-differential control action. In the bottom of the figure, only the arm-common current components used for this control action are shown. It can be observed that such currents exist only during the transient, and the fact that their amplitude is limited defines the slope of the arm-differential energy control reserve.

Finally **Fig. 4.10** shows the behaviour of the control scheme during and after clearance of the grid fault. It can be observed that the grid currents resume the value they had prior to the fault, the dc current responds during the transient to satisfy the converter energy needs, while SM voltages and respective energies experience insignificant change, except that the voltage ripple in the SMs is reduced to the value prior to the grid fault. In addition, due to resumed symmetry among the phases, the arm-common currents also become balanced.

To simulate the behaviour of the presented control scheme under balanced grid condition, energy references in arms were arbitrarily changed at time instant $t = 2$ s, and returned to normal condition after $t = 0.5$ s. The control scheme proves to have robust behaviour and is able to track the arbitrary arm energy references regardless of the grid conditions, not affecting its terminal variables.

All previous figures aim to demonstrate the behaviour of the energy control scheme of the MMC under balanced and unbalanced grid condition, when applied in the inverter configuration.

The following figures demonstrate the behaviour of the presented control scheme under the same grid conditions, yet when the MMC is used as a rectifier. Such conditions pose slightly more stringent requirements over the terminal variables, as the dc current should remain uninfluenced by the internal MMC energy control actions or grid conditions, while the three phase grid currents should remain symmetrical.

**Fig. 4.11** shows the response of the control scheme during the grid unbalance event, and while changing the energy references, the same as in **Fig. 4.7**. It can be observed that the grid currents change during the transients, respecting the power needs of the converter, all while preserving

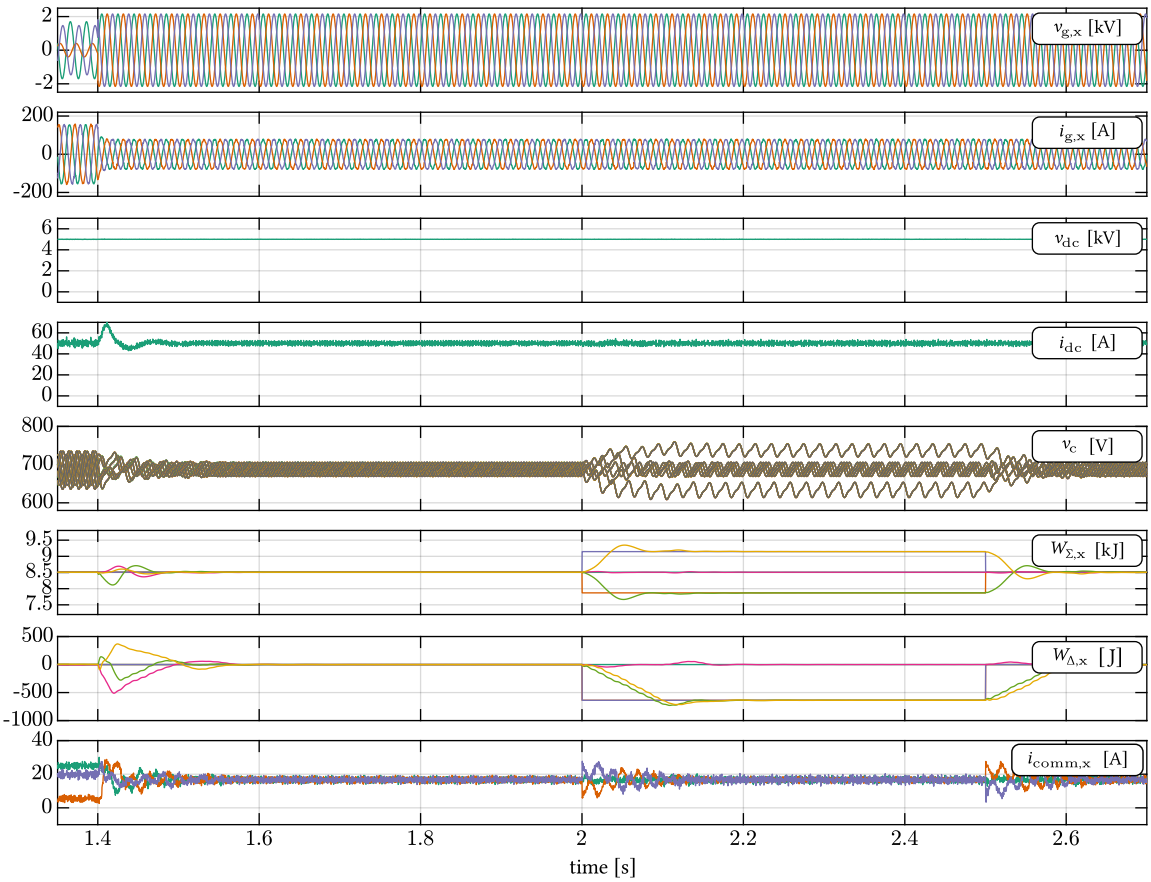


**Fig. 4.10** Behavior of the energy control scheme during and after the short circuit clearance on the grid side of the converter, for the inverter mode of operation. Top two graphs show phase voltages $u_{g,x}$ and currents $i_{g,x}$, followed by the dc voltage $u_{dc}$ and current $i_{dc}$. Individual SM voltages $v_c$ are shown in the fifth plot from the top, followed by the arm-sum $W_{\Sigma,x}$ and arm-differential $W_{\Delta,x}$ energies and respective references. The final plot shows arm-common currents $i_{comm,x}$ in the three phase legs.

symmetry among the phases. On the other hand, the generated dc voltage and current remain unaltered during the transients, which is one of the main objectives for the MMC as a rectifier. After the grid unbalance event, the SM voltages and corresponding energies remain balanced, while the arm-common currents redistribute among the phase legs according to the power needs of individual phases.

Energy references are changed at the time instant $t = 0.8$ s and returned back to their nominal values at $t = 1.1$ s. It can be observed that both the arm-sum and the arm-differential energy references are attained after approximately 100 ms. After the references are set back to their nominal values, the arm energies settle within approximately the same amount of time (100 ms).

Closer look into the arm-sum and the arm-differential energy reference changes and their effects is provided in **Fig. 4.12**-**Fig. 4.13**. Similarly to the inverter mode of operation, the arm-differential energy control scheme behaviour shown in **Fig. 4.12** indicates that the arm-common currents slightly change only during the transient, allowing for energy exchange between the legs. After the arm-sum energies are settled, the arm-common currents resume to their previous values.

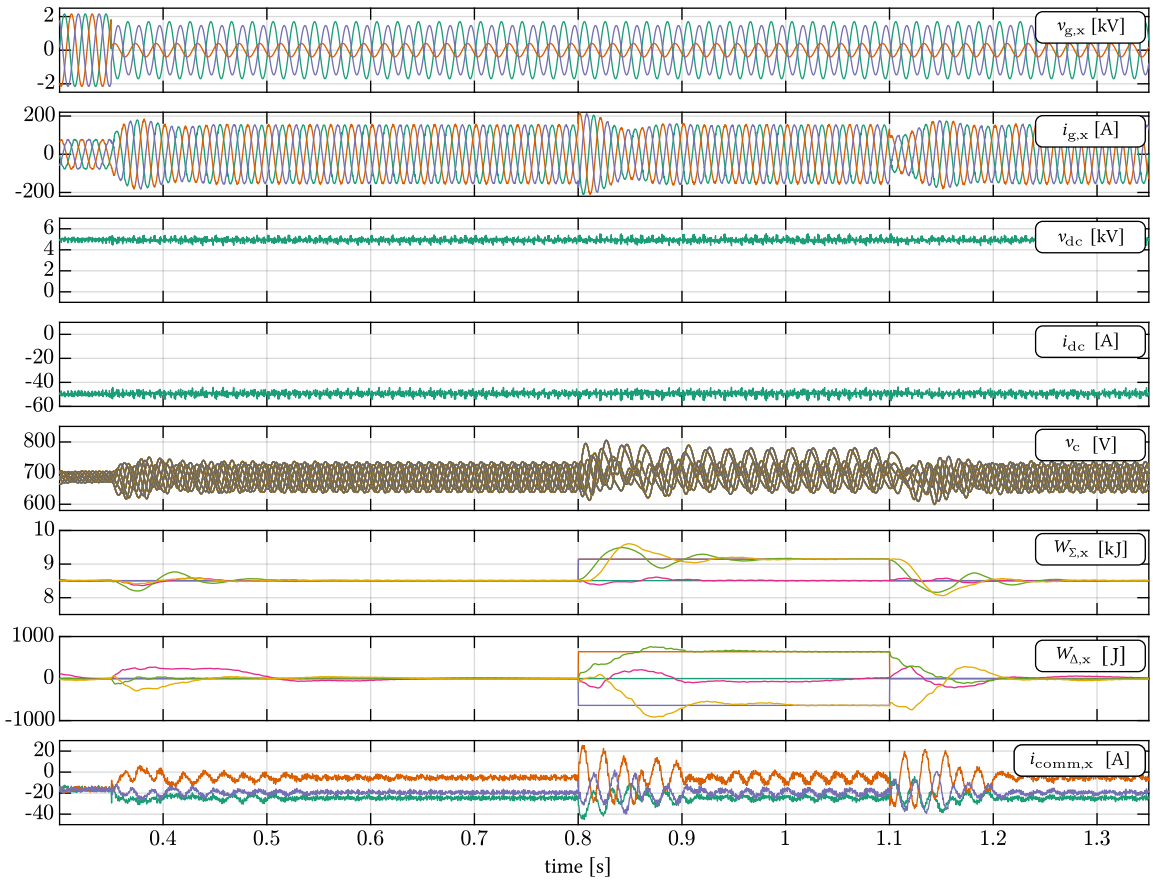


**Fig. 4.11** Behaviour of the energy control scheme during a short circuit on the grid side of the converter, for the rectifier mode of operation. Top two graphs show phase voltages $u_{g,x}$ and currents $i_{g,x}$, followed by the dc voltage $u_{dc}$ and current $i_{dc}$. Individual SM voltages $v_c$ are shown in the fifth plot from the top, followed by the arm-sum $W_{\Sigma,x}$ and arm-differential $W_{\Delta,x}$ energies and respective references. The final plot shows arm-common currents $i_{comm,x}$ in the three phase legs.

Similarly, the arm-differential energy control mechanism also manages to ensure reference tracking using sinusoidal arm-common currents. It can be noted that these current components almost completely disappear after the transient. Yet, one should recognize that a small oscillating current component remains, even though the arm-differential energies have closely reached their values. The reason for such a behaviour can be found in the fact that even for the small energy difference, arm-common current reference for arm-differential energy control is high in a phase where the phase voltage is relatively low during the fault. In addition, this relatively high arm-common current reference in a single phase influences arm-common current references in other phases, thus having a larger influence than it would normally have under balanced grid conditions. Nevertheless, the amplitude of such oscillations are relatively low, and have a tendency to decay over time, and thus do not represent any major disadvantage in using the method.

Lastly, the behaviour of the MMC during and after the grid fault clearance is captured in **Fig. 4.14**, where the same case was simulated as in **Fig. 4.10**. The results show that the control algorithm maintains the MMC rectifier operation objectives valid during both fault clearance and energy reference change. The latter is used to confirm that the proposed energy control method for the

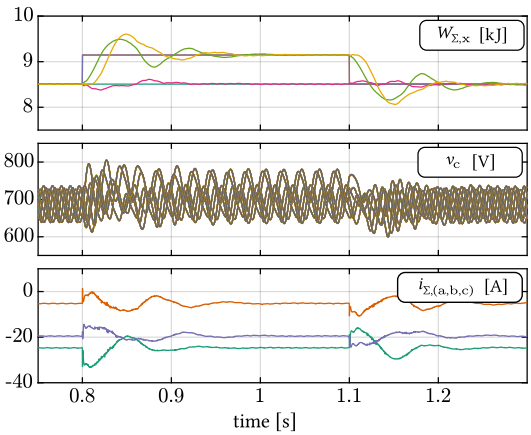


**Fig. 4.12** Effects of the arm-sum energy control during unbalanced grid conditions, for the rectifier mode of operation.

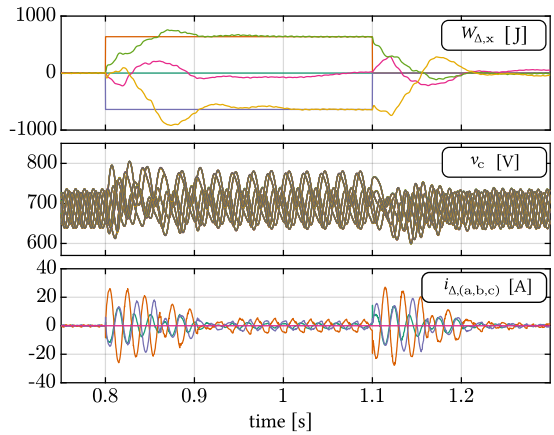


**Fig. 4.13** Effects of the arm-differential energy control during unbalanced grid conditions, for the rectifier mode of operation.

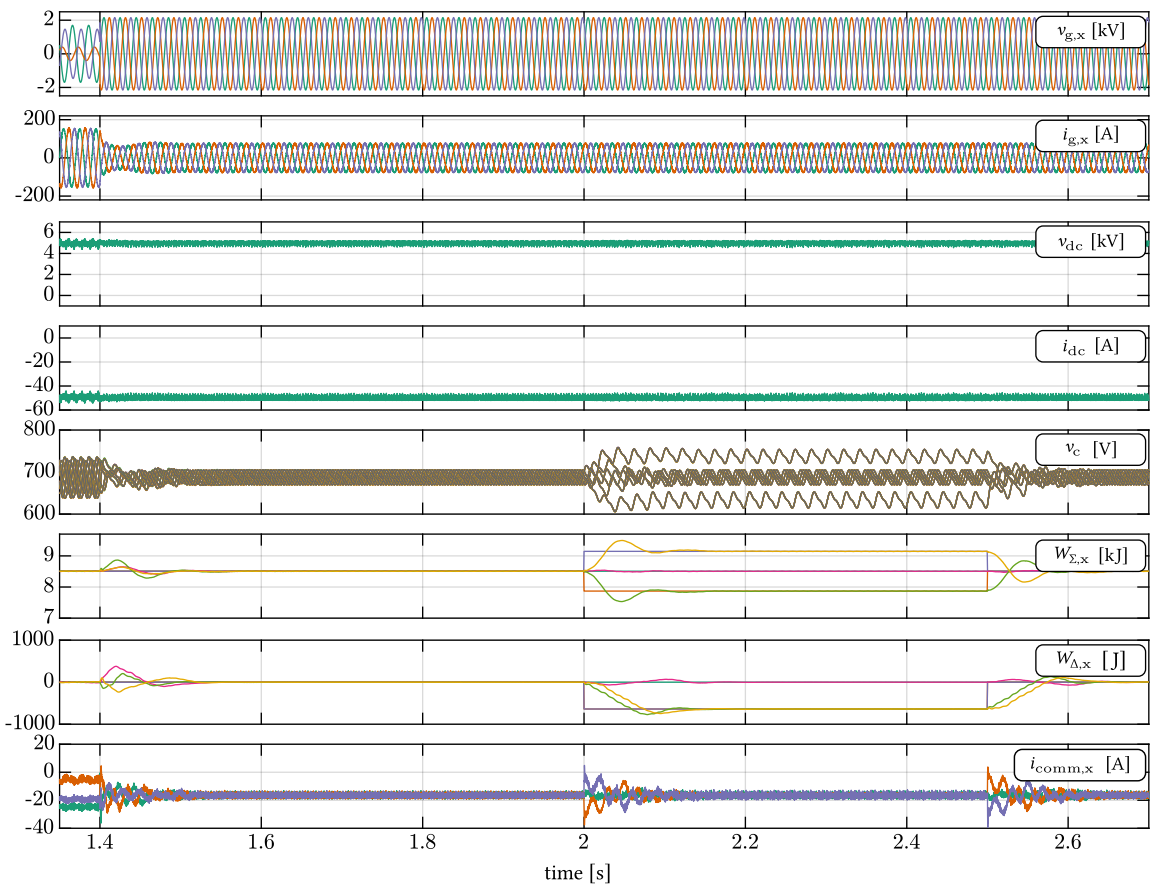


**Fig. 4.14** Behavior of the energy control scheme during and after the short circuit clearance on the grid side of the converter, for the rectifier mode of operation. Top two graphs show phase voltages $u_{g,x}$ and currents $i_{g,x}$, followed by the dc voltage $u_{dc}$ and current $i_{dc}$. Individual SM voltages $v_c$ are shown in the fifth plot from the top, followed by the arm-sum $W_{\Sigma,x}$ and arm-differential $W_{\Delta,x}$ energies and respective references. The final plot shows arm-common currents $i_{comm,x}$ in the three phase legs.

rectifier configuration is valid under both balanced and unbalanced grid conditions.

Previous results demonstrate that the presented control scheme can be readily used under both balanced and unbalanced grid conditions. Besides ensuring its primary function- arbitrary control of the arm energies, the control scheme ensures that the terminal variables are not affected for a given MMC configuration.

## 4.3 Arm energy control under a SM failure

In normal operation, the number of SMs per arm is equal in all converter arms, and the sum of their voltages is kept around their rated value. However, in case of a failure of one or several SMs within an arm, remaining SMs are typically surcharged so that the total arm voltage remains unaltered, as during the normal operation [105]. In this case, the arm with failed SM contains more energy stored compared to the other arms.

It is supposed that the monitoring system of the converter recognizes a fault in a SM, and bypasses it, informing the upper-level control system. The upper level control system recalculates the energy of the arm such that the remaining healthy SMs retain the same voltage capability as the complete arm before the fault. As a result, arm-sum and arm-differential energy references change for the respective arm, resulting in an increase of SM voltages of the affected arm. Therefore, each arm should be equipped with a dedicated energy controller in order to ensure direct control of their energy content.

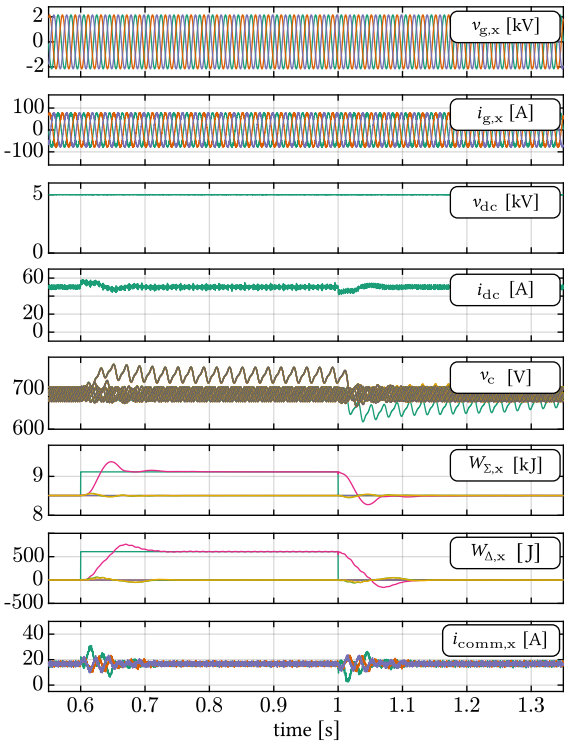


**Fig. 4.15** Simulation of a single SM fault during the inverter mode of operation of the MMC.

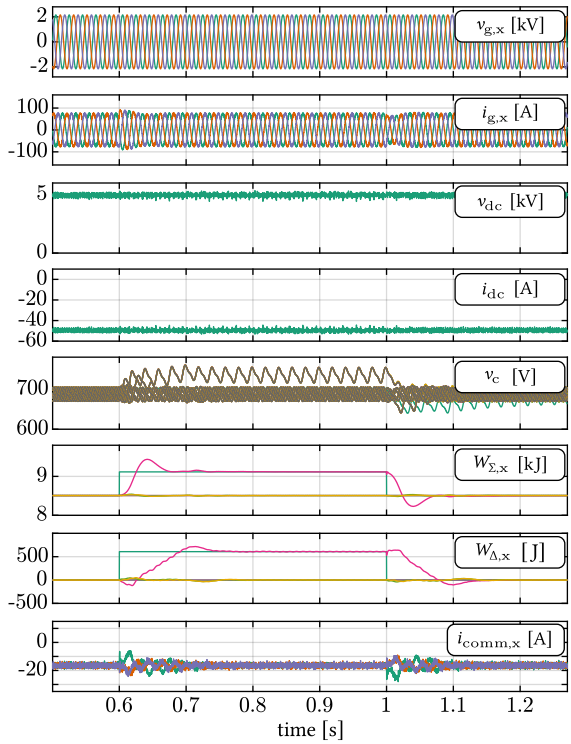


**Fig. 4.16** Simulation of a single SM fault during the rectifier mode of operation of the MMC.

One should be aware of the voltage capability of an individual SM, i.e. of its upper limit. Namely, such a scenario is feasible only in case when the SMs are designed so as to be able to withstand the voltage across their capacitors higher than in the rated case. Due to the fact that higher voltage capabilities lead to non-optimal converter design, such an approach is justified in case when the number of SMs per arm is relatively high (for example when $N \geq 8$).

References for the arm-energies change, and so do the references of $\Sigma$ and $\Delta$ energies of the corresponding phase. To demonstrate the effectiveness of the proposed control concepts in case of failure of a SM, a single SM within the upper arm of phase A is temporarily bypassed at the time instant $t = 0.6$ s and put back into operation at $t = 1$ s, thus emulating a failed SM.

Simulation of such a case was conducted for both configurations: inverter and rectifier, with the results being shown in **Fig. 4.15** and **Fig. 4.16**, respectively.

This scenario is valid for both converter configurations, with the only difference that the ac currents should not be affected for the inverter, while the dc current should not be affected for the rectifier configuration. Simulation results presented in **Fig. 4.15** and **Fig. 4.16** prove exactly this, again demonstrating robustness of the converter and its control scheme against SM failures.

## 4.4 Summary

This chapter aimed to show how the proposed energy control scheme can ensure robust operation of the MMC under various faulty conditions, specifically under grid unbalances, and a SM failure within an arm. The objective in both cases was that the MMC remains operational at its terminals, and that such faults do not influence its performance. An additional objective was that the internal variables, i.e. arm energies, remain controlled, thus allowing for a proper operation of the converter.

The two methods presented in the previous chapter were thoroughly studied for application under unbalanced grid conditions. It was found that both methods can be theoretically adjusted to such conditions, though the *Method II* requires only minor modifications with respect to the balanced grid conditions. In contrast, *Method I* would require knowledge of all the grid sequences, their phases and magnitudes, as well as complex calculations to determine the proper current references.

As a result, *Method II* was selected for further evaluation for the two converter configurations. It was shown that the converter manages to perform its primary functions, as well as to stay balanced under grid unbalances, step changes of the energy references during unbalances, as well as during and after the fault clearance.

Finally, the energy control scheme was applied in regulating the arm voltages in case of a SM failure within an arm. It was shown that the proposed energy control scheme ensures that the total arm voltage remains constant, irrespectively of the configuration, thus ensuring that the converter operation is not compromised.

In conclusion, it was demonstrated that the proposed energy control methods are applicable under both normal and faulty conditions, without the need for switchover between different control schemes, all while offering the benefits of extendibility, implementation simplicity and effective control of the arm energies.

# 5
# Energy Control of the Modular Multilevel Matrix Converter

*Arm energy control methods for a regular ac-dc MMC were presented in previous chapters. It was shown that they can be used under normal and faulty conditions, as well as for converters with multiple phases or paralleled arms. This chapter investigates extension of the energy control method used in* ***Chapter 4*** *to the M3C. It benefits from previously derived conclusions and energy control principles, and proposes various control actions to meet the objective of independent arm energy control. Proposed control concept is tested under normal conditions, no-load conditions, as well as under grid unbalances. Validity of the control concept was demonstrated using an in-house-developed hardware-in-the-loop simulator of the M3C, with control algorithms being deployed in the industrial-grade controller.*

## 5.1 Motivation

High reliability achieved through redundancy, high efficiency, elimination of bulky filters and transformers [35] come with the price of increased control complexity.

The most complex tasks are those related to monitoring the protection of the converter, and voltage (energy) control of the floating SMs. Even more challenging does it become in case when no energy is exchanged between the two converter ac terminals (no load conditions), or in case of grid faults.

Several publications have been made on the topic of arm energy control of the M3C. Reference [110] presents a generalized set of criteria for arm energy balancing, applicable to different MMC-alike topologies, such as the standard MMC, delta and star STATCOM, M3C and Hexverter. Although the stability of the method has been confirmed by means of simulation, using M3C as an example, this reference only mathematically formulates the criteria, and does not present a solution for any particular converter, neither does it provide guidelines for its implementation. In [126] authors use the approach from [110] to balance the energies inside a standard MMC converter, demonstrating that the application of this method requires profound mathematical expertise in obtaining a solution, even for a less complex converter topology, such as the MMC.

The first references successfully dealing with this topic [100], [127] propose a set of solutions for the M3C energy control, based on circulating currents and common-mode voltage injection, which might be used in different ways, depending on the operating mode. While it demonstrates the ability to create an arbitrary imbalance among the converter arms, implementation of this method is based on double-$\alpha\beta 0$ transformations, which might not be an intuitive approach and requires a considerable amount of direct and inverse double-$\alpha\beta 0$ transformations. A similar approach was used in [101], where the authors experimentally demonstrate the effectiveness of the balancing method. Apart from

a significant amount of double-$\alpha\beta 0$ transformations, validity of the method was not tested under unbalanced grid conditions.

Improvement of the method presented in [100] was proposed in [128], where an additional $\Sigma\Delta$ transformation is performed on the internal $\alpha\alpha$, $\alpha\beta$, $\beta\alpha$, $\beta\beta$ currents, in order to decouple specific frequency components. The same approach was used by the authors in [51], [129], which use the M3C as an interface between the wind generator and the ac utility grid. While this approach reduces the delay of the filtering chain in specific balancing directions, the overall delay is determined by the slowest among them. As a result, no significant benefits are expected in terms of control dynamics, while the realization of the control method gets even more complicated. In addition, relationship between the controlled current components in diagonal directions and the final arm currents become more complex, making it difficult to both understand and limit the influence of a certain control action on a particular arm current.

Authors in [130] present a generalized approach for current control and energy balancing, applicable to any of the modular multilevel converter topologies. The approach is based on using circulating current components at both grid and load frequency, as well as common-mode voltages and circulating current components at arbitrary frequencies. The optimal solutions, in terms of minimal RMS of the induced circulating currents, were presented in the form of matrices, which yield circulating current and common-mode voltage references from the arm power references. Two matrices are presented, where each one of them is optimal for different operating ranges of the M3C. While the solution poses lower current stress on the converter for some operating points compared to [101], the implementation of the method is not simple, due to the fact that the resulting matrices are of high order, and the elements of the matrix are variables dependent upon the operating condition, which are calculated in real time. High number of different elements in the matrices that are either used as inputs or calculated in real-time increases the risk of error during implementation of the method. In addition, a clear distinction between the application range of the two methods has not be presented, which could lead to transient behaviour of the converter during the hard switch-over between the two. Applicability of the method was not confirmed under unbalanced grid conditions. Although the proposal combines all degrees of freedom and yields an effective solution with the minimal current stress, its lack of simplicity of implementation might render it unattractive, particularly for engineers and researchers entering the field.

Complexity of the existing solutions for the M3C energy control was recognized by the authors in [131], who proposed an energy balancing solution that simplifies the energy control problem in the M3C, compared to the existing solutions. Although effectively achieving the balancing task within the converter under symmetrical conditions, proposed solution is unable to deal with the energy control in cases when different energy levels are required in different arms (as in the case of a SM failure in one arm). In addition, the solution might not be able to ensure decoupling of the inner energy control from the terminal currents during grid faults.

Another issue with operation of the M3C arises when the frequencies of the two ac systems it interconnects become similar or equal. In such a case, energy oscillations in the M3C arms become excessively high, resulting in a large ripple in the voltage of the arm capacitors. If not mitigated, excessively high voltage ripple would lead to overvoltages across SM capacitors, loss of the voltage generation capability, and consequently loss of control over the converter. Mitigation of such oscillations relies on introduction of a common-mode voltage and circulating currents, which together counteract the power components that provoke the oscillations [33], [101], [128], [129], [132], [133]. Regardless of

the control method being applied, what all of them have in common is the fact that the arm current increases significantly due to the introduced circulating currents. It can go up to 50% above the rated arm current [34], [134]. Additionally, voltage oscillations in case when the supply and load frequencies are equal are still 2.5 times higher in case of the M3C compared to the back-to-back MMC solution, yielding a requirement for a higher installed energy in the M3C. All these facts contribute to the conclusion that the M3C is a converter suitable for interconnecting two ac systems of unequal frequencies, or an ac motor drive with a rated frequency far below the grid frequency.

Therefore, voltage oscillation mitigation due to equal frequencies is considered by the author as a separate control issue, and is thus not part of the presented energy control scheme. It was treated as a separate control objective in [128], [129], [132], [133].

Focus of this chapter is on techniques for the arm energy control in the M3C, assuming that the frequencies of the interconnected systems are sufficiently different from each other. Its primary aim is to develop the arm energy control technique which can attain the objective of independent arm energy control under various grid/load conditions, all while using an intuitive and simple-to-implement control approach.

## 5.2 Energy control mechanisms in the M3C

To facilitate the derivation of the mechanisms that govern the energy control inside the M3C, **Fig. 2.11** is shown again **Fig. 5.1**.

Key variables determining the behaviour of the M3C are its terminal voltages $u_x$ and $u_y$, where $x = \{A, B, C\}$, and $y = \{R, S, T\}$, internal arm-generated voltages $u_{x,y}$, total arm SM voltages $v_{x,y}$, terminal currents $i_x$ and $i_y$, and internal arm currents $i_{x,y}$.

Arm currents $i_{x,y}$ can be expressed as a portion of the terminal current $i_x$ and $i_y$, and additional circulating current components $\Delta i_{x,y}^{(x)}$, and $\Delta i_{x,y}^{(y)}$, that exist typically temporarily and are in general sinusoidal components at angular frequencies $\omega_x$ and $\omega_y$, respectively.

Arm currents typically contain one third of their respective terminal currents under symmetrical

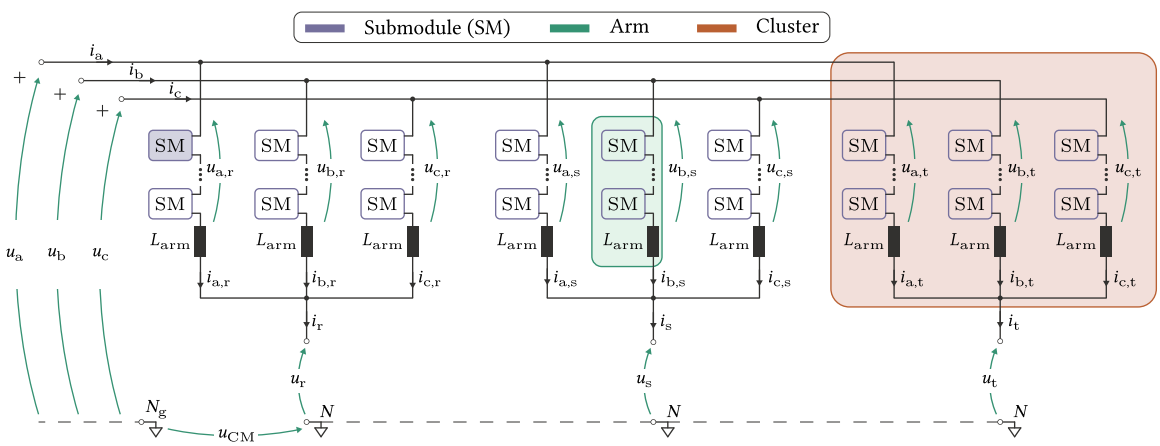


**Fig. 5.1** Layout of a 3PH ac-ac M3C topology, together with labelling of relevant converter variables (voltages and currents).

grid/load conditions. Under asymmetries, or during transients, additional circulating currents are injected to correspond to energy needs of each individual arm. Consequently, the arm current can be expressed as:

$$i_{\mathrm{x,y}} = i_{\mathrm{x}}/3 + i_{\mathrm{y}}/3 + \Delta i_{\mathrm{x,y}}^{(x)} + \Delta i_{\mathrm{x,y}}^{(y)} \tag{5.1}$$

Similarly, arm-generated voltage $u_{\mathrm{x,y}}$ counteracts corresponding terminal voltages, and contains components for arm-current control, as expressed in (5.2). For relatively small arm inductances, these components can be neglected, and the arm voltages can be expressed as in (5.3).

$$u_{\mathrm{x,y}} = u_{\mathrm{x}} - u_{\mathrm{y}} - u_{\mathrm{CM}} - L_{\mathrm{arm}} \frac{di_{\mathrm{x,y}}}{dt} \tag{5.2}$$

$$u_{\mathrm{x,y}} \approx u_{\mathrm{x}} - u_{\mathrm{y}} - u_{\mathrm{CM}} \tag{5.3}$$

The total voltage across the SMs capacitors inside an arm is a reflection of the total energy stored within these capacitors. The energy content is controlled by the arm power, which can be expressed as in (5.4).

$$p_{\mathrm{x,y}} = u_{\mathrm{x,y}} i_{\mathrm{x,y}} = \left(u_{\mathrm{x}} - u_{\mathrm{y}} - u_{\mathrm{CM}}\right)\left(i_{\mathrm{x}}/3 + i_{\mathrm{y}}/3 + \Delta i_{\mathrm{x,y}}^{(x)} + \Delta i_{\mathrm{x,y}}^{(y)}\right) \tag{5.4}$$

To analyse the average arm power components, the following definition of the quantities from (5.4) is adopted:

$$u_{\mathrm{x}} = \hat{u}_{\mathrm{x}} \sin(\omega_{\mathrm{x}} t) \tag{5.5}$$

$$u_{\mathrm{y}} = \hat{u}_{\mathrm{y}} \sin\left(\omega_{\mathrm{y}} t + \Theta_{\mathrm{y}}\right) \tag{5.6}$$

$$u_{\mathrm{CM}}^{(x)} = \hat{u}_{\mathrm{CM}}^{(x)} \sin\left(\omega_{\mathrm{x}} t + \Theta_{\mathrm{CM,x}}\right) \tag{5.7}$$

$$u_{\mathrm{CM}}^{(y)} = \hat{u}_{\mathrm{CM}}^{(y)} \sin\left(\omega_{\mathrm{y}} t + \Theta_{\mathrm{CM,y}}\right) \tag{5.8}$$

$$i_{\mathrm{x}} = \hat{i}_{\mathrm{x}} \sin(\omega_{\mathrm{x}} t + \phi_{\mathrm{x}}) \tag{5.9}$$

$$i_{\mathrm{y}} = \hat{i}_{\mathrm{y}} \sin\left(\omega_{\mathrm{y}} t + \Theta_{\mathrm{y}} + \phi_{\mathrm{y}}\right) \tag{5.10}$$

$$\Delta i_{\mathrm{x,y}}^{(x)} = \hat{i}_{\mathrm{x,y}}^{(x)} \sin\left(\omega_{\mathrm{x}} t + \phi_{\mathrm{x}} + \phi_{\Delta,\mathrm{x}}\right) \tag{5.11}$$

$$\Delta i_{\mathrm{x,y}}^{(y)} = \hat{i}_{\mathrm{x,y}}^{(y)} \sin\left(\omega_{\mathrm{y}} t + \Theta_{\mathrm{y}} + \phi_{\mathrm{y}} + \phi_{\Delta,\mathrm{y}}\right) \tag{5.12}$$

It was mentioned previously that the two systems (*ABC* and *RST*) are assumed to have unequal frequencies. On the other hand, arm power components in (5.4) can have non-zero average values over their periods only in case when the voltage and current components involved are of equal frequencies. Consequently, only the power terms stemming from interaction between the equal-frequency voltages and currents will be considered. The following non-zero-average power terms can be obtained from (5.4):

$$P_{\mathrm{x}} \ : \ \frac{u_{\mathrm{x}} i_{\mathrm{x}}}{3} \rightarrow \frac{\hat{u}_{\mathrm{x}} \hat{i}_{\mathrm{x}} \cos(\phi_{\mathrm{x}})}{6} \tag{5.13}$$

$$P_{\mathrm{y}} \ : \ -\frac{u_{\mathrm{y}} i_{\mathrm{y}}}{3} \rightarrow -\frac{\hat{u}_{\mathrm{y}} \hat{i}_{\mathrm{y}} \cos\left(\phi_{\mathrm{y}}\right)}{6} \tag{5.14}$$

$$P_{\mathrm{CM,x}} \ : \ -\frac{u_{\mathrm{CM,x}} i_{\mathrm{x}}}{3} \rightarrow -\frac{\hat{u}_{\mathrm{CM,x}} \hat{i}_{\mathrm{x}} \cos\left(\Theta_{\mathrm{CM,x}} - \phi_{\mathrm{x}}\right)}{6} \tag{5.15}$$

$$P_{\mathrm{CM,y}} \ : \ \frac{u_{\mathrm{CM,y}} i_{\mathrm{y}}}{3} \rightarrow \frac{\hat{u}_{\mathrm{CM,y}} \hat{i}_{\mathrm{y}} \cos\left(\Theta_{\mathrm{CM,y}} - \phi_{\mathrm{y}}\right)}{6} \tag{5.16}$$

$$P^{(\mathrm{x})}_{\Delta \mathrm{x,y}} \ : \ u_{\mathrm{x}} \Delta i^{(x)}_{\mathrm{x,y}} \rightarrow \frac{\hat{u}_{\mathrm{x}} \hat{i}^{(x)}_{\mathrm{x,y}} \cos(\phi_{\mathrm{x}})}{2} \tag{5.17}$$

$$P^{(\mathrm{y})}_{\Delta \mathrm{x,y}} \ : \ -u_{\mathrm{y}} \Delta i^{(y)}_{\mathrm{x,y}} \rightarrow -\frac{\hat{u}_{\mathrm{y}} \hat{i}^{(y)}_{\mathrm{x,y}} \cos\left(\phi_{\mathrm{y}}\right)}{2} \tag{5.18}$$

Power components shown in (5.13)-(5.18) stem from interaction between internal arm currents and terminal voltages. The first two power terms represent active power components of a respective arm to/from its respective ac terminals. The following two terms represent power components resulting from interaction between injected common mode voltage and a portion of the respective terminal current. One should notice that the common-mode voltage $u_{\mathrm{CM}}$ can in general have multiple frequency components. In this case, it was assumed that it might contain components at frequencies equal to those of the two terminals. The last two power terms (5.17)-(5.18) represent interaction between the ac terminal voltages and internal circulating currents.

In normal operation, only the first two terms are present. However, these terms cannot be used as means of complete arm energy control, as that would require altering the terminal variables, which is in general not permitted.

To facilitate discussion, terminals labelled by $x = \{A, B, C\}$ will be referred to as "grid", whereas terminals labelled by $y = \{R, S, T\}$ will be referred to as "load", referencing to the case where the M3C is used as an interface converter between an electric grid and a synchronous generator/motor.

Injection of a common-mode voltage $u_{\mathrm{CM}}$ at grid/load frequency for the purpose of arm energy control might be used, though it imposes the need to have an additional voltage reserve in the SMs, in order to be able to generate the common-mode voltage on top of the two terminal voltage components. This would result in increased converter size and cost, and is generally not the best practice. The only case where injection of the common-mode voltage at grid/load frequencies can be performed is in

cases when either of the terminal voltages is absent, e.g. no load conditions. In such a case, available voltage reserve can be used to inject the common-mode voltage and use it for the energy control in conjunction with the terminal currents.

The last two power terms (5.17)-(5.18) are normally used for energy control, as they do not necessitate increased voltage capability of the converter, but only injection of the circulating currents. Given the fact that they are based on interaction of circulating currents and terminal voltages, this solution is preferable due to naturally high terminal voltage, which in turn result in relatively low circulating current requirements.

Two power terms that could also exist according to (5.4) are those stemming from the interaction between the injected common-mode voltage components and circulating currents at equal frequencies. These power terms were not considered for energy control as they would require injection of both common-mode voltages and circulating currents, and might be considered only under extreme circumstances.

One should also observe that the common-mode voltages of frequencies equal to the grid/load frequencies have only been considered. It might be the case where the common-mode voltages would naturally exist due to applied modulation technique (space-vector, min-max, etc.), yet they appear as triplen harmonics of the base frequency. Consequently, this would require injection of circulating currents at these frequencies, or at least at the 3rd multiple of the base frequency. Such a requirement is in general not a problem, as the arm current control bandwidth is typically sufficiently high to support tracking. However, amplitude of the 3rd harmonic of generated voltage due to modulation is typically 6 times lower compared to the fundamental component. This would result in 6 times higher circulating current reference compared to the case when circulating currents interact with terminal voltages. Therefore, neither this possibility is considered further.

## 5.3 Proposed arm energy control method

In the following analysis it will be assumed that the load-side terminal currents are determined by application (motor drive), and thus must not be altered by the energy control method. As the converter configuration is symmetrical, the same reasoning could be applied for the grid side, in case when the M3C interconnects the grid and a synchronous generator.

Nevertheless, to facilitate the discussion, analysed use case will assume a MV grid connected to a synchronous generator/motor by means of the M3C. Grid currents shall remain symmetrical under all circumstances, though their amplitude could vary, depending on the power flow and the needs of the energy controllers. Load (generator/motor) currents are application dependent, and are thus not subject to change due to the energy controller requirements.

Similarly to the regular MMC, energy content within each arm is calculated and most dominant frequency components are filtered out ($2\omega_x$, $2\omega_y$, $(\omega_x + \omega_y)$, $(\omega_x - \omega_y)$). Nine PI controllers are utilized to control energies of the nine arms. Their outputs are power references $P^*_{x,y}$ for each individual arm.

To realize such power references using the degrees of freedom expressed in (5.13)-(5.18), different strategies should be employed.

### 5.3.1 Energy control of the load-grouped clusters

The main assumption used for such energy control scheme is the availability of the grid voltage. While the load voltage might not be generated, i.e. equal to zero, the grid voltage is assumed to be always present, even in case of unbalanced grid conditions.

This permits to use arm currents at grid frequency to control the energy content within arms, based on the power law expressed in (5.17). Two constraints have to be met while devising such a control scheme: no influence on the load terminals, and symmetrical grid currents. Both constraints can be met if the energy control scheme is designed for clusters of arms comprising those arms connected to the same load terminals, as shown in **Fig. 5.2**. Namely, if symmetrical currents are generated in each arm of a cluster, these currents will sum-up to zero at their respective load terminal, thus assuring that there is no influence on the load. On the other hand, grouping the arms into clusters permits to satisfy the power needs of a cluster, while still drawing symmetrical currents from the grid.

Power requirements of a cluster are equal to the sum of the individual arm power requirements and the active power drawn by the load at respective node:

$$P^*_{\mathrm{cl,y}} = P^*_{\mathrm{a,y}} + P^*_{\mathrm{b,y}} + P^*_{\mathrm{c,y}} + P_{\mathrm{y}} \tag{5.19}$$

To meet such power requirements, symmetrical grid-frequency currents are used, with their references being calculated as follows:

$$\gamma i^*_{\mathrm{x,y}}(t) = \frac{2P^*_{\mathrm{cl,y}}}{3\left(\hat{u}^+_{\mathrm{x}}\right)^2} u^+_{\mathrm{x}}(t) \tag{5.20}$$

where $\hat{u}^+_{\mathrm{x}}$ represents the amplitude of the positive-sequence arm voltage component at grid frequency, while $u^+_{\mathrm{x}}(t)$ is its time-domain value for a particular phase.

Under balanced grid condition, the positive sequence component constitutes the complete grid-frequency voltage, while under unbalanced grid conditions, negative and zero-sequence voltage component might also be present. The sum of the three cluster current sets constitutes the grid current, which shall remain symmetrical, hence the usage of only positive-sequence voltage components

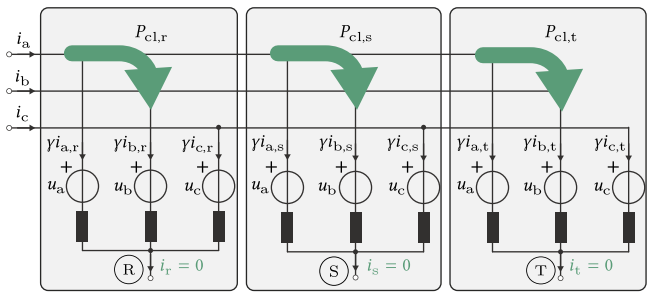


**Fig. 5.2** Grouping of the M3C arms into clusters connected to the same load terminals for the energy control purpose. Grid terminal currents $i_{\mathrm{a}}$, $i_{\mathrm{b}}$, $i_{\mathrm{c}}$ should remain symmetrical, while load currents $i_{\mathrm{r}}$, $i_{\mathrm{s}}$, $i_{\mathrm{t}}$ should remain equal to zero.

in (5.20). Regardless of the power needs of each individual cluster, the sum of the three sets of symmetrical currents represents the current drawn from the grid, and remains symmetrical.

Current references calculated as in (5.20) ensure that the power needs of each cluster are met. Thus obtained current references will be part of the total arm current reference, as it will be shown later.

One can notice that thus far presented control scheme ensures tracking of only three power requirements out of nine. Therefore, additional control actions are necessary.

### 5.3.2 Energy control of the grid-grouped clusters

As this control action is dependent upon the load-frequency voltages, two different strategies will be analysed, depending on the load voltage availability.

#### 5.3.2.1 Non-idle converter state

In case when the 3PH machine is in operation, and the voltage is generated across its terminals, it can be utilized to perform additional arm energy control actions, according to the power law expressed in (5.18). This state of the converter is referred to as "non-idle" state, as opposed to the state of operation where no voltages across machine terminals are generated, further referred to as "idle" state.

Following the same logic as before, arms can be regrouped into clusters comprised of arms connected to the same grid terminals, as shown in **Fig. 5.3**.

In order to maintain the effect of this control action invisible at the grid terminals, injected currents inside the cluster should sum up to zero, all while producing the desired cluster power reference. All arms within a single cluster have the same grid-frequency voltage component. To produce a non-zero power component on a cluster level, the sum of the injected grid-frequency arm currents must be greater than zero. Therefore, grid-frequency voltages cannot be used in such cluster grouping.

On the other hand, load-frequency voltages within a cluster configuration as in **Fig. 5.3**, constitute a 3PH symmetrical system. Therefore non-zero cluster-level power can be produced by injecting a set of symmetrical load-frequency arm currents. Due to their symmetry, their sum equals zero, so it does not impact the grid-side terminals.

To calculate current references for such a control action, one should determine power requirements of a cluster. Due to the fact that this control action remains internal, i.e. does not draw power from

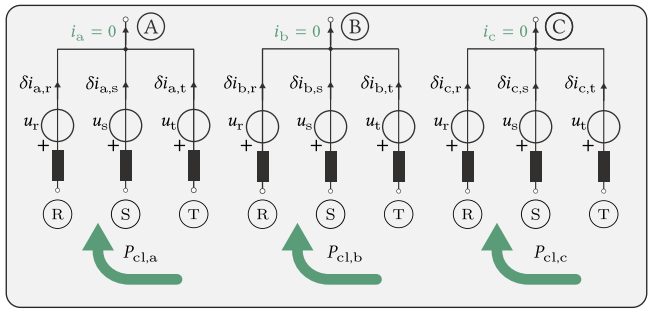


**Fig. 5.3** Grouping of the M3C arms into clusters connected to the same grid terminals for the energy control purpose. Grid terminal currents $i_a$, $i_b$, and $i_c$ should remain equal to zero.

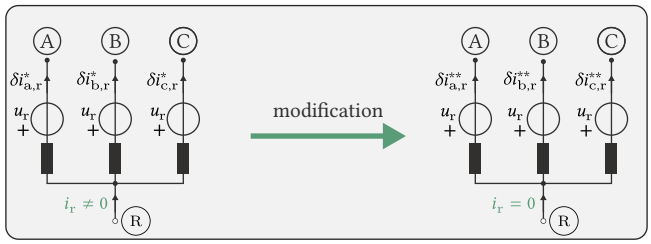


**Fig. 5.4** Illustration of the current modification effects for the energy control of grid-coupled clusters. Original current references at load frequency $\delta i^*_{x,y}$ are modified so that they do not influence the load terminals.

the M3C terminals, power requirements of a cluster are equal only to the power requirements of involved arm energy controllers:

$$P^*_{cl,x} = P^*_{x,r} + P^*_{x,s} + P^*_{x,t} \tag{5.21}$$

Arm current references at load frequency are calculated in the following manner:

$$\delta i^*_{x,y}(t) = \frac{2P^*_{cl,x}}{3(\hat{u}_y)^2} u_y(t) \tag{5.22}$$

It can be recognized that such arm current references have the opposite reference direction with respect to the current references generated at grid frequency. This is a consequence of the fact that the load-frequency voltages within arms have the opposite reference direction with respect to the grid frequency voltages, in order to counteract the load terminal voltages.

Due to the symmetry among the currents within a cluster, their sum at the grid terminals equals zero. However, due to different power requirements of individual clusters, amplitudes of the load-frequency arm currents are generally different among the clusters. As a consequence, undesired load-frequency currents appear at load terminals, which should remain internal to the M3C. Therefore, a modification of the generated current references is necessary, as illustrated in **Fig. 5.4**. Modification of the original current references $\delta i^*_{x,y}$ results in modified references $\delta i^{**}_{x,y}$ which sum-up to zero while achieving the same or similar power references.

Due to simplicity of implementation and its validity under both symmetrical and asymmetrical load conditions, a modification strategy similar to *Method II* is adopted here. It relies on subtraction of the zero-sequence component from the involved set of current references. It can be shown that the subtraction of the zero-sequence component from the current references has the same effect as the subtraction of the zero-sequence component from the cluster power references $P^*_{cl,a}$, $P^*_{cl,b}$, $P^*_{cl,c}$. The fact that the generated currents $\delta i^{**}_{x,y}$ remain within the converter means that they perform energy redistribution among the three clusters. Observing from the cluster power viewpoint, zero-sequence subtraction means that only differential power between the clusters is controlled, i.e. effectively only two power components.

#### 5.3.2.2 Idle converter state

This converter state might correspond to the case when the M3C is connected to both of its terminals, yet it does not provide any voltage at its load terminals, such as during machine standstill, or

STATCOM operation, i.e. providing only reactive power support to the grid.

In such a case, load-frequency circulating currents have no effects, and different means should be adopted. From the power equations (5.13)-(5.18) there are two possibilities: injection of the common-mode voltage $u_{\mathrm{CM}}$, at either grid or load frequency.

In the first case, common-mode voltage can interact with the existing grid currents, that are covering the converter losses, and thus provide energy control functionality. In the latter case, additional load-frequency circulating currents need to be generated. While one can opt for any of the two possibilities, only the first possibility is analysed here. One should note that similar logic as before can be followed even if the second option was chosen.

In case when there are no load currents, grid currents have small values, covering only the power losses of the switching converter. In such a case, no energy is drawn from the SM capacitors, and energy control actions, even if necessary, require negligible power levels. On the other hand, the M3C can operate as a STATCOM during the "idle" state, providing necessary reactive power to the grid. In such a case, grid currents exists, and can be used to control the energy of the converter in conjunction with the common-mode grid-frequency voltages. Although it might seem so, the first case is typically not unfavourable, even though the grid currents are almost negligible. Injection of high common-mode voltage would produce enough of arm power to cover the converter needs. This is a consequence of the fact that there are no currents in the converter, i.e. no sources of energy imbalance.

As the common-mode voltage of each grid-tied cluster should be in phase with the respective grid current, the common-mode voltage reference for each cluster $x$ is obtained as follows:

$$u^*_{\mathrm{CM,x}} = \frac{i_{\mathrm{x}}}{\hat{i}_{\mathrm{x}}} \hat{u}_{\mathrm{CM}} \tag{5.23}$$

The amplitude of the common-mode voltage $\hat{u}_{\mathrm{CM}}$ is determined depending on the available voltage reserve, and in case when the load voltage is equal to zero, it can be as high as the rated load voltage amplitude.

Three grid-tied clusters have different power requirements, while the common-mode voltage is determined by its amplitude and phase. Calculation of the common-mode voltage can be performed such that it reflects power requirements of different clusters, in the following way:

$$u^*_{\mathrm{CM}} = \frac{P_{\mathrm{cl,a}} u^*_{\mathrm{CM,a}} + P_{\mathrm{cl,b}} u^*_{\mathrm{CM,b}} + P_{\mathrm{cl,c}} u^*_{\mathrm{CM,c}}}{|P_{\mathrm{cl,a}}| + |P_{\mathrm{cl,b}}| + |P_{\mathrm{cl,c}}|} \tag{5.24}$$

In this way, common-mode voltage phase and amplitude are adjusted in order to reflect power requirements of specific clusters.

As a single common-mode voltage value is calculated, its product with the three phase currents sums-up to zero, meaning that the converter does not exchange active power with the grid. Instead, by means of common-mode voltage injection and its interaction with the grid currents, energy is redistributed among the clusters.

Depending on the operation mode, either of the two approaches can be selected, but both can be active at the same moment, with appropriate dynamic coefficient selection. In such a way, smooth switchover between the two modes of energy control can be achieved.

In conclusion, the previously described control actions ensure meeting five independent energy references in total, while to gain complete control over the M3C arms, nine control actions are necessary in total.

Therefore, additional four degrees of freedom should be utilized in order to gain full control over the arm energies.

### 5.3.3 Inter-arm energy distribution

The last control mechanism will redistribute the energy among the converter arms without considering specific clusters. Due to the fact that nine arm currents can be controlled, theoretically all nine arm power references can be respected. However, due to the constraint that the energy control actions should not alter the terminal currents, such control actions should remain internal to the converter.

It has been already stated that the grid voltage availability is assumed during the whole converter operation. Power references of all nine arms can be created by interaction of the grid-frequency arm currents and grid-frequency arm voltages, as illustrated in **Fig. 5.5**.

These current references are calculated as in (5.25). Nevertheless, due to arbitrary values of the power references, these currents do not generally sum up to zero, and should undergo modifications.

$$\Delta i^{*}_{\mathrm{x,y}} = 2\frac{P^{*}_{\mathrm{x,y}}}{\hat{u}^{2}_{\mathrm{x}}} u_{\mathrm{x}} \tag{5.25}$$

*Method II* approach can be used, where three current references entering a terminal node are grouped, and deprived of their zero-sequence component. The process is illustrated in **Fig. 5.6**, where such modification is applied first to the currents entering the nodes *R*, *S*, *T*, followed by regrouping the *modified* current references into those entering the nodes *A*, *B*, *C*, and applying the same procedure.

Due to the symmetry, the order of *Step 1* and *Step 2* could be reversed without influencing the end result. Finally obtained current references $\Delta i^{**}_{\mathrm{x,y}}$ are such that they ensure least power deviation from the original references, while ensuring that no terminal currents are affected.

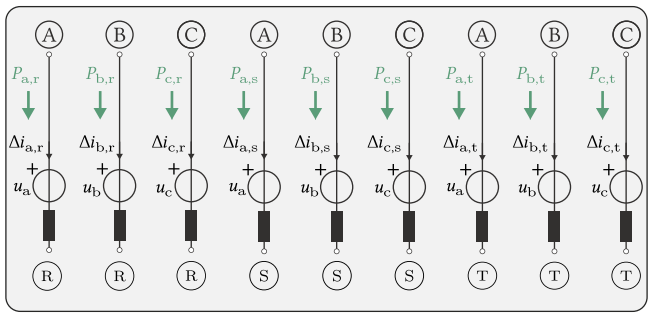


**Fig. 5.5** Arm power generation by means of grid-frequency circulating currents $\Delta i_{\mathrm{x,y}}$ and grid-frequency arm voltages $u_{\mathrm{x}}$ in nine converter arms.

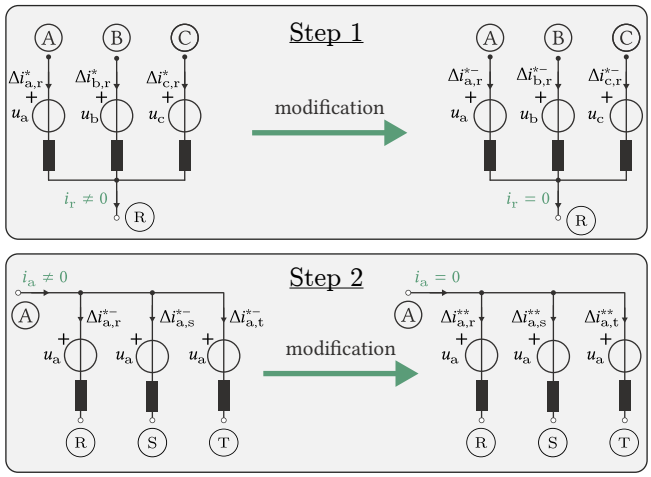


**Fig. 5.6** Modification of arm current references in order to provide decoupling from the terminal currents: (top) *Step 1* - performs modifications on current references belonging to the same load terminals; (bottom) *Step 2* - further modifications of modified current references belonging to the same grid terminals.

Given the fact that this modification is performed on six nodes, where currents of only five nodes are linearly independent, such modifications result in only four linearly-independent arm currents (nine initial currents undergo five nodal modifications). This results in four circulating currents, redistributing the energy among the arms.

With all previously-described control actions, arm energy control of the M3C is assured.

## 5.4 Implementation of the energy control scheme

Implementation of the proposed energy control scheme is shown in **Fig. 5.7**. Part a) shows nine energy controllers for nine arms, yielding arm power references.

Part b) shows energy control of load-grouped clusters, using grid-frequency arm current components $\gamma i^*_{\mathrm{x,y}}$. These current components are obtained from cluster power references $P^*_{\mathrm{cl,r}}$, $P^*_{\mathrm{cl,s}}$ and $P^*_{\mathrm{cl,t}}$, assuming a balanced load. This scheme can be applied even in case when the load active power is unbalanced among phases, by feeding the active power of each load terminal into the cluster power equation. Only positive sequence voltages are used, in order to avoid negative sequence currents in the grid during grid unbalances. Current references are calculated according to (5.20).

Part c) illustrates energy control of grid-grouped clusters, using load-frequency arm-current components $\delta i^*_{\mathrm{x,y}}$ in conjunction with the load-frequency arm voltages. One can observe that symmetrical load frequency voltages are assumed in this control scheme, whereas it can be equally applied if the load voltages were not symmetrical. The only difference in such a case is that the voltage amplitude $u_{\mathrm{y}}$, dividing the cluster power references $P^*_{\mathrm{cl,a}}$, $P^*_{\mathrm{cl,b}}$ and $P^*_{\mathrm{cl,c}}$, would need to be replaced by the three individual phase voltage amplitudes, obtained through SOGI or other means, as shown in **Chapter 4**.

Calculation of the current references $\delta i^*_{\mathrm{x,y}}$ is done according to (5.22). Further, currents are regrouped into the load-tied cluster currents, and modified through the current modification block. Its functionality is illustratively described in **Fig. 5.8**. Such modified current references $\delta i^{**}_{\mathrm{x,y}}$ are used for the arm energy control when the converter is in so-called "non-idle" operating mode.

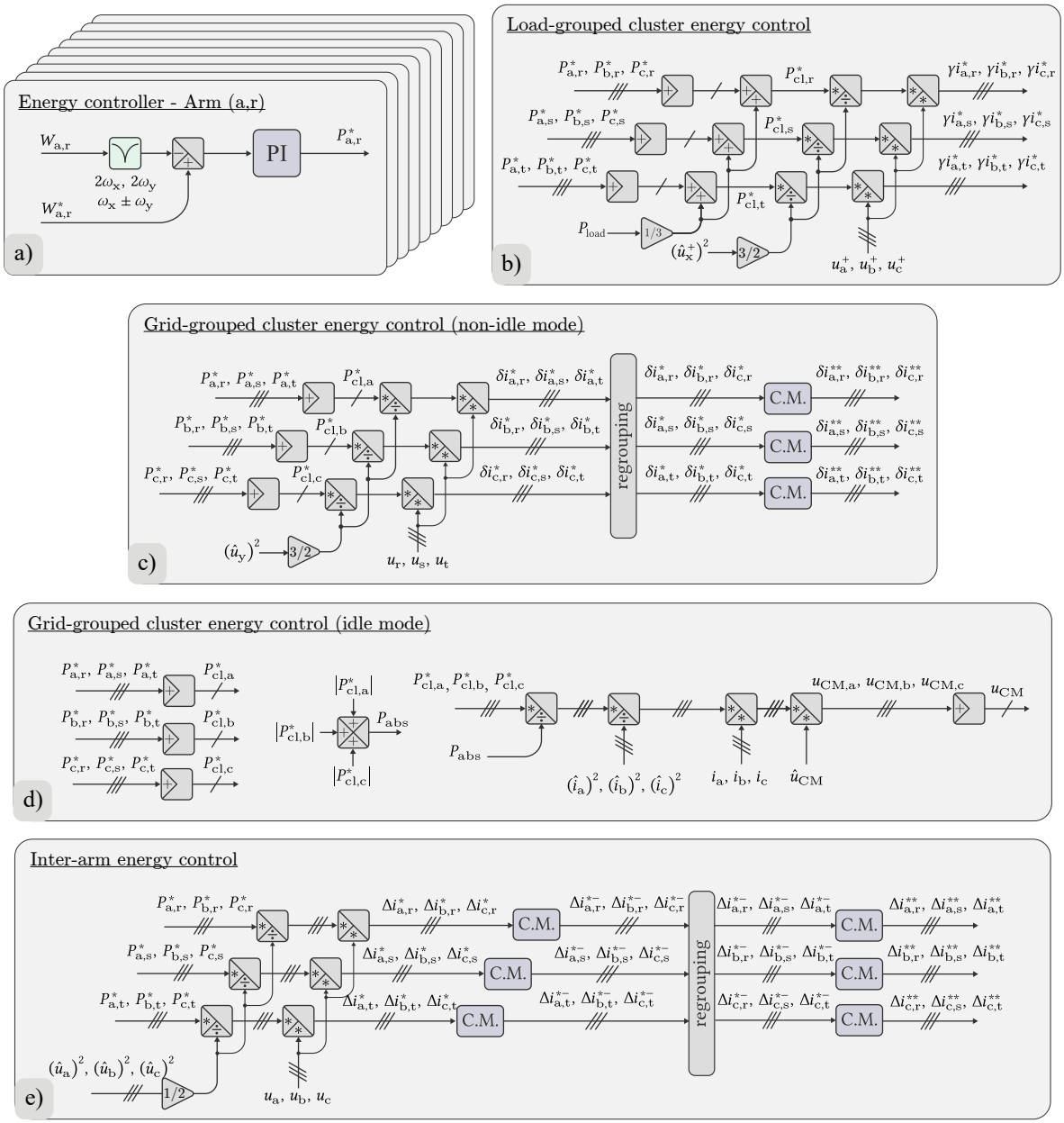


**Fig. 5.7** Implementation of the complete arm energy control scheme for the M3C converter: a) nine arm energies are measured, filtered and fed back to nine respective PI-based controllers, yielding nine arm power references; b) energy control of load-grouped clusters, yielding nine grid-frequency arm current references; c) energy control of grid-grouped clusters in non-idle mode, yielding nine load-frequency arm current references; d) energy control of grid-grouped clusters in idle mode, using the common-mode voltages; e) inter-arm energy control by means of grid-frequency circulating currents.

In case of "idle" operating mode, grid-grouped cluster power references are calculated (c.f. **Fig. 5.7.d**), and further used to calculate the common-mode voltage references, according to (5.24).

Finally, the inter-arm energy control is performed by generating the grid-frequency arm current references $\Delta i^*_{\mathrm{x,y}}$, from the respective arm power references, as illustrated in part e) of **Fig. 5.7**. It

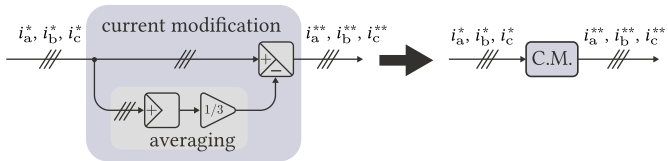


**Fig. 5.8** Description of the current modification block: reference currents are modified by subtracting their zero-sequence (average) component.

is important to note that the complete grid-frequency voltage component is used for such current reference generation, irrespectively of possible unbalanced grid conditions. This results in maximal utilization of grid voltages and minimal arm current references. Current references $\Delta i^*_{\mathrm{x,y}}$ are calculated according to (5.25), and further modified using the current modification block for all six nodes of the converter.

Finally, total arm current references are calculated taking into account the reference load currents and all previous control actions:

$$i^*_{\mathrm{x,y}} = i^*_{\mathrm{y}}/3 + \gamma i^*_{\mathrm{x,y}} - \delta i^{**}_{\mathrm{x,y}} + \Delta i^{**}_{\mathrm{x,y}} \tag{5.26}$$

Additionally, arm voltage references are determined based on grid and load voltage references (originating from respective current controllers), and calculated grid-frequency common-mode voltage:

$$u^*_{\mathrm{x,y}} = u^*_{\mathrm{x}} - u^*_{\mathrm{y}} - u^*_{\mathrm{CM}} \tag{5.27}$$

Other aspects of the converter control, such as the terminal and the arm current control, modulation and protection are not discussed in the thesis, even though all these control actions are implemented in the overall converter control.

So far, it can be assumed that the energy control of the M3C arms can be assured if its arm current and voltage references are determined as in (5.26) and (5.27). Nevertheless, its performance should be evaluated to confirm validity of the proposed scheme and its implementation.

## 5.5 Real-time HIL simulator description

An MMC converter rated for MV was developed in Power Electronics Laboratory for research purpose, as well as to support the MV laboratory infrastructure. To facilitate the development of control concepts for the MMC, a real-time (RT) HIL simulator was developed within the laboratory, described in [135], [136]. The control platform used in the MMC and RT HIL is based on ABB's AC 800PEC family of controllers, which are in charge of performing top-level MMC control tasks, such as converter pre-charging, control of terminal voltages and currents, energy control, exchanging references and measurements with the SMs, etc. The same platform is utilized to develop an RT HIL simulator of the M3C converter, shown in **Fig. 5.9**.

Converter SMs inside the HIL simulator are realized in a hybrid manner. Namely, the control part of the SMs is realized by the so-called *Control cards*, shown in **Fig. 5.9**, where the local SM controller is implemented, based on TI TMS320F28069 digital signal processor (DSP). Control cards also host a

communication interface between the SM controller and the top-level control. Power parts of the SMs, i.e. IGBTs, gate-drivers, DC capacitor, are modelled within a Plexim RT-Box 1, and there are in total eight SMs modelled within a single RT-Box. Control cards are interfaced to an RT-Box through the interface board, whereas they are communicating with the top-level controller (AC 800PEC) using the fibre-optic interface. Such a structure represents a single arm of the converter, and is referred to as *Arm unit* in **Fig. 5.9**. There are in total nine such units, each one modelling an arm. Due to the same communication interface and the same software running on the DSP of a control card, as it would in the real SM, it is achieved that there is no difference between the HIL-modelled arm and an arm in the real converter, from the perspective of the top-level controller.

Grid and load side of the converter, as well as the interconnections between the arms are modelled using a separate RT-Box and interface board, labelled as *Application unit* in **Fig. 5.9**. Thereby, all the power stages of the converter are modelled in the RT HIL simulator, whereas the control hardware corresponds to the one found in the real converter. Consequently, top-level control methods, as well

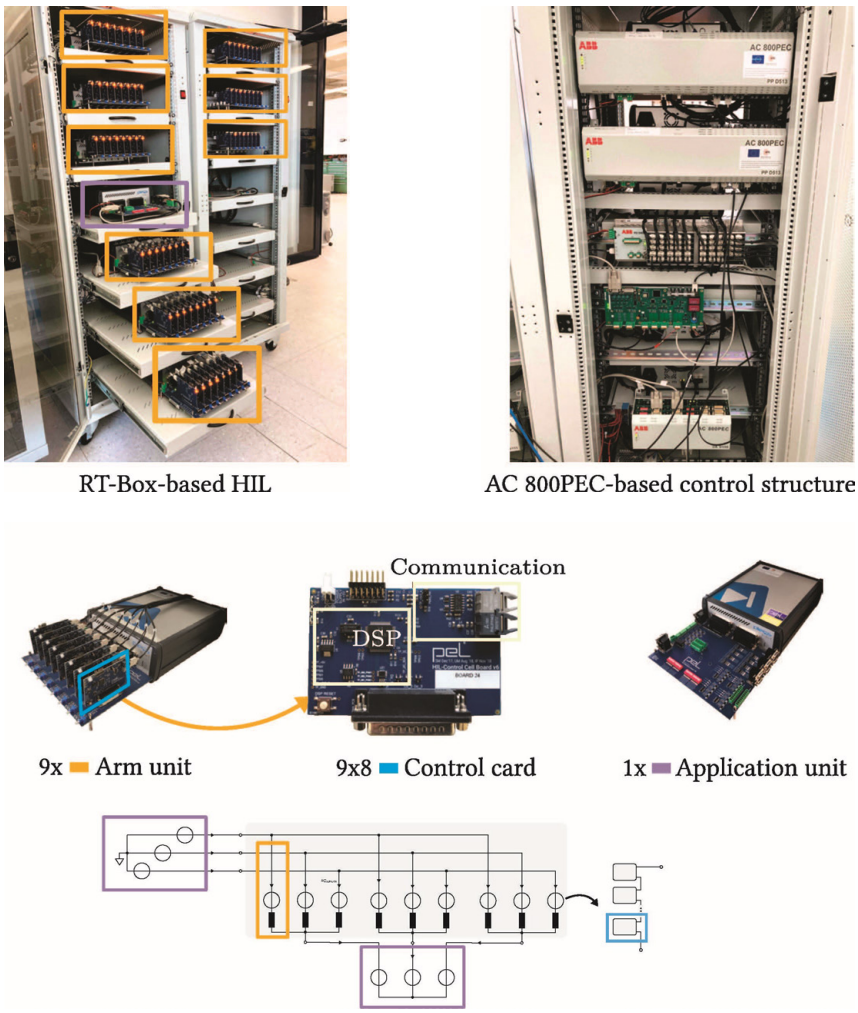


**Fig. 5.9** The structure of the HIL system modelling the M3C. RT-Box-based HIL consists of 9 arm units, and one application unit. Each arm unit contains N=8 control cards, corresponding to eight SMs within an arm. AC 800PEC control structure acts as the main control hardware of the converter.

as SM-level control (implemented on DSPs), can be safely developed and tested using such a system, without making difference between the real converter and the HIL system.

Additionally, it permits to validate the proposed control algorithms using the HIL system, without compromising validity of the results.

## 5.6 Control validation

The presented control concept was tested on the RT HIL simulator, modelling the M3C converter which interfaces a medium-voltage grid, and a synchronous machine, as a typical use case of the M3C [29], [137]. Parameters of the grid, converter and machine are provided in **Tab. 5.1**.

**Tab. 5.1** Physical and control parameters of the simulated M3C converter. The simulated converter represents a possible future solution, whereas the synchronous machine corresponds to the machine used in the laboratory.

| Parameter | Label | Value |
|---|---|---|
| Grid voltage (line-line) | $U_g$ | 3.3 kV |
| Grid voltage frequency | $f_g$ | 50 Hz |
| Converter rated power | $S_n$ | 250 kVA |
| No. of SMs per arm | $N$ | 8 |
| SM capacitance (tolerance ±5%) | $C_{SM}$ | 2.25 mF |
| Arm inductance (tolerance ±10%) | $L_{arm}$ | 2.5 mH |
| IGBT switching frequency | $f_{SW}$ | 1 kHz |
| Machine voltage (line-line) | $U_m$ | 2.1 kV |
| Machine rated power | $S_m$ | 170 kVA |
| Machine pole pairs | $p_m$ | 2 |
| Machine rated speed | $n_m$ | 500 rpm |
| Machine rated torque | $T_m$ | 3000 Nm |

The first test scenario is such that the machine is in the idle mode, i.e. at zero speed. Regardless of the fact that the machine is not operating, the converter should be synchronized to the grid, and control its arm energy content. Leftmost part of **Fig. 5.10** shows that the converter maintains the arm voltages around the predefined value during this operating mode. In addition, at $t = 1.12$ s voltage references of the SMs in two arms are modified from $v_c^* = 680$ V to $v_c^* = 710$ V and $v_c^* = 650$ V, and set back to the original reference at $t = 1.8$ s. In both cases the voltage references are attained within $\Delta t = 200$ ms.

The next scenario is shown as the middle plot of **Fig. 5.10**. It represents the machine speed-up to the rated speed, starting at $t = 6.2$ s, and load torque rising to the rated value, starting at $t = 6.7$ s. It can be observed that the arm voltages remain constant throughout the whole transition process, which verifies good performance of the presented control method.

While different transitions between the two scenarios might be adopted, the approach adopted here was the simplest one. Namely, for operating modes where the load voltage was higher than half

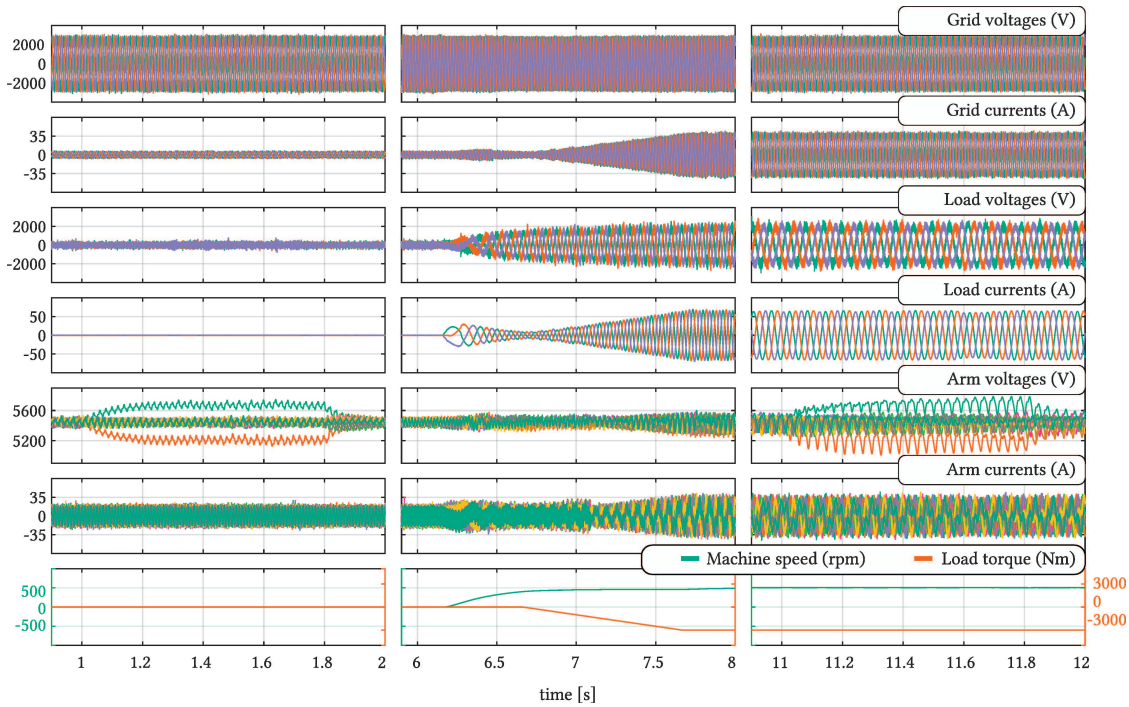


**Fig. 5.10** Results obtained from the RT HIL simulator. The leftmost plot shows relevant variables of the converter and the machine in idle mode. Energy references of two arms are changed from their rated values to demonstrate the effectiveness of the control principle in this mode. The middle plot shows the performance of the converter during dynamic conditions, i.e. the machine speed-up and the load torque increase. The rightmost plot demonstrates the performance of the energy control method in presence of the load voltage.

of its rated value, the load-frequency circulating currents for energy control were used, otherwise grid-frequency common-mode was injected. As it has been demonstrated, hard switch between the two does not cause any problem in the converter operation, which can be only improved by introducing a soft transition between two operating modes.

The rightmost plot in **Fig. 5.10** shows the converter operation at the rated speed and rated load torque. As in the first test scenario, voltage references of two arms were changed, and energy control was able to ensure reference tracking.

**Fig. 5.11** demonstrates the converter's capability to control its energy content under different dynamic conditions, namely during the speed reversal (leftmost plot), negative speed of the machine (middle plot), as well as during the machine de-loading and slowing down.

It is important to notice from **Fig. 5.10** and **Fig. 5.11** that the grid and load currents remain unaffected by the energy control actions. In addition, transition between different operating modes of the machine, and thus between the two energy control scenarios, remains seamless.

Finally, to verify performance of the presented control method under unbalanced grid conditions, single-phase-to-ground fault in the grid is simulated during both motor mode (c.f. **Fig. 5.12**) and idle mode of operation (c.f. **Fig. 5.13**). In both cases, arm voltages remained unaffected, thus demonstrating capability of the two control scenarios to properly work under unbalanced grid conditions.

Presented results show validity of the presented control methods under realistic operating conditions.

They show that the converter voltages are maintained around their reference values, and that converter terminals are not influenced by such control actions.

## 5.7 Discussion

The presented results verify the effectiveness of the proposed energy control method, under different imbalances, speed (frequency) reversal, grid unbalanced conditions, as well as under no-load operation. Compared to the methods based on double $\alpha\beta 0$ transformations, implementation of the method is simpler, using only the real-time values of the grid and load quantities, without multiple $\alpha\beta 0$ and $dq$ transformations.

Compared to the solution proposed by [130], bulky matrices with real-time variable elements are omitted, whereas the transition between the low-frequency (low load voltage) and high-frequency operating modes can be seamlessly performed. Additionally, the proposed solution was verified under unbalanced grid conditions, even under combined unbalance and no-load conditions, in contrast to [130].

Comparing the solution against another simple solution, proposed in [131], the solution in [131] cannot ensure an arbitrary energy control under normal conditions, neither can it ensure decoupling of the internal balancing currents from the terminal currents under grid faults. Therefore, although

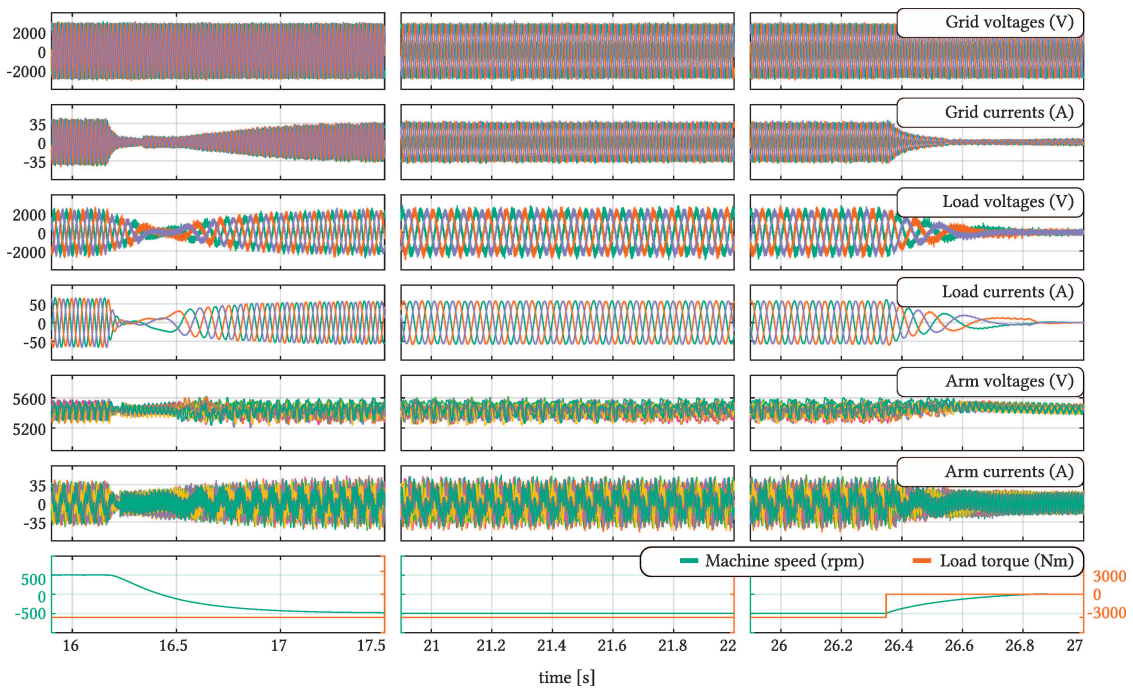


**Fig. 5.11** Results obtained from the RT HIL simulator. The leftmost plot shows the performance of the energy control method during the speed reversal of the synchronous machine. Even though the energy control changes between the idle and non-idle, and back to idle mode, the arm voltages remain unaffected and follow their reference. The middle plot demonstrates the effectiveness of the control principle in the generator mode of operation. The rightmost plot shows that despite the sudden de-loading, followed by the machine slowing-down, the effectiveness of the energy control is not compromised.

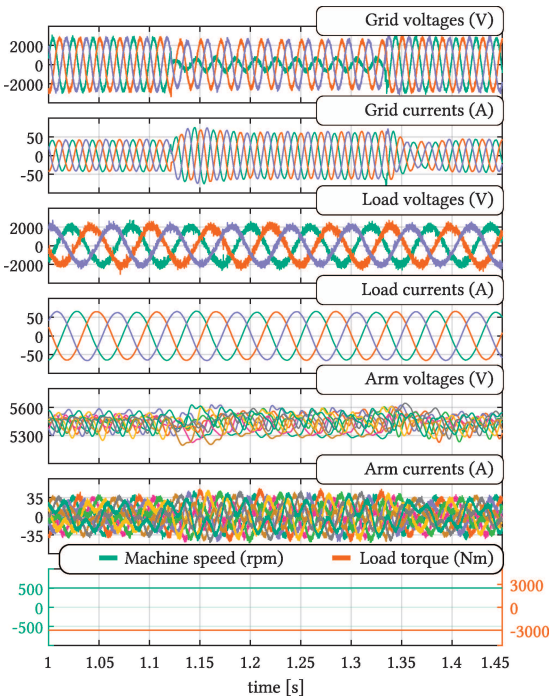


**Fig. 5.12** Performance verification of the energy control under unbalanced grid conditions. The synchronous machine is in the motor mode of operation, so the energy control is achieved using the load voltages.

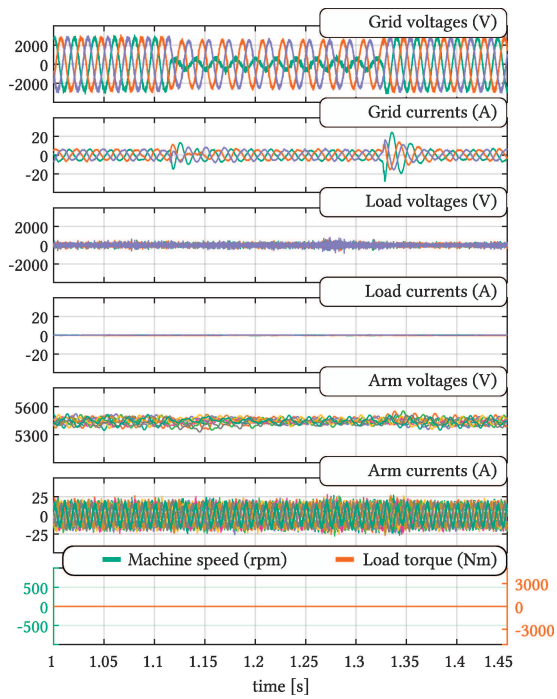


**Fig. 5.13** Performance verification of the energy control under unbalanced grid conditions. The synchronous machine is in the standby mode, so the energy control is achieved using the common-mode voltages- the idle mode.

the solution [131] seems as the simplest one, it in fact does not perform well under all operating modes.

One might argue that the proposed solution does not preserve all the power references yielded by the energy controllers, due to the current modification blocks. While this claim is true, the current modification block is optimized so as to minimize circulating currents imposed in the converter arms, while still ensuring the energy balancing under all conditions.

Finally, simplicity of implementation, coupled with the fact that the current modification is optimized to reduce the current stress on the converter while ensuring an arbitrary energy control, make this solution unique, simple to understand and implement, and robust under various operating modes.

## 5.8 Summary

In this chapter a novel energy control scheme for the M3C was proposed. First, the energy control mechanisms were identified, along with constraints that should be accounted for.

Further, the energy control strategy was methodologically developed, analysing the power needs of the arms, but also the available degrees of freedom. Energy control was at first performed on the cluster level, namely for arm clusters connected to the same load terminals. This control action benefits from the interaction of the grid-frequency arm voltages and the grid currents, all while preserving their symmetry. This control action ensures that each cluster receives from the grid the

amount of energy it needs.

To further exploit the degrees of freedom, the arms were further regrouped into the clusters connected to the same grid terminals, which appear symmetrical from the load side. For this control action two different strategies were adopted, based on the availability of the load voltage. In case when the load voltage were available, load-frequency circulating currents were injected, while in case when the load voltage were not available, a grid-frequency common-mode voltage was injected, interacting with the grid-frequency currents. In both cases, such control actions redistributed the total converter energy among the clusters of arms connected to the same grid terminals.

Remaining degrees of freedom in the energy control were used for the internal energy exchange between the converter arms, irrespectively of the cluster. Four circulating currents were created using the current modification strategy described in **Chapter 4**, which interact with the grid voltages.

It is important to note that the proposed control methods ensure arbitrary arm energy control, and it is applicable under both symmetrical and asymmetrical grid/load conditions. Their applicability was also demonstrated under the no-load voltage condition, as well as during the machine (load) speed (frequency) reversal. The control performance under all above-mentioned conditions was demonstrated using an RT-HIL M3C demonstrator, showing no difference with respect to the control system found in the actual converter.

Finally, a brief reflection on other M3C energy control solutions was done, highlighting advantages and disadvantages of the proposed method with respect to the other solutions.

# 6

# HIL-Aided Development of a Medium Voltage Test Platform for MMC Submodules

*The development of a medium-voltage, high-power modular multilevel converter is a complex project, which involves a proper insulation coordination, thermal management, different layers of protection and supervision, rather complex control, as well as a proper submodule design. Given such a complexity, and cost of the converter, commissioning of a medium-voltage converter is a challenging task, which has to be undertaken with great care and in several steps. Both the control software and the prototype hardware have to be independently tested under real operating conditions, before they are merged into a functional converter. This chapter presents development of a test platform, used for testing hardware and software features of the MMC SMs. The platform was developed with the aid of a HIL system, where important test scenarios were verified, prior to being carried out on the physical SMs. The HIL system is based on the same control architecture, real-time simulator and arm model, as the HIL system used for the development and testing of the converter-level control. The test platform was primarily used to expose the SMs to the electrical and thermal stresses, equivalent to those in the real converter. In addition, it also served to develop and test the SM-level control, in particular distributed current and voltage control. Finally, by comparing the results obtained on the HIL system and experimental test platform, fidelity of the HIL system used for development of the converter-level control can be successfully assessed.*

## 6.1 Motivation

Due to the high interest among researchers for the MMC and its deployment in different power conversion applications, many research laboratories have developed prototypes of the MMC, mainly as a test-bed for different control algorithms [34], [138]–[151]. Most of the developed prototypes are downscaled low-voltage, low-power prototypes, with the voltage ratings lower than 1000 V and power ratings not exceeding a few kW. Notable exceptions can be found in [138] where a 2 MW-rated prototype was developed, as well as recently presented SiC-based MMC prototype [151] with power rating of 1 MW.

To support research interests in MV applications, there is a need for a reliable and flexible MV power converter, which can perform different conversion tasks, and serve as a platform for testing novel control concepts. For such reasons, an MV high-power MMC converter is developed, with a possibility to serve different applications, as presented in **Fig. 6.1**.

For the moment, only the MMC configuration shown in **Fig. 6.1.a** is realized, although the developed SMs and the control platform allow to seamlessly realize other configurations from **Fig. 6.1**.

In general, the development of any MV converter within a research laboratory is a complex task,

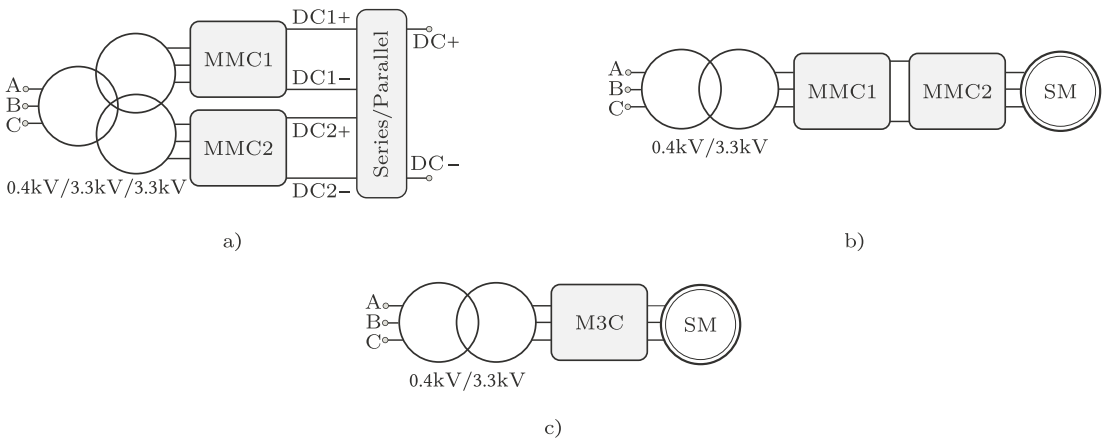


**Fig. 6.1** MMC configurations under development: a) MVdc power amplifier- either series or parallel connection of the two MMC units at the dc terminals; b) B2B connection of two MMCs used for powering a synchronous machine (SM); c) matrix/direct MMC (M3C) used as an interface between two ac systems/for powering a synchronous machine.

which involves a multitude of design constraints to be taken into account, either separately, or simultaneously. Because of high voltage and relatively high current ratings, insulation coordination [152] as well as thermal management [153] have to be carefully conducted. Cost of the equipment, as well as complexity in terms of a high number of SMs in the MMC, call for different layers of protection and supervision, which would minimize the risk of a great damage in case of undesired scenarios. Due to the complex structure involving dozens of SMs, main control of the converter has to be carefully developed and commissioned. Finally, in-house developed SMs [154]–[156], being the core of the MMC, have to be tested under realistic scenarios before their deployment into the converter.

In recent years HIL based digital-twins gained significant importance in rapid control prototyping of different converter types. Many researchers opt for demonstrating their control concepts solely on HIL systems, which with a great accuracy emulate the behaviour of the modelled converter [157]–[161]. In order to design and test the converter-level control software, a HIL system, based on PLEXIM RT-Box and ABB's AC800PEC industrial controller, was developed within the laboratory, mimicking the power hardware of the MMC discussed herewith [135], [161], [162].

In parallel, an MV test platform was developed to test the in-house-developed MMC SMs, exposing them to the electrical and thermal stresses identical to the ones experienced under real operating conditions, for various MMC configurations. The developed test platform allows for testing multiple SMs at once, which to a great extent reduces the effort and time needed for the converter commissioning. In addition, it allows for testing the SM-level control, in particular, the distributed current control and local voltage balancing. The test platform development was aided by a HIL system, based on the same control architecture, real-time simulator, and arm (branch) model as in the HIL system used for the converter-level control development. As a result, besides being used to test the SMs under different operating conditions and MMC configurations, the presented test platform is also utilized for fidelity verification of the HIL system developed for the purpose of the converter-level control design.

In the following sections a comprehensive insight into the development process of such an MV test platform is provided, along with the applied control concepts. Results collected both from the HIL system and the experimental test platform are presented and mutually compared.

## 6.2 MMC configurations and operating conditions

The core element of any MMC topology is an SM, typically realized as the HB type in applications which do not require dc terminal voltage reduction, or dc fault blocking capability. In case where the dc terminal voltage reduction is necessary, as well as in the M3C topology, the FB type SM is often used.

To have a reliable SM, that could be used in any application of interest, it is necessary to expose it to the electrical and thermal stresses during the testing phase, identical to the ones found in real applications. Therefore, this section presents different electrical requirements in terms of voltage and current stress, typical for the applications of interest. Derived currents and voltages will be used as references in the tests presented in Sections 6.5 and 6.6.

To support different research activities in the MV domain, there are several MMC-based converter architectures that are relevant for the work presented here, as shown in **Fig. 6.1**. One such an architecture is an MVdc power amplifier, i.e. a four quadrant converter able to act either as an MVdc voltage or current source. The converter is devised to utilize an MV transformer with two secondaries (normally used with a twelve-pulse rectifier), and two MMCs connected to each set of transformer secondary windings (c.f. **Fig. 6.1.a**), with a possibility to connect in series or in parallel their dc terminals, thus extending its voltage, or current capability, respectively [163]. A similar MVdc platform is presented in [164], [165]. Each unit (MMC) is rated at 250 kVA, and can generate a voltage at its dc terminals within the range of ±5 kV.

The second configuration of interest is the B2B connection of two MMCs (c.f. **Fig. 6.1**.b), which can be used as an MV drive, or as an interface converter for a pumped-hydro synchronous machine [73], [166]. When operating in a low-frequency region, there is a need for the dc link voltage reduction, as shown in [73].

Another application where the B2B connection of two MMCs can be used is a model of an HVdc transmission line, where the MMC is often found at each end of the transmission line. The simplest case of only two HVdc ports can be represented by a B2B connection of the two MMCs. Apart from blocking the dc faults, this application also requires operation under reduced dc voltage conditions, as a preventive measure to avoid flashovers under unfavorable atmospheric conditions [167].

The third configuration of interest, the M3C (c.f. **Fig. 6.1.c**), is not subject of the upcoming analyses and testing, even though the realized SMs can be seamlessly integrated into such a converter.

Given the configurations of interest, the MMC operation under rated and reduced dc terminal voltage is studied as a relevant operating condition. To support the reduced dc voltage operation, the SM is realized as a FB type. In any case, operating principles of the two analysed configurations correspond to the standard ac-dc MMC operation, with a variable dc terminal voltage. Hence, referring to a single MMC, arm voltages and currents are defined as:

$$u_{\mathrm{dc,arm}} = m_{\mathrm{dc}} v_{\mathrm{c}}^{\Sigma,n} \tag{6.1}$$

$$u_{\mathrm{ac,arm}} = -m_{\mathrm{ac}} v_{\mathrm{c}}^{\Sigma,n} \sin(\omega t) \tag{6.2}$$

$$i_{\mathrm{dc,arm}} = \frac{1}{3} I_{\mathrm{dc}} \tag{6.3}$$

$$i_{\mathrm{ac,arm}} = \frac{1}{2}\hat{i}_{\mathrm{ac}} \sin(\omega t + \phi) \tag{6.4}$$

where $m_{\mathrm{dc}}$ and $m_{\mathrm{ac}}$ represent dc and ac modulation indices, defined with respect to the rated total arm voltage $v_{\mathrm{c}}^{\Sigma,n}$, i.e. with respect to the nominal voltage available in the arm SMs. Amplitude and phase angle of the ac terminal current are given by $\hat{i}_{\mathrm{ac}}$ and $\phi$, whereas the dc terminal current is denoted as $I_{\mathrm{dc}}$. Arm power can be accordingly expressed as:

$$\begin{aligned} p_{\mathrm{arm}} =& u_{\mathrm{arm}} i_{\mathrm{arm}} = (u_{\mathrm{ac,arm}} + u_{\mathrm{dc,arm}})(i_{\mathrm{ac,arm}} + i_{\mathrm{dc,arm}}) = \underbrace{-\frac{1}{4} m_{\mathrm{ac}} \hat{i}_{\mathrm{ac}} v_{\mathrm{c}}^{\Sigma,n} \cos(\phi)}_{P_{\mathrm{ac}}} + \underbrace{\frac{1}{3} m_{\mathrm{dc}} I_{\mathrm{dc}} v_{\mathrm{c}}^{\Sigma,n}}_{P_{\mathrm{dc}}} \\ &+ \underbrace{\frac{1}{2} m_{\mathrm{dc}} \hat{i}_{\mathrm{ac}} v_{\mathrm{c}}^{\Sigma,n} \sin(\omega t + \phi) - \frac{1}{3} m_{\mathrm{ac}} I_{\mathrm{dc}} v_{\mathrm{c}}^{\Sigma,n} \sin(\omega t)}_{P_{1\mathrm{st}}} + \underbrace{\frac{1}{4} m_{\mathrm{ac}} \hat{i}_{\mathrm{ac}} v_{\mathrm{c}}^{\Sigma,n} \cos(2\omega t + \phi)}_{P_{2\mathrm{nd}}} \end{aligned} \tag{6.5}$$

To maintain the energy balance within an arm, an average ac and dc power should be equal under steady-state conditions, which establishes a relationship between the ac and dc current components, given in (6.6), resulting in the arm dc current reference $i_{\mathrm{dc}}^{*}$.

Harmonic arm power components only contribute to the arm energy ripple, or voltage ripple in the SM capacitors, therefore they should preferably be cancelled. The second harmonic power fluctuation ($P_{2\mathrm{nd}}$ in (6.5)) is identical in both arms of a phase in a standard MMC, and can thus be cancelled by injecting a second harmonic circulating current, which interacts with the dc voltage component [35]. This current component reference is given by (6.7) and can be fully or partially injected, depending on the adopted trade-off between the capacitor ripple tolerance and increased power losses [76].

$$i_{\mathrm{dc,arm}}^{*} = \frac{I_{\mathrm{dc}}}{3} = \frac{m_{\mathrm{ac}}}{m_{\mathrm{dc}}} \frac{\hat{i}_{\mathrm{ac}}}{4} \cos(\phi) \tag{6.6}$$

$$i_{2\mathrm{nd}}^{*} = -\frac{m_{\mathrm{ac}}}{m_{\mathrm{dc}}} \frac{\hat{i}_{\mathrm{ac}}}{4} \cos(2\omega t + \phi) \tag{6.7}$$

Finally, the arm voltage consists of the dc and ac components, given by (6.2) and (6.1), whereas the arm current consist of the dc, ac and an optional second harmonic component, given by (6.6), (6.4), and (6.7), respectively. Modulation indices $m_{\mathrm{ac}}$ and $m_{\mathrm{dc}}$ can theoretically take any value within the

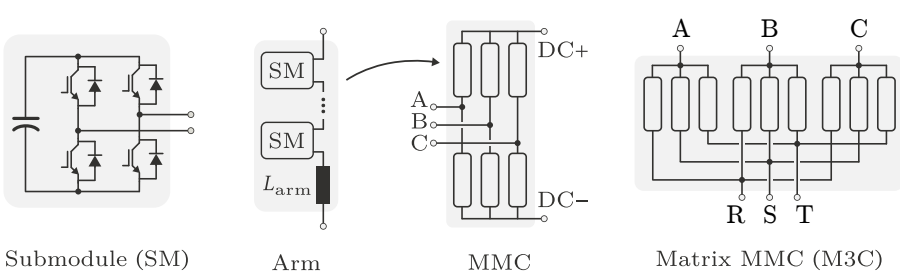


**Fig. 6.2** The structure of an MMC converter: a FB SM is utilized as a core element of an MMC, given the operating requirements; the MMC arm, as a common element to all MMC configurations of interest; layouts of a standard MMC and a matrix MMC topology.

range [-1, 1], yet the sum of their absolute values must not exceed unity. For a fixed grid voltage connection, rated arm voltage is selected such that the ac modulation index $m_{ac} \approx 0.5$, while the dc modulation index $m_{dc} \leq 0.5$.

## 6.3 Test platform description

To test the SMs under realistic condition, a test platform was developed taking into account the following requirements:

- it should be able to generate the same voltage and current waveforms as those that will be present in the real MMC, for different operating modes;
- it should be flexible so as to offer seamless reconfiguration between different MMC converter structures (MVdc power amplifier, B2B connection of the two MMCs, M3C configuration, shown in **Fig. 6.1**);
- it should offer a possibility to test various control software and hardware concepts, such as the distributed voltage and current control, protection features, etc.

From the theory of the MMC [23], [67], [85], [168], [169] and M3C [33], [100], [170], and observing these two topologies shown in **Fig. 6.2**, it can be concluded that all arms are exposed to the same voltage and current stress in a given MMC topology. Therefore, to reproduce the real circuit conditions, it is sufficient to observe only a single arm.

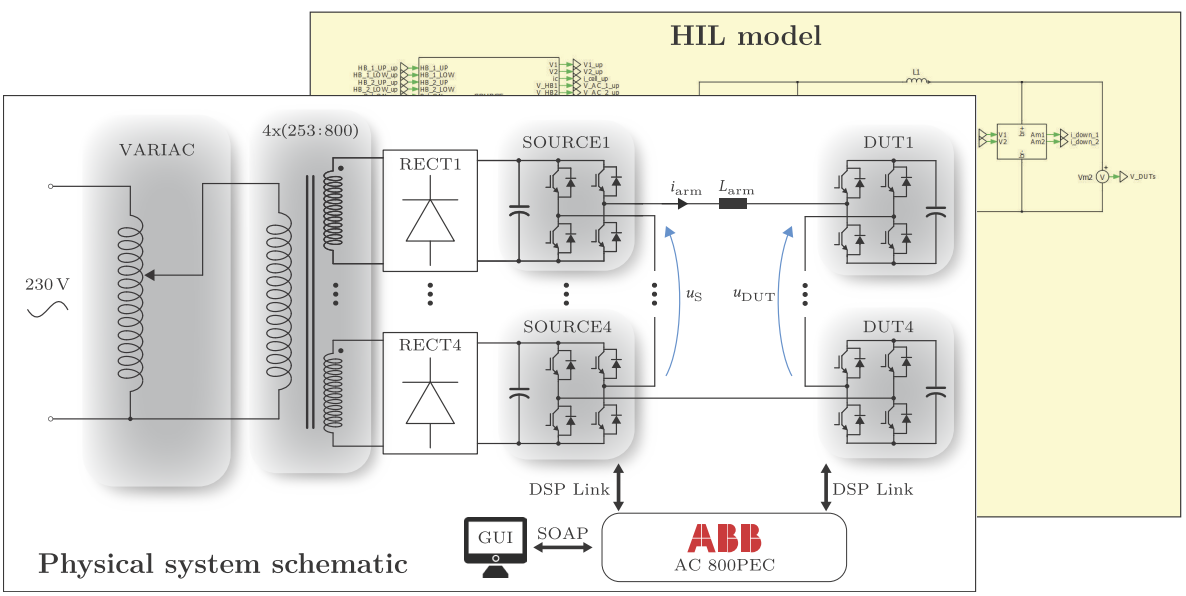


**Fig. 6.3** Electrical schematic of the realized test platform (top layer), and HIL model of the power part of the test platform, developed in Plexim RT-Box (bottom layer). Both the experimental tests and HIL tests are controlled by AC 800PEC (main controller). Communication between the main controller (AC 800PEC) and the SMs is achieved through fibre-optic links.

### 6.3.1 Experimental test platform

Electrical schematic of the realized test platform is shown in **Fig. 6.3**. As a trade-off between complexity and a good representation of an arm, the test platform is realized with $N = 4$ SMs per arm, further referred to as device under tests (DUTs), where the associated SMs are labelled as DUT1..DUT4.

Reduced number of SMs per arm with respect to $N = 8$ in the reference converter still allows for generating multilevel voltage waveforms, testing of the SM voltage balancing and distributed current control concept, thus accurately mimicking conditions in the real prototype. Parameters of the MMC prototype and of the realized test platform are given in **Tab. 6.1**, per arm, and do not depend on the actual MMC configuration.

To mimic the external circuit conditions, as well as to enable charging of the DUTs capacitors, another arm is introduced, consisting of the same, but externally supplied FB SMs, further referred to as source SMs, and labelled as SOURCE1..4. In-house developed MMC SM is shown in **Fig. 6.4**, whereas a simplified structure of its main circuits is shown in **Fig. 6.6**. It consists of the power board, which hosts the IGBT module, dc capacitors, bypass thyristors and relay, and the control board, where auxiliary power supply, gate-drivers, protection logic, DSP-based controller and communication are located [154].

Two arms are interconnected by an inductor, which emulates an arm inductor in the MMC prototype, enabling current control and limiting the current ripple. Source SMs are supplied from the four galvanically-isolated dc supplies, realized as four diode rectifiers (RECT1..RECT4), connected to the four secondaries of the step-up transformer. Adjusting the primary voltage of the step-up transformer with variac enables adjustment of the source SMs dc voltages.

Both the source SMs and DUTs are controlled by the industrial controller from ABB (AC 800PEC) [171], further referred to as the main controller. The main controller benefits from a floating-point CPU, as well as a high speed FPGA. It is programmable using MATLAB®/ Simulink®, which greatly facilitates control development. Communication between the SMs and the main controller is achieved through fibre-optic links, which are insusceptible to the electro-magnetic interference, and provide galvanic insulation. The whole process is monitored and controlled by a graphical user interface

**Tab. 6.1** Physical and control parameters of the real MMC converter prototype and its equivalent test platform.

| Parameter | Label | Real prototype | Test Platform |
|---|---|---|---|
| Number of SMs per arm | $N$ | 8 | 4 |
| Rated SM voltage | $v_c^n$ | 680 V | 680 V |
| Rated arm voltage | $v_c^{\Sigma,n}$ | 5.44 kV | 2.72 kV |
| Apparent arm power | $S_n$ | 41.67 kV | 20.84 kV |
| SM capacitance | $C_{SM}$ | 2.25 mF | 2.25 mF |
| Arm inductance | $L_{arm}$ | 2.5 mH | 5 mH |
| Switching frequency (per IGBT) | $f_{SW}$ | 1 kHz | 1 kHz |
| Switching frequency of a FB SM | $f_{PWM}$ | 2 kHz | 2 kHz |

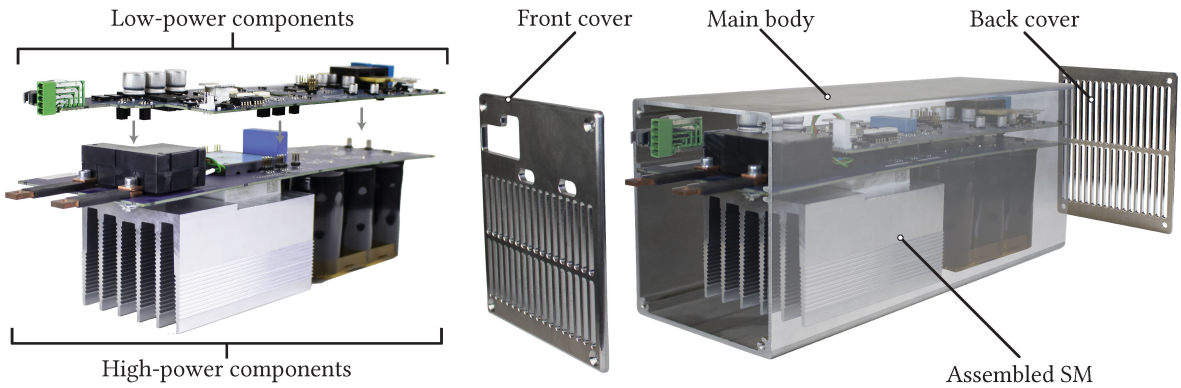


**Fig. 6.4** Developed FB SM [154]. Bottom PCB hosts power components. Top PCB hosts the SM main controller and auxiliary circuits.

(GUI), implemented on a PC using MATLAB®/ AppDesigner.

Note that all the parameters in **Tab. 6.1** retain the values from the real converter, except the rated arm voltage (and thus power) and the arm inductance. Rated arm voltage is a pure consequence of the number of SMs within an arm, whereas the arm inductance in the test setup was chosen to ensure the same arm current ripple as in the real converter.

The test platform is realized according to the electrical schematic shown in **Fig. 6.3**, and is shown in **Fig. 6.5**, along with the description of its main parts. Note that the rectifiers supplying the source SMs contain capacitors to improve the dc voltage quality across their output.

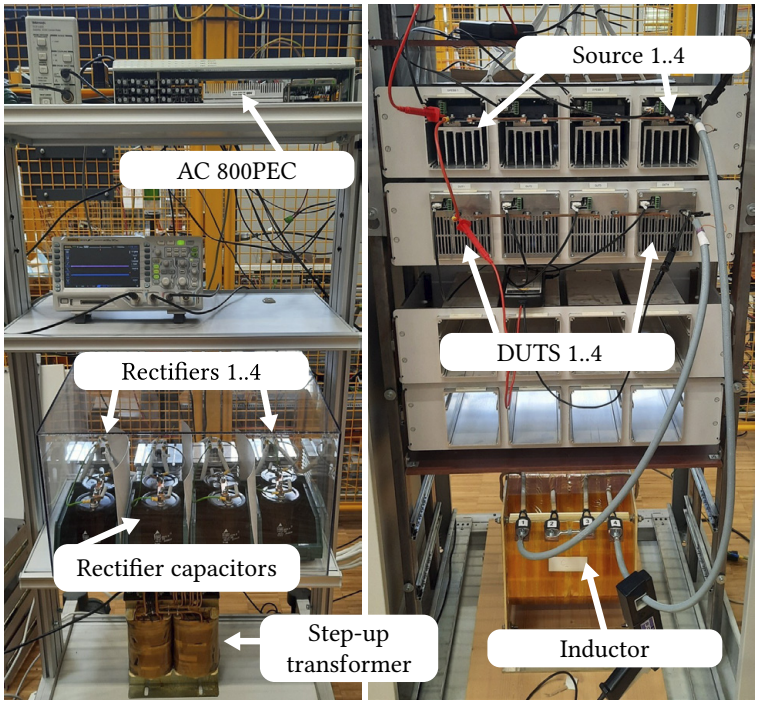


**Fig. 6.5** Photo of the realized experimental test platform, with its main components.

### 6.3.2 HIL model of the test platform

To safely develop the main control for the experimental test platform, a HIL test platform is developed to emulate the power components of the experimental test platform. It is based on Plexim RT-Box 1, an in-house developed interface board, and adapted SM boards, shown in **Fig. 6.6**.

Referring to the simplified schematic of the SMs, shown in **Fig. 6.6**, only the "DSP controller" and "Communication" parts are retained in the adapted SM board (HIL SM in **Fig. 6.6**), whereas the remaining parts of the original SM are modelled in the RTS. As a result, the same DSP code is running on both the adapted SM boards as on the real SMs, which allows for fast and safe testing of different control features on the HIL platform, prior to its deployment to the real SMs. In addition, communication part of the real SMs is identical to the one on the adapted SM boards, so the main controller (AC 800PEC) does not distinguish between the two. This allows for quick development and testing of the SM control software using the HIL test platform, and its seamless integration into the experimental test platform. Additionally, control software of the complete test platform, running in the main controller, is also safely tested in this way.

Finally, an RTS based on Plexim RT-Box 1 is used to model the power stages of the SMs, as well as the electrical circuitry of the test setup, identical to the one shown in **Fig. 6.3**. Inputs to the simulator are gate signals to the IGBTs, and SM bypass commands, coming from the adapted SM boards. The outputs of the simulator are SM capacitor and terminal voltages, and terminal currents of the SMs. Modelling of the arms inside the RTS is achieved using PLECS software, with the real-time execution period of 5 µs.

Not only does the HIL test platform facilitate development of the main control (running on AC 800PEC) and distributed control (running on individual DSPs), but it also allows to validate the modelling principles, which are used in another HIL platform (further referred to as Converter HIL), developed for the design of the converter-level control of the MMC. Further information regarding modelling and development of Converter HIL are provided in [135], [162]. It should only be mentioned that each

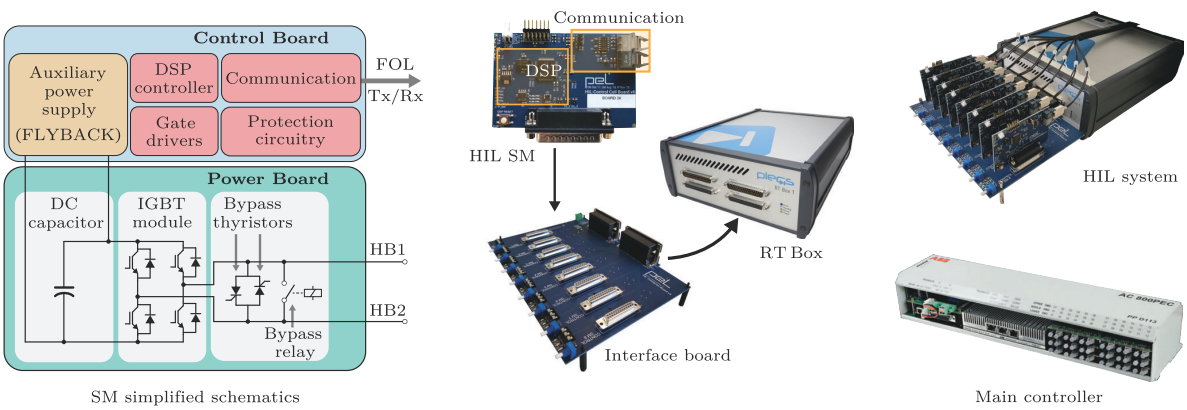


**Fig. 6.6** Outline of the major components used in the HIL test platform: (left) simplified schematic of a SM structure, with the main circuitry highlighted; (middle) adapted SM board- consisting only of the DSP and Communication circuitry of the real SM, together with the real-time simulator (RTS) and Interface board; (right- top) HIL system consisting of an RTS realized with PLEXIM RT-Box 1, eight adapted SM boards, and one interface board; (right- bottom) main controller of the test platform (ABB AC 800PEC) used both with the experimental and HIL test platforms.

arm in the Converter HIL is modelled using using the same approach, as well as the same resources as it was the case for the above-mentioned HIL system. Consequently, good correlation between the results collected from the HIL test platform and the experimental test platform indirectly verifies fidelity of the Converter HIL design concept, as it will be demonstrated in Section 6.7.

## 6.4 Distributed control concept

To successfully develop a SM-level control, with the objective of readily using such a SM in the MMC prototype, it should be tested along with different control concepts present in a real MMC. Those include the arm-voltage (energy) control, arm-current control, as well as intra-arm voltage balancing.

Arm-voltage control is realized in the main controller, where the output of the control action is the arm current reference, as shown in **Fig. 6.7**. PI controllers are used to generate dc current reference, according to the theoretical considerations provided above.

Conventional current control schemes are realized either in a centralized (all the arm currents are controlled by the main controller) or decentralized manner (every arm has its own controller). These control approaches suffer from a low bandwidth of the current control, due to the communication delays between the SMs and the associated current controllers, and non-negligible execution periods of the centralized/decentralized controllers. To fully utilize local current measurements and the availability of a DSP on the SMs, as well as to benefit from low closed-loop time delays, the arm-

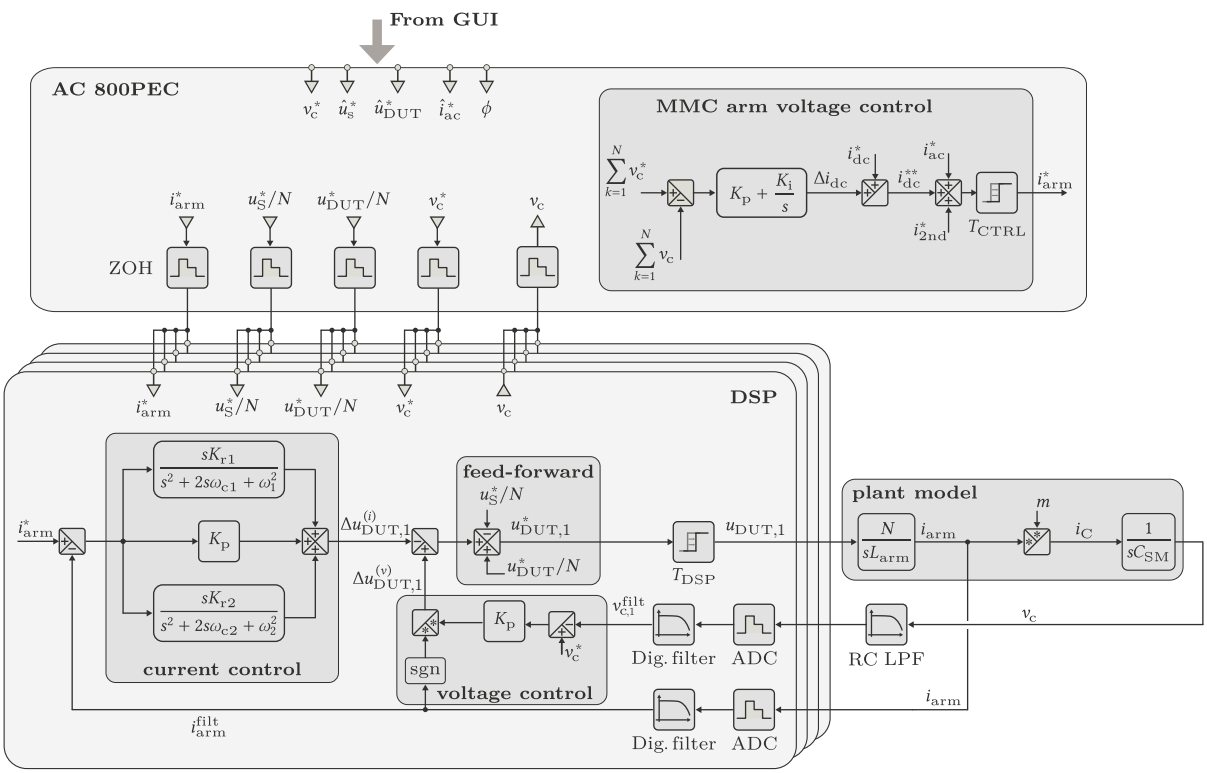


**Fig. 6.7** Illustration of the control concept used in the test platform: (top) high level arm energy control and reference generation; (bottom) SM level distributed voltage balancing and current control.

current control is realized in a distributed manner, where each SM is contributing to the arm-current control action. Similar control concept was introduced in [172], where the phase current of a cascaded H-bridge converter was controlled by means of distributed PR controllers. Local voltage balancing control actions are not present in this type of converter, as its SMs are externally supplied at their dc terminals.

Authors in [173] proposed a distributed current and voltage control method for the MMC, where the arm average voltage control, SM balancing, and arm-common current control are realized in a distributed manner, whereas the ac terminal current is centrally controlled. This control method suffers from a parasitic interaction between the average voltage controller and local voltage balancing, thus reducing the control dynamics. In addition parasitic ac and dc current components appear at converter dc and ac terminals, respectively, whenever the voltage imbalance occurs among the arms of the same phase-leg [174].

The control approach adopted here performs the total arm-current control on a SM level, using two PR controllers, tuned at the fundamental and the 2nd harmonic frequency. Owing to the small computational and measurement delays, higher bandwidth in current control is achieved with respect to the conventional methods. It is important to underline that the distributed current control is realized only on DUTs, whereas the source SMs act as voltage sources, emulating terminal voltages.

The intra-arm voltage balancing is generally achieved using two distinctive approaches. Decentralized approach is implemented on the arm level, and uses sorting algorithms to decide which SM should be turned on/off in the next switching instant [175]–[177]. Distributed control approach [64], [65] is implemented on the SM level, and modifies the modulation index of the respective SM, thus maintaining the voltage level around a predefined value. This approach was used in the presented test platform, due to the fact that each SM is equipped with its own DSP, and switching frequency is relatively high, which would not permit sorting algorithm implementation on the main controller in use.

A diagram of the realized control schemes is presented in **Fig. 6.7**. Arm terminal voltage and current references, as well as the nominal SM dc voltage reference, are provided by a user, from the graphical user interface (GUI).

## 6.5 HIL test platform results

To verify functionality of the developed control concepts, various tests are conducted, resembling different operating modes of an MMC.

**Fig. 6.8** shows relevant waveforms of an MMC arm, in a standard MMC configuration. Modulation indices were set to $m_{\mathrm{ac}} = m_{\mathrm{dc}} = 0.425$, grid current reference was set at maximum value of $\hat{i}_{\mathrm{ac}} = 62\,\mathrm{A}$, whereas the grid current phase angle $\phi$ was varied. Presented results demonstrate a proper generation of multilevel arm voltages, and good tracking of the voltage references. In addition, the arm current, controlled in a distributed manner, corresponds well to the arm current reference, consisting of a dc and fundamental ac component. Finally, the last plot shows capacitor voltages of the DUT SMs, demonstrating capability of the distributed voltage controller to maintain voltages balanced within the arm.

A similar test was repeated, with the 2nd harmonic current injection, shown in **Fig. 6.9**, again verifying

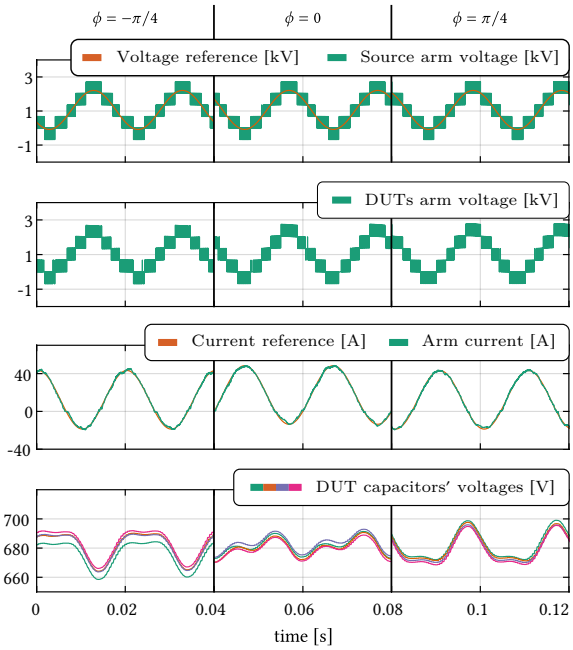


**Fig. 6.8** Results from the HIL test platform for a standard MMC operating mode, for three different phase angles of the grid current.

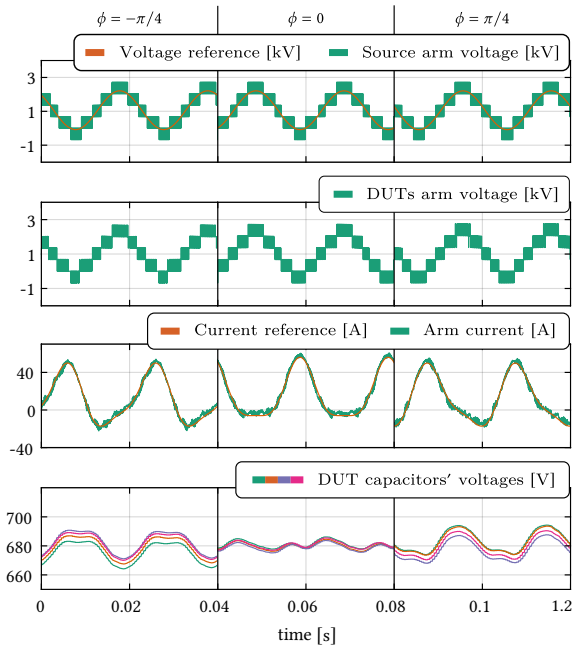


**Fig. 6.9** Results from the HIL test platform for a standard MMC operating mode with the insertion of the 2nd harmonic current component.

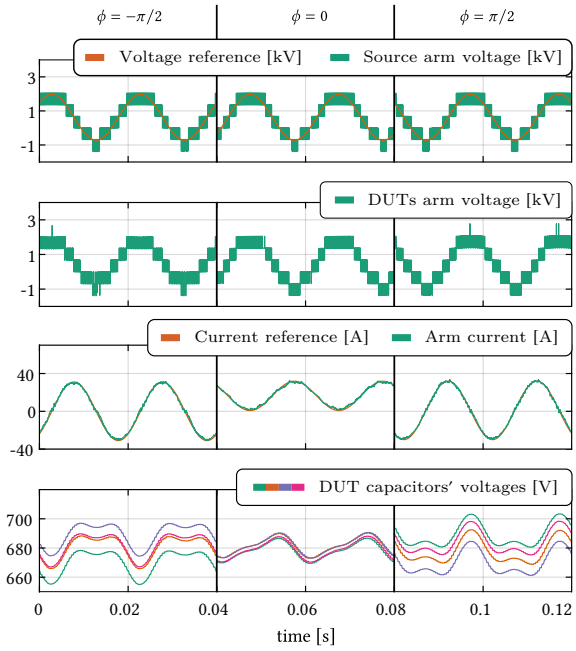


**Fig. 6.10** Results from the HIL test platform for a reduced DC terminal voltage operation. Results are collected for three different phase angles of the grid current. For the case of $\phi = 0$, grid current phase magnitude is halved to limit the DC current magnitude.

good performance of the distributed control concept. Finally, **Fig. 6.10** shows the relevant waveforms of an MMC arm in case when the modulation indices are set to $m_{\mathrm{ac}} = 1$, $m_{\mathrm{dc}} = 0.5$, confirming the

ability of a FB-based MMC to operate under reduced DC terminal voltage conditions.

Presented results verify the performance of the distributed control concept, presented in the previous section. They also demonstrate the validity of the HIL test platform through its ability to emulate the same conditions, as would appear in the real MMC. Due to the fact that both the control software and hardware are identical in the presented HIL platform and the experimental test platform, HIL platforms prove to be adequate tools for the rapid control prototyping.

## 6.6 Experimental verification

Electrical schematic of the experimental test platform is shown in **Fig. 6.3**, whereas its physical realization is shown in **Fig. 6.5**. The same main controller was used as in the HIL test platform, as well as the same software, both in the main controller and DSPs of the SMs.

**Figs. 6.11** to **6.13** show relevant waveforms of the MMC arm, collected from the experimental test platform. Conditions under which the waveforms are taken, and operating modes, are identical to the ones in the tests conducted on the HIL test platform. Due to the inaccessibility of the dc terminals of individual SMs, capacitor voltages were not measured during the tests, but their mean value was actively monitored through the GUI.

Presented results demonstrate that the voltage and current generation show equally good performance as on the HIL test platform.

In addition to the control examination, thermal performance of the SMs and the designed cooling system were also evaluated through the so-called *heat-run test*. Results of the test are shown in **Fig. 6.14**, where the operating conditions were changed, and SMs temperatures were monitored. The tests are conducted for more than four hours continuously, and the results demonstrate robustness of the SMs and proper thermal management. It is worth noting that two types of IGBT devices are evaluated during this test, SK50GH12T4T from Semikron for the source SMs, and SKiiP 26GH12T4V11

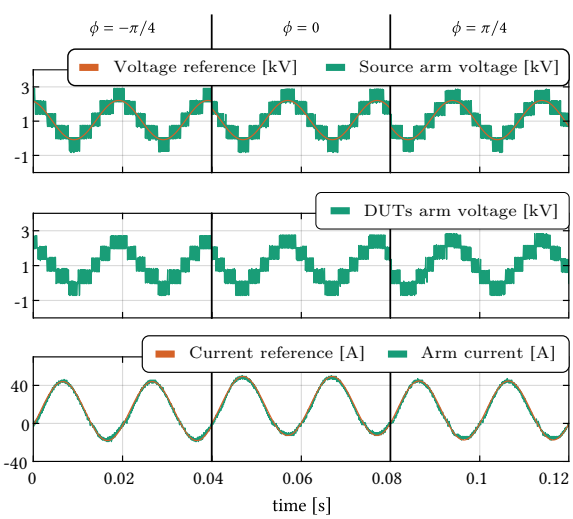


**Fig. 6.11** Results from the experimental test platform for a standard MMC operating mode, for three different phase angles of the grid current.

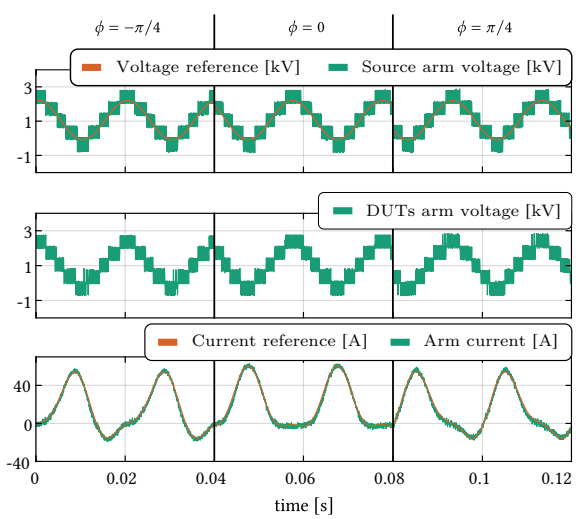


**Fig. 6.12** Results from the experimental test platform for a standard MMC operating mode with the insertion of the 2nd harmonic current component.

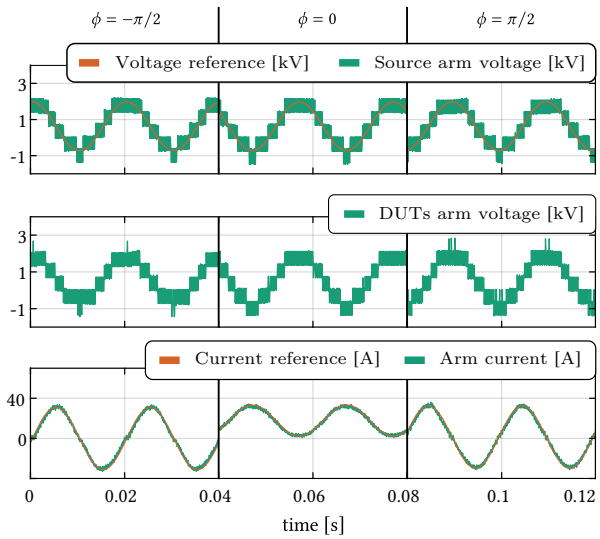


**Fig. 6.13** Results from the experimental test platform for a reduced DC terminal voltage operation. Results are collected for three different phase angles of the grid current. For the case of $\phi = 0$, grid current phase magnitude is halved to limit the DC current magnitude.

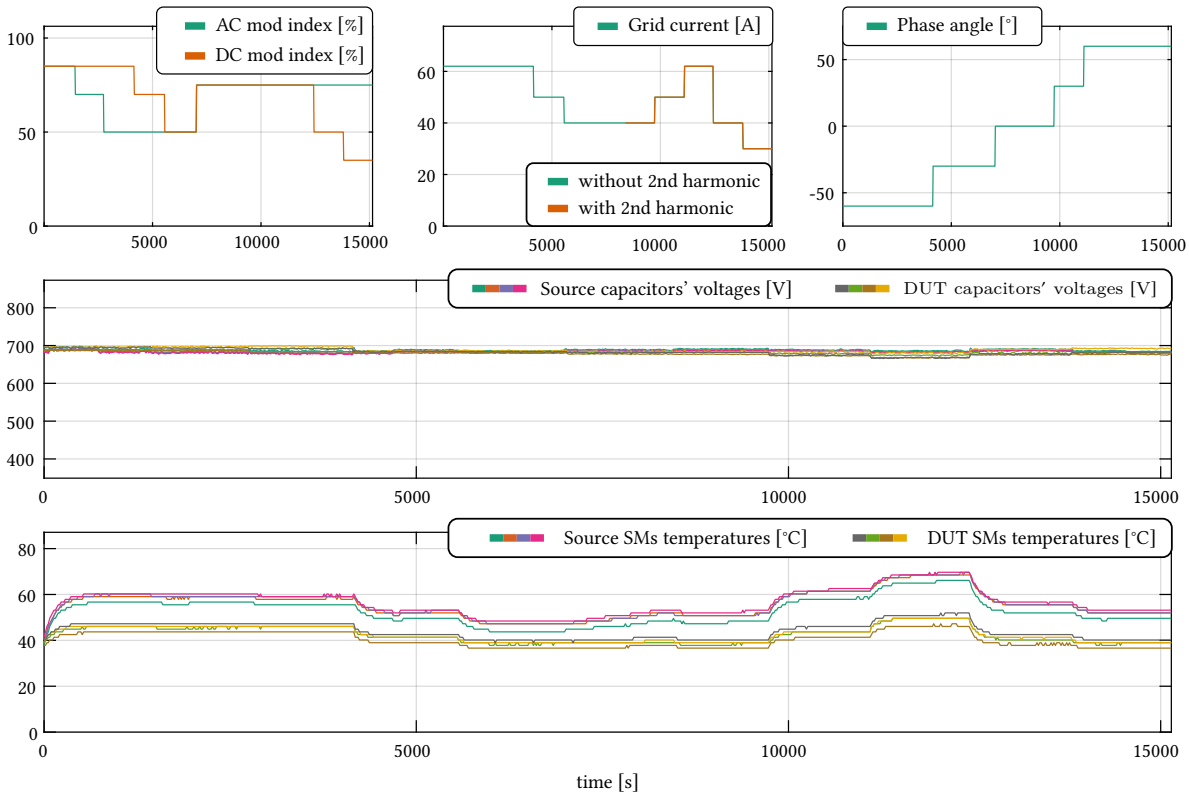


**Fig. 6.14** Results of the *heat-run test* conducted on the experimental platform. SMs temperatures are observed for different operating conditions, achieved by varying the modulation indices, maximal grid current, and grid current phase angle.

from Semikron, for DUT SMs. The latter has higher rated current, lower losses and better thermal conductivity, which resulted in a significantly lower temperature in the DUT SMs. As a result, the IGBT type SKiiP 26GH12T4V11 from Semikron was adopted as the IGBT module of all the SMs in the developed MMC.

## 6.7 Fidelity analysis of the HIL platform

Finally, to verify the fidelity of the HIL test platform, and thus the HIL modelling concept based on RT-Box 1, besides already presented results, additional tests are conducted.

**Fig. 6.15** shows terminal voltages and current of the two arms, during 2.4 ms. One can notice that switching events occur every 125 µs, which correspond to the apparent switching period of the arm of $N = 4$ SMs, each with the apparent switching frequency of 2 kHz. To compare the current ripple among the two platforms, the highest peak-to-peak values are magnified, showing a good match between the HIL and experimental test platforms. One can also notice that the shape of voltage pulses on the HIL test platform does not entirely correspond to the shape of the pulses on the experimental platform. This comes from the finite step size of 5 µs, and the sub-cycle averaging principle of the real-time simulator [178].

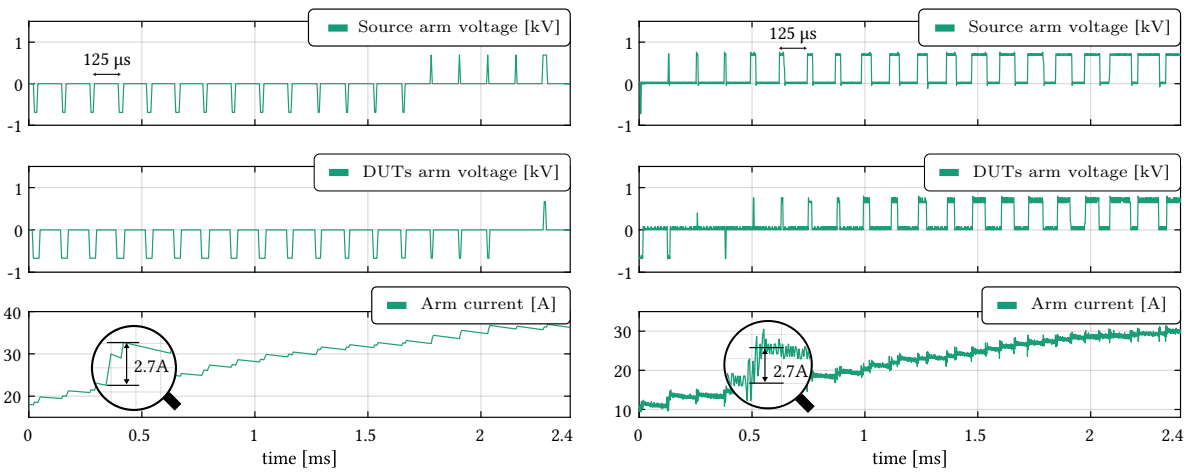


**Fig. 6.15** Comparison between the arm terminal voltages and currents obtained from the HIL test platform and experimental test platform.

Spectral analysis of the DUTs terminal voltages and current is also conducted to compare the two platforms. The results (c.f. **Fig. 6.16**) show good matching in the low-frequency component spectra, which is of particular interest. Even in the high frequency range, around the arm apparent switching frequency (8 kHz) and double apparent switching frequency (16 kHz), terminal voltage components obtained from the HIL and experimental test platform have high degrees of matching. A noticeable

**Tab. 6.2** Total harmonic distortion (THD) analysis of the DUT terminal voltages and currents

| Voltage | | Current | |
|---|---|---|---|
| THD HIL | THD Exp | THD HIL | THD Exp |
| 24.44% | 23.57% | 4.36% | 4.02% |

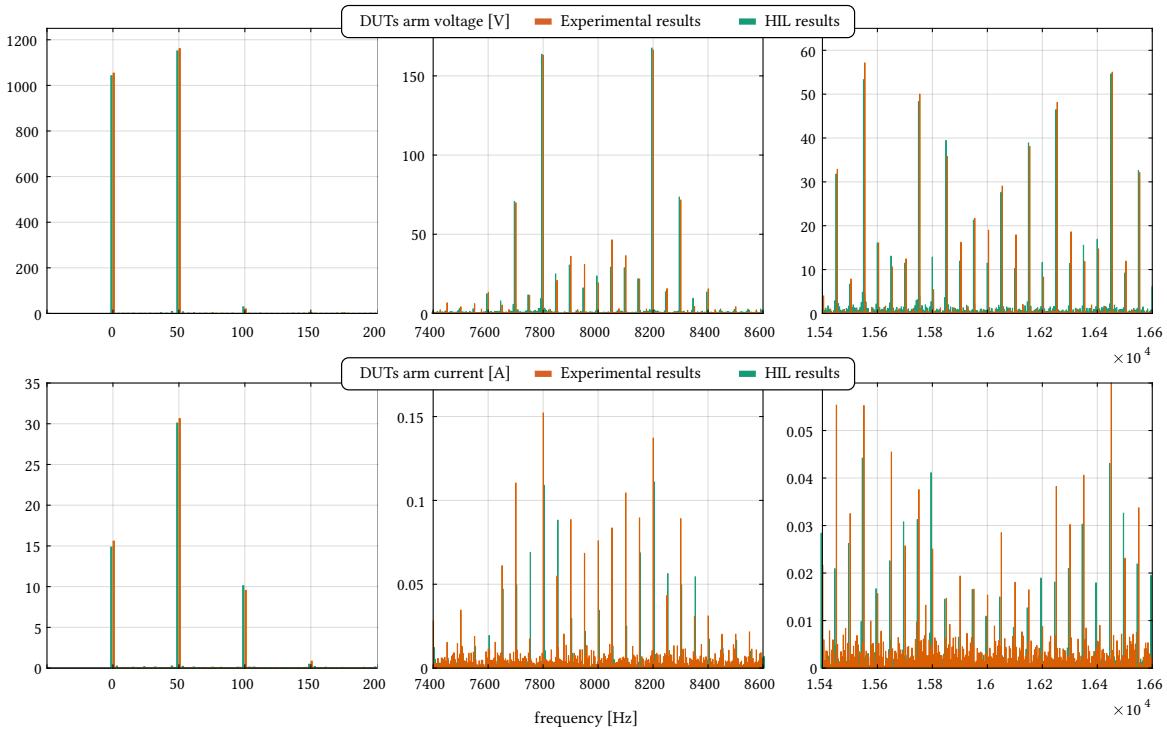


**Fig. 6.16** Comparison of spectral components of the terminal voltage and current in the HIL test platform and experimental test platform.

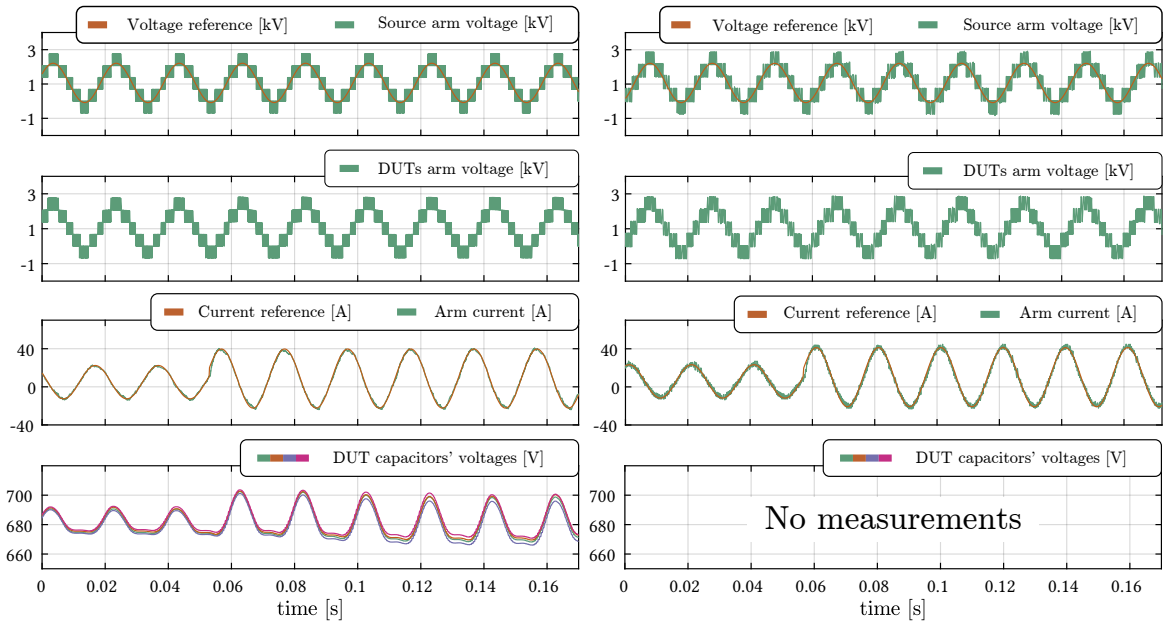


**Fig. 6.17** Step change in the current reference to verify performance of the distributed control concept: HIL results (left); experimental results (right). SM voltage measurements are not shown for the experimental test due to unavailability of their dc terminals.

difference exist in the arm current spectrum in the high frequency range, which might be attributed to non-linearities of the equivalent arm inductance and resistance in this frequency range, as well as to the finite resolution in the current measurements.

To quantify the degree of matching between the two platforms in terms of spectral components, the THD analysis was conducted, with the results presented in **Tab. 6.2**. For both the arm terminal voltage and current, the THD takes similar values in the HIL-simulated and experimental test platform, thus confirming fidelity of the HIL platform in modelling the MMC arm behaviour.

Finally, to test the performance of the distributed control concept both on the HIL and experimental test platform, the current reference was abruptly changed from $\hat{i}_{\mathrm{AC}} = 35\,\mathrm{A}$ to $\hat{i}_{\mathrm{AC}} = 62\,\mathrm{A}$, with grid current phase angle $\phi = 60^{\circ}$, and modulation indices $m_{\mathrm{ac}} = m_{\mathrm{dc}} = 0.85$. **Fig. 6.17** shows the relevant waveforms in both cases, demonstrating good dynamic performance of the distributed control system, as well as high level of matching between the HIL and experimental results.

## 6.8 Summary

A test platform for MMC SMs testing was presented in this chapter. The platform consists of a single MMC arm, where arm currents and terminal voltages correspond to those found in the real converter. This permits conducting tests of the real SMs under realistic conditions.

The development of the platform was aided by a HIL simulator, where the SM-level and platform-level control were firstly verified, before being used on the actual test platform.

Presented results demonstrate the validity of the modelling concepts employed in the RT-Box based HIL, through their ability to accurately model the behaviour of a real system. High degree of fidelity proves that the HIL platform used to emulate a real converter, based on the same architecture and modelling principles, can be used as a reliable tool for the converter-level rapid control prototyping.

In addition, the ability of developed SMs to be integrated in the MMC arm, produce phase-shifted voltages, perform local voltage and current control, and thermally sustain different operating conditions, was confirmed. Thus, such SMs can be readily deployed in the actual MMC converter.

It is worth to mention that all the SMs of the MMC converter configuration built within the lab underwent the tests described above, prior to being integrated into the actual converter setup.

# 7
# Summary and Future Works

## 7.1 Summary and contributions

A centrepiece of the thesis is the modular multilevel converter, an ingenious engineering product that has since its introduction quickly conquered many industrial areas, and became the object of interest of a countless number of researchers. This reputation has been well merited. The converter is said to be scalable, i.e. it offers a possibility to meet any voltage or power level by using readily available hardware, and without increasing the complexity of the control software. Additionally, its modularity permits to apply redundancy principles, resulting in the increased converter availability. It is highly efficient do the low switching frequency of the switching devices, while its multilevel voltage generation capability significantly reduces filtering requirements. Reduced costs due to the economy of scale, and the converter fast controllability of its terminal variables, along with the aforementioned benefits, make it a straightforward choice for certain applications, while a good candidate for benchmarking and research in other medium-voltage and high-voltage applications.

All these merits have drawn our attention towards this topology and its potential use in many medium-voltage applications. Principles of operation of a standard three-phase ac-dc modular multilevel converter have been outlined in **Chapter 2**, together with its fault-handling and voltage generating capabilities for two submodule types. In addition, voltage oscillations in floating submodule capacitors were analysed, and remedies for their mitigation were discussed. Different modulation techniques for multilevel converters were assessed, outlining individual advantages and disadvantages. In the same chapter, operating principles of the modular multilevel matrix converter were shown, as it is another member of the same family of converters.

It was shown that a prerequisite for an impaired operation of the converter is ensuring that the voltage within the submodule capacitors is maintained around its rated value. In other words, the energy content within the submodules should correspond to the reference value. Energy content within a single converter arm is controlled by controlling the arm power, i.e. the arm terminal voltages and currents. Due to the fact that the arm terminal voltages should correspond to the converter terminal requirements, the arm power can be controlled only by controlling the arm currents.

Arm energy control mechanisms and corresponding arm current generation techniques are discussed in **Chapter 3**. The control is decoupled into the arm-differential and arm-sum energy control, simply due to a difference in the respective control mechanisms. The arm-differential energy control mechanism is devised, based on the injection of fundamental-frequency arm-common currents. The main constraint in generating such currents is the fact that they should not influence the dc terminal current. On the other hand, a possible modification of the arm currents to satisfy this constraint should not alter the performance of the energy controllers. In that respect, two possible solutions are

proposed within this chapter. Both methods are characterized by an intuitive approach and a simple implementation. Evaluation results show that both methods manage to achieve the objectives, and confirm theoretical considerations presented in the chapter.

The arm-sum energy control was also analysed in this chapter, with a specific focus on its distinctive implementation for the inverter and rectifier modes of operation. This control method is based on the introduction of additional dc arm-common current components. Introduced currents should not alter the terminals currents, all while achieving the arm-sum energy control objectives. Presented control methods were evaluated by simulations for both operating modes, showing a good compliance with theoretical predictions.

Arm-sum and arm-differential control methods were also mutually evaluated in an arbitrary control of an arm energy. Apart from their good performance and simple implementation, it was also shown that presented principles of energy control can be applied to a modular multilevel converter with multiple phases, or multiple paralleled arms.

Extension of the presented energy control principles to faulty conditions in the modular multilevel converter was presented in **Chapter 4**. A specific focus was put on the converter operation under unbalanced grid conditions, as well as during a failure of a submodule. The arm-sum energy control under unbalanced grid condition was improved by introducing a 2nd harmonic filter in the feed-forward ac power terms for the inverter mode of operation. Two presented methods for the arm-differential energy control were evaluated for the use under unbalanced grid conditions. A more suitable method between the two is selected and used in further analyses. Compared to balanced grid conditions, it is adjusted by introducing a SOGI-based phase voltage amplitude estimator. These relatively simple improvements lead to a minor increase in complexity of the proposed energy control solution. Arm-sum and arm-differential energy control mechanisms were evaluated both separately and mutually under grid unbalances proving that they meet set control objectives, such as tracking the arm energy references, and not altering the terminal currents. The evaluation was performed for both modes of operation (rectifier and inverter), but also after the fault clearance in the ac grid. The latter proved that the presented control method is capable of ensuring a proper converter operation under all conditions.

Additionally, the converter operation during a failure of a submodule within an arm is evaluated. In such a case, one of the solutions is that the remaining submodules of the affected arm boost their energy content, in order to support normal converter operation. An independent arm energy control is necessary in such a case, and the presented control method was examined for cases of a submodule failure in both rectifier and inverter modes of operation. The control ensured that the converter remains in operation, without any visible effects on the converter terminals.

Another converter topology belonging the class of modular multilevel converters- the modular multilevel matrix converter- has similar control objectives as the standard modular multilevel converter. Namely, due to floating submodules, control of the energy stored within its arms is one of the principal control objectives. Control method presented in **Chapter 4** served as a basis for a novel control method for the modular multilevel matrix converter, proposed in **Chapter 5**. The proposed arm energy control is devised for a 3PH-3PH converter, and is applicable under normal operating conditions, under STATCOM operation, i.e. no voltage generation on one set of 3PH terminals, as well as under unbalanced grid conditions. Evaluation of the control method was performed on a hardware-in-the-loop test platform, comprised of real control software and hardware, and emulating

the power stages of a converter. The test scenario assumed a 3PH medium-voltage grid at one side, and a medium-voltage synchronous machine at the other side of the converter terminals. Ability of the control to support the converter operation under different machine and grid operating conditions was proven, all while ensuring a proper energy control, without influencing the terminal variables.

The development of a medium-voltage modular multilevel converter prototype requires extensive testing of its hardware and control software. Owing to its modularity, its building blocks (submodules) can be exposed to their real operating conditions prior to assembling the complete converter. This allows for testing the electrical, thermal and control properties of the submodules, thus de-risking their use in the medium-voltage converter prototype.

To test the submodules under realistic operating conditions, a test platform was developed, as presented in **Chapter 6**. The platform aims to emulate the behaviour of a single converter arm with a reduced number of submodules. Development of the platform was aided by a hardware-in-the-loop simulator, where the power parts of the platform were modelled, while using actual control software and hardware. Experimental tests on the submodules were conducted, where their ability to produce phase-shifted voltages, perform the local voltage and current control, and thermally sustain different operating conditions, was confirmed. Prior to the experimental validation, the same tests were conducted on the hardware-in-the-loop platform with the aim of validating the submodule-level and platform-level control concepts. Tests results from the hardware-in-the-loop and experimental test platform were mutually compared, showing a high level of matching. High degree of fidelity proves that the hardware-in-the-loop platform used to emulate a real converter, based on the same architecture and modelling principles, can be used as a reliable tool for the converter-level rapid control prototyping.

## 7.2 Ideas for future work

While the author of the thesis believes that the presented energy control methods have offered a simpler yet robust solution for the family of modular multilevel converters compared to the existing solutions, multitude of other possible improvements can be explored in the future.

**The energy control of multiphase modular multilevel converter** was briefly mentioned in **Chapter 3** of this thesis, with some guidelines provided regarding the extensibility of the proposed control concept to the multiphase variants of the converter. Suggested way of applying the proposed control concepts might be a simple and effective solution, yet it deserves a thorough analysis and validation, as well as a comparison with the existing solutions.

**The energy control of a 3PH-to-1PH modular multilevel matrix converter** is another potential area of application of the control principles applied in **Chapter 5**. The difference between the analysed 3PH-to-3PH modular multilevel matrix converter and its 3PH-to-1PH counterpart is one additional cluster of arms in case of the former. This points to the conclusion that the presented control method can be employed in the latter, resulting in even simpler energy control structure with respect to the 3PH-to-3PH converter.

**The distributed current control** is another area which deserves attention of the authors. Due to the fact that the converter submodules are equipped with local controllers, performing mainly monitoring and safety functions, some control improvements could be made if the computational power of the submodules was used to perform distributed current control. Namely, arm current reference

is calculated in a high-level controller, and sent to individual submodules that benefit from a low closed-loop delays, and can thus realize current control loop with higher bandwidths. This principle was applied in the arm current control in the experimental test platform presented in **Chapter 6**, and proved to yield good results in reference tracking on a single arm example. Nevertheless, independent current control of each arm in a functional converter brings several challenges that would require a thorough analysis.

The importance of the modular multilevel converter and similar topologies should not be only perceived through its current applications and contributions made thus far. Other applications, currently out of scope of the modular multilevel converter, could also benefit from the engineering concepts and experience gained through the challenges being addressed in high-voltage and medium-voltage applications. Modularity, redundancy, low switching frequency, high availability and scalability are, in the opinion of the author, desirable merits, that would lead to penetration of the modular multilevel converter concepts into other application areas, such as automotive, energy production and energy storage.

# Appendices

# A

# Internal dynamics of the direct-voltage-controlled MMC

To understand the self-balancing feature of the direct voltage control method, we should recall insertion index definition for this control method. According to the principles of the direct voltage control, the insertion indices are defined with respect to the expected average arm voltage $V_c^{\Sigma}$, such as:

$$n_p = \frac{u_p^*}{V_c^{\Sigma}} = \frac{u_{comm}^* - u_{diff}^*}{V_c^{\Sigma}} \quad \text{(A.1)} \qquad n_n = \frac{u_n^*}{V_c^{\Sigma}} = \frac{u_{comm}^* + u_{diff}^*}{V_c^{\Sigma}} \quad \text{(A.2)}$$

It was shown that the arm-common voltage reference $u_{comm}^*$ consists of the dc feed-forward term $u_{dc}/2$ and the arm-common current control term $\Delta u_{comm}^*$, as shown in (A.3). Only the proportional gain $K_p$ was considered in the analysis, although integral and resonant terms typically also exist in the arm-common current control structure. Nevertheless, the proportional term to a good extent represents the influence of the current control on the internal dynamics.

On the other hand, the arm-differential voltage reference $u_{diff}^*$ is in charge of the ac terminal voltage/current control, and thus consists of the ac terminal voltage feed-forward term $u_{ac}$, and the arm-differential current (ac terminal current) control term $\Delta u_{diff}^*$, as expressed in (A.4). The last term is also modelled as a simple proportional action $K_r$, even though it typically comprises a resonant term as well.

$$u_{comm}^* = \frac{u_{dc}}{2} + \Delta u_{comm}^* = m_{dc} V_c^{\Sigma} - K_p\left(i_{comm}^* - i_{comm}\right) \quad \text{(A.3)}$$

$$u_{diff}^* = u_{ac} + \Delta u_{diff}^* = m_{ac} V_c^{\Sigma} \sin\left(\omega_g t\right) + K_r\left(i_{diff}^* - i_{diff}\right) \quad \text{(A.4)}$$

Average values of the total arm voltages might differ from the reference average value $V_c^{\Sigma}$. To account for these small deviations with respect to the reference, the average values of the total arm voltages $V_{c,p}^{\Sigma}$ and $V_{c,n}^{\Sigma}$ are expressed as in ((A.5))-(A.6).

$$V_{c,p}^{\Sigma} = V_c^{\Sigma} + \Delta V_{c,p}^{\Sigma} \quad \text{(A.5)} \qquad V_{c,n}^{\Sigma} = V_c^{\Sigma} + \Delta V_{c,n}^{\Sigma} \quad \text{(A.6)}$$

Taking into account the definitions (A.1)-(A.6), the realized arm voltages take the following forms:

$$
\begin{aligned}
u_{\mathrm{p}} = n_{\mathrm{p}} V_{\mathrm{c,p}}^{\Sigma} = \frac{u_{\mathrm{comm}}^{*} - u_{\mathrm{diff}}^{*}}{V_{\mathrm{c}}^{\Sigma}} V_{\mathrm{c,p}}^{\Sigma} =& V_{\mathrm{c,p}}^{\Sigma} \Bigg( m_{\mathrm{dc}} - m_{\mathrm{ac}} \sin\left(\omega_{\mathrm{g}} t\right) + \ldots \\
& - \frac{K_{\mathrm{p}}\left(i_{\mathrm{comm}}^{*} - i_{\mathrm{comm}}\right)}{V_{\mathrm{c}}^{\Sigma}} - \frac{K_{\mathrm{r}}\left(i_{\mathrm{diff}}^{*} - i_{\mathrm{diff}}\right)}{V_{\mathrm{c}}^{\Sigma}} \Bigg)
\end{aligned}
\tag{A.7}
$$

$$
\begin{aligned}
u_{\mathrm{n}} = n_{\mathrm{n}} V_{\mathrm{c,n}}^{\Sigma} = \frac{u_{\mathrm{comm}}^{*} + u_{\mathrm{diff}}^{*}}{V_{\mathrm{c}}^{\Sigma}} V_{\mathrm{c,n}}^{\Sigma} =& V_{\mathrm{c,n}}^{\Sigma} \Bigg( m_{\mathrm{dc}} + m_{\mathrm{ac}} \sin\left(\omega_{\mathrm{g}} t\right) + \ldots \\
& - \frac{K_{\mathrm{p}}\left(i_{\mathrm{comm}}^{*} - i_{\mathrm{comm}}\right)}{V_{\mathrm{c}}^{\Sigma}} + \frac{K_{\mathrm{r}}\left(i_{\mathrm{diff}}^{*} - i_{\mathrm{diff}}\right)}{V_{\mathrm{c}}^{\Sigma}} \Bigg)
\end{aligned}
\tag{A.8}
$$

Based on (A.7)-(A.8), realized arm-common voltage can be expressed as follows:

$$
\begin{aligned}
u_{\mathrm{comm}} = \frac{u_{\mathrm{p}} + u_{\mathrm{n}}}{2} =& \frac{m_{\mathrm{dc}}}{2}\left(V_{\mathrm{c,p}}^{\Sigma} + V_{\mathrm{c,n}}^{\Sigma}\right) - \frac{m_{\mathrm{ac}}}{2}\left(V_{\mathrm{c,p}}^{\Sigma} - V_{\mathrm{c,n}}^{\Sigma}\right) \sin\left(\omega_{\mathrm{g}} t\right) + \ldots \\
& - \frac{K_{\mathrm{p}}}{2}\big(\underbrace{i_{\mathrm{comm}}^{*} - i_{\mathrm{comm}}}_{\Delta i_{\mathrm{comm}}}\big)\frac{V_{\mathrm{c,p}}^{\Sigma} + V_{\mathrm{c,n}}^{\Sigma}}{V_{\mathrm{c}}^{\Sigma}} - \frac{K_{\mathrm{r}}}{2}\big(\underbrace{i_{\mathrm{diff}}^{*} - i_{\mathrm{diff}}}_{\Delta i_{\mathrm{diff}}}\big)\frac{V_{\mathrm{c,p}}^{\Sigma} - V_{\mathrm{c,n}}^{\Sigma}}{V_{\mathrm{c}}^{\Sigma}} \\
=& \frac{m_{\mathrm{dc}}}{2}\Big(2V_{\mathrm{c}}^{\Sigma} + \underbrace{\Delta V_{\mathrm{c,p}}^{\Sigma} + \Delta V_{\mathrm{c,n}}^{\Sigma}}_{\Delta V_{\mathrm{c,\Sigma}}^{\Sigma}}\Big) - \frac{m_{\mathrm{ac}}}{2}\Big(\underbrace{\Delta V_{\mathrm{c,p}}^{\Sigma} - \Delta V_{\mathrm{c,n}}^{\Sigma}}_{\Delta V_{\mathrm{c,\Delta}}^{\Sigma}}\Big) \sin\left(\omega_{\mathrm{g}} t\right) + \ldots \\
& - K_{\mathrm{p}} \Delta i_{\mathrm{comm}} \Bigg(1 + \underbrace{\frac{\Delta V_{\mathrm{c,p}}^{\Sigma} + \Delta V_{\mathrm{c,n}}^{\Sigma}}{2V_{\mathrm{c}}^{\Sigma}}}_{\approx 0}\Bigg) - K_{\mathrm{r}} \Delta i_{\mathrm{diff}} \underbrace{\frac{\Delta V_{\mathrm{c,p}}^{\Sigma} - \Delta V_{\mathrm{c,n}}^{\Sigma}}{2V_{\mathrm{c}}^{\Sigma}}}_{\approx 0} \\
=& \frac{m_{\mathrm{dc}}}{2}\left(2V_{\mathrm{c}}^{\Sigma} + \Delta V_{\mathrm{c,\Sigma}}^{\Sigma}\right) - \frac{m_{\mathrm{ac}}}{2} \Delta V_{\mathrm{c,\Delta}}^{\Sigma} \sin\left(\omega_{\mathrm{g}} t\right) - K_{\mathrm{p}} \Delta i_{\mathrm{comm}}
\end{aligned}
\tag{A.9}
$$

Compared to the reference arm-common voltage $u_{\mathrm{comm}}^{*}$ in (A.3), realized arm-common voltage contains two additional terms, when the total arm voltages within the arms deviate from the desired value $V_{\mathrm{c}}^{\Sigma}$. Recalling the equivalent per-phase circuit for the arm-common current control:

$$
\begin{aligned}
2L_{\mathrm{arm}} \frac{di_{\mathrm{comm}}}{dt} + 2R_{\mathrm{arm}} i_{\mathrm{comm}} &= u_{\mathrm{dc}} - 2u_{\mathrm{comm}} \\
2L_{\mathrm{arm}} \frac{di_{\mathrm{comm}}}{dt} + 2R_{\mathrm{arm}} i_{\mathrm{comm}} &= -m_{\mathrm{dc}} \Delta V_{\mathrm{c,\Sigma}}^{\Sigma} + m_{\mathrm{ac}} \Delta V_{\mathrm{c,\Delta}}^{\Sigma} \sin\left(\omega_{\mathrm{g}} t\right) + 2K_{\mathrm{p}} \Delta i_{\mathrm{comm}}
\end{aligned}
\tag{A.10}
$$

As it can be seen from the last equation, the arm-common current has parasitic dc and ac terms, originating from the total arm voltage deviations. To observe the dynamics of these terms, arm-common current component can be expressed in terms of its reference value, and two additional terms, as in (A.11).

$$
i_{\mathrm{comm}} = i_{\mathrm{comm}}^{*} + \Delta i_{\mathrm{comm}}^{(\mathrm{dc})} + \Delta i_{\mathrm{comm}}^{(\mathrm{ac})} \qquad \Longrightarrow \qquad \Delta i_{\mathrm{comm}} = -\Delta i_{\mathrm{comm}}^{(\mathrm{dc})} - \Delta i_{\mathrm{comm}}^{(\mathrm{ac})}
\tag{A.11}
$$

As a result, dynamic equation (A.10) can be decoupled into two equations, governing the dynamics of the parasitic terms:

$$L_{\text{arm}}\frac{d\Delta i_{\text{comm}}^{(\text{dc})}}{dt}+\left(R_{\text{arm}}+K_{\text{p}}\right)\Delta i_{\text{comm}}^{(\text{dc})}=-\frac{m_{\text{dc}}}{2}\Delta V_{\text{c},\Sigma}^{\Sigma} \tag{A.12}$$

$$L_{\text{arm}}\frac{d\Delta i_{\text{comm}}^{(\text{ac})}}{dt}+\left(R_{\text{arm}}+K_{\text{p}}\right)\Delta i_{\text{comm}}^{(\text{ac})}=\frac{m_{\text{ac}}}{2}\Delta V_{\text{c},\Delta}^{\Sigma}\sin\left(\omega_{\text{g}}t\right) \tag{A.13}$$

The dynamic model for the arm-common current is established, and it is necessary to do it for the arm-differential current as well. Following a similar procedure, realized arm-differential voltage is found to be:

$$\begin{aligned}
u_{\text{diff}}=\frac{u_{\text{n}}-u_{\text{p}}}{2} &= -\frac{m_{\text{dc}}}{2}\left(V_{\text{c,p}}^{\Sigma}-V_{\text{c,n}}^{\Sigma}\right)+\frac{m_{\text{ac}}}{2}\left(V_{\text{c,p}}^{\Sigma}+V_{\text{c,n}}^{\Sigma}\right)\sin\left(\omega_{\text{g}}t\right)+\ldots \\
&\quad +\frac{K_{\text{p}}}{2}\left(i_{\text{comm}}^{*}-i_{\text{comm}}\right)\underbrace{\frac{V_{\text{c,p}}^{\Sigma}-V_{\text{c,n}}^{\Sigma}}{V_{\text{c}}^{\Sigma}}}_{\approx 0}+\frac{K_{\text{r}}}{2}\left(i_{\text{diff}}^{*}-i_{\text{diff}}\right)\frac{V_{\text{c,p}}^{\Sigma}+V_{\text{c,n}}^{\Sigma}}{V_{\text{c}}^{\Sigma}} \\
&= -\frac{m_{\text{dc}}}{2}\Delta V_{\text{c},\Delta}^{\Sigma}+\frac{m_{\text{ac}}}{2}\left(2V_{\text{c}}^{\Sigma}+\Delta V_{\text{c},\Sigma}^{\Sigma}\right)\sin\left(\omega_{\text{g}}t\right)+K_{\text{r}}\Delta i_{\text{diff}}\left(1+\underbrace{\frac{\Delta V_{\text{c},\Sigma}^{\Sigma}}{2V_{\text{c}}^{\Sigma}}}_{\approx 0}\right)
\end{aligned} \tag{A.14}$$

The dynamic model of the arm-differential current can be now derived, based on (A.14) and the equivalent circuit for the arm-differential current control. Note that the common-mode voltage $u_{\text{CM}}$ is disregarded, as it does not have particular influence on the dynamics.

$$\begin{aligned}
\frac{L_{\text{arm}}}{2}\frac{di_{\text{diff}}}{dt}+\frac{R_{\text{arm}}}{2}i_{\text{diff}} &= u_{\text{diff}}-u_{\text{ac}} \\
\frac{L_{\text{arm}}}{2}\frac{di_{\text{diff}}}{dt}+\frac{R_{\text{arm}}}{2}i_{\text{diff}} &= -\frac{m_{\text{dc}}}{2}\Delta V_{\text{c},\Delta}^{\Sigma}+\frac{m_{\text{ac}}}{2}\Delta V_{\text{c},\Sigma}^{\Sigma}\sin\left(\omega_{\text{g}}t\right)+K_{\text{r}}\Delta i_{\text{diff}}
\end{aligned} \tag{A.15}$$

From (A.15) one can conclude that the arm-differential current component will contain a parasitic dc component, as well as the parasitic fundamental frequency component. Although the latter will be compensated by the current control action, it is included in the analysis for the sake of completeness. Therefore, the arm-differential current can be expressed in terms of its reference value and its parasitic components as:

$$i_{\text{diff}}=i_{\text{diff}}^{*}+\Delta i_{\text{diff}}^{(\text{dc})}+\Delta i_{\text{diff}}^{(\text{ac})} \qquad \Longrightarrow \qquad \Delta i_{\text{diff}}=-\Delta i_{\text{diff}}^{(\text{dc})}-\Delta i_{\text{diff}}^{(\text{ac})} \tag{A.16}$$

As in the previous case, the differential equation (A.15) can be decoupled into two independent terms, the dc and the ac.

$$L_{\text{arm}}\frac{d\Delta i_{\text{diff}}^{(\text{dc})}}{dt}+\left(R_{\text{arm}}+2K_{\text{r}}\right)\Delta i_{\text{diff}}^{(\text{dc})}=-m_{\text{dc}}\Delta V_{\text{c},\Delta}^{\Sigma} \tag{A.17}$$

$$L_{\text{arm}}\frac{d\Delta i_{\text{diff}}^{(\text{ac})}}{dt}+\left(R_{\text{arm}}+2K_{\text{r}}\right)\Delta i_{\text{diff}}^{(\text{ac})}=m_{\text{ac}}\Delta V_{\text{c},\Sigma}^{\Sigma}\sin\left(\omega_{\text{g}}t\right) \tag{A.18}$$

From (A.12)-(A.13) and (A.17)-(A.18) one can conclude that the dynamics of the parasitic components is determined by the arm parameters, inductance and resistance, as well as the control gains. Their magnitudes are, however, determined by the magnitudes of the total arm voltage deviations, which are as well dynamically changing variables.

To understand the dynamics of the voltage deviations, and their coupling with the parasitic currents, one can start from the definition of the two arm energies, as a function of the total arm voltages, given in (A.19)-(A.20). The dynamics of the arm energies is governed by the corresponding arm powers, as expressed in (A.21)-(A.22).

$$W_{\mathrm{p}} = \frac{1}{2} C_{\mathrm{arm}} \left( V_{\mathrm{c,p}}^{\Sigma} \right)^2 \tag{A.19}$$

$$W_{\mathrm{n}} = \frac{1}{2} C_{\mathrm{arm}} \left( V_{\mathrm{c,n}}^{\Sigma} \right)^2 \tag{A.20}$$

$$\frac{dW_{\mathrm{p}}}{dt} = C_{\mathrm{arm}} V_{\mathrm{c,p}}^{\Sigma} \frac{dV_{\mathrm{c,p}}^{\Sigma}}{dt} = p_{\mathrm{p}} \tag{A.21}$$

$$\frac{dW_{\mathrm{n}}}{dt} = C_{\mathrm{arm}} V_{\mathrm{c,n}}^{\Sigma} \frac{dV_{\mathrm{c,n}}^{\Sigma}}{dt} = p_{\mathrm{n}} \tag{A.22}$$

The arm power is determined by the voltage and current of the corresponding arm. To facilitate the analysis without sacrificing accuracy, arm voltages will be represented only by the feed-forward terms, i.e. dc and ac terminal voltages. Additional voltage terms, originating from the current control are neglected, as they are typically of significantly lower values. On the other hand, all the arm current components will be accounted for, including the parasitic currents. The reason is the fact that these components are triggered by the total arm voltage deviation, and might as well influence its dynamics.

$$\begin{aligned} C_{\mathrm{arm}} \cancel{V_{\mathrm{c,p}}^{\Sigma}} \frac{dV_{\mathrm{c,p}}^{\Sigma}}{dt} = \cancel{V_{\mathrm{c,p}}^{\Sigma}} \Big( m_{\mathrm{dc}} - m_{\mathrm{ac}} \sin\left(\omega_{\mathrm{g}} t\right) \Big) \Big( & i_{\mathrm{comm}}^{*} + \Delta i_{\mathrm{comm}}^{(\mathrm{dc})} + \Delta i_{\mathrm{comm}}^{(\mathrm{ac})} + \ldots \\ & + \frac{i_{\mathrm{diff}}^{*}}{2} + \frac{\Delta i_{\mathrm{diff}}^{(\mathrm{dc})}}{2} + \frac{\Delta i_{\mathrm{diff}}^{(\mathrm{ac})}}{2} \Big) \end{aligned} \tag{A.23}$$

$$\begin{aligned} C_{\mathrm{arm}} \cancel{V_{\mathrm{c,n}}^{\Sigma}} \frac{dV_{\mathrm{c,n}}^{\Sigma}}{dt} = \cancel{V_{\mathrm{c,n}}^{\Sigma}} \Big( m_{\mathrm{dc}} + m_{\mathrm{ac}} \sin\left(\omega_{\mathrm{g}} t\right) \Big) \Big( & i_{\mathrm{comm}}^{*} + \Delta i_{\mathrm{comm}}^{(\mathrm{dc})} + \Delta i_{\mathrm{comm}}^{(\mathrm{ac})} + \ldots \\ & - \frac{i_{\mathrm{diff}}^{*}}{2} - \frac{\Delta i_{\mathrm{diff}}^{(\mathrm{dc})}}{2} - \frac{\Delta i_{\mathrm{diff}}^{(\mathrm{ac})}}{2} \Big) \end{aligned} \tag{A.24}$$

Adding and subtracting (A.23) and (A.24) yields the dynamic equations of the sum $\Delta V_{\mathrm{c},\Sigma}^{\Sigma}$ and differential $\Delta V_{\mathrm{c},\Delta}^{\Sigma}$ total arm voltage deviations, shown in (A.25)-(A.26). Note that only the products with non-zero mean are retained on the right-hand side, as the oscillating terms do not influence convergence of the analysed voltage deviations.

$$
\begin{aligned}
C_{\text{arm}}\frac{d\Delta V_{\text{c,}\Sigma}^{\Sigma}}{dt} &= 2m_{\text{dc}}\left(i_{\text{comm}}^{*}+\Delta i_{\text{comm}}^{(\text{dc})}+\Delta i_{\text{comm}}^{(\text{ac})}\right)-m_{\text{ac}}\sin\left(\omega t\right)\left(i_{\text{diff}}^{*}+\Delta i_{\text{diff}}^{(\text{dc})}+\Delta i_{\text{diff}}^{(\text{ac})}\right)\\
&= \underbrace{2m_{\text{dc}}i_{\text{comm}}^{*}-2m_{\text{ac}}\sin\left(\omega t\right)i_{\text{diff}}^{*}}_{=0}+2m_{\text{dc}}\Delta i_{\text{comm}}^{(\text{dc})}-m_{\text{ac}}\sin\left(\omega t\right)\Delta i_{\text{diff}}^{(\text{ac})}\\
&= 2m_{\text{dc}}\Delta i_{\text{comm}}^{(\text{dc})}-m_{\text{ac}}\sin\left(\omega t\right)\Delta i_{\text{diff}}^{(\text{ac})}
\end{aligned}
\tag{A.25}
$$

$$
\begin{aligned}
C_{\text{arm}}\frac{d\Delta V_{\text{c,}\Delta}^{\Sigma}}{dt} &= m_{\text{dc}}\left(i_{\text{diff}}^{*}+\Delta i_{\text{diff}}^{(\text{dc})}+\Delta i_{\text{diff}}^{(\text{ac})}\right)-m_{\text{ac}}\sin\left(\omega t\right)\left(2i_{\text{comm}}^{*}+2\Delta i_{\text{comm}}^{(\text{dc})}+2\Delta i_{\text{comm}}^{(\text{ac})}\right)\\
&= m_{\text{dc}}\Delta i_{\text{diff}}^{(\text{dc})}-2m_{\text{ac}}\sin\left(\omega t\right)\Delta i_{\text{comm}}^{(\text{ac})}
\end{aligned}
\tag{A.26}
$$

To completely eliminate the oscillating terms in (A.25)-(A.26), parasitic ac current components $\Delta i_{\text{comm}}^{(\text{ac})}$ and $\Delta i_{\text{diff}}^{(\text{ac})}$ should assume the form as in (A.27)-(A.28). Consequently, the two equations (A.25)-(A.26) are deprived of the oscillating terms, as expressed in (A.29)-(A.30).

$$\Delta i_{\text{comm}}^{(\text{ac})}=\Delta\hat{i}_{\text{comm}}^{(\text{ac})}\sin\left(\omega t+\beta\right) \tag{A.27}$$

$$\Delta i_{\text{diff}}^{(\text{ac})}=\Delta\hat{i}_{\text{diff}}^{(\text{ac})}\sin\left(\omega t+\alpha\right) \tag{A.28}$$

$$C_{\text{arm}}\frac{d\Delta V_{\text{c,}\Sigma}^{\Sigma}}{dt}=2m_{\text{dc}}\Delta i_{\text{comm}}^{(\text{dc})}-\frac{m_{\text{ac}}}{2}\Delta\hat{i}_{\text{diff}}^{(\text{ac})}\cos\left(\alpha\right) \tag{A.29}$$

$$C_{\text{arm}}\frac{d\Delta V_{\text{c,}\Delta}^{\Sigma}}{dt}=m_{\text{dc}}\Delta i_{\text{diff}}^{(\text{dc})}-m_{\text{ac}}\Delta\hat{i}_{\text{comm}}^{(\text{ac})}\cos\left(\beta\right) \tag{A.30}$$

Recalling the dynamic equations of the parasitic dc terms in the arm-common and arm-differential currents, and applying Laplace transformation, yields:

$$
\begin{aligned}
L_{\text{arm}}\frac{d\Delta i_{\text{comm}}^{(\text{dc})}}{dt}+\left(R_{\text{arm}}+K_{\text{p}}\right)\Delta i_{\text{comm}}^{(\text{dc})} &= -\frac{m_{\text{dc}}}{2}\Delta V_{\text{c,}\Sigma}^{\Sigma}\\
\Delta i_{\text{comm}}^{(\text{dc})}(s) &= \frac{-\frac{m_{\text{dc}}}{2}\Delta V_{\text{c,}\Sigma}^{\Sigma}}{sL_{\text{arm}}+\left(R_{\text{arm}}+K_{\text{p}}\right)}
\end{aligned}
\tag{A.31}
$$

$$
\begin{aligned}
L_{\text{arm}}\frac{d\Delta i_{\text{diff}}^{(\text{dc})}}{dt}+\left(R_{\text{arm}}+\underbrace{2K_{\text{r}}}_{K_{\text{p}}}\right)\Delta i_{\text{diff}}^{(\text{dc})} &= -m_{\text{dc}}\Delta V_{\text{c,}\Delta}^{\Sigma}\\
\Delta i_{\text{diff}}^{(\text{dc})}(s) &= \frac{-m_{\text{dc}}\Delta V_{\text{c,}\Delta}^{\Sigma}}{sL_{\text{arm}}+\left(R_{\text{arm}}+K_{\text{p}}\right)}
\end{aligned}
\tag{A.32}
$$

In the last equation, it was assumed that $2K_\mathrm{r} = K_\mathrm{p}$, which is a reasonable assumption, given the inductances of the ac and dc equivalent circuits. Dynamic equations of the ac parasitic current components in the arm-common and arm-differential current were derived in (A.13) and (A.18). The dynamic equation governing the parasitic ac component $\Delta i_\mathrm{comm}^{(\mathrm{ac})}$ is repeated in (A.33) Assuming that the ac parasitic currents have the form as defined in (A.27), the dynamic equation takes the form as in (A.34).

$$L_\mathrm{arm}\frac{d\Delta i_\mathrm{comm}^{(\mathrm{ac})}}{dt} + \left(R_\mathrm{arm} + K_\mathrm{p}\right)\Delta i_\mathrm{comm}^{(\mathrm{ac})} = \frac{m_\mathrm{ac}}{2}\Delta V_{\mathrm{c},\Delta}^{\Sigma}\sin\left(\omega_\mathrm{g}t\right) \tag{A.33}$$

$$L_\mathrm{arm}\frac{d}{dt}\left(\Delta\hat{i}_\mathrm{comm}^{(\mathrm{ac})}\sin\left(\omega t + \beta\right)\right) + \left(R_\mathrm{arm} + K_\mathrm{p}\right)\Delta\hat{i}_\mathrm{comm}^{(\mathrm{ac})}\sin\left(\omega t + \beta\right) = \frac{m_\mathrm{ac}}{2}\Delta V_{\mathrm{c},\Delta}^{\Sigma}\sin\left(\omega_\mathrm{g}t\right) \tag{A.34}$$

To determine the dynamics of the amplitude $\Delta\hat{i}_\mathrm{comm}^{(\mathrm{ac})}$, some assumption should be made. As it will be proved later, the time constant $T_\mathrm{i}$ of the dynamic process is significantly lower than the period of the fundamental oscillations $T_\mathrm{g}$. This assumption is expressed in (A.35). Based on this assumption, we can observe the sinusoidal terms as quasi-static, i.e. assume their constant values in time. A straightforward way is to evaluate the oscillating terms at $\omega_\mathrm{g}t = \pi/2$, yielding the expression (A.36). With all the coefficients in the differential equation (A.36) being constant, Laplace transformation can be applied, resulting in (A.37),

$$T_\mathrm{i} = \frac{L_\mathrm{arm}}{R_\mathrm{arm} + K_\mathrm{p}} \ll T_\mathrm{g} = \frac{2\pi}{\omega_\mathrm{g}} \tag{A.35}$$

$$L_\mathrm{arm}\cos\left(\beta\right)\frac{d\Delta\hat{i}_\mathrm{comm}^{(\mathrm{ac})}}{dt} + \left(R_\mathrm{arm} + K_\mathrm{p}\right)\cos\left(\beta\right)\Delta\hat{i}_\mathrm{comm}^{(\mathrm{ac})} = \frac{m_\mathrm{ac}}{2}\Delta V_{\mathrm{c},\Delta}^{\Sigma} \tag{A.36}$$

$$\Delta\hat{i}_\mathrm{comm}^{(\mathrm{ac})}(s) = \frac{\frac{m_\mathrm{ac}}{2\cos\left(\beta\right)}\Delta V_{\mathrm{c},\Delta}^{\Sigma}}{sL_\mathrm{arm} + \left(R_\mathrm{arm} + K_\mathrm{p}\right)} \tag{A.37}$$

The last equation shows how the magnitude of the parasitic ac current $\Delta i_\mathrm{comm}^{(\mathrm{ac})}$ changes with the change in the voltage deviation component $\Delta V_{\mathrm{c},\Delta}^{\Sigma}$. However, besides the magnitude, this oscillating current component is determined by the phase-shift $\beta$. Under the assumption that the voltage deviation $\Delta V_{\mathrm{c},\Delta}^{\Sigma}$ is constant, and thus the magnitude $\Delta\hat{i}_\mathrm{comm}^{(\mathrm{ac})}$, equation (A.34) becomes (A.38). The identity (A.38) is satisfied when the phase-shift $\beta$ is given by (A.39).

$$\omega_\mathrm{g}L_\mathrm{arm}\left(\Delta\hat{i}_\mathrm{comm}^{(\mathrm{ac})}\cos\left(\omega_\mathrm{g}t + \beta\right)\right) + \left(R_\mathrm{arm} + K_\mathrm{p}\right)\Delta\hat{i}_\mathrm{comm}^{(\mathrm{ac})}\sin\left(\omega_\mathrm{g}t + \beta\right) = \frac{m_\mathrm{ac}}{2}\Delta V_{\mathrm{c},\Delta}^{\Sigma}\sin\left(\omega_\mathrm{g}t\right) \tag{A.38}$$

$$\beta = -\arctan\left(\frac{\omega_\mathrm{g}L_\mathrm{arm}}{R_\mathrm{arm} + K_\mathrm{p}}\right) \tag{A.39}$$

Similar analysis can be conducted for the other ac parasitic current component $\Delta i_{\text{diff}}^{(\text{ac})}$. Based on the same assumptions, the magnitude $\Delta \hat{i}_{\text{diff}}^{(\text{ac})}$ and the phase-shift $\alpha$ are described by:

$$\Delta \hat{i}_{\text{diff}}^{(\text{ac})}(s) = \frac{\frac{m_{\text{ac}}}{\cos(\alpha)} \Delta V_{\text{c},\Sigma}^{\Sigma}}{sL_{\text{arm}} + \left(R_{\text{arm}} + K_{\text{p}}\right)} \qquad \text{(A.40)} \qquad\qquad \alpha = -\arctan\left(\frac{\omega_{\text{g}} L_{\text{arm}}}{R_{\text{arm}} + K_{\text{p}}}\right) \qquad \text{(A.41)}$$

Applying Laplace transformation on the equations (A.29)-(A.30) yields:

$$sC_{\text{arm}} \Delta V_{\text{c},\Sigma}^{\Sigma}(s) = 2m_{\text{dc}} \Delta i_{\text{comm}}^{(\text{dc})}(s) - \frac{m_{\text{ac}}}{2} \Delta \hat{i}_{\text{diff}}^{(\text{ac})}(s) \cos(\alpha) \tag{A.42}$$

$$sC_{\text{arm}} \Delta V_{\text{c},\Delta}^{\Sigma}(s) = m_{\text{dc}} \Delta i_{\text{diff}}^{(\text{dc})}(s) - m_{\text{ac}} \Delta \hat{i}_{\text{comm}}^{(\text{ac})}(s) \cos(\beta) \tag{A.43}$$

Taking into account Laplace transformations of the four parasitic current components, the two equations become:

$$sC_{\text{arm}} \Delta V_{\text{c},\Sigma}^{\Sigma}(s) = \frac{-m_{\text{dc}}^2 \Delta V_{\text{c},\Sigma}^{\Sigma}}{sL_{\text{arm}} + \left(R_{\text{arm}} + K_{\text{p}}\right)} - \frac{\frac{m_{\text{ac}}^2}{2} \Delta V_{\text{c},\Sigma}^{\Sigma}}{sL_{\text{arm}} + \left(R_{\text{arm}} + K_{\text{p}}\right)} \tag{A.44}$$

$$sC_{\text{arm}} \Delta V_{\text{c},\Delta}^{\Sigma}(s) = \frac{-m_{\text{dc}}^2 \Delta V_{\text{c},\Delta}^{\Sigma}}{sL_{\text{arm}} + \left(R_{\text{arm}} + K_{\text{p}}\right)} - \frac{\frac{m_{\text{ac}}^2}{2} \Delta V_{\text{c},\Delta}^{\Sigma}}{sL_{\text{arm}} + \left(R_{\text{arm}} + K_{\text{p}}\right)} \tag{A.45}$$

Regrouping the equations (A.44)-(A.45), yields the $s$-domain equations for the two voltage deviations $\Delta V_{\text{c},\Sigma}^{\Sigma}$ and $\Delta V_{\text{c},\Delta}^{\Sigma}$:

$$\Delta V_{\text{c},\Sigma}^{\Sigma}(s)\left(s^2 C_{\text{arm}} L_{\text{arm}} + sC_{\text{arm}}\left(R_{\text{arm}} + K_{\text{p}}\right) + \left(m_{\text{dc}}^2 + \frac{m_{\text{ac}}^2}{2}\right)\right) = 0 \tag{A.46}$$

$$\Delta V_{\text{c},\Delta}^{\Sigma}(s)\left(s^2 C_{\text{arm}} L_{\text{arm}} + sC_{\text{arm}}\left(R_{\text{arm}} + K_{\text{p}}\right) + \left(m_{\text{dc}}^2 + \frac{m_{\text{ac}}^2}{2}\right)\right) = 0 \tag{A.47}$$

The last two equations show the self-balancing property of the direct-voltage-controlled MMC. Namely, in case when any deviation appears in any arm voltage, it will induce parasitic current components, which will act as a negative feedback action, and drive the deviations to zero. Consequently, the induced currents will be driven to zero as well.

Convergence of the voltage deviations $\Delta V_{\text{c},\Sigma}^{\Sigma}$ and $\Delta V_{\text{c},\Delta}^{\Sigma}$ to zero is determined by the term $R_{\text{arm}} + K_{\text{p}}$, where the latter summand is often dominant. Including the integral term in the arm-common current control would result in compensating for the parasitic voltage from the voltage deviation, which can be equivalently modelled as $K_{\text{p}} = 0$ in (A.46)-(A.47). Consequently, self-balancing property of the converter becomes determined by the parasitic arm resistance $R_{\text{arm}}$, which is typically small, resulting in a slow convergence process.

# Bibliography


[1] B. N. E. Finance. "New energy outlook 2021 - executive summary." (2021), [Online]. Available: https://about.bnef.com/new-energy-outlook/.

[2] I. R. E. A. (IRENA). "Renewable capacity highlights." (2021), [Online]. Available: https://www.irena.org/publications/2021/March/Renewable-Capacity-Statistics-2021.

[3] McKinsey and Company. "Global energy perspective 2021." (2021), [Online]. Available: https://www.mckinsey.com/industries/oil-and-gas/our-insights/global-energy-perspective-2021.

[4] M. Guarnieri, "The alternating evolution of dc power transmission [historical]," *IEEE Industrial Electronics Magazine*, vol. 7, no. 3, pp. 60–63, 2013.

[5] M. Stieneker, B. J. Mortimer, N. R. Averous, H. Stagge, and R. W. De Doncker, "Optimum design of medium-voltage dc collector grids depending on the offshore-wind-park power," in *2014 IEEE Symposium on Power Electronics and Machines for Wind and Water Applications*, Jul. 2014, pp. 1–8.

[6] H. A. B. Siddique, S. M. Ali, and R. W. De Doncker, "Dc collector grid configurations for large photovoltaic parks," in *2013 15th European Conference on Power Electronics and Applications (EPE)*, Sep. 2013, pp. 1–10.

[7] J. P. S. Bala, "Dc connection of offshore wind power plants without platform," 2014.

[8] J. Carr, D. Das, J. Li, J. Pan, S. Ebner, and O. Apeldoorn, "Modular multilevel converter for direct mvdc connection of offshore wind farms," in *2015 IEEE Energy Conversion Congress and Exposition (ECCE)*, Sep. 2015, pp. 976–982.

[9] A. Shekhar, E. Kontos, A. R. Mor, L. Ramírez-Elizondo, and P. Bauer, "Refurbishing existing mvac distribution cables to operate under dc conditions," in *2016 IEEE International Power Electronics and Motion Control Conference (PEMC)*, Sep. 2016, pp. 450–455.

[10] M. Stieneker and R. W. De Doncker, "Medium-voltage dc distribution grids in urban areas," in *2016 IEEE 7th International Symposium on Power Electronics for Distributed Generation Systems (PEDG)*, Jun. 2016, pp. 1–7.

[11] U. Javaid, F. D. Freijedo, D. Dujic, and W. van der Merwe, "Marine mvdc multi-phase multi-pulse supply," in *IECON 2017 - 43rd Annual Conference of the IEEE Industrial Electronics Society*, Oct. 2017, pp. 6807–6812.

[12] "Ieee recommended practice for 1 kv to 35 kv medium-voltage dc power systems on ships," *IEEE Std 1709-2018 (Revision of IEEE Std 1709-2010)*, pp. 1–54, 2018.

[13] R. Marquardt, "Modular multilevel converters: State of the art and future progress," *IEEE Power Electronics Magazine*, vol. 5, no. 4, pp. 24–31, Dec. 2018.

[14] Hitachi Energy. "The world's most powerful transmission system facilitated by Hitachi ABB Power Grids Technologies." (2020), [Online]. Available: https://www.hitachienergy.com/news/web-stories/2020/07/the-world-s-most-powerful-transmis-sion-system-facilitated-by-hi.

[15] A. Lesnicar and R. Marquardt, "An innovative modular multilevel converter topology suitable for a wide power range," in *2003 IEEE Bologna Power Tech Conference Proceedings,*, vol. 3, Jun. 2003, 6 pp. Vol.3-.

[16] R. Marquardt, "Modular multilevel converters: State of the art and future progress," *IEEE Power Electronics Magazine*, vol. 5, no. 4, pp. 24–31, Dec. 2018.

[17] S. P. Engel, M. Stieneker, N. Soltau, S. Rabiee, H. Stagge, and R. W. De Doncker, "Comparison of the modular multilevel dc converter and the dual-active bridge converter for power conversion in hvdc and mvdc grids," *IEEE Transactions on Power Electronics*, vol. 30, no. 1, pp. 124–137, Jan. 2015.

[18] Siemens Energy. "Hvdc plus brochure." (2021), [Online]. Available: https://assets.siemens-energy.com/siemens/assets/api/uuid:9555eb71-7b92-40d3-99a1-20be282abc87/2021-09-23-hvdc-plus.pdf.

[19] Hitachi ABB Power Grids. "Hitachi abb power grids - hvdc light reference list." (2021), [Online]. Available: https://search.abb.com/library/Download.aspx?DocumentID=POW0027&LanguageCode=en&DocumentPartId=&Action=Launch.

[20] M. Hagiwara, K. Nishimura, and H. Akagi, "A medium-voltage motor drive with a modular multilevel pwm inverter," *IEEE Transactions on Power Electronics*, vol. 25, no. 7, pp. 1786–1799, 2010.

[21] A. J. Korn, M. Winkelnkemper, and P. Steimer, "Low output frequency operation of the modular multi-level converter," in *2010 IEEE Energy Conversion Congress and Exposition*, 2010, pp. 3993–3997.

[22] A. Antonopoulos, K. Ilves, L. Ängquist, and H.-P. Nee, "On interaction between internal converter dynamics and current control of high-performance high-power ac motor drives with modular multilevel converters," in *2010 IEEE Energy Conversion Congress and Exposition*, 2010, pp. 4293–4298.

[23] J. Kolb, F. Kammerer, and M. Braun, "Straight forward vector control of the modular multilevel converter for feeding three-phase machines over their complete frequency range," in *IECON 2011 - 37th Annual Conference of the IEEE Industrial Electronics Society*, Nov. 2011, pp. 1596–1601.

[24] J. Pan, Z. Ke, M. Al Sabbagh, *et al.*, "7-kv 1-mva sic-based modular multilevel converter prototype for medium-voltage electric machine drives," *IEEE Transactions on Power Electronics*, vol. 35, no. 10, pp. 10 137–10 149, 2020.

[25] M. Hiller, D. Krug, R. Sommer, and S. Rohner, "A new highly modular medium voltage converter topology for industrial drive applications," in *2009 13th European Conference on Power Electronics and Applications*, 2009, pp. 1–10.

[26] Siemens. "Sinamics sh150 for special requirements." (2021), [Online]. Available: `https://new.siemens.com/global/en/products/drives/sinamics/medium-voltage-converters/sinamics-sh150.html`.

[27] Benshaw. "M2l series- medium voltage variable frequency drive." (2021), [Online]. Available: `https://benshaw.com/wp-content/uploads/2020/01/benshaw-m2l-3000-brochure.pdf`.

[28] General Electric. "Mm7 modular multilevel converter." (2021), [Online]. Available: `https://www.gepowerconversion.com/sites/default/files/GEA34256_Modular%20Multilevel%20Converter_FLY_en_20210322.pdf`.

[29] M. Vasiladiotis, R. Baumann, C. Häderli, and J. Steinke, "Igct-based direct ac/ac modular multilevel converters for pumped hydro storage plants," in *2018 IEEE Energy Conversion Congress and Exposition (ECCE)*, 2018, pp. 4837–4844.

[30] P. K. Steimer, O. Senturk, S. Aubert, and S. Linder, "Converter-fed synchronous machine for pumped hydro storage plants," in *2014 IEEE Energy Conversion Congress and Exposition (ECCE)*, 2014, pp. 4561–4567.

[31] M. Basić, M. Utvić, and D. Dujić, "Hybrid modular multilevel converter design and control for variable speed pumped hydro storage plants," *IEEE Access*, pp. 1–1, 2021.

[32] R. W. Erickson and O. A. Al-Naseem, "A new family of matrix converters," in *IECON'01. 27th Annual Conference of the IEEE Industrial Electronics Society (Cat. No.37243)*, vol. 2, Nov. 2001, 1515–1520 vol.2.

[33] A. J. Korn, M. Winkelnkemper, P. Steimer, and J. W. Kolar, "Direct modular multi-level converter for gearless low-speed drives," in *Proceedings of the 2011 14th European Conference on Power Electronics and Applications*, 2011, pp. 1–7.

[34] Y. Okazaki, W. Kawamura, M. Hagiwara, *et al.*, "Experimental comparisons between modular multilevel dscc inverters and tsbc converters for medium-voltage motor drives," *IEEE Transactions on Power Electronics*, vol. 32, no. 3, pp. 1805–1817, 2017.

[35] M. Winkelnkemper, A. Korn, and P. Steimer, "A modular direct converter for transformerless rail interties," in *2010 IEEE International Symposium on Industrial Electronics*, Jul. 2010, pp. 562–567.

[36] D. Weiss, M. Vasiladiotis, C. Banceanu, N. Drack, B. Odegard, and A. Grondona, "Igct based modular multilevel converter for an ac-ac rail power supply," in *PCIM Europe 2017; International Exhibition and Conference for Power Electronics, Intelligent Motion, Renewable Energy and Energy Management*, May 2017, pp. 1–8.

[37] Siemens Mobility. "Sitras SFC plus." (2018), [Online]. Available: `https://assets.new.siemens.com/siemens/assets/api/uuid:34846022-3f14-41de-ad46-d4c66a3e004c/siemens-sitras-sfcplus-pi-en.pdf`.

[38] Hitachi ABB Power Grids. "Rail sfc light brochure." (2021), [Online]. Available: `https://search.abb.com/library/Download.aspx?DocumentID=9AKK107992A6964&LanguageCode=en&DocumentPartId=&Action=Launch`.

[39] K. Sun, D. Soto, M. Steurer, and M. Faruque, "Experimental verification of limiting fault currents in mvdc systems by using modular multilevel converters," in *2015 IEEE Electric Ship Technologies Symposium (ESTS)*, 2015, pp. 27–33.

[40] M. M. Steurer, K. Schoder, O. Faruque, *et al.*, "Multifunctional megawatt-scale medium voltage dc test bed based on modular multilevel converter technology," *IEEE Transactions on Transportation Electrification*, vol. 2, no. 4, pp. 597–606, Dec. 2016.

[41] S. Li, L. Chen, P. Yang, K. Wang, Z. Zheng, and Y. Li, "System control strategy of an mmc-based pmsg rectifier for ship mvdc integrated power system," in *2019 IEEE Electric Ship Technologies Symposium (ESTS)*, 2019, pp. 195–200.

[42] Q. Chen, R. Li, and X. Cai, "Analysis and fault control of hybrid modular multilevel converter with integrated battery energy storage system," *IEEE Journal of Emerging and Selected Topics in Power Electronics*, vol. 5, no. 1, pp. 64–78, 2017.

[43] R. Mo, R. Li, and H. Li, "Isolated modular multilevel (imm) dc/dc converter with energy storage and active filter function for shipboard mvdc system applications," in *2015 IEEE Electric Ship Technologies Symposium (ESTS)*, 2015, pp. 113–117.

[44] Y. Chen, S. Zhao, Z. Li, X. Wei, and Y. Kang, "Modeling and control of the isolated dc–dc modular multilevel converter for electric ship medium voltage direct current power system," *IEEE Journal of Emerging and Selected Topics in Power Electronics*, vol. 5, no. 1, pp. 124–139, 2017.

[45] L. Hong, Q. Xu, Z. He, F. Ma, A. Luo, and J. M. Guerrero, "Fault-tolerant oriented hierarchical control and configuration of modular multilevel converter for shipboard mvdc system," *IEEE Transactions on Industrial Informatics*, vol. 15, no. 8, pp. 4525–4535, 2019.

[46] V. Steinsland, L. M. Kristensen, R. Arghandeh, and S. Zhang, "Design of modular multilevel converters for the shipnet in medium voltage dc all-electric ships," in *2020 IEEE 21st Workshop on Control and Modeling for Power Electronics (COMPEL)*, 2020, pp. 1–8.

[47] T. Kellner. "This offshore wind turbine is full of energy: Meet the haliade-x 14 mw." (2021), [Online]. Available: https://www.ge.com/news/reports/this-offshore-wind-turbine-is-full-of-energy-meet-the-haliade-x-14-mw.

[48] B. Novakovic and A. Nasiri, "Modular multilevel converter for wind energy storage applications," *IEEE Transactions on Industrial Electronics*, vol. 64, no. 11, pp. 8867–8876, 2017.

[49] General Electric. "Haliade-x 14 mw datasheet." (2021), [Online]. Available: https://en.wind-turbine-models.com/turbines/2320-ge-general-electric-haliade-x-14-mw.

[50] J. Kucka, D. Karwatzki, and A. Mertens, "Ac/ac modular multilevel converters in wind energy applications: Design considerations," in *2016 18th European Conference on Power Electronics and Applications (EPE'16 ECCE Europe)*, 2016, pp. 1–10.

[51] M. Diaz, R. Cardenas, M. Espinoza, *et al.*, "Control of wind energy conversion systems based on the modular multilevel matrix converter," *IEEE Transactions on Industrial Electronics*, vol. 64, no. 11, pp. 8799–8810, 2017.

[52] S. Liu, X. Wang, Y. Meng, P. Sun, H. Luo, and B. Wang, "A decoupled control strategy of modular multilevel matrix converter for fractional frequency transmission system," *IEEE Transactions on Power Delivery*, vol. 32, no. 4, pp. 2111–2121, 2017.

[53] B. Alajmi, K. Ahmed, G. Adam, S. Finney, and B. Williams, "Modular multilevel inverter with maximum power point tracking for grid connected photovoltaic application," in *2011 IEEE International Symposium on Industrial Electronics*, 2011, pp. 2057–2062.

[54] J. Mei, B. Xiao, K. Shen, L. M. Tolbert, and J. Y. Zheng, "Modular multilevel inverter with new modulation method and its application to photovoltaic grid-connected generator," *IEEE Transactions on Power Electronics*, vol. 28, no. 11, pp. 5063–5073, 2013.

[55] F. Rong, X. Gong, and S. Huang, "A novel grid-connected pv system based on mmc to get the maximum power under partial shading conditions," *IEEE Transactions on Power Electronics*, vol. 32, no. 6, pp. 4320–4333, 2017.

[56] L. Maharjan, S. Inoue, and H. Akagi, "A transformerless energy storage system based on a cascade multilevel pwm converter with star configuration," *IEEE Transactions on Industry Applications*, vol. 44, no. 5, pp. 1621–1630, 2008.

[57] A. M. Abbas and P. W. Lehn, "A unified power delivery solution for integrating der into distribution networks through vsc based dc system," in *2009 IEEE Power Energy Society General Meeting*, 2009, pp. 1–6.

[58] I. Trintis, S. Munk-Nielsen, and R. Teodorescu, "A new modular multilevel converter with integrated energy storage," in *IECON 2011 - 37th Annual Conference of the IEEE Industrial Electronics Society*, 2011, pp. 1075–1080.

[59] T. Soong and P. W. Lehn, "Evaluation of emerging modular multilevel converters for bess applications," *IEEE Transactions on Power Delivery*, vol. 29, no. 5, pp. 2086–2094, 2014.

[60] M. Vasiladiotis and A. Rufer, "Analysis and control of modular multilevel converters with integrated battery energy storage," *IEEE Transactions on Power Electronics*, vol. 30, no. 1, pp. 163–175, 2015.

[61] P. Hammond, "A new approach to enhance power quality for medium voltage drives," in *Industry Applications Society 42nd Annual Petroleum and Chemical Industry Conference*, 1995, pp. 231–235.

[62] F. Z. Peng, J.-S. Lai, J. McKeever, and J. VanCoevering, "A multilevel voltage-source inverter with separate dc sources for static var generation," *IEEE Transactions on Industry Applications*, vol. 32, no. 5, pp. 1130–1138, 1996.

[63] A. Lesnicar and R. Marquardt, "An innovative modular multilevel converter topology suitable for a wide power range," in *2003 IEEE Bologna Power Tech Conference Proceedings,*, vol. 3, Jun. 2003, 6 pp. Vol.3-.

[64] M. Hagiwara and H. Akagi, "Pwm control and experiment of modular multilevel converters," in *2008 IEEE Power Electronics Specialists Conference*, 2008, pp. 154–161.

[65] M. Hagiwara and H. Akagi, "Control and experiment of pulsewidth-modulated modular multilevel converters," *IEEE Transactions on Power Electronics*, vol. 24, no. 7, pp. 1737–1746, 2009.

[66] C. Oates, "A methodology for developing 'chainlink' converters," in *2009 13th European Conference on Power Electronics and Applications*, Sep. 2009, pp. 1–10.

[67] A. Antonopoulos, L. Angquist, and H.-P. Nee, "On dynamics and voltage control of the modular multilevel converter," in *Power Electronics and Applications, 2009. EPE'09. 13th European Conference on*, IEEE, 2009, pp. 1–10.

[68] R. Marquardt, "Modular multilevel converter topologies with dc-short circuit current limitation," in *8th International Conference on Power Electronics - ECCE Asia*, 2011, pp. 1425–1431.

[69] K. Ilves, L. Bessegato, L. Harnefors, S. Norrga, and H.-P. Nee, "Semi-full-bridge submodule for modular multilevel converters," in *2015 9th International Conference on Power Electronics and ECCE Asia (ICPE-ECCE Asia)*, 2015, pp. 1067–1074.

[70] A. Nami, J. Liang, F. Dijkhuizen, and G. D. Demetriades, "Modular multilevel converters for hvdc applications: Review on converter cells and functionalities," *IEEE Transactions on Power Electronics*, vol. 30, no. 1, pp. 18–36, 2015.

[71] C. Dahmen and R. Marquardt, "Progress of high power multilevel converters: Combining silicon and silicon carbide," in *PCIM Europe 2017; International Exhibition and Conference for Power Electronics, Intelligent Motion, Renewable Energy and Energy Management*, 2017, pp. 1–7.

[72] W. Lin, D. Jovcic, S. Nguefeu, and H. Saad, "Full-bridge mmc converter optimal design to hvdc operational requirements," *IEEE Transactions on Power Delivery*, vol. 31, no. 3, pp. 1342–1350, 2016.

[73] M. Basić, A. Schwery, and D. Dujić, "Highly flexible indirect modular multilevel converter for high power pumped hydro storage plants," in *IECON 2020 The 46th Annual Conference of the IEEE Industrial Electronics Society*, 2020, pp. 5290–5295.

[74] S. Sau and B. G. Fernandes, "Modular multilevel converter based variable speed drives with constant capacitor ripple voltage for wide speed range," in *IECON 2017 - 43rd Annual Conference of the IEEE Industrial Electronics Society*, 2017, pp. 2073–2078.

[75] B. Li, J. Hu, S. Zhou, and D. Xu, "Hybrid back-to-back mmc system for variable speed ac machine drives," *CPSS Transactions on Power Electronics and Applications*, vol. 5, no. 2, pp. 114–125, 2020.

[76] S. P. Engel and R. W. De Doncker, "Control of the modular multi-level converter for minimized cell capacitance," in *Proceedings of the 2011 14th European Conference on Power Electronics and Applications*, Aug. 2011, pp. 1–10.

[77] R. Picas, J. Pou, S. Ceballos, V. G. Agelidis, and M. Saeedifard, "Minimization of the capacitor voltage fluctuations of a modular multilevel converter by circulating current control," in *IECON 2012 - 38th Annual Conference on IEEE Industrial Electronics Society*, 2012, pp. 4985–4991.

[78] R. Picas, J. Pou, S. Ceballos, J. Zaragoza, G. Konstantinou, and V. G. Agelidis, "Optimal injection of harmonics in circulating currents of modular multilevel converters for capacitor voltage ripple minimization," in *2013 IEEE ECCE Asia Downunder*, 2013, pp. 318–324.

[79] J. Kolb, F. Kammerer, M. Gommeringer, and M. Braun, "Cascaded control system of the modular multilevel converter for feeding variable-speed drives," *IEEE Transactions on Power Electronics*, vol. 30, no. 1, pp. 349–357, Jan. 2015.

[80] M. Hagiwara, I. Hasegawa, and H. Akagi, "Start-up and low-speed operation of an electric motor driven by a modular multilevel cascade inverter," *IEEE Transactions on Industry Applications*, vol. 49, no. 4, pp. 1556–1565, 2013.

[81] S. Debnath, J. Qin, and M. Saeedifard, "Control and stability analysis of modular multilevel converter under low-frequency operation," *IEEE Transactions on Industrial Electronics*, vol. 62, no. 9, pp. 5329–5339, 2015.

[82] B. Li, S. Zhou, D. Xu, *et al.*, "An improved circulating current injection method for modular multilevel converters in variable-speed drives," *IEEE Transactions on Industrial Electronics*, vol. 63, no. 11, pp. 7215–7225, 2016.

[83] J.-J. Jung, H.-J. Lee, and S.-K. Sul, "Control strategy for improved dynamic performance of variable-speed drives with modular multilevel converter," *IEEE Journal of Emerging and Selected Topics in Power Electronics*, vol. 3, no. 2, pp. 371–380, 2015.

[84] A. Antonopoulos, L. Angquist, and H. Nee, "On dynamics and voltage control of the modular multilevel converter," in *2009 13th European Conference on Power Electronics and Applications*, Sep. 2009, pp. 1–10.

[85] L. Harnefors, S. Norrga, A. Antonopoulos, and H.-P. Nee, "Dynamic modeling of modular multilevel converters," in *Power Electronics and Applications (EPE 2011), Proceedings of the 2011-14th European Conference on*, IEEE, 2011, pp. 1–10.

[86] M. Guan and Z. Xu, "Modeling and control of a modular multilevel converter-based hvdc system under unbalanced grid conditions," *IEEE Transactions on Power Electronics*, vol. 27, no. 12, pp. 4858–4867, 2012.

[87] L. Angquist, A. Antonopoulos, D. Siemaszko, K. Ilves, M. Vasiladiotis, and H.-P. Nee, "Open-loop control of modular multilevel converters using estimation of stored energy," *IEEE Transactions on Industry Applications*, vol. 47, no. 6, pp. 2516–2524, 2011.

[88] G. S. Konstantinou, M. Ciobotaru, and V. G. Agelidis, "Analysis of multi-carrier pwm methods for back-to-back hvdc systems based on modular multilevel converters," in *IECON 2011 - 37th Annual Conference of the IEEE Industrial Electronics Society*, 2011, pp. 4391–4396.

[89] Q. Tu, Z. Xu, and L. Xu, "Reduced switching-frequency modulation and circulating current suppression for modular multilevel converters," *IEEE Transactions on Power Delivery*, vol. 26, no. 3, pp. 2009–2017, 2011.

[90] K. Ilves, L. Harnefors, S. Norrga, and H.-P. Nee, "Analysis and operation of modular multilevel converters with phase-shifted carrier PWM," *IEEE Transactions on Power Electronics*, vol. 30, no. 1, pp. 268–283, 2015.

[91] A. Hassanpoor, S. Norrga, H.-P. Nee, and L. Ängquist, "Evaluation of different carrier-based pwm methods for modular multilevel converters for hvdc application," in *IECON 2012 - 38th Annual Conference on IEEE Industrial Electronics Society*, 2012, pp. 388–393.

[92] F. Deng and Z. Chen, "A control method for voltage balancing in modular multilevel converters," *IEEE Transactions on Power Electronics*, vol. 29, no. 1, pp. 66–76, 2014.

[93] B. Li, R. Yang, D. Xu, G. Wang, W. Wang, and D. Xu, "Analysis of the phase-shifted carrier modulation for modular multilevel converters," *IEEE Transactions on Power Electronics*, vol. 30, no. 1, pp. 297–310, 2015.

[94] K. Sharifabadi, L. Harnefors, H.-P. Nee, S. Norrga, and R. Teodorescu, "Modulation and submodule energy balancing," in *Design, Control, and Application of Modular Multilevel Converters for HVDC Transmission Systems*. 2016, pp. 232–271.

[95] Q. Tu and Z. Xu, "Impact of sampling frequency on harmonic distortion for modular multilevel converter," *IEEE Transactions on Power Delivery*, vol. 26, no. 1, pp. 298–306, 2011.

[96] Y. Wang, C. Hu, R. Ding, L. Xu, C. Fu, and E. Yang, "A nearest level pwm method for the mmc in dc distribution grids," *IEEE Transactions on Power Electronics*, vol. 33, no. 11, pp. 9209–9218, 2018.

[97] A. Pérez-Basante, S. Ceballos, G. Konstantinou, J. Pou, J. Andreu, and I. M. de Alegría, "(2n+1) selective harmonic elimination-pwm for modular multilevel converters: A generalized formulation and a circulating current control method," *IEEE Transactions on Power Electronics*, vol. 33, no. 1, pp. 802–818, 2018.

[98] K. Ilves, A. Antonopoulos, S. Norrga, and H.-P. Nee, "A new modulation method for the modular multilevel converter allowing fundamental switching frequency," in *8th International Conference on Power Electronics - ECCE Asia*, 2011, pp. 991–998.

[99] M. Vasiladiotis, A. Christe, and T. Geyer, "Model predictive pulse pattern control for modular multilevel converters," *IEEE Transactions on Industrial Electronics*, vol. 66, no. 3, pp. 2423–2431, 2019.

[100] F. Kammerer, J. Kolb, and M. Braun, "Fully decoupled current control and energy balancing of the modular multilevel matrix converter," in *2012 15th International Power Electronics and Motion Control Conference (EPE/PEMC)*, 2012, LS2a.3-1-LS2a.3–8.

[101] W. Kawamura, M. Hagiwara, and H. Akagi, "Control and experiment of a modular multilevel cascade converter based on triple-star bridge cells," *IEEE Transactions on Industry Applications*, vol. 50, no. 5, pp. 3536–3548, 2014.

[102] W. Kawamura, M. Hagiwara, and H. Akagi, "A broad range of frequency control for the modular multilevel cascade converter based on triple-star bridge-cells (mmcc-tsbc)," in *2013 IEEE Energy Conversion Congress and Exposition*, 2013, pp. 4014–4021.

[103] R. Zeng, L. Xu, L. Yao, and S. J. Finney, "Analysis and control of modular multilevel converters under asymmetric arm impedance conditions," *IEEE Transactions on Industrial Electronics*, vol. 63, no. 1, pp. 71–81, Jan. 2016.

[104] P. Hu, D. Jiang, Y. Zhou, Y. Liang, J. Guo, and Z. Lin, "Energy-balancing control strategy for modular multilevel converters under submodule fault conditions," *IEEE Transactions on Power Electronics*, vol. 29, no. 9, pp. 5021–5030, 2014.

[105] B. Li, Z. Xu, J. Ding, and D. Xu, "Fault-tolerant control of medium-voltage modular multilevel converters with minimum performance degradation under submodule failures," *IEEE Access*, vol. 6, pp. 11 772–11 781, 2018.

[106] N. Thitichaiworakorn, M. Hagiwara, and H. Akagi, "Experimental verification of a modular multilevel cascade inverter based on double-star bridge-cells (mmci-dsbc)," in *2012 IEEE Energy Conversion Congress and Exposition (ECCE)*, 2012, pp. 4196–4202.

[107] S. Fan, K. Zhang, J. Xiong, and Y. Xue, "An improved control system for modular multilevel converters with new modulation strategy and voltage balancing control," *IEEE Transactions on Power Electronics*, vol. 30, no. 1, pp. 358–371, 2015.

[108] H. Saad, X. Guillaud, J. Mahseredjian, S. Dennetière, and S. Nguefeu, "Mmc capacitor voltage decoupling and balancing controls," *IEEE Transactions on Power Delivery*, vol. 30, no. 2, pp. 704–712, 2015.

[109] P. Münch, D. Görges, M. Izák, and S. Liu, "Integrated current control, energy control and energy balancing of Modular Multilevel Converters," in *IECON 2010 - 36th Annual Conference on IEEE Industrial Electronics Society*, Nov. 2010, pp. 150–155.

[110] A. J. Korn, M. Winkelnkemper, P. Steimer, and J. W. Kolar, "Capacitor voltage balancing in modular multilevel converters," in *6th IET International Conference on Power Electronics, Machines and Drives (PEMD 2012)*, Mar. 2012, pp. 1–5.

[111] G. Bergna, E. Berne, P. Egrot, *et al.*, "An energy-based controller for hvdc modular multilevel converter in decoupled double synchronous reference frame for voltage oscillation reduction," *IEEE Transactions on Industrial Electronics*, vol. 60, no. 6, pp. 2360–2371, 2013.

[112] Y. Wan, S. Liu, and J. Jiang, "Generalised analytical methods and current-energy control design for modular multilevel cascade converter," *IET Power Electronics*, vol. 6, no. 3, pp. 495–504, 2013. eprint: `https://ietresearch.onlinelibrary.wiley.com/doi/pdf/10.1049/iet-pel.2012.0494`.

[113] S. Cui, S. Kim, J.-J. Jung, and S.-K. Sul, "A comprehensive cell capacitor energy control strategy of a modular multilevel converter (mmc) without a stiff dc bus voltage source," in *2014 IEEE Applied Power Electronics Conference and Exposition - APEC 2014*, 2014, pp. 602–609.

[114] J. Kolb, F. Kammerer, M. Gommeringer, and M. Braun, "Cascaded control system of the modular multilevel converter for feeding variable-speed drives," *IEEE Transactions on Power Electronics*, vol. 30, no. 1, pp. 349–357, 2015.

[115] J.-J. Jung, S. Cui, Y. Lee, and S.-K. Sul, "A cell capacitor energy balancing control of mmc-hvdc under the ac grid faults," in *2015 9th International Conference on Power Electronics and ECCE Asia (ICPE-ECCE Asia)*, 2015, pp. 1–8.

[116] D. Karwatzki, L. Baruschka, M. Dokus, J. Kucka, and A. Mertens, "Branch energy balancing with a generalised control concept for modular multilevel topologies — using the example of the modular multilevel converter," in *2016 18th European Conference on Power Electronics and Applications (EPE'16 ECCE Europe)*, 2016, pp. 1–10.

[117] D. Karwatzki and A. Mertens, "Generalized control approach for a class of modular multilevel converter topologies," *IEEE Transactions on Power Electronics*, vol. 33, no. 4, pp. 2888–2900, 2018.

[118] M. Basić, S. Milovanović, and D. Dujić, "Comparison of two modular multilevel converter internal energy balancing methods," in *2019 20th International Symposium on Power Electronics (Ee)*, 2019, pp. 1–8.

[119] S. Milovanović and D. Dujić, "Comprehensive comparison of modular multilevel converter internal energy balancing methods," *IEEE Transactions on Power Electronics*, vol. 36, no. 8, pp. 8962–8977, 2021.

[120] S. Milovanovic and D. Dujic, "On power scalability of modular multilevel converters: Increasing current ratings through branch paralleling," *IEEE Power Electronics Magazine*, vol. 7, no. 2, pp. 53–63, 2020.

[121] S. Milovanovic and D. Dujic, "On power scalability of modular multilevel converters: Increasing current ratings through branch paralleling," *IEEE Power Electronics Magazine*, vol. 7, no. 2, pp. 53–63, 2020.

[122] Z. Ou, G. Wang, and L. Zhang, "Modular multilevel converter control strategy based on arm current control under unbalanced grid condition," *IEEE Transactions on Power Electronics*, vol. 33, no. 5, pp. 3826–3836, 2018.

[123] M. Schroeder, F. Mahr, J. Jaeger, and S. Haensel, "Energy balancing in the modular multilevel converter under unbalanced grid conditions," in *2017 19th European Conference on Power Electronics and Applications (EPE'17 ECCE Europe)*, 2017, P.1–P.10.

[124] A. E. Leon and S. J. Amodeo, "Energy balancing improvement of modular multilevel converters under unbalanced grid conditions," *IEEE Transactions on Power Electronics*, vol. 32, no. 8, pp. 6628–6637, Aug. 2017.

[125] P. Rodríguez, A. Luna, R. S. Muñoz-Aguilar, I. Etxeberria-Otadui, R. Teodorescu, and F. Blaabjerg, "A stationary reference frame grid synchronization system for three-phase grid-connected power converters under adverse grid conditions," *IEEE Transactions on Power Electronics*, vol. 27, no. 1, pp. 99–112, Jan. 2012.

[126] M. Basić, S. Milovanović, and D. Dujić, "Comparison of two Modular Multilevel Converter Internal Energy Balancing Methods," *20th International Symposium on Power Electronics, Ee 2019*, pp. 1–8, 2019.

[127] F. Kammerer, J. Kolb, and M. Braun, "A novel cascaded vector control scheme for the modular multilevel matrix converter," in *IECON 2011 - 37th Annual Conference of the IEEE Industrial Electronics Society*, 2011, pp. 1097–1102.

[128] F. Kammerer, M. Gommeringer, J. Kolb, and M. Braun, "Energy balancing of the modular multilevel matrix converter based on a new transformed arm power analysis," in *2014 16th European Conference on Power Electronics and Applications*, 2014, pp. 1–10.

[129] M. Diaz, R. Cardenas, M. Espinoza, *et al.*, "Vector control of a modular multilevel matrix converter operating over the full output-frequency range," *IEEE Transactions on Industrial Electronics*, vol. 66, no. 7, pp. 5102–5114, 2019.

[130] D. Karwatzki and A. Mertens, "Generalized control approach for a class of modular multilevel converter topologies," *IEEE Transactions on Power Electronics*, vol. 33, no. 4, pp. 2888–2900, 2018.

[131] J. Ma, M. S. A. Dahidah, V. Pickert, and J. Yu, "A hierarchical energy balance control method for m3c based on injecting output frequency circulating currents," *IEEE Transactions on Power Electronics*, vol. 35, no. 3, pp. 2424–2435, 2020.

[132] W. Kawamura, Y. Chiba, M. Hagiwara, and H. Akagi, "Experimental verification of an electrical drive fed by a modular multilevel tsbc converter when the motor frequency gets closer or equal to the supply frequency," *IEEE Transactions on Industry Applications*, vol. 53, no. 3, pp. 2297–2306, 2017.

[133] B. Fan, K. Wang, P. Wheeler, C. Gu, and Y. Li, "A branch current reallocation based energy balancing strategy for the modular multilevel matrix converter operating around equal frequency," *IEEE Transactions on Power Electronics*, vol. 33, no. 2, pp. 1105–1117, 2018.

[134] K. Ilves, L. Bessegato, and S. Norrga, "Comparison of cascaded multilevel converter topologies for ac/ac conversion," in *2014 International Power Electronics Conference (IPEC-Hiroshima 2014 - ECCE ASIA)*, 2014, pp. 1087–1094.

[135] S. Milovanovic, I. Polanco, M. Utvic, and D. Dujic, "Flexible and efficient mmc digital twin realized with small-scale real-time simulators," *IEEE Power Electronics Magazine*, vol. 8, no. 2, 2021.

[136] P. Bontemps, S. Milovanovic, and D. Dujic, "Distributed real-time model of the m3c for hil systems using small-scale simulators," *IEEE Open Journal of Power Electronics*, vol. 2, pp. 603–613, 2021.

[137] P. Bontemps, N. Hugo, and D. Dujic, "Flexibility enhancements in pumped hydro storage power plants through variable speed drives," in *IECON 2020 The 46th Annual Conference of the IEEE Industrial Electronics Society*, 2020, pp. 1820–1825.

[138] M. Glinka, "Prototype of multiphase modular-multilevel-converter with 2 mw power rating and 17-level-output-voltage," in *2004 IEEE 35th Annual Power Electronics Specialists Conference (IEEE Cat. No.04CH37551)*, vol. 4, 2004, 2572–2576 Vol.4.

[139] E. Solas, G. Abad, J. A. Barrena, S. Aurtenetxea, A. Cárcar, and L. Zając, "Modular multilevel converter with different submodule concepts—part ii: Experimental validation and comparison for hvdc application," *IEEE Transactions on Industrial Electronics*, vol. 60, no. 10, pp. 4536–4545, 2013.

[140] Binbin Li, Dandan Xu, Dianguo Xu, and Rongfeng Yang, "Prototype design and experimental verification of modular multilevel converter based back-to-back system," in *2014 IEEE 23rd International Symposium on Industrial Electronics (ISIE)*, 2014, pp. 626–630.

[141] Y. Zhou, D. Jiang, P. Hu, J. Guo, Y. Liang, and Z. Lin, "A prototype of modular multilevel converters," *IEEE Transactions on Power Electronics*, vol. 29, no. 7, pp. 3267–3278, 2014.

[142] M. Moranchel, F. M. Sanchez, E. J. Bueno, F. J. Rodriguez, and I. Sanz, "Six-level modular multilevel converter prototype with centralized hardware platform controller," in *IECON 2015 - 41st Annual Conference of the IEEE Industrial Electronics Society*, 2015, pp. 003 863–003 868.

[143] F. Gao, Z. Li, P. Wang, *et al.*, "Prototype of smart energy router for distribution dc grid," in *2015 17th European Conference on Power Electronics and Applications (EPE'15 ECCE-Europe)*, 2015, pp. 1–9.

[144] M. Vasiladiotis, N. Cherix, and A. Rufer, "Impact of grid asymmetries on the operation and capacitive energy storage design of modular multilevel converters," *IEEE Transactions on Industrial Electronics*, vol. 62, no. 11, pp. 6697–6707, 2015.

[145] D. Siemaszko, E. T. Louokdom, H. Parisod, *et al.*, "Implementation and experimental set-up of a modular multilevel converter in a multi terminal dc/ac transmission network," in *2016 18th European Conference on Power Electronics and Applications (EPE'16 ECCE Europe)*, 2016, pp. 1–12.

[146] L. Dong, G. Lu, and K. Longze, "A design method of mmc-hvdc physical simulation system," in *2017 IEEE Conference on Energy Internet and Energy System Integration (EI2)*, 2017, pp. 1–6.

[147] L. Bessegato, A. Narula, P. Bakas, and S. Norrga, "Design of a modular multilevel converter prototype for research purposes," in *2018 20th European Conference on Power Electronics and Applications (EPE'18 ECCE Europe)*, 2018, P.1–P.10.

[148] S. Sau and B. G. Fernandes, "Modular multilevel converter based variable speed drive with reduced capacitor ripple voltage," *IEEE Transactions on Industrial Electronics*, vol. 66, no. 5, pp. 3412–3421, 2019.

[149] N. Herath and S. Filizadeh, "Design and implementation of a laboratory prototype of a modular multilevel converter with embedded storage," in *2019 14th Conference on Industrial and Information Systems (ICIIS)*, 2019, pp. 234–238.

[150] W. Dong, X. Zhang, L. Jing, and W. Wu, "Design of rapid-control-prototype platform for modular multilevel converter based on rt-lab," in *2019 IEEE 10th International Symposium on Power Electronics for Distributed Generation Systems (PEDG)*, 2019, pp. 94–98.

[151] J. Pan, Z. Ke, M. Al Sabbagh, *et al.*, "7-kv 1-mva sic-based modular multilevel converter prototype for medium-voltage electric machine drives," *IEEE Transactions on Power Electronics*, vol. 35, no. 10, pp. 10 137–10 149, 2020.

[152] A. Christe, E. Coulinge, and D. Dujic, "Insulation coordination for a modular multilevel converter prototype," in *2016 18th European Conference on Power Electronics and Applications (EPE'16 ECCE Europe)*, 2016, pp. 1–9.

[153] E. Coulinge, A. Christe, and D. Dujic, "Electro-thermal design of a modular multilevel converter prototype," in *PCIM Europe 2016; International Exhibition and Conference for Power Electronics, Intelligent Motion, Renewable Energy and Energy Management*, 2016, pp. 1–8.

[154] M. Utvic, I. Polanco, and D. Dujic, "Low voltage modular multilevel converter submodule for medium voltage applications," in *PCIM Europe 2019; International Exhibition and Conference for Power Electronics, Intelligent Motion, Renewable Energy and Energy Management*, May 2019, pp. 1–8.

[155] I. Polanco and D. Dujic, "Thermal study of a modular multilevel converter submodule," in *PCIM Europe digital days 2020; International Exhibition and Conference for Power Electronics, Intelligent Motion, Renewable Energy and Energy Management*, 2020, pp. 1–8.

[156] A. Christe, M. Petkovic, I. Polanco, M. Utvic, and D. Dujic, "Auxiliary submodule power supply for a medium voltage modular multilevel converter," *CPSS Transactions on Power Electronics and Applications*, vol. 4, no. 3, pp. 204–218, 2019.

[157] H. Saad, T. Ould-Bachir, J. Mahseredjian, C. Dufour, S. Dennetière, and S. Nguefeu, "Real-time simulation of mmcs using cpu and fpga," *IEEE Transactions on Power Electronics*, vol. 30, no. 1, pp. 259–267, 2015.

[158] W. Li and J. Bélanger, "An equivalent circuit method for modelling and simulation of modular multilevel converters in real-time hil test bench," *IEEE Transactions on Power Delivery*, vol. 31, no. 5, pp. 2401–2409, 2016.

[159] C. Dong, W. Yan-kun, M. Yu-long, Y. Ping-ping, and W. Zhi-peng, "Real time digital simulation and hil test of xiamen mmc-hvdc demonstration project," in *2016 International High Voltage Direct Current Conference (HVDC 2016)*, 2016, pp. 1–5.

[160] G. Li, D. Zhang, Y. Xin, S. Jiang, W. Wang, and J. Du, "Design of mmc hardware-in-the-loop platform and controller test scheme," *CPSS Transactions on Power Electronics and Applications*, vol. 4, no. 2, pp. 143–151, 2019.

[161] D. Dujic. "Accelerate power electronics development- Choose your tools wisely." (2020), [Online]. Available: `https://www.power-and-beyond.com/accelerate-power-electronics-development--choose-your-tools-wisely-a-976994/`.

[162] S. Milovanovic and D. Dujic, "Upscaling small real-time simulators for large power electronic systems," *Bodo's Power Systems*, no. 0, pp. 72–74, May 2021.

[163] M. Utvić, S. Milovanović, and D. Dujić, "Flexible medium voltage dc source utilizing series connected modular multilevel converters," in *2019 21st European Conference on Power Electronics and Applications (EPE '19 ECCE Europe)*, 2019, pp. 1–9.

[164] M. M. Steurer, K. Schoder, O. Faruque, *et al.*, "Multifunctional megawatt-scale medium voltage dc test bed based on modular multilevel converter technology," *IEEE Transactions on Transportation Electrification*, vol. 2, no. 4, pp. 597–606, 2016.

[165] P. Blaszczyk, M. Steurer, D. Soto, *et al.*, "Modular multilevel converter based test bed for mvdc applications — a case study with a 12 kv, 5 mw setup," in *2016 IEEE International Power Electronics and Motion Control Conference (PEMC)*, 2016, pp. 139–145.

[166] B. Li, S. Zhou, D. Xu, S. J. Finney, and B. W. Williams, "A hybrid modular multilevel converter for medium-voltage variable-speed motor drives," *IEEE Transactions on Power Electronics*, vol. 32, no. 6, pp. 4619–4630, 2017.

[167] W. Lin, D. Jovcic, S. Nguefeu, and H. Saad, "Full-bridge mmc converter optimal design to hvdc operational requirements," *IEEE Transactions on Power Delivery*, vol. 31, no. 3, pp. 1342–1350, 2016.

[168] M. Hagiwara, R. Maeda, and H. Akagi, "Control and analysis of the modular multilevel cascade converter based on double-star chopper-cells (mmcc-dscc)," *IEEE Transactions on Power Electronics*, vol. 26, no. 6, pp. 1649–1658, Jun. 2011.

[169] L. Harnefors, A. Antonopoulos, S. Norrga, L. Angquist, and H. Nee, "Dynamic analysis of modular multilevel converters," *IEEE Transactions on Industrial Electronics*, vol. 60, no. 7, pp. 2526–2537, Jul. 2013.

[170] W. Kawamura and H. Akagi, "Control of the modular multilevel cascade converter based on triple-star bridge-cells (mmcc-tsbc) for motor drives," in *2012 IEEE Energy Conversion Congress and Exposition (ECCE)*, 2012, pp. 3506–3513.

[171] ABB. "AC 800PEC - The high-performance control system for model-based design." (2011), [Online]. Available: `https://library.e.abb.com/public/a7566254919255a0c12578c3003355f7/AC%20800PEC%20Sales%20Brochure.pdf`.

[172] B. P. McGrath, D. G. Holmes, and W. Y. Kong, "A decentralized controller architecture for a cascaded h-bridge multilevel converter," *IEEE Transactions on Industrial Electronics*, vol. 61, no. 3, pp. 1169–1178, 2014.

[173] S. Yang, Y. Tang, and P. Wang, "Distributed control for a modular multilevel converter," *IEEE Transactions on Power Electronics*, vol. 33, no. 7, pp. 5578–5591, 2018.

[174] S. Yang, S. Liu, J. Huang, H. Su, and H. Wang, "Control conflict suppressing and stability improving for an mmc distributed control system," *IEEE Transactions on Power Electronics*, vol. 35, no. 12, pp. 13 735–13 747, 2020.

[175] Q. Tu, Z. Xu, and L. Xu, "Reduced switching-frequency modulation and circulating current suppression for modular multilevel converters," *IEEE Transactions on Power Delivery*, vol. 26, no. 3, pp. 2009–2017, 2011.

[176] K. Ilves, A. Antonopoulos, S. Norrga, and H. Nee, "A new modulation method for the modular multilevel converter allowing fundamental switching frequency," *IEEE Transactions on Power Electronics*, vol. 27, no. 8, pp. 3482–3494, 2012.

[177] K. Wang, Y. Li, Z. Zheng, and L. Xu, "Voltage balancing and fluctuation-suppression methods of floating capacitors in a new modular multilevel converter," *IEEE Transactions on Industrial Electronics*, vol. 60, no. 5, pp. 1943–1954, 2013.

[178] J. Allmeling and N. Felderer, "Sub-cycle average models with integrated diodes for real-time simulation of power converters," in *2017 IEEE Southern Power Electronics Conference (SPEC)*, 2017, pp. 1–6.

# Milan Utvić

*PhD candidate in Power Electronics*

✉ *milan.utvic@alumni.epfl.ch*
*born 07.10.1992*
*Serbian*

## HIGHER EDUCATION

### École Polytechnique Fédérale de Lausanne, Lausanne, Switzerland

2018-2023 PhD Candidate, *Doctoral School in Energy*
On Energy Control of Modular Multilevel Converters

### University of Belgrade, School of Electrical Engineering, Belgrade, Serbia

2015-2017 MSc, The Department of Power Converters and Drive Systems

### University of Belgrade, School of Electrical Engineering, Belgrade, Serbia

2011-2015 BSc, The Department of Power Converters and Drive Systems

## PROFESSIONAL EXPERIENCE

2016-2017 Teaching and Research Assistant, University of Belgrade, School of Electrical Engineering
2018-2022 Doctoral Assistant, École Polytechnique Fédérale de Lausanne, Lausanne, Switzerland
2022-present Power Electronics Engineer, H55 SA, Sion, Switzerland

## LANGUAGES

Serbian Native
English Fluent
French Upper intermediate

## REVIEW

Regular reviewer for IEEE Transactions on Power Electronics and IEEE Transactions on Industrial Electronics, plus various conferences.